UNIVERSITY of CALIFORNIA
Santa Barbara

Adventures in high-field electron paramagnetic resonance

A dissertation submitted in partial satisfaction of the
requirements for the degree of

Doctor of Philosophy

in

Physics

by

Christopher Blake Wilson

Committee in charge:

Professor Mark S. Sherwin, Co-chair
Professor Songi Han, Co-chair
Professor Ania Bleszynski Jayich
Professor Philip A. Pincus

September 2019

The dissertation of Christopher Blake Wilson is approved.

Professor Ania Bleszynski Jayich

Professor Philip A. Pincus

Professor Songi Han, Co-chair

Professor Mark S. Sherwin, Co-chair

July 2019

Acknowledgements

I would like to thank my advisors Mark Sherwin and Songi Han for all of their tireless support over the course of my Ph.D. dissertation. Mark and Songi, thank you for making me a part of your research groups. Thank you for your advice, for your patience, for the freedom you gave me, and most of all for teaching me how to be a scientist.

I would like to thank close collaborator Prof. Steffen Glaser for his countless good ideas and always valuable insights, and for spending so much time at UCSB. I would also like to thank Prof. Ania Jayich for sharing her advice, and Prof. Fyl Pincus for his input. Thank you also to Prof. Bob Griffin for introducing me to magnetic resonance, to Dr. Garnier for introducing me to spectroscopy, and to Dr. Baganoff for introducing me to scientific research.

Thank you to my labmates, for all of your help, and for making the FEL lab what it is. Thank you Jessica Clayton, for being my teacher, mentor, and closest collaborator over the course of graduate school, for all your help in lab, and for all of our useful discussions. Thank you Marzieh Kavand and Cocoa Wang for sharing your research experience, and for your input towards building a better instrument. Thank you Chung-ta Han and Matt Idso for teaching me about the wonderful world of molecular biology. From the Han lab, thank you Alisa Leavesley, Ilia Kaminker, Tim Keller, Ting Ann Siaw, Sheetal Jain, and Asif Equbal for all of your help and input over the years. From the Sherwin lab, thank you Darren Valovcin for sharing your physics and FEL-related wisdom, and thank you Sam Aronson, Michael Balcewicz, and Kunal Lakhanpal for dedicating time and energy to conducting research with me. Thank you Hunter Banks, Changyun Yoo, Seamus O'Hara, Joe Costello, Andrew Pierce, Qile Wu, Carmen Roelcke, Alicia Lund, Ryan Barnes, Tarnuma Tabassum, Kan Tagami, Miranda Li, and many others, for being a wonderful labmates and partners in crime.

The UCSB free electron lasers made possible much of the work in this dissertation. Thank you Dave Enyeart, Gerry Ramian, and Nick Agladze for all of the work you have done, to make the FEL facility what it is today and to keep the FEL running. Thank you Devin Edwards, Susumu Takahashi, and Louis-Claude Brunel for all the work you did to make FEL-EPR possible.

The UCSB physics department staff are a wonderful group who have helped me countless times. Thank you Jennifer Farrar, Rob Marquez, Rita Makogon, Elizabeth Strait, Mike Deal, Dave Prine, Dan Stack, and Erin Ferguson for all of your hard work.

Graduate school would have been dull indeed without the help of my friends and housemates KS, LB, RB, ZG, RS, JG, DI, MS, EB, KB, GC, NB, JF, TS, DK, and many, many others.

Thank you Aubrey, for your patience and your support. Finally, I would like to thank my family, my parents, my brother, and the Middleton Lane crew for encouraging me, humoring my "what if?" questions, and always believing in me.

Curriculum Vitæ

Christopher Blake Wilson

Education

2019	Ph.D., Physics, University of California, Santa Barbara, California
2016	M.A., Physics, University of California, Santa Barbara, California
2013	B.S., Physics, Massachusetts Institute of Technology, Cambridge, Massachusetts
2009	Bethesda Chevy Chase High School, Bethesda, Maryland

Professional Experience

2014-2019	Graduate research assistant, Department of Physics, UCSB
2013-2014	Teaching assistant, Department of Physics, UCSB
2011-2013	Undergraduate research assistant, Francis Bitter Magnet Lab, MIT
2011-2013	Undergraduate teaching assistant, Department of Physics, MIT
2010-2011	Undergraduate research assistant, Plasma Science and Fusion Center, MIT

Publications

"Anomalous Bloch sphere dynamics in a crystalline organic radical observed by pulsed electron paramagnetic resonance at 240 GHz," Wilson, C. B., Edwards, D. T., Clayton, J. A., Han. S., and Sherwin, M. S., *arXiv:1904.03578* (2019)

"High-Resolution ^{17}O NMR Spectroscopy of Structural Water", Keeler, E. G., Michaelis, V. K., Wilson, C. B., Hung, I., Wang, X., Gan, Z., and Griffin, R. G., *The Journal of Physical Chemistry B*, Vol. 123, 3061-3067 (2019)

"Multi-step phase-cycling in a free-electron laser-powered pulsed electron paramagnetic resonance spectrometer", Wilson, C. B., Aronson, S., Clayton, J. A., Glaser, S. J., Han, S., and Sherwin, M. S., *Physical Chemistry Chemical Physics*, Vol. 20, 18097-18109 (2018)

"Effect of water/glycerol polymorphism on dynamic nuclear polarization", Leavesley, A., Wilson, C. B., Sherwin, M. S., and Han, S., *Physical Chemistry Chemical Physics*, Vol. 20, 9897-9903 (2018)

"Reversal of paramagnetic effects by electron spin saturation"', Jain., S. K., Siaw., T. A., Equbal, A., Wilson, C. B., Kaminker, I., Han, S., *The Journal of Physical Chemistry C*, Vol, 122, 5578-5598 (2018)

Abstract

Adventures in high-field electron paramagnetic resonance

by

Christopher Blake Wilson

Electron paramagnetic resonance (EPR) is a powerful technique for studying paramagnetic species and their environments, with applications in chemistry, biology, physics, and material science. When combined with site-directed spin-labeling, EPR can be used to answer important questions about the structure, function, and dynamics of biomolecules in their native environments. EPR becomes more powerful as it moves to higher magnetic fields, and as it moves from continuous wave (CW) techniques to pulsed techniques, however technological challenges have slowed the progress of high-field EPR and limited its application to a few select systems. This work takes a multi-directional approach to expanding the capabilities of high-field EPR.

The main factors limiting high-field pulsed EPR have been challenges associated with generating high-frequency sub-THz and THz microwave radiation of sufficient power. This limitation has been directly addressed at UCSB by the development of a novel high-power EPR spectrometer operating at 8.5 T which uses the UCSB mm-wave free electron laser (FEL) as a source of kW 240 GHz microwave radiation. The FEL-powered EPR is the highest power pulsed EPR experiment operating over 100 GHz, and is capable

of broadband, coherent spin manipulations at high magnetic fields on ∼ns timescales. In this work, an all-quasioptical, optomechanical phase control procedure is described and implemented at 240 GHz, providing transformative capabilities including facilitating coherence transfer pathway selection, reducing experimental deadtimes, and enabling high-field, room-temperature spin relaxation time measurements. High-bandwidth pulses are used to explore nonlinear spin dynamics in BDPA, an organic crystalline radical, and to map out the spin system's anomalous Bloch sphere trajectories.

High-field EPR can be powerfully combined with high-spin Gd^{3+} spin labels for enhanced sensitivity and access to a wider range of distance constraints in protein structure measurements. Relaxation and decoherence mechanisms in Gd^{3+} spin are studied, and a model describing Gd^{3+} spin coherence lifetimes at high magnetic field is proposed and validated. New insights into the mechanisms driving spin decoherence in Gd^{3+} lead to more sensitive measurements of local average inter-spin distances. Sample geometries for high-field EPR designed and optimized based on optics principles demonstrate dramatic signal enhancements, especially for lossy, aqueous samples.

Finally, high-field EPR is applied to study the protein proteorhodopsin (PR), a light-activated trans-membrane ^{1}H pump found in marine bacterioplankton. A paramagnetic spin probe tethered to PR reports on protein conformational changes brought on by photoexcitation. Time-resolved 240 GHz EPR, together with time-resolved optical absorption spectroscopy, is applied to explore the relationships between structure and function in PR.

Contents

List of Figures

List of Tables

Chapter 1

Introduction

Electron paramagnetic resonance (EPR) is a spectroscopic technique which studies interactions between unpaired electrons and electromagnetic fields. EPR, also called electron spin resonance (ESR), is a lesser-known cousin of nuclear magnetic resonance (NMR). NMR spectroscopy is widely used in analytical chemistry and material science, and NMR imaging has become an important tool in modern medicine. NMR studies interactions between electromagnetic fields and nuclear spins, which are abundant in nearly all materials, since virtually every element in the periodic table has at least one stable NMR-active isotope. EPR, by contrast, has a narrower scope of applications and potential since it is limited to materials with unpaired electrons. Furthermore, NMR is typically performed with electromagnetic fields at frequencies of 10's of MHz to, recently, up to 1 GHz, which are easy to generate and detect using mature, widely commercially available technology. EPR, on the other hand, requires much higher frequencies, typically 10s of GHz on the

low end and extending to THz frequencies, which are difficult to generate and detect and require specialized equipment and knowledge.

EPR was discovered in 1944 in the USSR by Zavoisky [1], and has progressed over the last seven decades into a useful tool in several fairly specialized applications, including materials characterization, quantum information science, analytical chemistry, and biochemistry. Over the same timeframe, NMR was discovered, was awarded four Nobel prizes in three different disciplines (physics, chemistry (twice), and medicine), and has become a standard tool used by scientists, doctors, and technicians in a number of disciplines.

Nevertheless, EPR offers vast potential for growth and development, particularly as a technique for studying biological systems. Paramagnetic spin probes tethered to biomolecules [2] can be used as site-specific reporters to extract structural information, local information about surface hydration, measurements of side-chain mobility, of pH, and of dynamics, and to probe protein docking or oligomerization. EPR hyperfine spectroscopy can be used to study paramagnetic centers in metalloenzymes and metalloproteins with near-atomic resolution [3, 4], and EPR dipolar spectroscopy can be used to measure distances between unpaired electron spins separated by 1-10 nm, providing long-range distance constraints even in disordered, highly heterogeneous materials.

For structure studies, EPR is highly complementary to other commonly used techniques such as X-ray crystallography and electron microscopy (EM) [5]. X-ray crystallography and EM offer atomic resolution, but require extensive sample preparation and

come with restrictions on the types of samples which can be addressed, with membrane proteins and protein-lipid assemblies proving to be particularly challenging. EPR does not require crystallization, and can be performed in relatively "dirty," biologically relevant environments, including inside living cells [6], where complex biomolecular activity and crowded conditions preclude the application of most other techniques. In addition, EPR can provide information about ensembles, and dynamics which are frozen out in X-ray crystallography and EM.

Compared to NMR, which also offers atomic resolution structural information and which can be performed on proteins in biologically relevant conditions, EPR offers significantly improved sensitivity and access to long-range distances to which NMR is typically blind. EPR is 2-3 orders of magnitude more sensitive than NMR performed on even the most favorable nuclei, such as ^{1}H, ^{3}H, and ^{19}F, and is 3-4 orders of magnitude more sensitive than a range of less favorable nuclei. This sensitivity is made all the more powerful by the relative scarcity of unpaired electrons in most materials, so that signals only come from specific sites of interest, and not from a background of unwanted spins, as is often the case in NMR. EPR can be powerfully employed to study defects and interfaces in materials, where NMR struggles due to low sensitivity and due to lack of discrimination between the signals of interest and the often much larger signals from nuclei in the bulk.

This dissertation describes efforts to expand the impact and scope of EPR spectroscopy by extending EPR to higher fields and frequencies, which is desirable for several reasons. Fundamentally, moving to higher field increases the intrinsic sensitivity of EPR

due to the larger Boltzmann spin polarizations at routinely-achievable experimental temperatures (> 4 K). In addition, high field EPR provides improved time resolution and spectral resolution. These advantages are particularly useful for studying biological samples [7, 8, 9] where high resolution is required but sample volumes are often extremely limited, or for performing precision measurements of electron g tensors [8, 10, 11]. Improved spectral resolution can be leveraged by pulsed dipolar spectroscopy techniques [12, 13] conducted at high field to probe inter-spin distances with orientation selectivity, [14, 15, 16].

Most EPR is performed at fields below 0.5 T, and at frequencies below 10 GHz, where instrumentation which has benefitted from flexible signal generators and powerful amplifiers developed originally for radar applications and adopted by spectroscopists. In past decades, EPR experiments have begun to adopt higher magnetic fields, with many research institutions operating 1.2 T / 35 GHz EPR spectrometers. Higher frequency spectrometers, with fields in excess of 5 T, exist only in a few specialized labs. The limiting factor for moving EPR to higher magnetic fields is the microwave source, which must scale up in frequency in proportion to the increased magnetic field. NMR, by contrast, is routinely performed at fields above 20 T, with high-resolution NMR experiments operating at up to 35.2 T [17], and with limited resolution at up to 44 T [18]. The limiting factor for moving NMR to higher fields is magnet technology- if stronger, sufficiently stable, magnetics were available, NMR could easily be adapted to higher fields.

Going to high fields and frequencies is often essential for studying electron spins with

$S > 1/2$. For high-spin systems, large zero field splitting (ZFS) can make it impossible to employ EPR at low fields and frequencies, if the ZFS strength is much larger than the Zeeman energy. High-field EPR is an invaluable tool for studying half-integer high-spin electron systems, which have favorable high-field spectral properties as discussed in section 1.2.1. Dipolar spectroscopy with half-integer high-spin metal centers, using pulsed EPR techniques [19, 20, 6, 21, 22, 23] or EPR lineshape analysis [24, 25] is a powerful and sensitive way of measuring inter-electron dipolar couplings for distance determination in biological or material systems.

EPR spectroscopy is a powerful technique on its own, but really shows its true strength and flexibility when paired with NMR spectroscopy. A variety of two-frequency experiments where both electron and nuclear spins are addressed have been developed to great success, leveraging the high sensitivity provided by EPR with the high resolution of NMR spectroscopy. Examples of such techniques include Electron-Nuclear DOuble Resonance (ENDOR) [26, 27, 28], and dynamic nuclear polarization (DNP)- enhanced NMR [29, 30]. NMR becomes increasingly powerful at higher magnetic fields and frequencies. NMR spectrometers operating at 23.5 T for a 1 GHz ^{1}H Larmor frequency are commercially available, with 28.2 T (1.2 GHz ^{1}H Larmor frequency) soon to be commercialized. In order to reap the full benefits of double resonance techniques, EPR should move to join NMR at these high fields.

Many of the principle advantages of high-field EPR are difficult to realize in practice, unfortunately, due to the lack of techniques for generating high-power, high-frequency

microwave and THz radiation. For this reason, high-field EPR is typically limited to low power (<10 mW) continuous wave experiments, foregoing the advantages of pulsed techniques, or is restricted to specific systems, where relaxation times are long enough to allow for long (>100 ns) pulses for spin manipulations, or which are compatible with extremely volume- and experimental bandwidth-limiting microwave cavities.

Pulsed EPR spectrometers powered by frequency-multiplied solid-state microwave sources are available commercially at 263 GHz with 10s of mW of power, and at similar frequencies in a few specialized labs [31, 32, 33, 34, 35, 36, 37, 38]. Extended interaction Klystron (EIK) amplifiers have been employed in EPR spectrometers operating at up to 95 GHz [39, 40, 41], where they can provide up to ∼kWs of power. In recent years, gyrotron-amplifiers [42, 43] have developed as promising candidates for high-power microwave sources at > 100 GHz, however this technology is still maturing and has not yet been successfully demonstrated in an EPR or DNP ospectrometer.

High-powered oscillators such as gyrotrons and free electron lasers are alternative methods for generating high-power microwaves at high frequencies. Oscillators can generate power much in excess of 1 kW in the sub-THz frequency range [44, 45, 46, 47]. Even modest improvements in power over high-frequency amplifier technologies have been shown to be beneficial: for example, DNP-enhanced NMR has been performed with gyrotrons producing 5-20 W of power [48, 49], with revolutionary gains in NMR sensitivity. Work by Barnes and collaborators [50] demonstrated DNP-enhanced NMR with electron spin decoupling using a frequency-agile gyrotron operating at 250 GHz.

Over the last 10 years, a 240 GHz EPR spectrometer [51] which operates using the UCSB mm-wave FEL (mm-FEL) has been developed and demonstrated as part of a collaboration between Professor Mark Sherwin and Professor Songi Han at UCSB. Operating at microwave powers of ∼500 W to ∼9 kW, and capable of applying coherent inversion pulses to spin-1/2 electrons in 12 ns, the UCSB "FEL-EPR" spectrometer provides transformative capabilities. Chapters 2 and 3, and part of Chapter 5 of this dissertation detail experiments performed with the FEL-EPR spectrometer. The FEL-EPR spectrometer can additionally operate with a 55 mW 240 GHz solid-state microwave source, enabling complementary continuous-wave (CW) EPR and low-power pulsed EPR in the same experimental platform. Chapters 4, 5, and 6 of this dissertation deal primarily with measurements performed in the dual, low-power operating mode.

Chapter 2 deals with improvements made to the FEL-EPR spectrometer over the last several years, and the new science that has been made accessible by these improvements. The key development has been the ability to independently control the phases and amplitudes of high-power FEL-generated EPR pulses, enabling phase cycling and coherence transfer pathway selection in FEL-EPR.

Chapter 3 presents an FEL-EPR study of non-linear electron spin dynamics which arise at room temperature in a crystalline organic radical. Experiments performed on crystalline BDPA (1,3-bisdiphenylene-2-phenylallyl) showed, in a surprising result, that the EPR frequency shifts as a function of magnetization tip angle. This frequency shift has never before been observed in a paramagnet. The spin dynamics on the Bloch sphere

under a strong driving field are characterized, and potential applications are discussed.

Chapter 4 outlines a series of measurements which characterize electron spin relaxation and decoherence in Gd^{3+} complexes at high magnetic fields, where a number of interesting effects emerge. At high field and at low temperature, the electron spin bath can become polarized to a very high degree, freezing out certain spin states and removing spin bath fluctuations as a source of decohering magnetic field noise. High-field electron spin-lattice and spin-spin relaxation time measurements are presented for a series of high-spin (S=7/2) Gd^{3+} complexes. A model of high-spin dipolar-coupling-driven decoherence is proposed, and is successfully used to describe the temperature and concentration dependence of the Gd^{3+} phase memory time, allowing for relaxation-based measurements of inter-spin distances with Gd^{3+} spin labels.

Moving away from the low temperature, highly spin-polarized regime, Chapter 5 deals with another challenge associated with high field EPR: performing experiments under biologically relevant temperatures and conditions. Most biology takes place near room temperature, in aqueous conditions. Aqueous samples are challenging for high-field EPR because water is extremely lossy at microwave and THz frequencies. Chapter 5 describes a type of sample holder optimized for room temperature, liquid, solution-state experiments.

The sixth and final chapter of this dissertation presents work done over the last year and a half using high-field time-resolved EPR together with site-directed spin labeling to study protein dynamics and motion at room temperature, in biologically relevant

conditions. Chapter 6 focuses on the protein proteorhodopsin (PR), a protein which lives in the membranes of marine bacteria and which functions as an energy source in the form of a light-activated proton pump. EPR measurements of PR tagged with a paramagnetic spin-label at judiciously chosen sites can be used to probe light-activated conformational changes that accompany protein function. Time-resolved high-field EPR, which offers superior spectral resolution and clarity, is paired with time-resolved optical spectroscopy to correlate protein structural changes with protein optical photointermediate states.

1.1 Fundamentals of Electron Paramagnetic Resonance

The rest of this introductory chapter is intended to familiarize the reader with the physics of EPR. The material presented in this section was drawn from a number of sources, including excellent textbooks focusing on EPR by Poole [52], Weil and Bolton [53], and Schweiger and Jeschke [54], and Solyom's textbook [55] on solid-state physics. The interested reader is encouraged to read the theses of Dr. Devin Edwards [56] and Dr. Jessica Clayton [57] for more information about the particular opportunities and challenges of performing EPR at 240 GHz.

1.1.1 The Electron Magnetic Moment

The wavefunction of a single electron $|\Psi(\mathbf{r},\{s\})\rangle$ can be written can be written as a product of a spatial wavefunction $|\psi_{\text{space}}(\mathbf{r})\rangle$, which depends on spatial coordinates $\{\mathbf{r}\}$ with a spin wavefunction $|\psi_{\text{spin}}(\{s\}\rangle$, which depends on spin degrees of freedom $\{s\}$ [58],

$$\Big|\Psi(\mathbf{r},s)\Big\rangle = \Big|\psi_{\text{space}}(\mathbf{r})\Big\rangle \otimes \Big|\psi_{\text{spin}}(\{s\})\Big\rangle \tag{1.1}$$

Electrons are charged particles which carry angular momentum in their spatial and spin degrees of freedom. Orbital angular momentum L is associated with the electron spatial wavefunction, and can be thought of semi-classically as arising from electron motion. Spin is a fundamentally quantum mechanical degree of freedom, and is associated with an intrinsic angular momentum S which all electrons possess. Because electrons carry both charge and angular momentum, they also carry magnetic moments μ_L and μ_S associated with their orbital and spin angular momentum [52],

$$\boldsymbol{\mu}_L = -g_L\mu_B\mathbf{L}/\hbar \tag{1.2a}$$

$$\boldsymbol{\mu}_s = -g_S\mu_B\mathbf{S}/\hbar \tag{1.2b}$$

where $\mu_B = e\hbar/2m_e$ is the Bohr magneton, g_L and g_S are the orbital and spin g-factors, and $\mathbf{L}$ and $\mathbf{S}$ have units of $\hbar$. The negative sign comes from the fact that electrons are negatively charged. Typically, $g_L \simeq 1$ and $g_S \simeq g_e$, where $g_e \simeq 2.00319$ is the free electron g-factor [59, 60, 61]. $\mathbf{L}$ and $\mathbf{S}$ are vectors of angular momentum operators, whose

components satisfy the usual commutation relations of angular momentum

$$[\hat{L}_i, \hat{L}_j] = i\hbar\epsilon_{ijk}\hat{L}_k \tag{1.3a}$$

$$[\hat{S}_i, \hat{S}_j] = i\hbar\epsilon_{ijk}\hat{S}_k \tag{1.3b}$$

where ϵ_{ijk} is the totally antisymmetric Levi-Cevita symbol [58].

An electron can therefore be thought of as a tiny magnetic dipole with a total electron magnetic moment $\boldsymbol{\mu}_e = \boldsymbol{\mu}_L + \boldsymbol{\mu}_S$ that couples to a magnetic field $\mathbf{B}$ through the Hamiltonian

$$H = -\boldsymbol{\mu}_e \cdot \mathbf{B} = \mu_B \left(g_L \mathbf{L} + g_E \mathbf{S}\right) \cdot \mathbf{B}/\hbar \tag{1.4}$$

Equation 1.4 is accurate in the high magnetic field limit. In systems with spin-orbit coupling, where the spin and orbital degrees of freedom interact, $\mathbf{L}$ and $\mathbf{S}$ are not conserved quantities. Instead, it is the total angular momentum $\mathbf{J} = \mathbf{L} + \mathbf{S}$ which is conserved. In a weak magnetic field, such that Equation 1.4 is small compared to spin-orbit coupling, only the projection of the total magnetic moment $\boldsymbol{\mu}_e$ which lies along $\mathbf{J}$ in Equation 1.4 need to be kept, so that

$$H = \frac{\langle (g_L \mathbf{L} + g_S \mathbf{S}) \cdot \mathbf{J} \rangle}{J^2} \mu_B \mathbf{J} \cdot \mathbf{B}/\hbar \tag{1.5}$$

The quantity

$$g_J = \frac{\langle (g_L \mathbf{L} + g_S \mathbf{S}) \cdot \mathbf{J} \rangle}{J^2} \tag{1.6}$$

is known as the Landé g-factor. The weak-field interaction of an electron magnetic

moment with a magnetic field is given by

$$H = g_J \mu_B \mathbf{J} \cdot \mathbf{B}/\hbar \tag{1.7}$$

The bulk of the work presented in this dissertation deals either with systems where spin-orbit coupling is small, or where L can be neglected, or both, and the interaction between an electron spin and a magnetic field $\mathbf{B}$ can be described by an effective spin Hamiltonian of the form

$$H = g\mu_B \mathbf{S} \cdot \mathbf{B}/\hbar = \gamma \mathbf{S} \cdot \mathbf{B} \tag{1.8}$$

where g is an effective g-factor, $g \simeq g_S$, and γ is the electron gyromagnetic ratio

$$\gamma = \frac{g\mu_B}{\hbar} \tag{1.9}$$

The Hamiltonian in Equation 1.8 describes the energy of a single spin in an external magnetic field. If the magnetic field is taken to point along the $\hat{z}$ direction so that $\mathbf{B} = B_0 \hat{z}$, then Equation 1.8 becomes

$$H = \gamma B_0 S_z \tag{1.10}$$

The eigenstates of H are the $2S + 1$ eigenstates $|m\rangle$ of S_z labeled by m,

$$s_z|m\rangle = \hbar m|m\rangle \tag{1.11}$$

where $m = \{-S, -S+1, \ldots, S-1, S\}$, so that

$$H|m\rangle = \hbar\gamma B_0 m|m\rangle \tag{1.12}$$

1.1.2 Spin-1/2

A single electron has $S = 1/2$. Considering only spin degrees of freedom, Equation 1.10 has two energy eigenstates $|+1/2\rangle$ and $|-1/2\rangle$ labeled by the eigenvalues of S_z, with energy eigenvalues $E_{+1/2}, E_{-1/2}$ given by

$$\begin{aligned} E_{+1/2} &= \frac{\hbar\gamma B_0}{2} \\ E_{-1/2} &= -\frac{\hbar\gamma B_0}{2} \end{aligned} \tag{1.13}$$

The two states $|+1/2\rangle$ and $|-1/2\rangle$ correspond to the electron spin being aligned or anti-aligned with the external field. The energy difference at $\Delta E = E_{+1/2} - E_{-1/2}$, called the Zeeman energy, is given by

$$\Delta E = \hbar\gamma B_0 \tag{1.14}$$

corresponding to a frequency $\omega_L = \Delta E/\hbar$

$$\omega_L = \gamma B_0 \tag{1.15}$$

where ω_L is the Larmor frequency. Table 1.1 shows the scale of the energy splitting ΔE and the corresponding Larmor frequency ω_L for $g = 2$ electron spins over a range of magnetic fields.

The two states $|+1/2\rangle$ and $|-1/2\rangle$ are coupled by a magnetic dipole transition [53, 55]. A time-varying magnetic field which oscillates at the Larmor frequency can drive transitions $|\pm 1/2\rangle \rightarrow |\mp 1/2\rangle$.

For $g \simeq 2$ electrons in moderate magnetic fields and temperatures, the Zeeman energy is small compared to thermal fluctuations. From Equation 1.14, $\Delta E/B_0 \sim 0.14$ meV/T.

Magnetic Field (T)	ΔE (meV)	$\omega_L/2\pi$ (GHz)	T_z (K)
0.34	3.9×10^{-2}	9.5	0.46
1.24	0.14	34	1.6
3.4	0.39	95	4.6
5.0	0.58	140	6.8
8.56	1.0	240	11.6

Table 1.1: Energy difference, Larmor frequency, and Zeeman temperature corresponding to transitions between two adjacent spin energy levels for $g = 2$ electrons at magnetic fields where EPR is typically performed.

For an ensemble of non-interacting spins, the two states $|+1/2\rangle$ and $|-1/2\rangle$ will be thermally populated according to Boltzmann statistics. The ratio $n_{-1/2}/n_{+1/2}$ of spins in the ground state $|-1/2\rangle$ to spins in the excited state $|+1/2\rangle$ is

$$\frac{n_{-1/2}}{n_{+1/2}} = \exp\left(\frac{\Delta E}{k_B T}\right) = \exp\left(\frac{\hbar\gamma B_0}{k_B T}\right) \tag{1.16}$$

In the high-temperature limit $k_B T \gg \Delta E$, the ratio $n_{-1/2}/n_{+1/2}$ is close to 1 and the populations of the two states are nearly equal. At temperatures below the Zeeman temperature T_z, given by

$$T_z = \frac{\hbar\gamma B_0}{k_B} \tag{1.17}$$

thermal fluctuations are small compared to the Zeeman energy and the spins will tend towards being fully anti-aligned with the magnetic field.

The spin of a $S = 1/2$ unpaired electron can be described by a wavefunction $|\psi\rangle$ which can be written in terms of the eigenstates $|\pm 1/2\rangle$ of S_z, which span the $S = 1/2$ Hilbert space [58]

$$|\psi(t)\rangle = \alpha(t)|+1/2\rangle + \beta(t)|-1/2\rangle \tag{1.18}$$

where $|\alpha|^2+|\beta|^2 = 1$. The dynamics of the spin are governed by the Schrödinger equation

with Hamiltonian given in Equation 1.10,

$$i\hbar\frac{\partial}{\partial t}|\psi(t)\rangle = H|\psi(t)\rangle \tag{1.19}$$

Taking the projection of both sides of Equation 1.19 with $\langle\pm 1/2|$ gives differential equations for $\alpha(t)$ and $\beta(t)$,

$$\dot{\alpha} = -i\frac{\gamma B_0}{2}\alpha \qquad \dot{\beta} = i\frac{\gamma B_0}{2}\beta$$

with solutions

$$\alpha = |\alpha_0|e^{i\phi_\alpha}e^{-i\gamma B_0 t/2} \qquad \beta = |\beta_0|e^{i\phi_\beta}e^{i\gamma B_0 t/2}$$

Calculating the expectation values of the operators $S_x = (S^+ + S^-)/2$, $S_y = (S^+ - S^-)/2i$, and S_z in the state $|\psi\rangle$ gives

$$\langle S_x(t)\rangle = \hbar|\alpha_0||\beta_0|\cos(\gamma B_0 t + \phi) \tag{1.20a}$$

$$\langle S_y(t)\rangle = \hbar|\alpha_0||\beta_0|\sin(\gamma B_0 t + \phi) \tag{1.20b}$$

$$\langle S_z(t)\rangle = \frac{\hbar}{2}\left(|\alpha|^2 - |\beta|^2\right) \tag{1.20c}$$

where $\phi = \phi_\beta - \phi_\alpha$. A vector $\vec{S} = (\langle S_x\rangle, \langle S_y\rangle, \langle S_z\rangle)$ whose components are given by the expectation values of the spin angular momentum operators can be seen to precess about the direction of the magnetic field, which points in the z-axis, with a precession frequency $\gamma B_0 = \omega_L$ given by the Larmor condition.

1.1.3 Bulk Properties

In a sample with a large number N of non-interacting electron spins per unit volume V, the sum of the magnetic moments of each spin defines a magnetization $\mathbf{M}$ [55],

$$\mathbf{M} = \frac{1}{V}\sum_{n=1}^{N}\left(-\frac{g\mu_B}{\hbar}\langle\mathbf{S}_n\rangle\right) = -\frac{\gamma}{V}\sum_{n=1}^{N}\langle\mathbf{S}_n\rangle \tag{1.21}$$

Taking the magnetic field to point along the $\hat{z}$ direction, $\mathbf{B} = B_0\hat{z}$, the magnetization at thermal equilibrium $\mathbf{M}_{eq}$ can be calculated from Equation 1.21,

$$\langle\mathbf{S}\rangle = \mathrm{Tr}\left(\mathbf{S}\rho_0\right) \tag{1.22}$$

where ρ_0 is the density matrix describing a spin at thermal equilibrium

$$\rho_0 = \frac{e^{-H/k_BT}}{\mathrm{Tr}\left(e^{-H/k_BT}\right)} \tag{1.23}$$

and $H = \gamma B_0 S_z$ is given by Equation 1.10, so that

$$\rho_0 = \frac{e^{\gamma B_0\hbar/2k_BT}|-1/2\rangle\langle-1/2| + e^{-\gamma B_0\hbar/2k_BT}|1/2\rangle\langle1/2|}{e^{\gamma B_0\hbar/2k_BT} + e^{-\gamma B_0\hbar/2k_BT}} \tag{1.24}$$

Using Equations 1.21, 1.22, and 1.24, the equilibrium magnetization $\mathbf{M}_{eq}$ is given by

$$\mathbf{M}_{eq} = \frac{N}{V}\frac{g\mu_B}{2}\tanh\left(\frac{g\mu_B B_0}{2k_BT}\right)\hat{z} \tag{1.25}$$

In the high-temperature limit $k_BT \gg g\mu_B B_0$, $\mathbf{M}_{eq}$ is given by

$$\mathbf{M}_{eq} = \frac{N}{V}\frac{(g\mu_B)^2}{4k_BT}B_0\hat{z} \tag{1.26}$$

From Equation 1.26, the magnetic susceptibility χ_0 in the high-temperature limit is given by

$$\chi_0 = \mu_0\frac{N}{V}\frac{(g\mu_B)^2}{4k_BT} \tag{1.27}$$

1.1.4 The Bloch Equations

The Bloch equations [62] are a semi-classical model of magnetic resonance, in which the magnetization $\mathbf{M}$ is treated as a classical vector. In a magnetic field $\mathbf{B}$, $\mathbf{M}$ feels a torque τ given by

$$\tau = \mathbf{M} \times \mathbf{B} \tag{1.28}$$

Equations 1.21 and 1.28 combined give the equations of motion for $\mathbf{M}$,

$$\frac{d}{dt}\mathbf{M} = \gamma \mathbf{B} \times \mathbf{M} \tag{1.29}$$

As with Equation 1.20, Equation 1.29 predicts that if $\mathbf{M}$ is not aligned with $\mathbf{B}$, it will undergo precession with frequency $\omega_L = \gamma B$.

Bloch precession is accompanied by two relaxation processes, which occurs on two different timescales, designated T_1 and T_2. The component of $\mathbf{M}$ which points in the direction of $\mathbf{B}$ decays back to thermal equilibrium due to interactions with the lattice with a time constant T_1 [63]. At the same time, the components of $\mathbf{M}$ which point transverse to $\mathbf{B}$ decay with time constant T_2, both due to interactions with the lattice and due to dephasing, which is generally shorter than T_1. Dephasing occurs due to small variations in the precession frequency ω_L, and to small time-variations in phase ϕ of each of the underlying spins (Equation 1.20). The Bloch equations with relaxation [62] are

given by

$$\frac{d}{dt}M_x = \gamma(\mathbf{B} \times \mathbf{M})_x - \frac{M_x}{T_2} \tag{1.30a}$$

$$\frac{d}{dt}M_y = \gamma(\mathbf{B} \times \mathbf{M})_y - \frac{M_y}{T_2} \tag{1.30b}$$

$$\frac{d}{dt}M_z = \gamma(\mathbf{B} \times \mathbf{M})_z - \frac{M_z - M_0}{T_1} \tag{1.30c}$$

The Bloch equations, despite being a semi-classical approximation, provide valuable intuition for magnetic resonance, particularly when it comes to relaxation.

1.2 EPR Spectroscopy

EPR spectroscopy consists of a number of techniques designed to probe with high accuracy the energy differences between electron spin states. These energy differences depend on the local magnetic fields seen by the electron spins, and so are sensitive probes of the local magnetic environments around unpaired electrons.

EPR spectroscopy is a broad field with many sub-disciplines, and it is difficult to make generalization about the discipline. Nevertheless, it is fair to say that EPR spectroscopy is concerned (for the most part) with dilute electron spins in otherwise diamagnetic materials, and that the goal of the EPR spectroscopist is to use magnetic fields (both static and time-varying) to study dilute, (nearly) isolated spins associated with (usually localized) unpaired electrons. In the dilute spin limit, where unpaired electrons are separated by ∼nm distances (or longer), EPR spectroscopy probes perturbations on

the ground electronic state of a system which arise due to interactions between spin magnetic moments and magnetic fields. These low-energy states are governed by an effective spin Hamiltonian, which encodes information about the ground electronic state (and sometimes excited electronic states), and which govern low-energy spin excitations.

1.2.1 The Effective Spin Hamiltonian

If the density of unpaired electrons is not too high, and any external magnetic fields are not too large, so that contributions to the total energy E of a system from the spin degrees of freedom $\{s\}$ can be treated as perturbations on top of the much larger electronic energy E_0, then an effective spin Hamiltonian can be defined which governs the spin degrees of freedom in the electronic ground state.

The effective spin Hamiltonian H_S can be written as a sum of interaction Hamiltonians by grouping together terms which are similarly behaved,

$$H_S = H_Z + H_{dd} + H_{Ex} + H_{HF} + H_{ZFS} \tag{1.31}$$

where H_Z is the Zeeman interaction, H_{dd} is the inter-electron dipole-dipole interaction, H_{Ex} is the exchange interaction, H_{HF} is the electron-nuclear hyperfine interaction, and H_{ZFS} is the electron zero-field splitting (ZFS) interaction.

Zeeman Interaction

The Zeeman interaction H_z is a generalization of Equations 1.4 and 1.7, and is written for a single electron spin S

$$H_z = \mu_B \mathbf{S} \cdot \mathbf{g} \cdot \mathbf{B} \tag{1.32}$$

where $\mathbf{g}$ is the electron g-tensor. A great many interactions are wrapped up into the electron g-tensor in the effective spin Hamiltonian, including spin-orbit coupling, diamagnetic shielding, and relativistic corrections to Equation 1.8 [53].

Electron-nuclear coupling

The hyperfine interaction describes coupling between one electron spin S and one nuclear spin I,

$$H_{HF} = \mathbf{S} \cdot \mathbf{A} \cdot \mathbf{I} \tag{1.33}$$

where A is the hyperfine tensor. The hyperfine interaction can be further broken down into two parts: the isotropic hyperfine interaction $H_{HF,iso}$, sometimes called the Fermi contact term [53], and the anisotropic hyperfine interaction $H_{HF,aniso}$, which can be thought of as electron-nuclear through-space magnetic dipole coupling [53, 55]. The isotropic portion is given by

$$H_{HF,iso} = -\mu_0 (g\mu_B)(g_N \mu_N)\rho(\mathbf{r})\mathbf{S} \cdot \mathbf{I} \tag{1.34}$$

where g_N is the g-factor of the particular nucleus, μ_N is the nuclear magneton, and $\rho(\mathbf{r})$ is the electron spatial wavefunction density at the location of the nucleus [55].

The anisotropic portion of the hyperfine coupling is a dipole-dipole interaction be-

tween the electron magnetic dipole $\boldsymbol{\mu}_e$ and the nuclear magnetic dipole moment $\boldsymbol{\mu}_I$ separated by $\mathbf{r}$ [55],

$$H_{HF,aniso} = \frac{\mu_0}{4\pi}\left(\frac{\boldsymbol{\mu}_e \cdot \boldsymbol{\mu}_I}{r^3} - \frac{3(\boldsymbol{\mu}_e \cdot \mathbf{r})(\boldsymbol{\mu}_I \cdot \mathbf{r})}{r^5}\right) \tag{1.35}$$

Electron-electron coupling

Electron-electron couplings can take at least three forms: the exchange interaction, the dipolar interaction, and the zero-field splitting interaction. Of these three, it is useful to distinguish the first two forms from the third form.

The exchange interaction and the dipolar interaction describe couplings between spins that are sufficiently isolated that they can be described as independent degrees of freedom in the effective spin Hamiltonian. The exchange interaction H_{Ex} describes the electron-electron coupling due to wavefunction overlap and the fact that electrons are fermionic, indistinguishable particles, and is written for two electrons S_1 and S_2 as

$$H_{Ex} = -J\mathbf{S}_1 \cdot \mathbf{S}_2 \tag{1.36}$$

where J is the exchange integral [54]. The dipolar or dipole-dipole interaction H_{dd} for two spins with magnetic dipole moments $\boldsymbol{\mu}_{e1}$ and $\boldsymbol{\mu}_{e2}$ separated by $\mathbf{r}$ is given by

$$H_{dd} = \frac{\mu_0}{4\pi}\left(\frac{\boldsymbol{\mu}_{e1} \cdot \boldsymbol{\mu}_{e2}}{r^3} - \frac{3(\boldsymbol{\mu}_{e1} \cdot \mathbf{r})(\boldsymbol{\mu}_{e2} \cdot \mathbf{r})}{r^5}\right) \tag{1.37}$$

which can be written in terms of the two electron g factors g_1 and g_2

$$H_{dd} = \frac{\mu_0}{4\pi}\frac{g_1 g_2 \mu_B^2}{r^3}\left(\mathbf{S}_1 \cdot \mathbf{S}_2 - \frac{3(\mathbf{S}_1 \cdot \mathbf{r})(\mathbf{S}_2 \cdot \mathbf{r})}{r^2}\right) \tag{1.38}$$

The dipole-dipole interaction can be expanded in a series of terms sometimes referred to as the "ABC" expansion or the "dipolar alphabet" [64]

$$H_{dd} = \frac{\mu_0}{4\pi}\frac{g_1 g_2 \mu_B^2}{r^3}\Big(A + B + C + D + E + F\Big) \tag{1.39}$$

where

$$A = (1 - 3\cos^2\theta)S_{1z}S_{2z} \tag{1.40a}$$

$$B = -\frac{1}{4}(1 - 3\cos^2\theta)\left(S_1^+ S_2^- + S_1^- S_2^+\right) \tag{1.40b}$$

$$C = -\frac{3}{2}\sin\theta\cos\theta e^{-i\phi}\left(S_{1z}S_2^+ + S_1^+ S_{2z}\right) \tag{1.40c}$$

$$D = -\frac{3}{2}\sin\theta\cos\theta e^{i\phi}\left(S_{1z}S_2^- + S_1^- S_{2z}\right) \tag{1.40d}$$

$$E = -\frac{3}{4}\sin^2\theta e^{-i2\phi}S_1^+ S_2^+ \tag{1.40e}$$

$$F = -\frac{3}{4}\sin^2\theta e^{i2\phi}S_1^- S_2^- \tag{1.40f}$$

S^+ and S^- are the angular momentum raising and lowering operators, respectively,

$$S^\pm = S_x \pm iS_y \tag{1.41}$$

The two most important terms in the "alphabet expansion" are A, the secular term which commutes with H_Z, and the B, the dipolar flip-flop term which flips one spin up while simultaneously flipping another spin down.

In the case where multiple electrons are in close proximity (less than ~ 1 nm apart) so that the ground state wavefunction has $S > 1/2$, dipolar coupling and exchange can be very strong and cause significant energy splittings in the spin system at zero

external field, and their combined effects are dubbed zero-field splitting (ZFS). The ZFS interaction H_{ZFS} is written for a spin $\mathbf{S}$ with $S > 1/2$

$$H_{ZFS} = \mathbf{S} \cdot \mathbf{D} \cdot \mathbf{S} \tag{1.42}$$

where $\mathbf{D}$ is the zero-field splitting tensor. $\mathbf{D}$ is symmetric and traceless. In the principal axis of the $\mathbf{D}$ tensor, Equation 1.42 can be written [54]

$$H_{ZFS} = 3D\left(3S_z^2 + S(S+1)\right) + E\left(S_x^2 - S_y^2\right) \tag{1.43}$$

where D and E are the ZFS parameters.

Molecular Motion

In real physical systems, motion of the atoms and molecules which make up the ground electronic state of a system can also influence spin dynamics. Many of the terms in the effective spin Hamiltonian H_S couple spatial and spin degrees of freedom, either through spin-orbit coupling (H_z through $\mathbf{g}$, H_{ZFS}), or through a distance and orientation dependence (H_Z again through $\mathbf{g}$, $H_{HF,aniso}$, H_{dd}, H_{ZFS}).

The degree to which atomic and molecular motion is important for describing spin dynamics depends on the kind of motion, the rate of motion, and the particulars of H_S.

1.2.2 Continuous Wave EPR Spectroscopy

Microwave radiation can drive magnetic dipole transitions between different states in the spin manifold. Continuous wave (CW) EPR spectroscopy uses continuous microwave magnetic fields $\mathbf{B}_1(t)$ to probe the response of a spin system. When the microwave

radiation matches a magnetic dipole transition between two states in the effective spin Hamiltonian 1.31, the spin system absorbs microwave radiation. The EPR lineshape contains all of this information and more. The EPR lineshape characterizes a spin system's response to an external perturbation in the form of a time-varying magnetic field. Typically, the experimentalist will apply an external, static magnetic field $\mathbf{B}_0$ much larger than $\mathbf{B}_1$, and observe the absorption at a fixed microwave frequency field as a function of $\mathbf{B_0}$, to measure an "EPR lineshape." Measurements are usually performed with a third, time-varying magnetic field aligned along the direction of $\mathbf{B}_0$ which is used to modulate the amplitude of B_0. The response of the spin system to the microwave field $\mathbf{B}_1$ is then measured using lock-in detection.

The EPR lineshape reports on the effective spin Hamiltonian, as well as on relaxation processes, spin-lattice coupling, and on molecular motion. Interpreting the EPR lineshape requires some knowledge of the underlying effective spin Hamiltonian, and is typically accomplished by iterative lineshape simulation and fitting procedures.

CW EPR lineshape simulations are carried out using a number of different frameworks, with the correct choice of framework depending on the underlying physical properties of spin system. When spin dynamics are entirely governed by the effective spin Hamiltonian H_S, and when atomic and molecular motion can be neglected, the most straightforward approach is to simply diagonalize H_S. Microwave absorption will occur for states connected by magnetic dipole transitions, with a linewidths determined by relaxation processes and by orientational averaging.

If atomic and molecular motion occur with characteristic timescales t_c comparable to $1/\Delta\omega$, where $\Delta\omega$ is the contribution to the inhomogeneous linewidth from an anisotropic interaction in the effective spin Hamiltonian, then motion can modify the EPR lineshape and must be taken into account.

Motion in EPR experiments breaks down roughly into three cases: the "rigid limit" $t_c\Delta\omega \gg 1$, when motion can be neglected, the "fast motion" limit $t_c\Delta\omega \ll 1$, and the "slow motion" limit $t_c\Delta\omega \approx 1$ [65].

In the fast motion limit, anisotropic interactions in the effective spin Hamiltonian are completely averaged out, and only the isotropic averages contribute to the EPR lineshape.

The slow motion limit is the most difficult to treat theoretically. In general, the approach is to solve the Liouville-von Neumann equation for time-evolution of the density matrix ρ which describes the spin system, with an operator Γ which describes the rotation of the molecule on which the spins are localized,

$$\frac{d}{dt}\rho(\mathbf{\Omega}, t) = -i[H_S(\mathbf{\Omega}), \rho(\mathbf{\Omega}, t)] - \Gamma(\rho(\mathbf{\Omega}, t) - \rho_0) \tag{1.44}$$

where $\mathbf{\Omega}$ are the Euler angles describing the molecular orientation and ρ_0 is the equilibrium density matrix [65].

Much work has been done by Freed and collaborators [66, 67, 68] to develop procedures to simulate EPR lineshapes by writing Equation 1.44 in Liouville space and solving the Stochastic Liouville equation [67, 69] which treats molecular tumbling as rotational diffusion. Another approach which has been successful is to use molecular dynamics simulations to calculate molecular trajectories and orientations, and to compute the

lineshape based on Equation 1.44 using these trajectories [70].

1.2.3 Pulsed EPR

Pulsed EPR spectroscopy uses microwave pulses to coherently manipulate spin populations and coherences. Spins are quantum mechanical objects. In a pulsed EPR experiment, microwaves are applied in pulses separated by evolution or interaction periods, during which the spin system is allowed to evolve.

Pulsed EPR spectroscopy can be used to perform EPR lineshape measurements. Earlier in the Chapter, the EPR lineshape was described as the spin system's response to an external perturbation. An equivalent description of the EPR lineshape is that it is the Fourier transform of the time-correlation function of the magnetic dipole transition operator. The time-correlation function can be measured in a pulsed EPR experiment by the application of a short microwave pulse which tips spins our of thermal equilibrium and away from the $\hat{z}$ direction. After the short pulse, the spins precess and dephase, emitting a decaying magnetic dipole radiation signal called a Free Induction Decay (FID). In the limit that pulse has infinite bandwidth, or at least has a much larger bandwidth than the EPR linewidth, the FID is the impulse response of the spin system, which is the inverse Fourier transform of the EPR lineshape [54].

Pulsed EPR has many advantages of CW EPR. In the limit where pulse excitation bandwidths are larger than the EPR spectrum, then pulsed EPR can be used to acquire the entire EPR lineshape in a single short experiment at a fixed field position. Unfor-

tunately, it is quite difficult to reach this limit in most EPR experiments, where lines are typically broad and microwave pulses are limited in power. In most cases, it is only possible to excite a narrow portion of the EPR lineshape with a single microwave pulse.

There are many other advantages of pulsed EPR which still make it an attractive alternative to CW EPR, include the ability to perform straightforward measurements of electron spin relaxation times, and the ability to design experiments which selectively address particular terms in the effective spin Hamiltonian.

1.3 EPR for Biological Applications

EPR is a powerful tool for studying structure and dynamics in biological systems, including individual proteins, protein assemblies, nucleic acids, and lipids. Around 40% of all enzymes crystallized to date have at least one bound metal center, which are most often EPR active and are thought to be functionally relevant in most cases [71]. However, even proteins which do not have a native paramagnetic center can be studied by EPR using a technique called site-directed spin labeling (SDSL) [2, 72, 73, 74]. SDSL involves using site directed mutagenesis to attach a small molecule containing a stable unpaired electron spin, called a spin label, to a specific location on a protein or other biological macromolecule. The EPR signal from that unpaired electron is then relied upon to report on the local magnetic environment and dynamics seen at the location on the protein where it is tagged.

The most commonly used spin label for protein EPR studies is MTSL (S-(2,2,5,5-

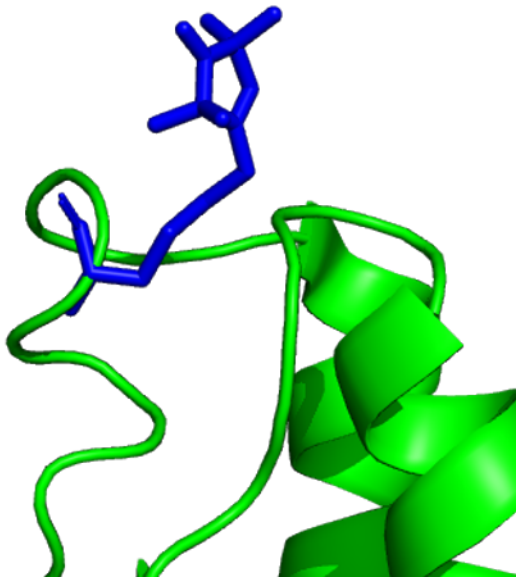

Figure 1.1: An MTSL spin-label (blue) attached to a protein (green). An unpaired electron localized along the N-O bond of MTSL acts as a local reporter of dynamics, hydration, and solvent accessibility, and can provide long-range distance constraints on protein structure.

tetramethyl-2,5-dihydro-1H-pyrrol-3-yl)methyl methanesulfonothioate), a stable nitroxide free radical with a single unpaired electron localized along its N-O bond [75]. MTSL can be made to react and bind to the thiol group of the amino acid cysteine, resulting in the addition of a tethered spin-probe wherever a cysteine is found on a protein of interest. Site-directed mutagenesis can be used to selectively introduce cysteine residues to particular locations on a protein, and to remove any other cysteines which would cause MTSL to bind where it is not wanted.

Spin-labeling can be disruptive to protein structure and function, but it is typically possible to find many residues on a protein which may be labeled without substantially modifying structure or function. Additionally, there are a range of different labeling molecules, with different tethering chemistries, so that even if one type of mutation is

prohibitively disruptive to a particular protein or protein domain, it is usually possible to find a different, less disruptive spin-labeling protocol.

Paramagnetic spin probes tethered to biomolecules can be used as reporters to extract many different kinds of information. Here, two particular examples are addressed: structure studies, where EPR can provide both short-range, atomic-resolution distance and orientation information and long-range, inter-electron distance constraints, and local dynamics, which can be used to report on protein conformational changes.

1.3.1 EPR for biological structure studies

EPR can be used for structure studies in a variety of ways. The environment immediately around an unpaired electron can be probed with atomic resolution through careful characterization of the electron g tensor and of hyperfine coupling. A number of tools exist to aid isolating and characterizing particular interactions, including hyperfine spectroscopy and ENDOR [26, 27, 28].

EPR can also be used to measure long-range (1-10 nm) distances between two spatially separated unpaired electrons through inter-electron dipolar coupling. Dipolar couplings can be measured through EPR lineshape analysis [5, 76, 25], through pulsed dipolar spectroscopy experiments such as double electron-electron resonance (DEER) [77, 12, 78], single-frequency techniques for refocusing (SIFTER) [79], and relaxation induced dipolar modulation enhancement (RIDME) [13, 80, 16], and double quantum coherence methods (DQC) [81, 82, 83] or through relaxation [63, 84, 85]. Relaxation-based distance

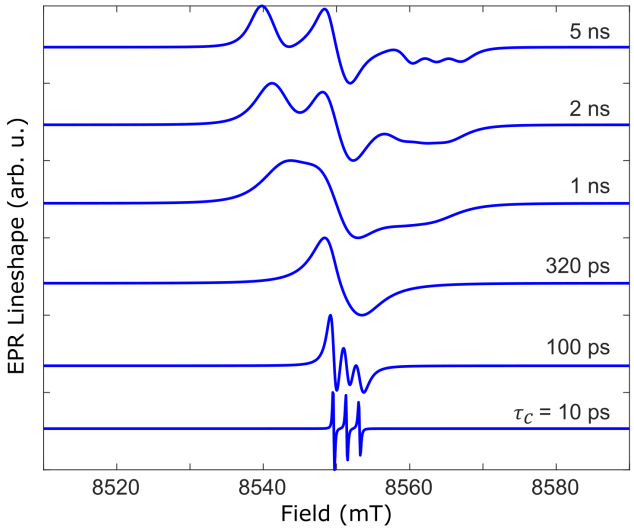

Figure 1.2: 240 GHz EPR lineshape of a nitroxide-type radical undergoing isotropic tumbling, simulated for several rotational correlation times τ_c. Lineshapes were simulated from the stochastic Liouville equation, as implemented in the EasySpin toolbox through the function *chili*.

measurements are discussed in detail in Chapter 4.

1.3.2 Dynamics

Spin labels tethered to biomolecules can report on local molecular mobility and solvent accessibility through their motion. When anisotropic interactions contribute significantly to the width of the EPR spectrum, the EPR lineshape becomes sensitive to motion. Rotation will tend to average anisotropic interactions, leading to line narrowing. In the limit of motion which is much faster than the inverse width of an anisotropic interaction $\Delta\omega^{-1}$, all anisotropic information will be washed out and that interaction can be replaced by its average value.

In a room-temperature, liquid environment, an MTSL label attached to a protein

will tend to undergo rapid rotation about the bonds that make up the molecular tether. At high magnetic field, the MTSL linewidth is dominated by an anisotropic g tensor (Equation 1.32) and an anisotropic hyperfine interaction (Equations 1.33 and 1.35) between the electron spin and the spin of the nitrogen nucleus in the N-O bond. The 240 GHz linewidth of MTSL in a frozen solution, where molecular tumbling is negligible, is roughly $\sim$1 GHz. Therefore, we can expect line narrowing in non-frozen conditions when the label rotates on the ns timescale.

EPR line narrowing due to the molecular motion of a tethered spin label can be quantified by performing EPR lineshape simulations using formalisms which take into account molecular rotation, such as the Stochastic Liouville Equation [66]. Figure 1.2 shows the 240 GHz EPR lineshape of a nitroxide-type radical assuming the molecule is undergoing isotropic rotational diffusion with a characteristic rotational correlation time τ_c. When $\tau_c > \Delta\omega^{-1}$, rotations do not efficiently average out g anisotropy or hyperfine anisotropy, and the EPR lineshape approaches the "rigid limit." When $\tau_c \ll \Delta\Omega^{-1}$, the anisotropic g-tensor is well described by a single isotropic g value, and the anisotropic hyperfine interaction (Equation 1.35) averages completely to zero. The isotropic hyperfine interaction due to the Fermi contact term (Equation 1.34) between the electron spin and the paramagnetic ^{14}N nuclear spin ($I = 1$) is not averaged by motion and remains even in the limit of fast rotation, and is responsible for the line splitting seen for $\tau_c = 10$ ps.

The timescale of the motion to which EPR is sensitive depends strongly on the properties of the reporter spin, and on the EPR frequency. The strength of anisotropic inter-

actions in the effective spin Hamiltonian will determine the motional timescale needed to achieve line narrowing, so that spin labels with larger anisotropic interactions will be sensitive to faster timescale motion, while spin labels with weak anisotropic interactions may not be sensitive to motion at all. The EPR frequency plays a role because anisotropy of the g tensor, which is the dominant anisotropy in nitroxide-type radicals, leads to line broadening that scales linearly with magnetic field (Equation 1.32). Because of this linewidth dependence on magnetic field, high- and low-field EPR of nitroxide-type radicals are sensitive to different motional timescales.

Molecular motion as reported by tethered spin probes is a convolution of the motion of the spin label with the underlying protein motion. Protein backbone motion is typically much slower than the motion of the spin label, and so contributes significantly less to lineshape narrowing. In order to separate the spin label motion from the protein motion, it is often advantageous to perform EPR at multiple frequencies, where the different motional regimes will contribute differently to line narrowing. High-field EPR, with its improved sensitivity to fast timescale motion, can be used characterize the spin-label dynamics, which can then be deconvolved from protein backbone motion captured using low-field EPR lineshape measurements.

Chapter 2

Phase cycling in FEL-EPR

Abstract

Electron paramagnetic resonance (EPR) is a powerful tool for research in chemistry, biology, physics, and materials science, which can benefit significantly from moving to frequencies above 100 GHz. In pulsed EPR spectrometers driven by powerful sub-THz oscillators, such as the free electron laser (FEL)-powered EPR spectrometer at UCSB, control of the duration, power and relative phases of the pulses in a sequence must be performed at the frequency and power level of the oscillator. Here we report on the implementation of an all-quasioptical four-step phase cycling procedure carried out directly at the kW power level of the 240 GHz pulses used in the FEL-powered EPR spectrometer. Phase shifts are introduced by modifying the optical path length of a 240 GHz pulse with precision-machined dielectric plates in a procedure we call phase cycling with optomechanical phase shifters (POPS), while numerical receiver phase cycling is implemented in

post-processing. The POPS scheme was successfully used to reduce experimental dead times, enabling pulsed EPR of fast-relaxing spin systems such as gadolinium complexes at temperatures above 190 K. Coherence transfer pathway selection with POPS was used to perform spin echo relaxation experiments to measure the phase memory time of P1 centers in diamond in the presence of a strong unwanted FID signal in the background. The large excitation bandwidth of FEL-EPR, together with phase cycling, enabled the quantitative measurement of instantaneous electron spectral diffusion, from which the P1 center concentration was estimated to within 10%. Finally, phase cycling enabled saturation-recovery measurements of T_1 in a trityl-water solution at room temperature – the first FEL-EPR measurement of electron spin T_1.

Acknowledgements

CBW performed FEL-powered EPR experiments, selected and prepared all samples, and performed all data analysis. Jessica Clayton assisted in FEL-EPR experiments. Sam Aronson fabricated precision polyethylene phase shifter plates in the physics department student machine shop. Professor Steffen Glaser suggested these experiments, and provided theoretical guidance. David Enyeart and Nick Agladze were instrumental in maintaining, repairing, and assisting with the operation of the UCSB FEL.

Much of the material in Chapter 2 has been previously published, and is reproduced from Wilson *et al.* [86] with permission from the PCCP Owner Societies.

2.1 Introduction to Phase Cycling

In order to take full advantage of the quantum control offered by microwave pulses in an EPR experiment, it is desirable to control the frequency, phase, and amplitude of the pulses. This chapter describes how phase and amplitude control are implemented in a FEL-EPR experiment.

2.1.1 Theory of Coherence Transfer Pathway Selection

Pulse control is an important part of modern pulsed EPR and NMR experiments. Phase control allows for the ability to create experiments designed to act differently on different coherence orders. A coherence order in a magnetic resonance experiment is a property of a quantum operator, which describes how that operator behaves under rotations about the z axis [87]. An operator $A^{(p)}$ is said to have coherence order p if it obeys the transformation

$$A^{(p)} \xrightarrow{\text{rotate by } \varphi \text{ about } \hat{z}} A^{(p)} e^{-ip\varphi} \tag{2.1}$$

Under a rotation about $\hat{z}$ by an angle φ, an operator with coherence order p picks up a phase $-p\varphi$. As an example, the operators S_z, $S^+ = S_x + iS_y$, and $S^- = S_x - iS_y$

transform under such a rotation as

$$S_z \rightarrow S_z \tag{2.2a}$$

$$S^+ \rightarrow S^+ e^{-i\phi} \tag{2.2b}$$

$$S^- \rightarrow S^- e^{i\phi} \tag{2.2c}$$

and therefore have coherence orders of 0, +1, and −1, respectively.

A density matrix ρ which describes the state of an electron spin may be decomposed into a sum of components of definite coherence [87],

$$\rho = \sum_p \rho^{(p)} \tag{2.3}$$

Writing the density matrix in this form is useful for describing a pulsed EPR experiment. At the start of an EPR experiment, if the spin system is a thermal equilibrium, the density matrix contains only terms of coherence order $p = 0$ [87]. In quadrature detection, where the EPR signal is detected phase-sensitively at the end of an experiment, only a single coherence order is detected, which is chosen by convention to be $p = -1$. Therefore, only coherence transfer pathways which end at coherence order $p = -1$ produce a directly detectable signal.

A pulsed EPR experiment consists of a series of microwave pulses and delays, which manipulate coherences and can introduce transitions between coherence orders. During delays between pulses, coherence orders do not change, except through relaxation. During pulses, however, coherence order can change, leading to the phase of the microwave pulse

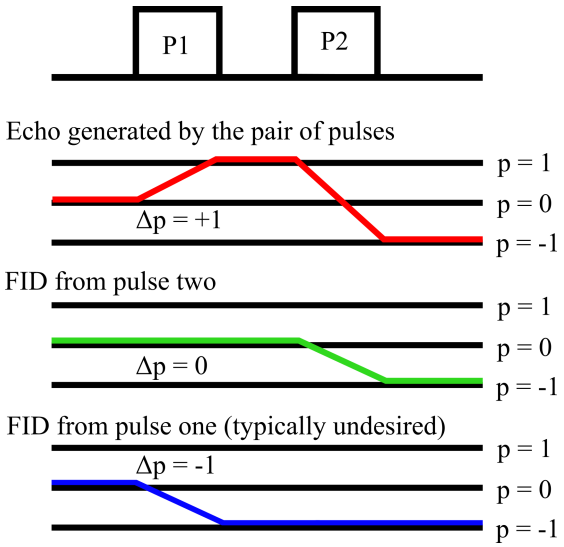

Figure 2.1: Three coherence transfer pathways generate observable signal in a standard two-pulse EPR experiment. The top path and the middle path trace the coherences corresponding to the two-pulse echo and the FID generated by the second pulse, respectively. The bottom path traces the coherence corresponding to the FID generated by the first pulse, and is not desired in a standard two-pulse experiment. The coherence order change during pulse one is different for the three paths. This allows for phase cycling to be used to separate each of the three coherence pathways. Wilson, Aronson, Clayton, Glaser, Han, and Sherwin, Phys. Chem. Chem. Phys., 2018, 20, 18097-18109 - Reproduced by permission of the PCCP Owner Societies.

driving the transition being imprinted on the state of the spin system, which picks up a phase shift proportional to the change in coherence order Δp. Because these phase shifts apply differently to different coherence orders, they can be used to isolate signals arising from particular coherences and suppress signals arising from unwanted coherences [88, 89, 54].

To illustrate how this works, consider an EPR experiment consisting of two microwave pulses, separated by a delay τ, performed on an ensemble of non-interacting S=1/2 electrons. Figure 2.1 shows the three coherence transfer pathways which generate directly observable signals: a free induction decay (FID) generated by the first pulse, an FID

generated by the second pulse, and a spin-echo generated by the pair of pulses. Suppose that the two microwave pulses were not ideal, so that all three of these signals were generated by the same experiment. This would lead to a confused superposition of signals with different amplitudes and phases in the detection window. In reality, this is a common problem in pulsed EPR and NMR experiments, where pulses are never perfect, nor ever have infinite bandwidth.

The important thing to note is that these three signals travel through different coherence transfer pathways. Notice that during the first pulse the pathway corresponding to the FID generated by the first pulse changes coherence order by $\Delta p = -1$, while the pathway corresponding to the FID generated by the second pulse changes by $\Delta p = 0$, and the pathway corresponding to the echo changes by $\Delta p = +1$. If the first pulse is applied with phase φ_A, then after this pulse each pathway will have picked up a phase $\varphi(\Delta p, \varphi_A) = \Delta p \varphi_A$.

Consider further that this simple two-pulse experiment is repeated, with the first pulse applied with a different phase $\varphi_{A'}$. Then in this second experiment, each pathway will pick up a different phase $\varphi(\Delta p, \varphi_{A'}) = \Delta p \varphi_{A'}$.

During phase-sensitive detection, the phase of the experimental receiver is also a quantity which can be controlled. Suppose that during the first two-pulse experiment, the phase of the first pulse P1 was 0, so that $\varphi_A = 0$, and that when the experiment was repeated, the phase was chosen to be $\varphi_{A'} = \pi$. Suppose further that the phase of the second pulse, and the receiver phase φ_R, were both held constant. The signal

$S(\Delta p = -1)$, corresponding to the FID generated by the first pulse where $\Delta p = -1$, which was produced in the second experiment will be phase-shifted by $-\pi$ relative to the signal produced in the first experiment. Likewise, the signal $S(\Delta p = +1)$, corresponding to the spin-echo generated by the pair of pulses, which was produced in the second experiment will be phase-shifted by π relative to the signal produced in the first experiment. If the total signals from the two experiments are added together, the signals corresponding to the $\Delta p = \pm 1$ pathways will interfere destructively, and no FID from the first pulse, nor any spin-echo from the pair of pulses, will be detected. Only the FID from the second pulse will survive.

This process of systematically varying the phases of pulses and of the receiver is called phase cycling, and the procedure by which signals from select coherence transfer pathways can be enhanced and signals from other coherence transfer pathways can be suppressed is called coherence transfer pathway selection [88, 54, 87].

Phase cycling is standard in pulsed NMR and most pulsed EPR experiments, and is typically achieved using electronic phase shifters. Electronic phase shifters become increasingly difficult to implement, however, as frequencies rise above 100 GHz. High-frequency EPR experiments based on amplifier-multiplier chains (AMCs) have overcome this challenge by implementing appropriate phase control at low frequencies, where electronic phase control is straightforward, before frequency multiplication. In recent years, EPR spectrometers integrated with arbitrary waveform generators have been developed which are capable of rapid phase (and amplitude) modulation [90], including at high

frequencies in an AMC-based spectrometer [91].

However, electronic phase shifting is not currently possible when using a high-power sub-THz or THz oscillator such as a gyrotron, or the UCSB mm-wave FEL. FEL-EPR operates in an entirely different modality as compared to EPR with conventional amplifier sources. As discussed in Chapter 1, the UCSB mm-FEL is not an amplifier, it is a high-power, quasi-CW oscillator. Rather than generating low-power pulses with programable length and phase, and then amplifying those pulses to high power, the FEL produces pulses of 240 GHz microwave radiation which are already at high power ($\sim$500 W to 9 kW), are several μs long with only loosely controllable pulse lengths, and at a fixed repetition rate of $\sim$ 1 Hz.

When operating with an oscillator source like the FEL, phase and amplitude control must be implemented directly in the high-power, high frequency beam. Further complicating matters is the fact that the phase of each FEL pulse is not controlled, nor is the spectrometer phase-locked to the FEL output. Therefore, the phase of each quasi-CW FEL pulse is essentially random. Previous work by Edwards *et al.* [92] has shown that despite the each quasi-CW pulse's random phase, coherent signal averaging is still made possible if the residual (heavily attenuated) FEL pulse is digitized along with the EPR signal for each experiment, and used in post-processing phase correct the EPR signal experiment-by-experiment. In addition, it was shown that the phase difference between two short pulses "sliced" from the same quasi-CW FEL pulse by light-activated semiconductor switches could be modified by inserting dielectrics into the beam path of one of

the two pulses [92].

The rest of this Chapter begins where Edwards *et al.* left off, and ends with a fully operational phase cycling procedure which can be used for coherence transfer pathway selection in FEL-EPR. First, precision-machined dielectric plates are demonstrated to be capable of accurately controlling the phase differences between two "sliced" pulses, in the form of eight high density polyethylene (HDPE) places machined to $\sim$10 μm precision. These plates were used to vary the relative optical path lengths of the two "sliced" pulses, in a procedure dubbed Phase cycling with optomechanical Phase Shifters (POPS). Second, POPS is used perform two-pulse FEL-EPR experiments at 240 GHz which would otherwise be impossible. POPS is used to reduce the experimental dead time in two-pulse Hahn echo experiments, enabling phase memory time measurements of frozen solutions of $GdCl_3$ at temperatures as high as 192 K. Third, coherence transfer pathway selection is performed to separate overlapping signals generated by a FID and a two-pulse Hahn echo generated from P1 centers in type 1b diamond, enabling both accurate measurements of the spin-spin relaxation time T_1 and a quantification of electron instantaneous spectral diffusion. Fourth, phase-cycled saturation recovery experiments are performed on a solution of trityl radical in a room temperature aqueous solution, and are used to measure the electron spin-lattice relaxation time T_1 for the first time in a FEL-EPR experiment.

2.2 EPR with a Free Electron Laser

The UCSB free electron lasers operate with an electron beam with a beam energy between 2 MeV and 6 MeV. The electron beam is accelerated to high energies by an electrostatic accelerator, and is steered and focused by dipole and quadrupole electromagnets into an undulator, a region of periodically varying magnetic field which causes the electron beam to wiggle from side to side as shown in Figure 2.2A. This wiggling generates coherent radiation at a frequency which depends on the period of the undulator magnets and on the beam energy. The undulator is located inside a ∼6 m quasioptical resonator, which produces radiation with a longitudinal mode spacing of ∼25 MHz. At 240 GHz, the mm-wave FEL produces pulses which consist of a forest of frequencies spaced by the ∼25 MHz cavity frequency and spread out over a ∼1 GHz bandwidth, as shown in Figure 2.2A. Lasing is initiated by spontaneous emission into one of the cavity modes. As a result, the amplitude of each mode in the forest varies from pulse to pulse.

Single frequency operation made possible by seeding the FEL cavity with radiation from a low power solid-state 240 GHz source (Virginia Diodes, Inc.) which is resonant with one of the cavity modes, a process called injection locking [93]. Microwaves are coupled out of the FEL cavity either through a small hole in one of the end mirrors, or, more commonly for EPR experiments, by reflections off of a high resistivity silicon wafer mounted near the Brewster angle. The silicon coupler also functions as a light-activated switch [94], which can be activated by a pulse of 532 nm light from a high-power, frequency-doubled, Q-switched Nd:YAG laser (Big Sky Laser). High-energy green light

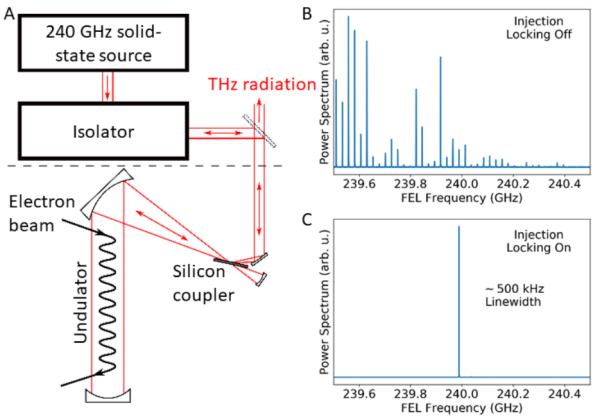

Figure 2.2: The UCSB mm-wave FEL producing a 240 GHz quasi-CW microwave pulse with injection locking. A shows the electron beam passing through the undulator and interacting with the lasing cavity, a ∼6 m long quasioptical resonator consisting of three mirrors. A silicon coupler mounted near the Brewster angle outcouples a small fraction of the energy stored in the cavity, while simultaneously in-coupling single-mode 240 GHz radiation from a solid state source for injection locking. B shows the power spectrum of a 2 μs FEL pulse when injection locking is not used. C shows the power spectrum of a 2 μs FEL pulse when injection locking is being used.

generates free carriers in the high-resistivity silicon, making the previously transparent silicon wafer highly conductive for the length of the carrier lifetime (a few μs), ruining the cavity Q and dumping all of the stored energy in one short $\sim$ 40 ns pulse, in a process termed cavity dumping [45]. Quasi-CW FEL pulses are typically 1 to 5 μs long, and can be generated at a 1 Hz repetetion rate.

Sub-THz radiation coupled out of the FEL is transported to the EPR lab through the Optical Transport System (OTS), consisting of quasioptical mirrors and polymethylpentene (TPX) lenses inside a vacuum transport line. In the EPR lab, a series of pulse slicing optics are used to "slice" either one or two short pulses with controllable lengths and inter-pulse delays out of the quasi-CW FEL pulse. High resistivity silicon switches activated by Q-switched Nd:YAG lasers are used to turn each short pulse on and off. A

pulse slicer schematic is shown in Figure 2.4.

"Sliced" pulses are coupled quasioptically into a 1.25 m long, 18 mm diameter corrugated waveguide (Thomas Keating Ltd). The waveguide ends in a corrugated taper with a 5 mm inner diameter above the sample position. Samples are mounted at the end of the taper, and backed by a flat silvered mirror. The waveguide and sample are housed in an EPR probe, which is placed into the center of an actively shielded, sweepable superconducting magnet (Oxford Instruments plc). The magnet's main superconducting coil can be swept from -12.5 T to +12.5 T, though for 240 GHz EPR experiments it is typically kept around 8.56 T, where the Larmor condition is met for $g = 2$ electrons. The magnet also contains a superconducting sweep coil with a $\pm$60 mT sweep range.

Reflected signals are measured using induction mode detection. The "sliced" FEL pulses, which are linearly polarized, are transmitted to the sample through a wire grid polarizer aligned for complete transmission, but oriented so that the pulses are incident on the grid at 45°. The reflected FEL pulse is transmitted back through the wire grid, but the EPR signal, which is circularly polarized, is partially transmitted and partially reflected. This reflected signal is sent to a subharmonic Schottky diode mixer (VDI, WR4.3SHM) driven by a 110 GHz local oscillator. This wire grid setup provides $\sim$30 dB of isolation [56], partially protecting the Schottky diode detector from the high-power FEL pulse. Further, active protection is provided by a second isolation mechanism, a silicon switch which is activated by a frequency doubled Nd:YAG laser only after the FEL pulse has fired. Even with both isolation mechanisms, some of the FEL pulse makes

it to the detector, and is digitized along with the EPR signal. Instrumental deadtime (in the absence of phase cycling) is limited to ~ 70 ns, primarily due to this leaked light.

The spectrometer utilizes super-heterodyne detection with an intermediate frequency (IF) of 10 GHz. The 10 GHz IF is mixed down to 500 MHz by a pair of quadrature mixers, and then recorded using a 12.5 GS/s digitizer (National Instruments PXIe-5186).

2.3 Phase cycling with optomechanical phase shifters

In a sequence consisting of two pulses, only the relative phase of the two pulses is important. Without loss of generality, assume in the following that only the phase of the first pulse is systematically varied in a phase cycle, while the phase of the second pulse is fixed. Revisiting the two-pulse EPR example, recall first that the system begins at thermal equilibrium with coherence order $p = 0$, and second that only coherence order $p = -1$ is observed during the detection window. Therefore, only three coherence transfer pathways need to be considered. During the first pulse, these three pathways undergo coherence order changes Δp of $+1$, 0, and -1.

Since there are three coherence transfer pathways associated with three different signals, it is possible to select any one of the three signals with a phase cycle with three steps, with pulse phases of 0°, 120°, and 240°. Rather than this minimum cycle, phase cycling employed in FEL-EPR was designed to operate with a (slightly redundant) four-step phase cycle, with pulse phases of 0°, 90°, 180°, and 270°. This four-step phase cycle can be used to select any one of the three coherence transfer pathways. Alternatively, as

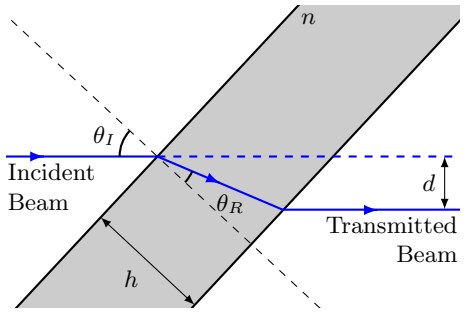

Figure 2.3: Schematic of a THz beam, shown in blue, incident with angle Θ_I on a slab of thickness h with refractive index n. The material on either side of the slab is taken to be air, with a refractive index of 1. After propagating through the slab, the beam is deflected a distance d. Wilson, Aronson, Clayton, Glaser, Han, and Sherwin, Phys. Chem. Chem. Phys., 2018, 20, 18097-18109 - Reproduced by permission of the PCCP Owner Societies.

in the earlier example, a two-step phase cycle of 0° and 180° can be used to separate the $\Delta p = 0$ pathway from the $\Delta p = \pm 1$ pathways. In practice, two-step phase cycling is sufficient for experiments which do not generate observable FIDs, where it can be employed to suppress leaked or scattered light from the second pulse.

Phase cycling schemes are accomplished in FEL-EPR at 240 GHz by varying the relative optical path lengths of two short pulses sliced from the same quasi-CW pulse. Phase shifts were engineered by selectively varying the optical path length (OPL) of the first pulse in a two-pulsed EPR experiment with precision-machined high density polyethylene (HDPE) plates, shown in Figure 2.4. HDPE was chosen because it is transparent to 240 GHz radiation [95, 96] and can be machined to precise tolerances. Figure 2.3 shows the path taken by a 240 GHz beam as it passes through a phase shifter plate of thickness h and refractive index n at an angle of incidence Θ_I. The optical path length difference

ΔOPL caused by the phase shifter plate is given by

$$\Delta OPL = \frac{nh}{\cos\Theta_R} - \frac{h}{\cos\Theta_R}\cos\left(\Theta_I - \Theta_R\right) \tag{2.4}$$

Θ_I and Θ_R are related by Snell's law, giving

$$\Delta OPL = h\left(n\sqrt{1 - \frac{\sin^2\Theta_I}{n^2}} - \cos\Theta_I\right) \tag{2.5}$$

Phase shifter plates were designed to operate near the Brewster angle to minimize losses due to reflections. At the Brewster angle $\tan\Theta_I = n$, and Equation 2.5 simplifies to

$$\Delta OPL = h\frac{n^2 - 1}{\sqrt{n^2 + 1}} \tag{2.6}$$

The change in optical path length produces a phase shift $\Delta\varphi$ given by

$$\Delta\varphi = 2\pi\Delta OPL/\lambda_0 \tag{2.7}$$

where $\lambda_0 = 1.249$ mm is the wavelength of the THz beam in air.

The transmitted beam is offset from the incident beam by a distance d given by

$$d = h\sin\Theta_I\left(1 - \frac{\sin\Theta_I/n}{\sqrt{1 + \sin^2\Theta_I/n^2}}\right) \tag{2.8}$$

or, at the Brewster angle,

$$d = \frac{h}{n}\frac{n^2 - 1}{\sqrt{n^2 + 1}} \tag{2.9}$$

HDPE plates were employed in pairs in order to minimize beam offset, with each plate contributing $\Delta\varphi/2$.

The plate thicknesses h were chosen to generate total relative phase shifts, $\Delta\varphi$, of $0°, 90°, 180°$, and $270°$, satisfying

$$\frac{\Delta OPL}{\lambda_0} = \frac{1}{2}(a + m) \tag{2.10}$$

Desired Total $\Delta\varphi$	a	m	Thickness (mm)
0°	0	3	2.60 ± 0.01
90°	1/4	2	1.95 ± 0.01
180°	1/2	2	2.17 ± 0.01
270°	3/4	2	2.39 ± 0.01

Table 2.1: Thicknesses of each HDPE phase-shifter plate machined for use in POPS experiments. The phase shift produced by each plate is half of the shift quoted in the left hand column, as plates are designed to work in pairs.

at Brewster's angle, where m is a positive integer and a is given in Table 2.1, so that

$$h = \frac{1}{2}\frac{\sqrt{1+n^2}}{n^2-1}(a+m)\lambda_0 \tag{2.11}$$

The plate thicknesses were chosen to be as thin as possible while satisfying Equation 2.11, and while remaining thick enough to avoid warping during machining.

Phase cycling with optomechanical phase shifters (POPS) was carried out in several steps, which are outlined here.

Step 1: Stochastic phase cycling and coherent signal averaging. Figure 2.4 illustrates schematically a two-pulse FEL-EPR experiment. POPS is applied in batches, so that a series of transients is acquired at a given inter-pulse phase difference $\Delta\varphi$. The FEL phase Ψ_{FEL} is random from FEL pulse to FEL pulse, but is stable during a given FEL pulse. Phase-sensitive signal averaging is implemented using a procedure described by Edwards *et al.* [92]. Briefly, the method leverages the fact that heavily attenuated residual light from the FEL reaches the detector and is digitized prior to the acquisition of the EPR signal. The random FEL phase Ψ_{FEL} is determined from the residual light, and is used to phase-correct each transient in post-processing. These transients are then coherently added for a particular $\Delta\varphi$ achieved by POPS to produce a complex signal $S(t)$.

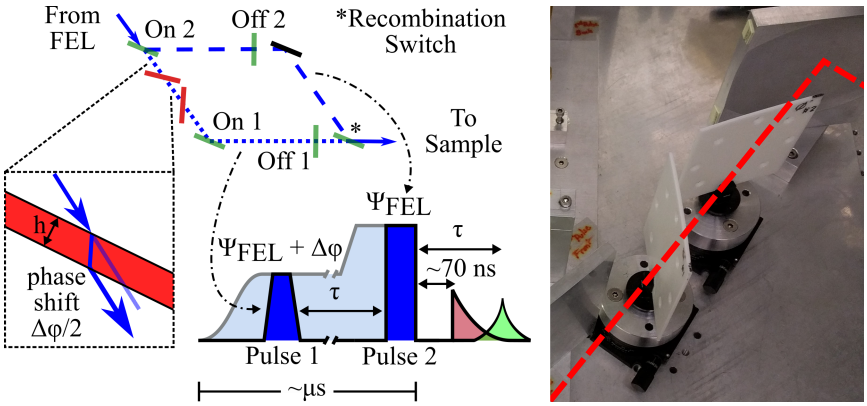

Figure 2.4: Schematic illustrating the pulse slicer used in a typical two-pulse FEL-EPR experiment. Optically activated silicon switches are used to slice two short pulses out of the FEL pulse, which travel down two spatially separated optical paths and which are recombined before being sent to the sample. Two silicon switches function as "On" switches, which re-direct the 240 GHz beam into the sample path, while another two switches function as "off" switches, terminating each short pulse. The recombination switch turns on simultaneously with the second "On" switch ("On 2"), and allows for the two beams to be recombined into the same final path to the sample. Dielectric phase shifter plates inserted into the path of the first pulse increment the phase difference $\Delta\varphi$ between the two pulses. Phase shifter plates operate at the Brewster angle in pairs, to minimize beam offset, with each plate inducing a phase shift of $\Delta\varphi/2$. Also shown is a time-domain schematic of a two-pulse FEL-EPR experiment, showing the FEL pulse (light blue), the two pulses sliced from the longer FEL pulse (dark blue), and the signals generated by the pair of pulses: a FID (red) and an echo (light green), which often overlap in time. To the right is a photo of a pair of phase shifter plates inserted into the optical path of the first pulse. Wilson, Aronson, Clayton, Glaser, Han, and Sherwin, Phys. Chem. Chem. Phys., 2018, 20, 18097-18109 - Reproduced by permission of the PCCP Owner Societies.

This approach to coherent signal averaging is comparable to the CYCLOPS (CYClical Ordered Phase Sequence)[97] in the limit of many pulses [92]. In a two-pulse experiment as implemented here, the residual light from the second pulse is used to determine Ψ_{FEL}.

Step 2: Modify the relative phase between the two pulses. After completing the experiment with a fixed phase difference $\Delta\varphi_0$ between pulses one and two, producing a complex signal $S_0(t)$, the phase difference $\Delta\varphi_i$ is modified by inserting dielectric phase shifter plates into the optical path of the first pulse. After this has been accomplished, a second batch of transients, $S_1(t)$, with a fixed $\Delta\varphi_1$ is coherently averaged.

Sampling all desired inter-pulse phase differences, a set of averaged complex signals, $\{S_i(t)\}$, is acquired, with one averaged signal for each $\Delta\varphi_1$ sampled. Each signal of this set is stored separately for further processing. The "global" phase for this data set is determined by choosing one averaged signal $S_0(t)$ to act as a reference, and adjusting the phase of the other averaged signals $S_i(t)$ relative to the reference in the same manner as outlined above, again using the residual FEL light from the second pulse.

Step 3: Measure the applied phase shifts. In practice, the set of experimentally determined phase shifts $\{\Delta\varphi_i\}$ were found to differ, sometimes by several degrees, from experiment to experiment, likely due to the difficulty of reproducibly inserting the phase shifter plates into the pulse slicer with sufficient precision. It was therefore necessary to measure each phase $\Delta\varphi_i$ for each experiment, using the same method of post-processing phase correction as was used in steps 1 and 2. Here, the residual light from the first pulse was used to experimentally determine the set of phase differences $\{\Delta\varphi_i\}$ induced

by POPS.

Step 4: Apply numerical phase shifts in post-processing. An additional set of numerical receiver phase shifts $\{\theta_i\}$ is finally applied to the recorded signals $\{S_i(t)\}$, in order to perform coherence transfer pathway selection in a multiplexed fashion [98]. The N recorded signals are then added together to generate the final output signal $S(t)$

$$S(t) = \frac{1}{N} \sum_i S_i(t) \exp(-i\theta_i) \tag{2.12}$$

The final output signal of a two-pulse POPS experiment, where the phase of the second pulse is held constant, contains contributions from each coherence transfer pathway Δp weighted by the complex coefficients $P(\{\Delta\varphi_i\}, \{\theta_i\}, \Delta p)$[98]

$$P(\{\Delta\varphi_i\}, \{\theta_i\}, \Delta p) = \frac{1}{N} \sum_i \exp(-i(\Delta p \Delta\varphi_i + \theta_i)) \tag{2.13}$$

Numerical phase shifts $\{\theta_i\}$ are chosen so that

$$P(\{\Delta\varphi_i\}, \{\theta_i\}, \Delta p) = \begin{cases} 1 & \text{Desired } \Delta p \\ 0 & \text{Undesired } \Delta p \end{cases} \tag{2.14}$$

As an example, if the phase of the first pulse is cycled through $\{\Delta\varphi_i\} = \{0, \pi/2, \pi, 3\pi/2\}$, then any of the three pathways shown in Figure 2.1 can be selected by choosing appropriate sets of numerical receiver phase shifts. With the phase of the second pulse held effectively constant, the three coherence transfer pathways each pick up difference phases given by $\{-\Delta p \Delta\varphi_i\}$. In this example, the $\Delta p = +1$ pathway, corresponding to the echo, concludes the two-pulse experiment with a phase which is stepped through

$\{0, -\pi/2, \pi, -3\pi/2\} = \{0, 3\pi/2, \pi, \pi/2\}$. Therefore, the echo can be selected by cycling the numerical receiver phase through $\{\theta_i\} = \{0, 3\pi/2, \pi, \pi/2\}$, so that $P(\{\Delta\varphi_i\}, \{\theta_i\}, \Delta p = +1) = 1$. At the same time, the phase of the $\Delta p = 0$ pathway, corresponding to the FID from the second pulse, is not changed as $\Delta\varphi$ is cycled, while the phase of the $\Delta p = -1$ pathway, corresponding to the FID from the first pulse, is stepped through $\{0, \pi/2, \pi, 3\pi/2\}$, so that $P(\{\Delta\varphi_i\}, \{\theta_i\}, \Delta p = 0) = P(\{\Delta\varphi_i\}, \{\theta_i\}, \Delta p = -1) = 0$. Therefore, the choice of the numerical receiver phase shifts $\{\theta_i\} = \{0, 3\pi/2, \pi, \pi/2\}$ selects the echo and suppresses the other two coherences. However, by instead choosing $\{\theta'_i\} = \{0, 0, 0, 0\}$, the same set of signals $\{S_i(t)\}$ can be used to select the FID from the second pulse, since $P(\{\Delta\varphi_i\}, \{\theta'_i\}, \Delta p = 0) = 1$ and $P(\{\Delta\varphi_i\}, \{\theta'_i\}, \Delta p = \pm 1) = 0$. Finally, by choosing $\{\theta''_i\} = \{0, \pi/2, \pi, 3\pi/2\}$, the same set of signals $\{S_i(t)\}$ can be used to select the $\Delta p = -1$ pathway, corresponding to the FID from the first pulse, as $P(\{\Delta\varphi_i\}, \{\theta'_i\}, \Delta p = -1) = 1$ in this case and $P(\{\Delta\varphi_i\}, \{\theta'_i\}, \Delta p = +1) = P(\{\Delta\varphi_i\}, \{\theta'_i\}, \Delta p = 0) = 0$.

2.3.1 Correcting for non-ideal pulse phases

There are many sets of pulse phase shifts $\{\Delta\varphi_i\}$ and numerical receiver phase shifts $\{\theta_i\}$ that can be used to select a particular coherence transfer pathway. For the example illustrated previously, where $\{\Delta\varphi_i\} = \{0, \pi/2, \pi, 3\pi/2\}$, it was possible to select any of the three coherence transfer pathways by finding sets of $\{\theta_i\}$ for which Equation 2.14 is exactly satisfied. However, when the phase of the first pulse is cycled through an arbitrary set of angles $\{\Delta\varphi_i\} = \{\Delta\varphi_0, \Delta\varphi_1, \Delta\varphi_2, \Delta\varphi_3\}$, selecting the correct set

of numerical receiver phases $\{\theta_i\}$ to select a particular coherence transfer pathway is not straightforward. Following the previous example, when the applied phase shifts $\{\Delta\varphi_i\}$ deviate from $\{0, \pi/2, \pi, 3\pi/2\}$, it is necessary to choose new and different sets of numerical phase shifts $\{\theta_i\}$ for the receiver phase to correctly select each of the three Δp pathways. In general, for an arbitrary set of phase shifts $\{\Delta\varphi_i\}$, Equation 2.14 cannot be exactly satisfied. The optimal choice of numerical receiver phases should both maximally attenuate unwanted coherences and maximally preserve desired coherences. Note that this situation is different from the scenario typically encountered in magnetic resonance experiments, where the optimal choices of pulse and receiver phases are made together.

Two procedures were developed to estimate the optimal numerical phase shifts $\{\theta_i\}$ in a four-step POPS phase cycle, given a set of phases $\{\Delta\varphi_i\}$. The "least squares method" relies on least-squares minimization to assign the approximately correct receiver phases $\{\theta_i\}$ to minimize unwanted coherences. The "echo-optimized method" was designed specifically to isolate the echo pathway ($\Delta p = +1$, see Fig. 2.1), and does not involve any minimization routine. The echo-optimized method has the advantage of always guaranteeing complete cancellation of unwanted coherences, and can in addition be modified to select for the $\Delta p = -1$ coherence pathway. The least-squares method is by contrast more flexible, as it can be used to select for $\Delta p = 0$.

The least-squares method was based on varying the receiver phases $\{\theta_i\}$ to both minimize signals from unwanted coherences, and to correctly set the phase of the desired coherence. To accomplish this, Equation 2.14 was solved for the four values of the receiver

phase $\{\theta_i\}$ in a least-squares sense. When trying to select one Δp, the real and imaginary parts of Equations 2.14 together provide six equations from which to extract the four unknown phases $\{\theta_i\}$. This method can be modified by assigning weights to the quantities $P(\{\Delta\varphi_i\}, \{\theta_i\}, \Delta p)$ in Equation 2.14, in order to determine receiver phase shifts which penalize one unwanted coherence pathway over another. This is desirable in cases where, for example, there is no signal in the detection window corresponding to the FID from the first pulse (the $\Delta p = -1$ pathway). The least-squares method can be used to select any of the three coherence transfer pathways corresponding to Δp .

The echo-optimized method, by contrast, uses a combination of receiver phase shifts and selective signal scaling to completely remove contributions from the $\Delta p = -1$ and the $\Delta p = 0$ coherence transfer pathways (corresponding to the FIDs from the first and second pulses, respectively), leaving only the contributions from the $\Delta p = +1$ pathway (corresponding to the echo). The echo-optimized method consists of two steps.

Step 1. Two signals $F_1(t)$ and $F_2(t)$ are created from the set of four complex signals $\{S_0(t), S_1(t), S_2(t), S_3(t)\}$ by adding the four signals with individual phase shifts as follows,

$$F_1(t) = \frac{1}{2}\left(S_0(t) + S_1(t) - S_2(t) - S_3(t)\right) \tag{2.15a}$$

$$F_2(t) = \frac{1}{2}\left(S_0(t) - S_1(t) - S_2(t) + S_3(t)\right) \tag{2.15b}$$

Because the $\Delta p = 0$ pathway does not change sign as the phase of the first pulse is varied, the difference of two signals $S_i(t) - S_j(t)$ does not contain any signal corresponding to

this pathway. Therefore, by construction, these two signals only include contributions from the $\Delta p = \pm 1$ pathways.

Step 2. Contributions from the $\Delta p = -1$ pathway are eliminated by taking a linear combination of $F_1(t)$ and $F_2(t)$, yielding the complex echo signal $E_{+1}(t)$,

$$E_{+1}(t) = c_1 F_1(t) + c_2 F_2(t) \tag{2.16}$$

The complex coefficients c_1 and c_2 can be calculated by tracking the evolution of $P(\{\Delta\varphi_i\}, \{\theta_i\}, \Delta p)$ (Equation 2.14) through the phase shifts applied in Equation 2.15, given by the two complex numbers

$$v_1 = e^{-i\varphi_0} + e^{-i\varphi_1} - e^{-i\varphi_2} - e^{-i\varphi_3} \tag{2.17a}$$

$$v_2 = e^{-i\varphi_0} - e^{-i\varphi_1} - e^{-i\varphi_2} + e^{-i\varphi_3} \tag{2.17b}$$

so that $c_1 = iv_1/|v_1|^2$ and $c_2 = -iv_2/|v_2|^2$. For the case where $\{\varphi_i\} = \{0, \pi/2, \pi, 3\pi/2\}$, this method reproduces the expected result $E_{+1}(t) = (S_0 + S_1 e^{-i3\pi/2} + S_2 e^{-i\pi} + S_3 e^{-i\pi/2})/4$.

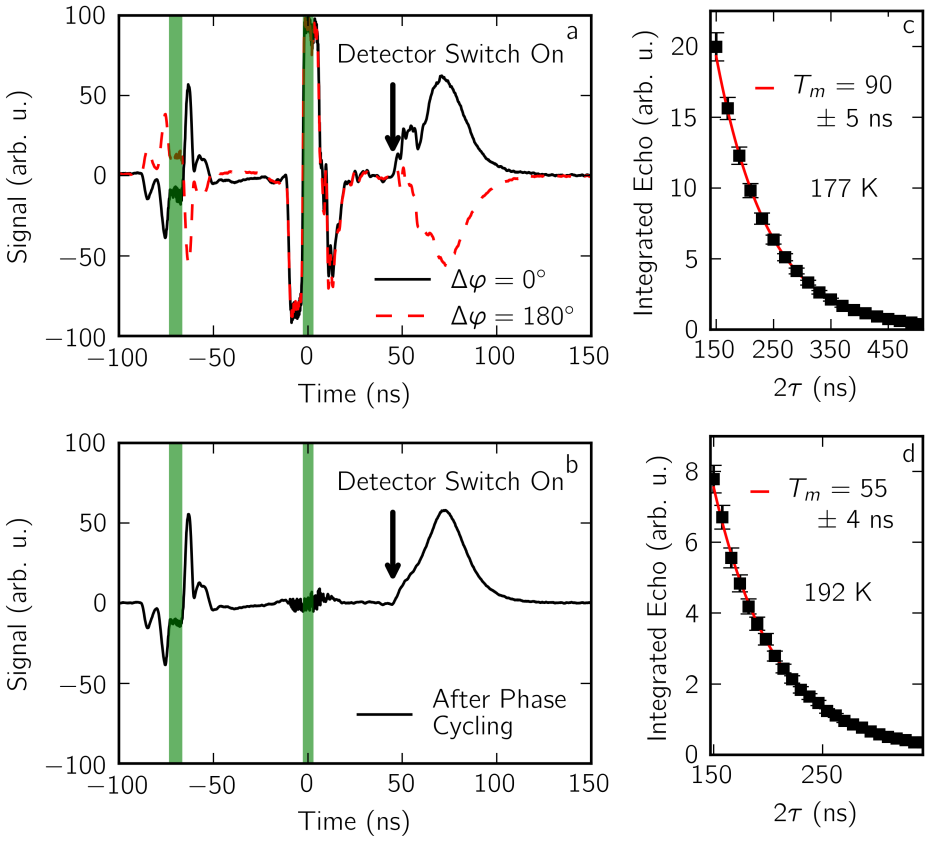

Figure 2.5: (a) Time domain signal from a two-pulse FEL-EPR experiment, performed on 1 mM $GdCl_3$ in a 0.6:0.4 v:v solution of glycerol$-d_8/D_2O$ at 177 K. The pulse lengths were 11 ns for pulse one and 7 ns for pulse two, with the pulse positions shown in green. A silicon protection switch is activated by a pulse of 530 nm light from a Nd:YAG laser 50 ns after the second pulse, when there is still appreciable scattered light reaching the detector. Signal recorded before this is due to incomplete detector isolation, which is exploited to enable phase sensitive detection. The solid black trace shows real channel signal when no phase shifter plates are inserted, and the red dashed trace shows the real channel signal when the phase of the first pulse is shifted by 180°. The initial echo is distorted by scattered light reaching the detector. Both signals are demodulated from the 500 MHz digitization frequency. (b) The real channel signal after two-step POPS, showing much reduced echo distortion and cancellation of the leaked light from the second pulse. Two-step POPS was used to perform phase memory time measurements at (c) 177 K and (d) 192 K, with the pulse lengths described above. Wilson, Aronson, Clayton, Glaser, Han, and Sherwin, Phys. Chem. Chem. Phys., 2018, 20, 18097-18109 - Reproduced by permission of the PCCP Owner Societies.

2.4 Spin relaxation time measurements using FEL-EPR and POPS

2.4.1 High temperature phase memory time measurements of Gd^{3+} ions with two-step POPS

Gadolinium complexes are often used as spin labels[99] for distance measurements using pulsed dipolar spectroscopy techniques [100], lineshape measurements [24, 25], or other experimental schemes, such as relaxation-induced dipolar modulation (RIDME)[101] spectroscopy. Therefore, high-field measurements of gadolinium phase memory times at or near physiological temperatures are extremely important. T_M for gadolinium complexes in frozen glassy matrices decreases strongly with increasing temperature and field [102], making it impossible to perform Hahn echo experiments above ∼100 K at 240 GHz with a 50 mW solid-state microwave source and our current non-resonant probe design. Two-step POPS was used to reduce the experimental dead time in electron spin echo decay experiments performed on frozen glassy solutions of $GdCl_3$ containing Gd^{3+} ions as shown in Figure 2.5. Reducing the dead time makes it possible to measure shorter phase memory times T_M, and improves the accuracy of T_M measurements.

In FEL-EPR Hahn echo experiments without phase cycling, detection artifacts caused by standing waves and scattered light produced by the second pulse partially obscure the desired EPR signal, limiting the experimental dead time to ∼70 ns. These artifacts appear in Figure 2.5a as distortions in the beginning of the echo signal. These artifacts

are effectively eliminated by a two-step phase cycle, as shown in Figure 2.5b. When the Hahn echo experiment is repeated with the phase of the first pulse inverted but the phase of the second pulse held constant, the phase of the echo also inverts. However, the phase of artifacts due to scattered light and standing waves produced by the second pulse does not change. By subtracting the complex signal generated by the second experiment from the complex signal generated by the first experiment, such detection artifacts are largely eliminated, allowing for nearly artifact-free data acquisition to begin ∼50 ns after the end of the second pulse, representing an improvement of the dead time before detection by ∼20 ns. With POPS-assisted FEL-EPR, the phase memory time T_M was measured for 1 mM $GdCl_3$ in a frozen glassy solution to be 90 ± 5 ns at 177 K (Figure 2.5c), and 55 ± 4 ns at 192 K (Figure 2.5d).

2.4.2 Measurements of phase memory time and instantaneous spectral diffusion in diamond P1 centers

P1 centers in diamond are substitutional nitrogen defects, which in type 1b diamond are typically present at about 10 - 100 parts per million (ppm) [38]. P1 center concentration and spatial configuration have been shown to play a dominant role in the decoherence rate, $1/T_2$, of both P1 centers and nitrogen-vacancy (NV) centers in type 1b diamond [103, 104]. Precisely determining the concentration of P1 centers in diamond is therefore of great interest, especially in light of recent efforts to fabricate NV center ensembles for NV-based quantum devices [105, 106, 107]. Recently, double electron-electron resonance

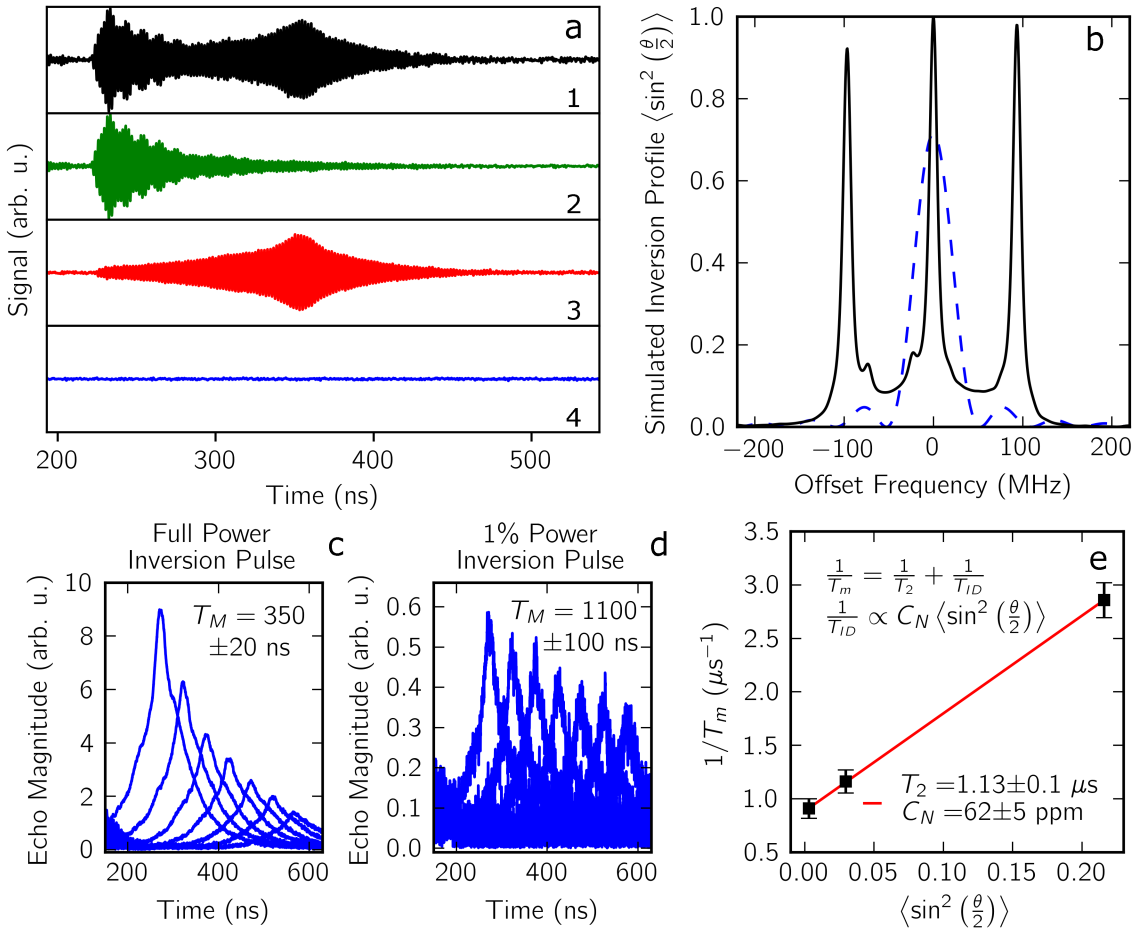

Figure 2.6: (a) Signal generated by a two-pulse experiment performed on P1 centers in type 1b diamond, measured on the central line (1) without phase cycling, and with four-step POPS to isolate (2) the FID from the second pulse, (3) the echo generated by the pair of pulses, and (4) the FID from the first pulse. The lengths of pulses one and two were 11 ns and 18 ns, respectively, with an inter-pulse delay of 350 ns. The FID generated by the first pulse has decayed below the detection threshold. (b) EPR lineshape of P1 centers in diamond for the sample in question, acquired by field-swept CW EPR at 240 GHz with the field axis converted to frequency. The dotted line shows the simulated inversion profile of the second pulse, for which $B_1 = 6.4$ Gauss in the rotating frame. (c) Time domain echo magnitude signals as a function of inter-pulse delay τ, for full power in the second pulse ($B_1 = 6.4$ Gauss in the rotating frame) and (d) for 1% power in the second pulse $B_1 = 0.64$ Gauss in the rotating frame). (e) Inverse phase memory time as a function of the calculated inversion profile of the second pulse $\langle \sin^2(\theta/2) \rangle$, quantifying the effect of instantaneous spectral diffusion on echo dephasing. Extrapolating to $\langle \sin^2(\theta/2) \rangle = 0$, $T_2 = 1.13 \pm 0.1$ μs. From the inverse T_M dependence on B_1, the concentration C_N of P1 centers is estimated to be 62 ± 5 ppm (relative to carbon). Wilson, Aronson, Clayton, Glaser, Han, and Sherwin, Phys. Chem. Chem. Phys., 2018, 20, 18097-18109 - Reproduced by permission of the PCCP Owner Societies.

(DEER) measurements at 115 GHz have been used to quantify P1 center concentration [38]. Instantaneous spectral diffusion provides another method for quantifying P1 center concentration. Two-pulse FEL-EPR experiments were performed on P1 centers in type 1b diamond to demonstrate coherence transfer pathway selection with POPS, and to explore the effects of instantaneous spectral diffusion on P1 center echo decay.

Instantaneous spectral diffusion (ID) can be understood in terms of the dephasing of the observed spins due to flips of neighboring dipole-coupled electron spins, which are caused by the applied microwave pulses. Spin flips which occur during the second pulse produce changes in the local magnetic field seen by observed spins which are not refocused by the Hahn echo. ID leads to spin echo dephasing with a rate $1/T_{ID}$, modifying the phase memory time T_M, the experimentally measured echo decay time constant, according to $1/T_M = 1/T_{ID} + 1/T_2$ [108]. T_{ID} depends on the P1 center concentration C_N, and on the refocusing pulse tip angle θ according to[109]

$$\frac{1}{T_{ID}} = C_N \frac{\pi}{9\sqrt{3}} \frac{\mu_0 g^2 \mu_B^2}{\hbar} \left\langle \sin^2\left(\frac{\theta}{2}\right) \right\rangle \tag{2.18}$$

where the inversion profile of the refocusing pulse $\left\langle \sin^2\left(\frac{\theta}{2}\right) \right\rangle$ with Rabi frequency $\Omega_R = \gamma B_1$ and length t_p is given by

$$\left\langle \sin^2\left(\frac{\theta}{2}\right) \right\rangle = \int_{-\infty}^{\infty} \frac{\Omega_R^2}{\delta^2 + \Omega_R^2} \sin^2\left(\frac{t_p}{2}\sqrt{\delta^2 + \Omega_R^2}\right) f(\delta) d\delta \tag{2.19}$$

where $\delta = \omega - \omega_L$ is the detuning, $f(\delta)$ is the normalized lineshape, and ω_L is the Larmor frequency. When the bandwith of the inversion pulse is small relative to the inhomogeneous EPR linewidth so that $\left\langle \sin^2\left(\frac{\theta}{2}\right) \right\rangle \ll 1$, ID is negligible. When the bandwith of the inversion pulse is not small relative to the EPR linewidth, T_M becomes tip-angle

dependent proportional to the concentration C_N. However, by systematically varying the tip angle, and therefore the inversion profile $\left\langle \sin^2\left(\frac{\theta}{2}\right)\right\rangle$ of the inversion pulse, the electron spin concentration C_N and the true electron spin T_2 can be ascertained [110].

POPS was used to measure the room temperature phase memory time of P1 centers in diamond as a function of the inversion profile of the second pulse, as show in Figure 2.6. Figure 2.6a-1 shows the time-domain signal generated by a pair of pulses separated by 350 ns which are on resonance with the central hyperfine peak of the P1 center. The FID from the second pulse and the spin-echo overlap substantially in time, and so distort each other. The FID displays modulations due to partial excitation of the outer two hyperfine peaks, while the echo does not as only the central peak is refocused.

In order to cleanly separate the echo signal from the FID signal so that T_M could be measured, coherence transfer pathway selection was performed by repeating the two-pulse experiment while using POPS to cycle the phase of the first pulse through four steps, generating four time traces. The first pulse was cycled through four phases, nominally $\{\Delta\varphi_i\} = \{0°, 90°, 180°, 270°\}$, and experimentally measured to be $\{\Delta\varphi_i\} = \{0°, 79°, 179°, 252°\}$. Figures 2.6a-2, 2.6a-3 and 2.6a-4 show the post-processed signals generated from the same four time traces, where the numerical phase shifts were chosen using the least-squares method to select for the FID from the second pulse (Fig. 2.6a-2), for the echo (Fig. 2.6a-3), and for the FID from the first pulse (Fig. 2.6a-4), which has decayed below the detection threshold. The inversion profile $\left\langle \sin^2\left(\frac{\theta}{2}\right)\right\rangle$ of the second pulse at full power was calculated from the measured EPR lineshape, using $t_p = 18$ ns

and $B_1 = 6.4$ Gauss. When using an 18 ns, 2.7 kW inversion pulse, T_M was found to be 350 ± 20 ns (Fig. 2.6c). When the power, and therefore the tip angle, of the inversion pulse was reduced, the echo amplitude decreased, but T_M was found to increase, consistent with the occurrence of instantaneous spectral diffusion. Figure 2.6d shows that with the inversion pulse attenuated to 1% power, the phase memory time was extended to 1100 ± 100 ns, an increase of more than a factor of three. Varying the tip angle of the inversion pulse and extrapolating to $\left\langle \sin^2\left(\frac{\theta}{2}\right)\right\rangle = 0$, a value of $T_2 = 1130 \pm 100$ ns was calculated (Fig. 2.6e). T_2 extrapolated in this way is consistent with phase memory time measurements performed on the same sample using 500 ns, low power pulses generated by a 50 mW solid state source, where $T_M = 1230 \pm 70$ ns was measured. From the dependence of $1/T_M$ on $\left\langle \sin^2\left(\frac{\theta}{2}\right)\right\rangle$ in Equation 2.18, the concentration of P1 centers C_N was estimated to be 62 ± 5 ppm. While the exact P1 center concentration is not known for this sample, this is a reasonable number for type 1b diamond [38].

2.4.3 T_1 Measurements

Two-pulse saturation-recovery experiments with POPS were used to perform room temperature T_1 measurements on liquid samples of trityl OX063. This result, shown in Figure 2.7, represents the first measurement of T_1 with FEL-EPR. Figure 2.7a shows a free induction decay generated by a 10 ns, 5 kW pulse with $\gamma B_1 = 11$ Gauss applied to a sample of 3.7 mM trityl OX063 dissolved in D_2O. The Fourier transform of the digitized FID is shown in Figure 2.7b, and is well-approximated by a Lorentzian with a FWHM of

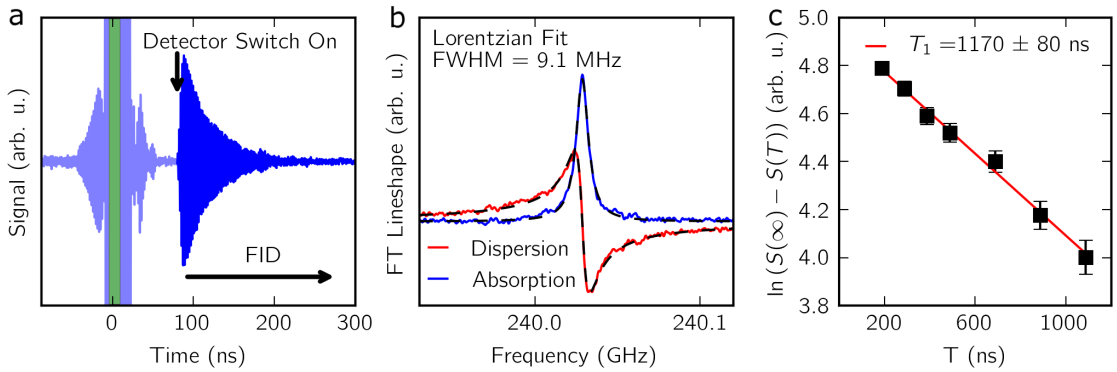

Figure 2.7: (a) Time domain FID from 3.7 mM trityl OX063 in D_2O at 291 K, generated by a 10 ns pulse (represented by the green bar) with 15 averages. Arrows mark the time when the detector switch is activated, and indicate the position of the FID. Signal before activation of the detector switch, shown in light blue, is due to incomplete isolation. (b) Fourier transform of the FID from left figure. The complex lineshape is well described by a Lorentzian with a FWHM of 9.1 MHz. (c) Saturation-recovery experiment performed on 3.7 mM trityl OX63 Data plotted is natural log of the difference between the integrated FID $S(T)$ as a function if inter-pulse delay T and the integrated FID in the absence of a saturation pulse $S(\infty)$. $T_1 = 1170 \pm 80$ ns is extracted from a linear fit to the data. Wilson, Aronson, Clayton, Glaser, Han, and Sherwin, Phys. Chem. Chem. Phys., 2018, 20, 18097-18109 - Reproduced by permission of the PCCP Owner Societies.

9.1 MHz, corresponding to $T_2^* = 35$ ns. This relatively narrow linewidth is fully excited by a 10 ns pulse, so that the sample magnetization can be read out with an FID.

The liquid solution sample containing trityl radical was sealed inside a flat rectangular cross-section glass capillary backed by a mirror. Sandwiched between the capillary and the mirror was a dielectric consisting of a 190 μm piece of high-resistivity silicon and two layers of Teflon tape. The details of this sample mounting scheme are discussed in more detail in Chapter 5 of this dissertation.

Saturation recovery experiments were performed utilizing the entire long FEL pulse, including the build-up to lasing [45], as the saturation pulse. Saturation pulses were typically $\sim 1.5 - 2$ μs long, with ~ 500 W of power. This was achieved by replacing the first "on" switch in the pulse slicer, shown in Figure 2.4, with a mirror. The saturation pulse was shut off with the first "off" switch. After a recovery period T, the magnetization was read out with an FID generated by a 10 ns, 5 kW pulse. Four step POPS was employed to correct for incomplete saturation, and to reduce experimental artifacts. The resulting sequence of FIDs were Fourier transformed, and the integral of the lineshape $V(T)$ used to determine T_1 from the slope of a linear fit to $\ln(V(\infty) - V(T))$, where $V(\infty)$ is the integrated lineshape in the absence of a saturation pulse. T_1 measured by this saturation recovery method was found to be 1170 ± 80 ns. In liquid solutions containing O_2, both T_1 and T_2 relaxation times for both trityl-type radicals and nitroxide radicals are influenced by collisions with paramagnetic O_2 [111, 112], are highly dependent on the oxygen partial pressure [113, 114], and are considerably shorter than in deoxygenated

aqueous samples [112, 115, 116]. The value of T_1 reported here is consistent with spin-lattice relaxation times performed at lower fields on oxygenated liquid samples with moderate oxygen concentrations [114, 111].

2.5 Discussion and Outlook

Phase cycling enabled by POPS dramatically extends the capabilities of the 240 GHz FEL-EPR spectrometer. First, phase cycling enables a ∼30 percent reduction in the dead time of the FEL-EPR spectrometer when performing Hahn echo experiments. High power pulses provided by FEL-EPR generate rapid $<$ 10 ns spin manipulations which allow for the study of samples with short relaxation times and broad EPR lines. However, the usefulness of FEL-EPR in studying fast relaxing systems is limited if the experimental dead time restricts the detection of EPR signals to long times. Dead time in FEL-EPR experiments is currently limited by scattered 240 GHz light, and 240 GHz light leaking through imperfect induction-mode isolation. This light, when it reaches the detector, is digitized and distorts or completely masks the EPR signals of interest. POPS can efficiently separate the echo generated by a pair of pulses from digitized signals caused by scattered light, reducing the experimental dead time from $\sim$ 70 ns to ∼50 ns. This development dramatically improves the capability of measuring fast-relaxing systems, such as spin-labeled biomolecules at temperatures close to physiological conditions ($>$ $200K$) or metal complexes such as gadolinium complexes in the same temperature range.

Second, phase cycling enables one to disentangle signals from a FID and an echo if they

overlap in time. Without phase cycling, detection of an echo is limited to experiments with inter-pulse delays significantly longer than the FID lifetime. This restriction is reduced in the same manner as the restriction imposed by scattered light, by using phase cycling to select the echo and suppress the FID. However, since all experimental signals recorded are stored during acquisition, the same set of experiments can be used to select either the echo, suppressing the FID, or to select the FID, suppressing the echo. The former is desired in a two-pulse echo experiment to measure T_2, while the latter is desired in a two-pulse inversion recovery or saturation recovery experiment to measure T_1. If appropriate pulse lengths are chosen, both experiments could be carried out simultaneously in a multiplexed fashion.

Third, phase cycling provides improved sensitivity for all samples by allowing one to probe short inter-pulse delays which maximize the echo amplitude. This improvement in sensitivity, together with the ability to disentangle FID and echo, enabled the identification of instantaneous spectral diffusion in phase memory time measurements of P1 centers in diamond. Beyond the experiments demonstrated in this dissertation, detection of short-τ echoes is especially crucial for correctly analyzing echo decays with multiple components, or for severely signal-limited samples.

Finally, phase cycling has enabled the first direct measurement of T_1 in a FEL-EPR experiment. A modification of the pulse slicing optics used to generate short pulses for spin manipulations from the long FEL pulse has allowed for the generation of long saturation pulses which, together with FID detection, was used to conduct saturation-

recovery experiments. This new development opens the door to measuring spin-lattice relaxation times of narrow line radicals at room temperature and in liquid samples, a regime of enormous importance for studying biological systems.

2.6 Chapter Summary

Robust two- and four-step phase cycling with optomechanical phase shifters (POPS) procedures have been developed for two-pulse FEL-EPR experiments. This method of phase cycling relies on retrospective phase correction, and is generally applicable to any experiment where the source phase is not locked. Phase shifts in POPS are applied quasioptically directly at the detection frequency, with the only requirement being the ability to perform retrospective phase detection and correction [92]. Phase cycling with nearly arbitrary phase shifts was addressed, greatly simplifying the construction of potential future phase cycling experiments. Phase cycling has enabled measurements of the spin-lattice relaxation time T_1 in samples which are amenable to FID detection. POPS as implemented here could also find applications in EPR and DNP experiments employing gyrotrons, provided the gyrotron is phase-stable on the timescale of the desired pulse sequence.

Chapter 3

Anomalous Bloch sphere dynamics in a crystalline organic radical

Abstract

Pulsed electron paramagnetic resonance (EPR) enables the creation and manipulation of states of interacting spins far from thermal equilibrium. Free electron laser-powered pulsed EPR experiments performed at 240 GHz / 8.56 T on crystalline BDPA, an organic radical, reveal a nonlinear dependence on sample magnetization not typically encountered in EPR, which manifests as a tip-angle dependent resonant frequency. Frequency shifts as large as 11 MHz (45 ppm) are observed during a single Rabi oscillation. These frequency shifts are attributed to a large sample magnetization and to strong spin-spin interactions. A semi-classical model which includes a demagnetizing field is developed, and subsequently used to map out the magnetization's Bloch sphere dynamics during

anomalous Rabi oscillations. Nonlinear interactions are tunable, by modifying temperature and sample geometry. Measurements of anomalous Bloch sphere dynamics provide the first steps towards using pulsed EPR to measure long-range electron spin quantum correlations.

Acknowledgements

CBW performed 240 GHz FEL-EPR measurements, analyzed all data, and designed and carried out the numerical simulations. Jessica Clayton assisted in performing FEL-EPR measurements. Devin Edwards and Susumu Takahashi conducted the initial FEL-EPR measurements where frequency shifts were observed. David Enyeart and Nick Agladze were instrumental in maintaining, repairing, and assisting with the operation of the UCSB FEL. Gerry Ramian participated in important discussions.

Material presented in Chapter 2 is being prepared in a different format for publication as C. Blake Wilson, Devin T. Edwards, Jessica A. Clayton, Songi Han, and Mark S. Sherwin, "Anomalous Bloch sphere dynamics in a crystalline organic radical observed by pulsed electron paramagnetic resonance at 240 GHz."

3.1 Introduction

Understanding the magnetic properties of systems with unpaired electrons is at the heart of much of modern condensed matter physics. Over the past decades, extensive efforts have focused on understanding systems at thermal equilibrium. As a result, ordered

ground states such as the ferromagnet (FM) and antiferromagnet (AFM) are now well understood. Recent research has led to an improved understanding of more exotic, highly entangled ground states such as quantum spin liquids in frustrated magnets [117, 118, 119, 120, 121]. The behavior of large numbers of interacting spins far from equilibrium, however, remains challenging to study despite intense theoretical[122] and experimental investigations[123].

Electron paramagnetic resonance (EPR) spectroscopy is a powerful and precise tool for studying excitations in magnetic media. Here, we use high-power pulsed EPR, which enables rapid, tunable, and coherent spin control[124, 54], to prepare and then probe a variety of out-of-equilibrium magnetic states. We leverage extremely high-bandwidth excitation pulses to observe complex spin dynamics which emerge at high magnetic fields in an out-of-equilibrium spin system.

3.1.1 BDPA

BDPA (1,3-bisdiphenylene-2-phenylallyl) is an organic spin-1/2 radical first synthesized by Frederick Koelsch at Harvard University in 1931-1932. It was the first stable organic radical to be discovered. However, Koelsch's 1932 manuscript, which he submitted to the Journal of the American Chemical Society (JACS), was rejected by the journal referee on the grounds that BDPA could not be a stable organic radical, because such a thing could not exist [125]. Koelsch's manuscript sat on his shelf for over 20 years until EPR measurements in 1955 confirmed BDPA was in fact a stable organic radical. Koelsch

subsequently published his synthesis of BDPA in 1957 [125]. In his publication, again submitted to JACS, Koelsch included a footnote where he explained the publication history. Koelsch's footnote ends with the following [125]:

> Because the structure originally suggested appears to be confirmed, and because many requests for samples and preparational details are being received, it appears desirable to publish the work now. In the interest of historical accuracy, the only important changes in the original paper are the additions of footnotes 5, 6 and 8.

Since 1957, BDPA its derivative radicals have become widely used as standard samples calibrating and characterizing EPR spectrometers [126, 40, 127] because of their strong, narrow EPR lineshape, and because of their stability. Koeslsch notes in his 1957 JACS publication that

> A sample kept in air 23 years is unchanged in appearance and shows a high free-radical content.

BDPA has also been used successfully as a polarizing agent in DNP-enhanced NMR experiments [128, 129].

Outside of the magnetic resonance community, BDPA has been the subject of much theoretical and experimental study [130, 131, 132, 133, 134]. BDPA crystallized 1:1 with benzene (BDPA-Bz) is well described by a quasi-one dimensional Heisenberg antiferromagnetic linear chain model, with an exchange integral of $J/k_B = -4.4$ K along the chain and an effective interchain coupling $|J'/k_B| \sim 0.04$ K [130, 133]. BDPA-Bz was the

first organic crystal radical whose phase transition from paramagnet to antiferromagnet was observed, a transition which occurs at 1.7 K [130, 131]. Azuma *et al.* reported that BDPA-Bz exhibits an in-plane isosceles triangle type spin frustration [131].

At room temperature, where BDPA-Bz is a paramagnet, one important effect of the strong exchange interaction is to narrow the EPR line though a process known as exchange narrowing [135].

Write more about exchange narrowing here

3.1.2 BDPA at 8.56 T

BDPA has a g value of 2.0026 [130]. BDPA-Bz crystals and exhibit a narrow, extremely strong EPR resonance at 8.56 T. For this reason, crystals of BDPA-Bz were selected as ideal samples characterizing the FEL-EPR spectrometer in the early stages of instrument development.

Some of the first FEL-EPR experiments performed were nutation experiments intended to characterize the microwave magnetic field strength at the sample position. Nutation experiments in FEL-EPR are performed with a single short, resonant pulse "sliced" from a quasi-CW FEL pulse. This short pulse tips the BDPA magnetization away from thermal equilibrium. When the pulse is on, the magnetization undergoes Rabi oscillations [136] with a Rabi frequency ω_1 given by $\omega_1/2\pi = g\mu_B B_1/h$, where B_1 is the magnetic field of the 240 GHz pulse in the rotating frame. When the pulse turns off, the magnetization remains partially tipped and precesses about the external magnetic

field at the Larmor frequency, $\omega_L = g\mu_B B_0/\hbar$, emitting circularly polarized magnetic dipole radiation in the form of a free induction decay (FID). The FID amplitude is proportional to the magnetization's projection onto the transverse plane. By measuring the FID amplitude as a function of pulse length, the period of Rabi oscillations can be measured, which can be used to measure the rotating frame magnetic field B_1 if g is known.

In 2012, Takahashi *et al.* demonstrated FEL-driven electron spin nutation experiments performed on BDPA-Bz crystals, with a nutation period of $\sim$ 24 ns [51]. From this nutation period, the π pulse length with FEL-powered EPR was inferred to be $\sim$ 12 ns, around two orders of magnitude shorter than what was possible with what was at the time a state-of-the-art 30 mW solid-state microwave source.

However, it was quickly noticed that it was difficult to achieve full electron spin inversion in BDPA-Bz. The reason for this incomplete inversion was partially revealed with the subsequent, surprising discovery that the BDPA-Bz magnetization precession frequency appeared to change during the course of the EPR experiment.

This chapter explores these two effects, the apparent poor resonant population inversion efficiency and the changing precession frequency. Both effects are attributed to a large sample magnetization at high magnetic field, and to strong spin-spin interactions within the sample. A semi-classical, non-linear model is presented which explains both effects, and is used to characterize the magnetizations Bloch sphere dynamics, which are revealed to be quite anomalous.

3.2 BDPA probed by 240 GHz FEL-EPR

Figure 3.1 shows the response of a single BDPA-Bz grain placed in a 8.56 T magnetic field to a 2 ns long, resonant excitation pulse "sliced" from the 40 ns long FEL cavity dump [45]. The BDPA-Bz grain was mounted on a silver-coated mirror and placed at the end of the waveguide taper. The short, resonant pulse tips the sample magnetization away from thermal equilibrium which subsequently precesses at 240 GHz, emitting a circularly polarized FID. $\sim$ 75 ns after the end of the FEL pulse, a silicon switch is activated by a high-power, 532 nm pulse from a frequency-doubled Nd:YAG lser. This switch protects the detector, a subharmonically pumped Schottky diode mixer mounted at the end of a microwave horn, from the high-power FEL pulse. The FID signal is mixed down in two steps, first to an intermediate frequency (IF) of 10 GHz, and then to a final offset frequency of 500 MHz where it is digitized. The complex FID signal is then Fourier transformed to extract the Fourier transform-EPR (FT-EPR) lineshape (Figure 3.1b).

Figure 3.1c shows the integrated FT-EPR intensity as a function of pulse length. As the pulse length increases, the magnetization rotates further in the Bloch sphere, undergoing Rabi oscillations. At the first signal maximum, occurring for a 10 ns excitation pulse duration, the magnetization has rotated by $\pi/2$ in the Bloch sphere, while at the first minimum, occurring at around 20 ns, the magnetization has nominally been inverted. From the period of the observed Rabi oscillations, the Rabi frequency in this experiment can be inferred to be around 25 MHz. However, the fact that the integrated FID at 20 ns is not zero indicates that spin inversion is far from perfect.

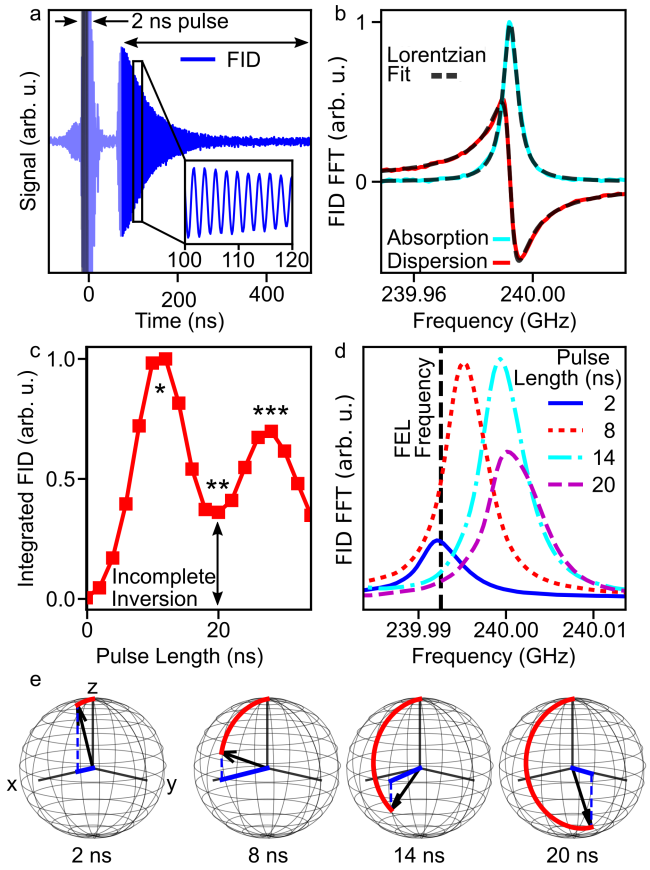

Figure 3.1: **a** Room-temperature FID signal generated by a 2 ns FEL pulse, highlighted in grey, applied to a BDPA-Bz grain. Inset: the signal digitized at the intermediate frequency (IF = 500 MHz, shown in inset). **b** Fourier transform of the FID generated by a 2 ns pulse. The FT-EPR lineshape complex lineshape is well described by a Lorentzian with a FWHM of 5.9 ± 0.1 MHz. **c** Integrated FT-EPR intensity as a function of pulse length, demonstrating Rabi oscillations. The magnetic field was chosen so the FID generated by a 2 ns pulse is on resonance with the FEL pulse. For pulse lengths corresponding to the two maxima, the sample magnetization is rotated by $\pi/2$ (*) and by $3\pi/2$ (***), while at the minimum (**) the magnetization has been rotated by π. The minimum of the Rabi oscillation is not at zero, indicating incomplete population inversion. **d** FT-EPR absorption lineshape plotted for four pulse lengths. The FID generated by a 2 ns pulse is on resonance with the FEL pulse, FIDs generated by longer pulses are not. **e** In red, the trajectory taken by the sample magnetization on the Bloch sphere. In blue, the magnetization vector projected onto the x-y plane.

Imperfect spin inversion can be caused by a number of effects, including an inhomogeneous static B_0 field (so that the Larmor condition varies across the sample), an inhomogeneous drive B_1 field (so that different parts of the sample are inverted at different times), or poor field/frequency stability. Steps were taken to eliminate each of these factors. BDPA-Bz crystalls were limited to $\sim$300 to $\sim$500 μm in diameter, which is significantly smaller than the 1.249 mm wavelenth of 240 GHz radiation, which minimizes both B_0 and B_1 inhomogineity. Frequency and field stability were judged to not be significant contributors, due to the measured stable, Fourier-limited FEL linewidth and to the reproducibility of experiments.

Analysis of the FT-EPR signal in frequency space reveals the frequency of the FID, as measured by the FT-EPR signal, changes as a function of pulse length (Figure 3.1d). This indicates that the EPR frequency ω_0, typically given by the Larmor condition $\omega_L = \gamma B_0$ and where $\gamma = g\mu_B/\hbar$ is the gyromagnetic ratio, changes as a function of pulse length. This is quite an unexpected situation in conventional EPR experiments. Indeed, frequency shifts were confirmed in all BDPA-Bz grains measured, but were completely absent in other EPR experiments [51, 86].

The change in the magnetization precession frequency observed in BDPA-Bz crystals can be explained by two factors. First, BDPA-Bz has a very large thermal magnetization at room temperature in an 8.56 T field, much larger than that encountered in typical EPR samples, due to the high spin concentration. Second, the spin-spin interactions are strong. The -4.4 K exchange interaction corresponds in frequency units to $J/h \sim 90$

GHz, which is quite large in the context of EPR experiments. These two factors can be modeled in a mean-field sense by modifying the semiclassical Bloch equations to include the crystal's demagnetizing field H_M, by analogy to ferromagnetic resonance (FMR) [137].

The demagnetizing field H_M is non-zero for any material with non-zero net magnetization, but it is typically negligible under the conditions where EPR is performed. The demagnetizing field depends on both the magnetization $\mathbf{M}$ and the sample geometry, and in general is quite challenging to calculate. For samples with ellipsoidal geometries, however, the demagnetizing field simplifies to

$$H_M = -N \cdot \mathbf{M} \tag{3.1}$$

where N is the demagnetization tensor [138]. The total magnetic field seen by the spins in the sample is given by $\mathbf{B} = \mu_0(\mathbf{H} + \mathbf{M})$. Plugging this field total field into the Bloch equations and neglecting relaxation gives

$$\frac{d}{dt}\mathbf{M} = \gamma \mathbf{M} \times \mu_0\big(\mathbf{H}_0 - N \cdot \mathbf{M}\big) \tag{3.2}$$

where $\mathbf{H}_0 = \mathbf{B}_0/\mu_0$ is the externally applied magnetic field.

If the BDPA-Bz grain can be modeled as an ellipsoid, with the external magnetic field aligned along one of the principle axes of N, then the freely precessing sample

magnetization obeys the equations of motion

$$\frac{d}{dt}M_x = \mu_0\gamma\Big(H_0 - (\delta_z - \delta_x)M_z\Big)M_y - M_x/T_2 \tag{3.3a}$$

$$\frac{d}{dt}M_y = -\mu_0\gamma\Big(H_0 - (\delta_z - \delta_x)M_z\Big)M_x - M_y/T_2 \tag{3.3b}$$

$$\frac{d}{dt}M_z = \mu_0\gamma(\delta_x - \delta_y)M_xM_y - (M_z - M_0)/T_1 \tag{3.3c}$$

where $\delta_x, \delta_x, \delta_z$ are the principal values of the demagnetization tensor, M_0 is the equilibrium magnetization, and T_1 and T_2 are the phenomenological Bloch spin-spin and spin-lattice relaxation times.

Notice here that these modified Bloch equations are nonlinear. In general, this could lead to turbulent spin dynamics. There are two special case where the dynamics simplify: spherically symmetric samples, and axially symmetric samples.

Suppose that the sample is perfectly spherical, in which case N is proportional to the identity matrix, $\delta_x = \delta_y = \delta_z$, and these modified Bloch equations reduce to the familiar, linear Bloch equations.

Suppose instead that the sample is not spherically symmetric but does have axial symmetry. In this case, $\delta_x = \delta_y = \delta_\perp$ and $\delta_z = \delta_\parallel$. If the external field $B_0 = \mu_0 H_0$ is aligned along the z axis of N, then the equations of motion given in Equation 3.3 simplify

to

$$\frac{d}{dt}M_x = \mu_0\gamma\Big(H_0 - (\delta_\parallel - \delta_\perp)M_z\Big)M_y - M_x/T_2 \tag{3.4a}$$

$$\frac{d}{dt}M_y = -\mu_0\gamma\Big(H_0 - (\delta_\parallel - \delta_\perp)M_z\Big)M_x - M_y/T_2 \tag{3.4b}$$

$$\frac{d}{dt}M_z = -(M_z - M_0)/T_1 \tag{3.4c}$$

Defining

$$\theta_d = \delta_\parallel - \delta_\perp \tag{3.5}$$

and

$$\omega(M_z) = \mu_0\gamma(H_0 - \theta_d M_z) \tag{3.6}$$

then Equation 3.4 further simplifies to

$$\frac{d}{dt}M_x = \omega(M_z) - M_x/T_2 \tag{3.7a}$$

$$\frac{d}{dt}M_y = -\omega(M_z) - M_y/T_2 \tag{3.7b}$$

$$\frac{d}{dt}M_z = -(M_z - M_0)/T_1 \tag{3.7c}$$

Equations 3.4 and 3.7 show, neglecting terms of $|M_z/H_0|^2$ and higher, that the effect of the demagnetization field for an axially symmetric sample geometry is to shift the EPR resonance frequency away from the Larmor condition by $\Delta\omega = -\mu_0\gamma\theta_d M_z$. This is quite analogous to the FMR condition, which appears in the Kittel equations [137].

However, unlike FMR, which is nearly always performed in the small tip-angle regime, for a paramagnet the full magnetization $\mathbf{M}$ can be rotated into the transverse plane or even inverted by resonant microwaves. Put another way, while FMR is confined to a tight cone at the top of the Bloch sphere, EPR has access to the full Bloch sphere.

Equation 3.7 shows that the effect of a near-resonant microwave pulse which tips the sample magnetization will shift the resonance frequency by an amount proportional to the change in M_z. If the initial magnetization is given by $\mathbf{M} = M_0\hat{z}$, the maximum frequency shift ΔF will occur after the magnetization is inverted,

$$\Delta F = \frac{1}{2\pi} 2\gamma\mu_0\theta_d M_0 \tag{3.8}$$

The magnetization M_0 for BDPA-Bz was measured as a function of temperature by Duffy *et al.* [130], and at room temperature is given by $M_0 = 270$ A/m. Plugging this into Equation 3.8, and taking $\theta_d \sim 1$ (corresponding to a perfectly flat disk), the maximum expected frequency shift is predicted to be $\Delta F \sim 19$ MHz. This is consistent with the observed frequency shifts, and is several times larger than the EPR linewidth at 240 GHz (see Figure 3.1).

Incomplete inversion is explained by this magnetization-dependent frequency shift as follows. In the nutation experiment shown in Figure 3.1, the spin system begins on resonance with the drive field ω_{FEL}, so that

$$\omega_{\mathrm{FEL}} = \omega(M_0) = \omega_L - \mu_0\gamma\theta_d M_0 \tag{3.9}$$

As the magnetization is tipped away from the $\hat{z}$ direction, the spin system is driven off resonance by the changing demagnetization field, by an amount proportional to $M_0 - M_z$.

This has two consequences. First, the changing resonance condition results in a changing effective field in the rotating frame, which causes the spins to nutate about a changing axis. Second, as the spin system moves off resonance, the instantaneous detuning δ modifies the frequency at which the spins nutate, from the on-resonance Rabi frequency ω_1 to an off-resonance effective Rabi frequency Ω_1,

$$\omega_1 \rightarrow \Omega_1 = \sqrt{\omega_1^2 + \delta^2} \tag{3.10}$$

For an arbitrary sample geometry, the magnetization dynamics can become extremely complicated.

3.3 Characterizing anomalous Bloch sphere dynamics

For the following experiments, a single grain of crystalline BDPA-Bz was selected. Criteria for selection were 1) the grain should be as axially symmetric as possible, and 2) the grain should be as flat as possible. A grain with a geometry which fairly approximates an oblate spheroid was selected. The grain was measured with optical microscopy to have an aspect ratio of roughly 7:1, for $\theta_d = 0.65$ [138]. Figure 3.2b shows a nutation experiment performed on this BDPA-Bz grain, with the colorbar indicating the FT-EPR amplitude and with the FT-EPR frequency indicated on the vertical axis. The magnetic field was chosen so that the excitation pulse satisfies the unmodified Larmor condition, rather than the small tip-angle precession frequency. The spin system initially has an EPR fre-

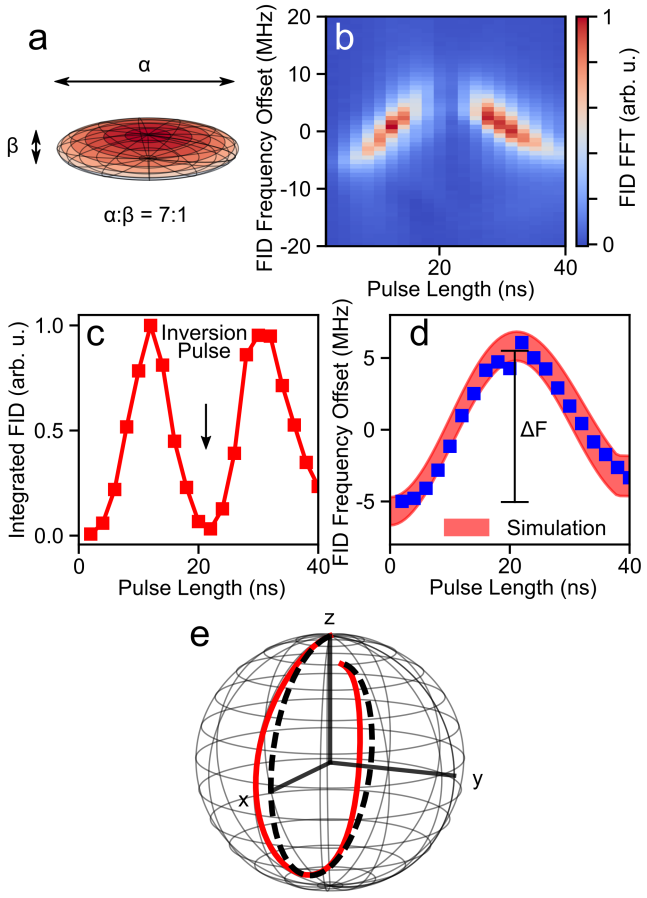

Figure 3.2: **a** Schematic representation of a BDPA-Bz crystal as an oblate spheroid, with a ratio of major to semi-major axes of 7:1. **b** Contour plot of the FT-EPR absorption lineshape, **c** integrated FID intensity, and **d** mean FID frequency, as a function of pulse length as BDPA-Bz magnetization undergoes Rabi oscillations. The FID frequency axes are referenced to the FEL frequency. The magnetic field is chosen so that the FID generated by a $\pi/2$ pulse has the same frequency as the FEL. The Rabi oscillations minimum is close to zero, indicating nearly complete population inversion is achieved with the magnetic field thus chosen. **e** In red, the simulated Bloch sphere trajectory for BDPA-Bz undergoing one Rabi oscillation. In black, the simulated trajectory in the absence of a demagnetization field.

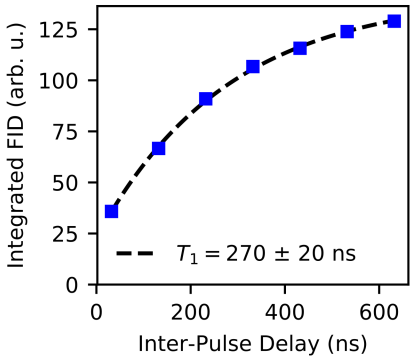

Figure 3.3: Integrated FT-EPR amplitude as a function of inter-pulse delay T between the saturation pulse and the read-put pulse, the latter of which generates a FID. Dashed line shows a functional fit of the form $y(T) = C - A \times e^{-T/T_1}$, from which T_1 was extracted.

quency below the excitation frequency, is driven towards resonance as the magnetization is tipped away from the z axis. At the end of a $\pi/2$ pulse, the precession frequency matches the excitation frequency. For larger tip angles, the precession frequency moves higher than the drive frequency, is maximally shifted from the initial precession frequency for a π pulse, and then returns to match the drive frequency for a $3\pi/2$ pulse. Nutation experiments performed in this way achieve nearly complete magnetization inversion, as evidenced by the minimum of the integrated FT-EPR signal being almost zero in Figure 3.2.

The observed frequency shift with pulse length can be simulated by numerically integrating in Equation 3.4, if the sample geometry, initial magnetization, and phenomenological relaxation rates are known. The sample geometry was taken to be an oblate spheroid with an aspect ratio of 7:1, for $\theta_d = 0.65$. The initial magnetization was set to be $M_0 = 270$ A/m. The phenomenological Bloch relaxation times T_1 and T_2 at 240 GHz were measured experimentally.

T_1 was estimated using an FID-detected saturation-recovery experiment. A ~ 1.5 μs long, 450 W pulse "sliced" from a quasi-CW FEL pulse was used to saturate the BDPA-Bz resonance. After a delay T, a second, 10 ns long pulse "sliced" from the portion of the FEL pulse boosted by the cavity dump was used to generate a FID. The second, 10 ns pulse had around 5.5 kW of power, for a Rabi frequency of 25 MHz, while the saturation pulse had a Rabi frequency of 8 MHz. Four-step phase cycling was used [86], as described in Chapter 2 of this dissertation. The FID amplitude, shown in Figure 3.3, reads off how much the magnetization has recovered to the equilibrium value after the saturation pulse, which occurs with time constant T_1. T_1 was extracted by fitting the amplitude of the integrated FT-EPR absorption lineshape $Y(T)$ after delay T to a function of the form

$$Y(T) = Y(\infty) - \Big(Y(\infty) - Y(0)\Big) \times e^{-T/T_1} \tag{3.11}$$

$Y(\infty)$ is the amplitude of the FT-EPR absorption lineshape in the absence of an inversion pulse, and $Y(0)$ is the amplitude of immediately after the inversion pulse, which is included to account for imperfect saturation. T_1 was measured to be 270 ± 40 ns. This value of T_1 is probably a low estimate, since Equation 3.11 does not take into account the shift in the precession frequency caused by the changing demagnetization field. $Y(\infty)$ and $Y(0)$ were left as fit parameters.

T_2 was estimated using a two-pulse Hahn echo decay sequence. Two short pulses were "sliced" with an inter-pulse delay of τ, with lengths of 11.5 ns and 14 ns for the first and second pulse. As for the saturation-recovery experiment, the first pulse was sliced from the 450 W portion of the FEL pulse, with a Rabi frequency $\omega_1/2\pi = 8$ MHz,

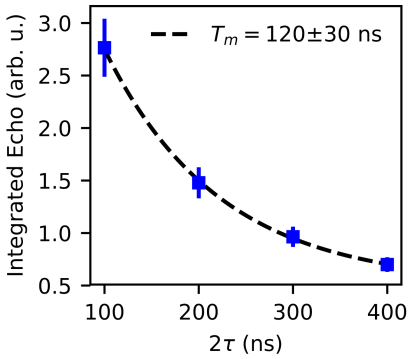

Figure 3.4: Integrated electron spin echo as a function of twice the delay τ between the first pulse and the refocusing pulse. The electron spin echo decay was fit to a function of the form $E(2\tau) = A \times e^{-2\tau/T_2} + C$, from which T_2 was extracted.

and was therefore a small tip-angle pulse. The second pulse was applied to refocus the magnetization into a Hahn echo. The power in the refocusing pulse was attenuated to as low as possible while still producing an echo, which turned out to be 55 W, for an on-resonance Rabi frequency of 2.5 MHz. The pulse was attenuated in order to minimize the effects of instantaneous spectral diffusion [108, 109, 54, 86] and the demagnetizing field shift. Four-step phase cycling, as described in Chapter 2, was used to isolate the echo signal. The integrated spin-echo was acquired as a function of the inter-pulse delay τ, as shown in Figure 3.4. T_2 was extracted by fitting the integrated echo signal $E(\tau)$ after an inter-pulse delay τ to a function of the form

$$E(\tau) = A \times e^{-2\tau/T_2} + C \tag{3.12}$$

where A and C were left as fit parameters. In this way, T_2 was estimated to be 120 ± 30 ns. As for the T_1 measurement, this value of T_2 is probably a low estimate due to residual precession frequency shift instantaneous spectral diffusion. However, the measured value of T_2 is in good agreement with values measured at low-field [132], which is encouraging.

Armed with these estimates for T_1 and T_2, simulations of the FID frequency dependence on pulse length over a full Rabi oscillation were carried out. The result, shown in Figure 3.2, were in excellent agreement with experimental results. Uncertainties in T_1, T_2, the Rabi frequency ω_1, and the FEL detuning were taken into account through a Monte-Carlo method. Simulations were repeated with different values for T_1, T_2, ω_1, and FEL detuning, all randomly drawn from Gaussian distributions with their respective uncertainties. The width of the simulated frequency shift indicates the 95% confidence interval as calculated by this Monte-Carlo method.

The simulated magnetization trajectory in the rotating frame is shown in Figure 3.2, along with a trajectory simulated for a spherical sample ($\theta_d = 0$). The simulated trajectories begin to deviate as the tip angle increases, with the deviation reaching a maximum for a $\pi/2$ tip angle. As the trajectories continue, the deviation decreases between tip angles of $\pi/2$ and π, until the two trajectories nearly intersect for a π pulse.

3.3.1 Magnetization evolution over many nutation cycles

The data shown in Figure 3.2 was taken using the cavity dump to boost the FEL power, in order to observe rapid Rabi oscillations. The cavity dump pulse is only 40 ns long, however, which is only long enough to observe one full nutation in the Bloch sphere. In order to probe the magnetization evolution over many nutation cycles, experiments were performed with longer pulses "slicing" from the lower power, but longer-lasting, quasi-CW FEL pulse. Long pulses can be generated either using the mm-wave silicon

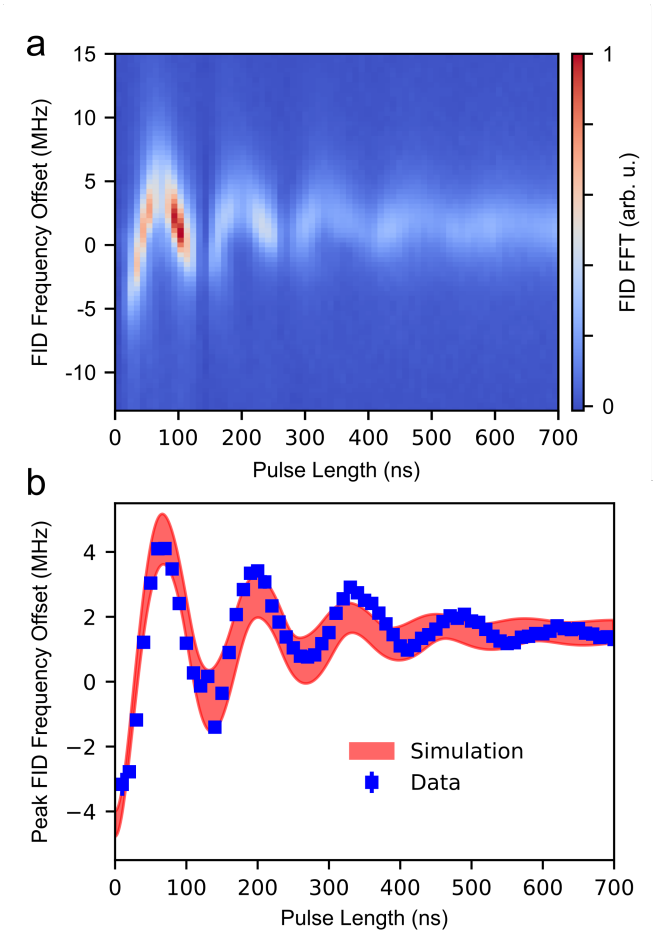

Figure 3.5: **a** Contour plot of the FT-EPR absorption lineshape, and **b** mean FID frequency, as a function of pulse length as BDPA-Bz crystal undergoes Rabi oscillations over many cycles. Simulated mean FID frequencies match experimental results over multiple oscillations.

coupler, or the hole coupler. At 240 GHz, the silicon coupler produces higher power in a long pulse.

The evolution of the magnetization over many Rabi cycles was probed by varying the length of a pulse "sliced" from the quasi-CW FEL pulse from the silicon coupler. The cavity dump was not used, in order to maintain a uniform microwave B_1 field over the length of the pulse. Figure 3.5 shows the result of a nutation experiment performed with

an on-resonance Rabi frequency $\omega_1/2\pi = 8MHz$ for pulse lengths between 0 and 700 ns. At least five Rabi cycles are observed. Figure 3.5a is a contour plot which shows the evolving FID precession frequency (vertical axis) and FT-amplitude (indicated by color) as a function of pulse length (horizontal axis). Numerical simulations of the modified, nonlinear Bloch equations are once again in excellent agreement with experimental results. The width of the simulation curve shown in Figure 3.5 indicates the 95% confidence interval, calculated using the Monte Carlo procedure. The decay in the observed Rabi oscillations is primarily related to spin-lattice (T_1) and spin-spin (T_2) relaxation.

3.3.2 Temperature dependence

The maximum tip-angle dependent precession frequency shift varies with temperature, since the BDPA-Bz magnetization is temperature dependent. Assuming a paramagnetic sample consisting of spin-1/2 electrons with density n,

$$M_0 = \frac{g\mu_B}{2} n \tanh\left(\frac{\mu_0 g\mu_B H_0}{2k_B T}\right) \tag{3.13}$$

In the high temperature limit where $k_B t \gg \mu_0 g\mu_B H_0$,

$$M_0 = \frac{(g\mu_B)^2}{4k_B T} n\mu_0 H_0 = \frac{g\mu_B \hbar}{4k_B T} n\omega_L \tag{3.14}$$

In this limit, the fractional frequency shift away from the Larmor condition $|\Delta\omega/\omega_L|$ is given by

$$\frac{\Delta\omega}{\omega_L} = \mu_0 n \frac{(g\mu_B)^2}{4k_B T} \tag{3.15}$$

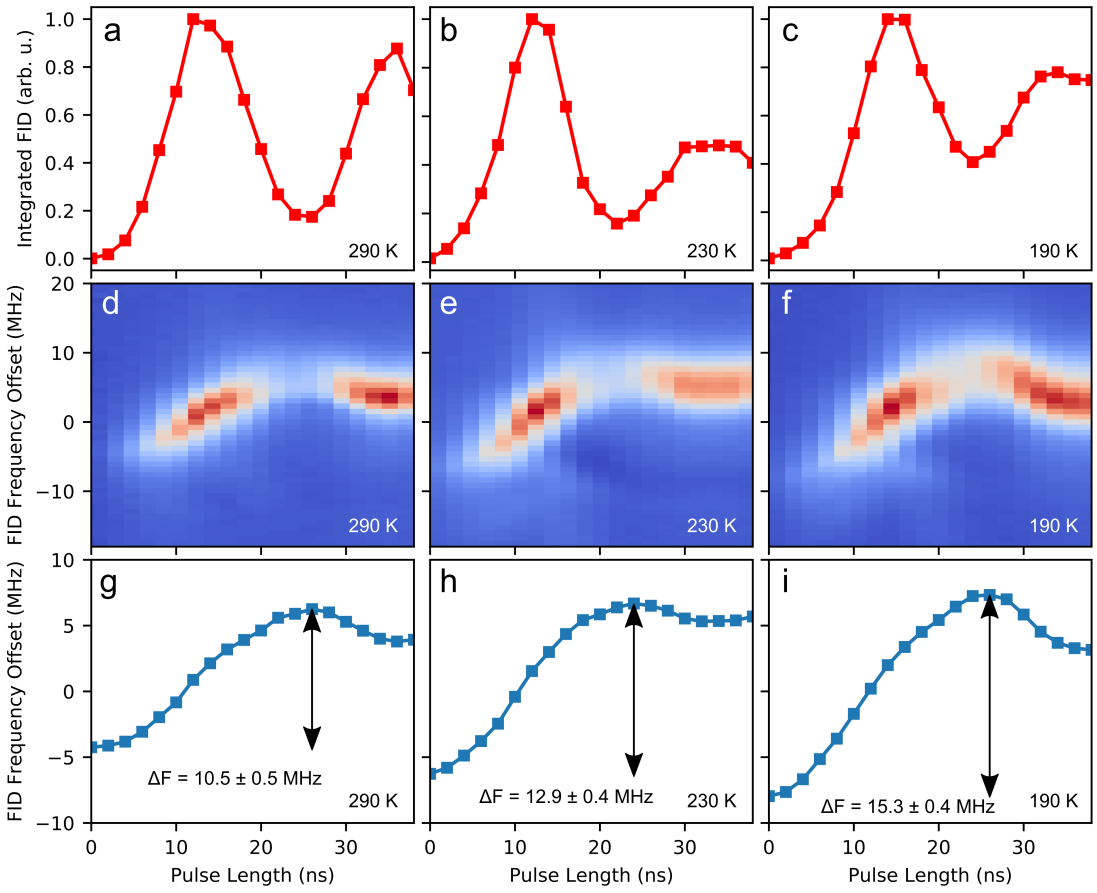

Figure 3.6: Top: Integrated FT-EPR amplitude as a function of pulse length, demonstrating Rabi oscillations at 290 K **a**, 230 K **b**, and 190 K **c**. **d-f**: Contour plots showing the FT-EPR absorption lineshape as a function of pulse length, showing the shift in the EPR condition. **g-i**: Mean FID frequency as a function of pulse length. The maximum frequency shift ΔF is recorded for each temperature.

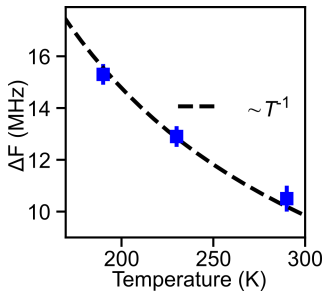

Figure 3.7: Temperature dependence of the maximum observed FID frequency shift ΔF, consistent with Eq. 3.15, indicating shift is proportional to magnetization.

Nutation experiments were performed on the a grain of crystalline BDPA-Bz at three temperatures: 290 K, 230 K, and 190 K. All three temperatures are well above the electron Zeeman temperature T_z at 8.56 T, given by $T_z = g\mu_B\mu_0 H_0/k_B = 11.6$ K, and so can be treated in the high-temperature limit. The results are shown in Figure 3.6. Going to lower temperature resulted in a larger frequency shift by an amount inversely proportional with temperature (Figure 3.7), as predicted by Equation 3.15.

As the temperature decreased, the BDPA-Bz EPR linewidth was observed to broaden slightly, as shown in Figure 3.6. Furthermore, the nutation was found to depend extremely sensitively on the field position relative to the unmodified Larmor condition. One explanation for these two effects could be that the magnetization, now larger than at room temperature by a factor of 1.5, is large enough so that the onset of turbulent spin dynamics is observed.

3.3.3 Small tip-angle nutation experiments

Pulsed EPR experiments performed on grains of crystalline BDPA-Bz in the small tip-angle regime do not show tip-angle dependent frequency shifts. This is consistent with

Equations 3.6, 3.7, and 3.8, since in the small tip-angle approximation $\Delta M_z/M_z \ll 1$. Figure 3.8 shows nutation experiments performed on a single grain of BDPA-Bz at 290 K at different offsets between the unmodified Larmor frequency and the driving field from the FEL. The offset frequency was varied by changing the external magnetic field $B_0 = \mu_0 H_0$ while keeping the FEL frequency constant. Experiments were performed with field offsets ΔB_0 of 0 mT, 2 mT, and -2 mT, corresponding to frequency offsets of 0, 56 MHz, and - 56 MHz.

For the experiments performed at $\pm$ 56 MHz, the integrated FT-EPR amplitude shows a dependence on pulse length characteristic of off-resonance nutation experiments. The spin system nutates in the small tip-angle regime at an effective Rabi frequency given by Equation 3.10, where the detuning $\delta = \gamma \Delta B_0 - \mu_0 \gamma \theta_d M_0$ takes into account the demagnetization field.

It is worth noting that the FEL power available was lower than usual on the day this experiment was performed, which resulted in a slower-than-normal on-resonance nutation frequency $\omega_1/2\pi = 17$ MHz. Nevertheless, when B_0 was set so that the FEL driving field matches the Larmor condition, the magnetization dynamics left the small tip-angle regime and a tip-angle dependent frequency shift was observed.

3.4 Demagnetization fields and nonlinear interactions

Demagnetization fields are typically neglected in EPR experiments, but are commonly encountered in ferromagnetic resonance [137], where sample geometry plays an important

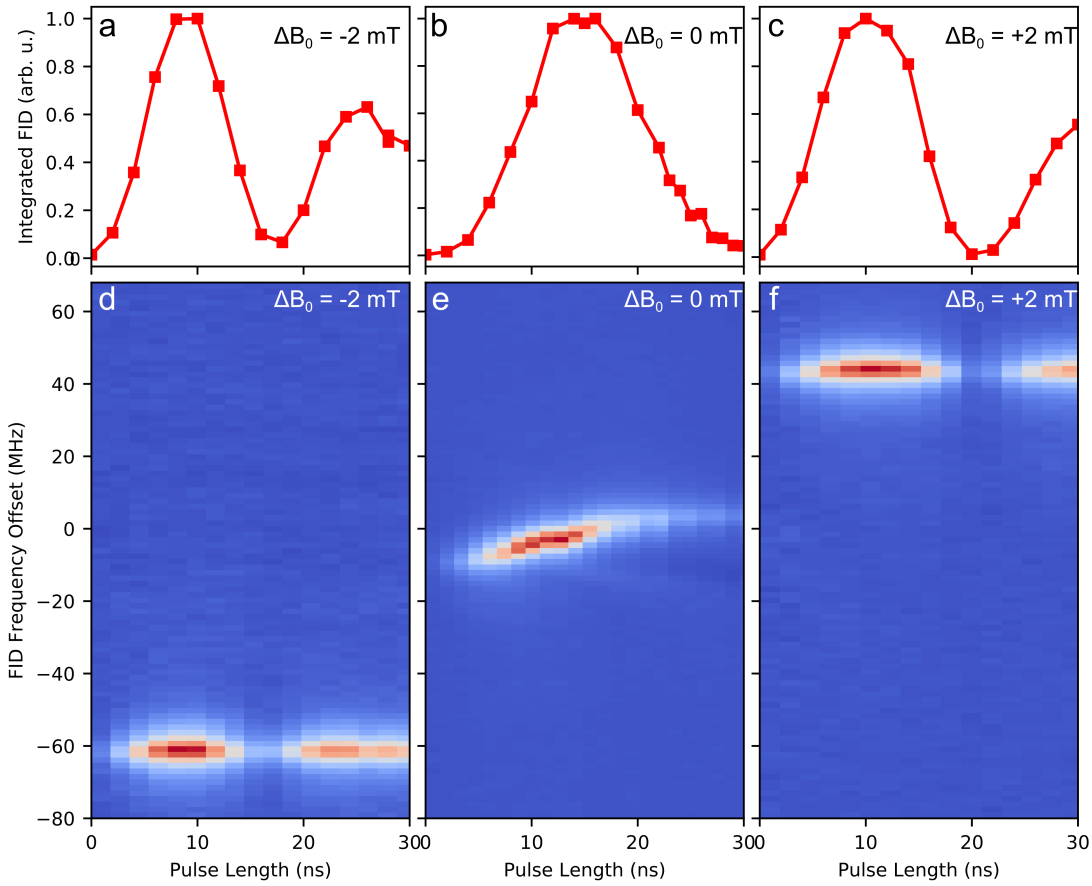

Figure 3.8: Integrated FT-EPR amplitude as a function of pulse length with the magnetic field B_0 set 2 mT below the Larmor condition **a**, at the Larmor condition **b**, and 2 mT above the Larmor condition **c**. **d-f** show the corresponding contour plots of the FT-EPR amplitude as a function of pulse length. When B_0 is moved away from the Larmor condition, the spin system evolves in the small tip-angle regime and no tip-angle dependent frequency shift is observed, while when $\Delta B_0 = 0$, the spin precession frequency shifts as the magnetization is inverted.

role in determining the resonance condition. Demagnetization field effects have also been encountered in NMR experiments in highly concentrated spin systems [139].

Equation 3.15 predicts the ^{1}H NMR resonance measured in room-temperature water to be $\sim$ 4 ppb, if θ_d is assumed to be of order 1. 4 ppb is a 1.6 Hz shift in a 9.4 T magnetic field. In 1990, Edzes reported an anomalous ^{1}H NMR frequency shift of $\sim$ 2.5 ppb in protonated solvents, consistent with Equation 3.15 for $\theta_d \sim 0.6$ [140]. Outside of this example, however, demagnetization field-induced frequency shifts are not commonly observed in NMR, which can be explained by the fact that the gyromagnetic ratio of electrons in 657 times larger than that of protons, together with the γ^2 dependence of Equation 3.15. Indeed, Edzes had to go to great lengths to observe this frequency shift, which required disabling his spectrometer's automatic magnetic field lock which would have otherwise partially corrected for the shift [140].

Instead, nonlinear magnetization-dependent effects in NMR manifest in other, more mild ways, in the generation of multiple spin-echos by a pair of radio frequency pulses [141, 142, 143] or in anomalous frequency correlations appearing in correlation spectroscopy experiments [144, 145]. Much work has been done by Warren others to investigate in particular these anomalous frequency correlations, which can be interpreted as inter-molecular multiple-quantum coherences in a fully quantum-mechanical treatment which arise from long-range nuclear spin dipolar coupling [146]. In 2000, Jeener showed that a semi-classical model of concentrated nuclear spins which invokes the demagnetizing field is equivalent the fully quantum-mechanical "Warren" approach [147].

Since the mid-1990s, NMR experiments taking advantage of non-linear, magnetization-dependent effects been developed. One such experiment, called Correlated spectroscopy Revamped by Asymmetric Z-gradient Echo Detection (CRAZED), is used in both in spectroscopy and in NMR imaging [146].

3.5 Outlook

Nonlinear spin-spin interactions are an essential ingredient for generating squeezed spin states [148]. Schemes for realizing squeezed states of electron spin ensembles have been proposed involving phonon-induced interactions between nitrogen-vacancy (NV) centers in diamond [149], or by coupling a NV center ensemble to a magnetic tip attached to a nanomechanical resonator [150].

The demagnetization field offers an alternative method of engineering nonlinear spin-spin interactions. The nonlinear interaction strength can be tuned by changing the sample geometry, shown in Equation 3.3 for an ellipsoidal sample. Ellipsoidal samples have the property that the demagnetizing field is constant throughout the entire sample volume, as long as the sample has uniform magnetization (Equation 3.1) For non-ellipsoidal sample geometries, the demagnetization field is not in general uniform across the entire sample volume, even if the magnetization is uniform [138]. Interesting possibilities exist for optimizing sample geometry to tailor local nonlinear interaction strengths, as opposed to the sample-wide, long-range interactions seen in the BDPA grains studied carefully here.

The temperature dependence of the precession frequency shift was explored in the

high-temperature approximation (Figures 3.6 and 3.7). However, it would be interesting to explore the spin dynamics in the regime where the high-temperature approximation breaks down. One important consequence of the exchange interaction in BDPA-Bz is to narrow the EPR line [135], as discussed earlier in this chapter. This occurs because the exchange interaction modulates the weaker electron-electron dipolar interaction, which would otherwise lead to line broadening. At temperatures below the Zeeman temperature $T_z = \hbar\omega_L/k_B$, the spin system become highly polarized and fast-timescale spin dynamics moderated by the exchange interaction become effectively frozen out. This may result in intense line-broadening, and in more complicated, likely turbulent magnetization dynamics. Other consequences of the breakdown of the high temperature approximation for dilute spins will be discussed in the next chapter of this dissertation.

Chapter 4

Electron spin relaxation at high magnetic field

Abstract

Favorable relaxation processes, together with their equally favorable high-field spectral properties and their biological compatibility, have lead to Gd-based spin-labels being extensively explored for high-field inter-spin distance measurements for protein structure studies using a variety of techniques [100, 99, 19, 20, 6, 101, 24, 25]. Still, there are many gaps in our understanding of the physics behind high-field electron spin relaxation and decoherence in Gd^{3+} complexes [151, 152, 153]. Gd^{3+} electron spin phase memory time T_M and spin-lattice relaxation time T_1 measurements are presented for a pair of model compounds which can be functionalized as spin labels. A model describing the Gd^{3+} central $m = -1/2 \rightarrow m = +1/2$ transition coherence lifetime is proposed, and is

shown to adequately describe both the temperature and concentration dependence of T_M in deuterated solvents. New insights into the mechanisms driving spin decoherence in Gd^{3+} lead to more sensitive measurements of local average inter-spin distances, and to the intriguing possibility of extending T_M-based distance or concentration measurements to higher temperatures and to lower, more commonly available magnetic fields.

Acknowledgements

CBW performed EPR measurements data analysis under the supervision of Mark Sherwin and Songi Han. Mian Qi designed and synthesized the iodo-(Gd-PyMTA) complexes used in this chapter under the supervision of Adelheid Godt.

4.1 Introduction

Spin-labels based on Gd^{3+} ions offer several advantages over more commonly used nitroxide-based spin probes when paired with EPR performed at high magnetic fields. Favorable spectral properties, chemical stability, and biological compatibility have lead to the increased adoption of Gd^{3+}-based spin-labels at high-field for inter-spin distance measurements for structure studies in biological systems [100, 99, 19, 20, 6, 101, 24, 25]. Electron spin relaxation and decoherence at high magnetic field and at cryogenic temperatures where these measurements are performed is an area of active research, particularly in regimes where inter-electron dipolar coupling is important [151, 152, 153]. In particular, understanding the processes which limit coherence lifetimes in Gd^{3+} is extremely impor-

tant, since coherence lifetimes are one of the factors limiting applications of Gd-based spin labels for pulsed dipolar spectroscopy.

This chapter begins with a discussion of mechanisms which are important drivers of coherence loss in dilute electron spin systems at low temperatures. Then, turning to Gd^{3+} complexes, a series of electron spin phase memory time T_M and spin-lattice relaxation time T_1 measurements are presented, for a pair of Gd^{3+} spin-label compounds. A model is proposed which describes the Gd^{3+} phase memory time in the $m = -1/2 \rightarrow m = +1/2$ transition, and is shown to adequately describe both the temperature and concentration dependence of T_M in deuterated solvents.

Electron spin coherence times can themselves be used to extract inter-spin distances between nearest-neighbors in disordered, weakly associated clusters of spins, where T_M is sensitive to nearest-neighbor spin flip-flops. New insights into the mechanisms driving spin decoherence in Gd^{3+} lead to more sensitive measurements of local average inter-spin distances, and to the intriguing possibility of extending T_M-based distance measurements to higher temperatures and to lower, more commonly available, magnetic fields.

4.2 Relaxation Overview

Spin relaxation processes can be understood in terms of fluctuating local magnetic fields felt by the spins. Fluctuating local magnetic fields arise due to the presence of other electron spins, nuclear spins, lattice distortions, and molecular motion, though they can also be caused by remote sources, such as time-varying background magnetic fields. Re-

laxation can give valuable information about spin-spin and spin-lattice interactions, and can act as a probe of the field fluctuations around a spin.

In Chapter 1, the effective spin Hamiltonian was introduced as a way of characterizing electron spin physics in the ground electronic state, and T_1 and T_2 were introduced as phenomenological relaxation times in the Bloch equations. In Chapter 2, FEL-powered high-field EPR was used to measure electron spin-lattice and spin-spin relaxation times T_1 and T_2 in a variety of physical systems. In Chapter 3, T_1 and T_2 were measured as an important step in characterizing the high-field spin dynamics of a strongly interacting electron spin system.

Electron spin relaxation processes can be roughly broken down into two categories: "longitudinal" processes in which the spin system exchanges energy with degrees of freedom outside of the effective spin Hamiltonian ("the lattice"), such as phonons, electronic excitations etc. [63], and "transverse" processes which are not accompanied by energy exchange with the environment. Longitudinal processes tend to drive a spin system into thermal equilibrium with its environment. Transverse processes tend to cause electron spins to lose phase coherence and are often dominated by spin-spin interactions [54].

In Chapter 2, we saw an example of a case where electron spins lost phase coherence due to interactions with microwave pulses in a process called instantaneous spectral diffusion [108, 109, 54]. Instantaneous spectral diffusion occurs whenever microwave pulses are applied. As pulses rotate some or all of the spins in the material, they change the local dipolar fields felt by those spins whose neighbors were rotated. This change in

the local dipolar field leads to a loss of phase coherence, since the dipolar field contributes to the precession frequency of each individual spin.

Phase coherence persists for an ensemble of spins for a characteristic lifetime T_M, called the phase memory time. T_M is related to T_2, the intrinsic coherence lifetime of a single spin, but is generally shorter than T_2. The contribution made by the instantaneous spectral diffusion mechanism to the total rate of electron spin decoherence $1/T_M$ in a Hahn echo experiment can be quantified as

$$\frac{1}{T_M} = \frac{1}{T_2} + \frac{1}{T_{ID}} \tag{4.1}$$

where $1/T_{ID}$ is given by

$$\frac{1}{T_{ID}} = \frac{\pi}{9\sqrt{3}} \frac{\mu_0 g^2 \mu_B^2}{\hbar} \frac{N}{V} \left\langle \sin^2\left(\frac{\theta}{2}\right) \right\rangle \tag{4.2}$$

where N/V is density or concentration of unpaired electron spins, and $\langle \sin^2 \theta/2 \rangle$ is the inversion profile of the second, refocusing, pulse. In Chapter 2, it was shown that the concentration of electron spins N/V, and the intrinsic T_2, can be measured by systematically varying $\langle \sin^2 \theta/2 \rangle$.

When excitation bandwidths are narrow relative to the EPR linewidth, as is usually the case for high-field EPR with conventional, low-power microwave sources, instantaneous spectral diffusion can be neglected since $\langle \sin^2 \theta/2 \rangle \to 0$. In this chapter, a different decoherence process more commonly observed in high-field EPR will be explored. Like instantaneous spectral diffusion, this process causes spin flips which change the local dipolar field felt by each spin. However unlike instantaneous spectral diffusion, these spin flips are driven, not by microwave pulses, but by dipolar coupling. The contribution

this process makes to the electron spin coherence lifetime can be quantified by performing EPR at high magnetic fields and low temperatures.

4.3 Dipolar Flip-Flops and Spin-bath Polarization

The dipolar interaction Hamiltonian H_{dd} was introduced in Chapter 1. H_{dd} can be written as a sum of terms [64]

$$H_{dd} = \frac{\omega_{dd}(r)}{\hbar}\Big(A + B + C + D + E + F\Big) \tag{4.3}$$

where $\omega_{dd}(r)$ is the dipolar coupling frequency

$$\omega_{dd}(r) = \frac{\mu_0}{4\pi}\frac{(g\mu_B)^2}{\hbar}\frac{1}{r^3} \tag{4.4}$$

The two most important terms in Equation 4.3 are A, the secular term,

$$A = (1 - 3\cos^2\theta)S_{1z}S_{2z} \tag{4.5}$$

and B, the flip-flop term

$$B = -\frac{1}{4}(1 - 3\cos^2\theta)\left(S_1^+S_2^- + S_1^-S_2^+\right) \tag{4.6}$$

where θ is the angle between the vector $\mathbf{r}$ connecting the two spins and the external static magnetic field, which is aligned along the $\hat{z}$ direction.

4.3.1 Dipolar Flip-Flops

In the vast majority of EPR experiments, dipolar coupling is much smaller than the Zeeman interaction. The dipolar coupling frequency for two $S = 1/2$ electrons separated by 1 nm is $\omega_{dd} \simeq 52$ MHz, while Larmor frequencies are typically ∼GHz to ∼100's of

GHz.

The two terms A and B in the dipolar "alphabet" expansion behave quite differently. Consider their effects on a system of two $S = 1/2$ electron spins with Zeeman Hamiltonian $H_z = \omega_{L1} S_{z1} + \omega_{L2} S_{z2}$. A commutes with the Zeeman interaction. To first order in perturation theory, A will cause a spin with S_z quantum number m' to modify the energy of a spin with S_z quantum number m a distance r away and at orientation θ, which will shift the spin's precession frequency by an amount

$$\Delta\omega_{Lm}(r, \theta, m') = \omega_{dd}(r)(1 - 3\cos^2\theta)mm' \tag{4.7}$$

The flip-flop term B, by contrast, does not in general commute with the Hamiltonian, but rather

$$[B, H] = -\frac{1}{4}(1 - 3\cos^2\theta)\hbar\Delta\omega \left(S_1^+ S_2^- - S_1 - S_2^+\right) \tag{4.8}$$

where $\Delta\omega_L = \omega_{L1} - \omega_{L2}$. If the two spins have different resonance frequencies, then the flip-flop term does not commute with H_Z, and spin "flip-flops" are not energy-conserving (Equation 4.8). However, if the two spins have the same resonance frequencies $\omega_{L1} = \omega_{L2}$, the flip-flop term commutes with the Zeeman Hamiltonian, and can drive energy-conserving pairs of spin "flip-flops", where one spin is "flipped" from $|-1/2\rangle \rightarrow |+1/2\rangle$ and the other is "flopped" from $|+1/2\rangle \rightarrow |-1/2\rangle$.

There are three criteria for spins to be able to participate in energy conserving flip-flops. First, as already stated, the spins must have the same precession frequency ω_L. Second, they must be physically close to each other, since dipolar coupling falls off as r^{-3}.

In an inhomogeneously broadened EPR line, spin packets which overlap in frequency are able to participate in energy-conserving flip-flops if the spins in those spin packets are also spatially close. Third, two spins can only undergo flip-flops if one is in the $|+1/2\rangle$ state and the other is in the $|-1/2\rangle$ state, since only then can both change their Zeeman energy and have the process conserve energy overall.

In a typical pulsed EPR experiment performed on an inhomogeneously broadened EPR line with pulse bandwidths that are narrower than the EPR spectrum, spins can be grouped into two populations: α spins, which fall within the pulse bandwidths, are addressed by the pulses, and which are directly participating in the EPR experiment, and β spins, which are not addressed by the EPR pulses and which participate in the EPR experiment only to the extent that they interact with the α spins. In this scenario, spin flip-flops can lead to decoherence in at least two ways.

First and most directly, one or two of the α spins can participate in a spin flip-flop. This leads immediately to a loss of coherence for that spin or pair of spins. This direct flip-flop process increases in importance as the population of α spins in an experiment increases. The more broad-band the pulses, and the narrower the EPR line, the more α spins there will be to participate in spin flip-flops. In the limit where pulses excite the entire EPR line, spin flip-flops compete with instantaneous spectral diffusion, with the degree of spectral overlap between spin packets determining which process dominates.

Second, and more indirectly, spin flip-flops which take place among β spins modulate the dipolar fields felt by the α spins, which causes the resonance frequencies of individual

α spins to shift. If two β spins undergo a flip-flop, and one of those β spins is close to an α spin, the flip (or flop) of the β spin will change the precession frequency of the α spin by an amount given by Equation 4.7. This process can occur often, and many pairs of β spins can participate in flip-flops which each modify the precession frequency of a given α spin. The indirect spin flip-flop decoherence process is more important than the direct flip-flop process when only a small fraction of spins are excited by the pulses in an EPR experiment, so that most spins fall into the β population.

4.3.2 Highly Polarized Spin Baths

Let's revisit the third of the three criteria which must be satisfied in order for two spins to undergo a flip-flop: one of the spins must be in the $|+1/2\rangle$ state and the other must be in the $|-1/2\rangle$ state. For temperatures higher than the electron Zeeman temperature T_Z

$$T_Z = g\mu_B B_0/k_B \tag{4.9}$$

thermal fluctuations are larger than the Zeeman energy difference between $|-1/2\rangle$ and $|+1/2\rangle$. In this regime, both states are populated, and spin flip-flops can proceed. However, for temperatures lower than T_Z, thermal fluctuations are smaller than the Zeeman energy. For temperature much smaller than T_Z, the spin system becomes highly polarized into the ground $|-1/2\rangle$ state, with all electron magnetic moments aligned in the direction of the external magnetic field. When all of the spins are in the $|-1/2\rangle$ state, dipolar flip-flops are effectively frozen out, since there are no $|+1/2\rangle$ states to flop

when one of the $|-1/2\rangle$ states flips.

Dipolar-driven flip-flops increase the rate of phase coherence loss according to [154, 155, 85]

$$\frac{1}{T_M} = n_{1/2} n_{-1/2} \times F \times \omega_{dd}(\bar{r}) + \Gamma \tag{4.10}$$

where Γ is the residual electron flip-flop independent decoherence rate, $n_{\pm 1/2}$ is the thermal occupation number of the $|\pm 1/2\rangle$ state

$$n_{\pm 1/2} = \frac{1}{Z} e^{\mp g\mu_B B_0 / 2k_B T} \tag{4.11}$$

Z is the partition function

$$Z = e^{g\mu_B B_0 / 2k_B T} + e^{-g\mu_B B_0 / 2k_B T} \tag{4.12}$$

and $\omega_{dd}(\bar{r})$ is the dipolar coupling frequency between two spins separated by the average nearest-neighbor inter-spin distance $\bar{r}$. F is a parameter which characterizes the amount of spectral overlap between electron spin packets, and is a property of the EPR line. For isotropically dispersed solutions of the nitroxide radical 4-amino-TEMPO, $F = 1/10.2$ was empirically determined [85].

At temperatures $T < T_Z$, the occupation number $n_{+1/2}$ of spins in the excited state drops to zero as $T \to 0$, and the frozen-out dipolar flip-flops no longer contribute to electron spin decoherence. In order to freeze out dipolar flip-flops as a decoherence pathway, high magnetic fields and low temperatures are necessary. At 9.5 GHz, where EPR is most widely performed, $T_Z = 0.46$ K. Quenching dipolar flip-flops in a 9.5 GHz EPR experiment requires cooling to 100s to 10s of mK, necessitating expensive cooling equipment not widely available to EPR spectroscopists. At 240 GHz, $T_Z = 11.6$ K, which

can be easily reached using gaseous or liquid helium cooling.

4.3.3 Local Concentration From Electron Spin Phase Memory Time

From Equation 4.10, the contribution to the phase memory time T_M from dipolar flip-flops will depend on temperature through the occupation numbers $n_{\pm 1/2}$. Careful characterization of the electron spin phase memory time as a function of temperature can therefore be used to extract the product $F \times \omega_{dd}(\bar{r})$, where $\omega_{dd}(\bar{r})$ is the dipolar coupling frequency evaluated at the average nearest-neighbor distance and F depends on the EPR lineshape and spectral overlap.

Edwards *et al.* showed [85] that phase memory time measurements conducted at high magnetic field as a function of temperature can be used to extract average inter-spin nearest-neighbor distances in uniformly distributed, isotropic frozen solutions. Immediately after performing this result, the question arose- could measurements of the phase memory time temperature dependence be used to extract average nearest-neighbor distances in non-uniformly distributed solutions? Suppose the electron spin density varies across a material, such that there are pockets with high spin-density and pockets with low spin-density. The phase memory time temperature dependence should be sensitive to the elevated local spin concentrations in the high-density pockets, where dipolar spin-flips will be more efficiently driven than in the low-density pockets.

Edwards *et al.* [85] performed temperature-dependent phase memory time measure-

ments at 8.56 T on lipid vesicles which were spin-labeled with PC-TEMPO, a lipid with a TEMPO spin probe functionalized to the its headgroup. It was found that indeed, the electron spin phase memory time was sensitive to the elevated spin concentration at the surface of the vesicles.

Edwards *et al.* [85, 56] went on to show that the contribution to spin decoherence of 4-amino-TEMPO from electron spin flip-flops becomes negligible in fully protonated solvents for average nearest-neighbor electron spin distances $\bar{r} >\sim 1.5$ nm, where electron spin relaxation becomes dominated by the residual relaxation Γ caused by nuclear spin flip-flops. Further, even in deuterated solvents, Edwards *et al.* found dipolar flip-flops could be neglected for concentrations below 1 mM, for average nearest-neighbor distances $\bar{r} \geq 6.6nm$ or longer.

4.4 High-Field Gd Electron Spin Relaxation

So far, we have dealt with dipolar flip-flops in spin-1/2 radicals. Niroxide radicals like 4-amino-TEMPO have long spin-lattice relaxation times around or below the 240 GHz Zeeman temperature, and at high field their EPR lineshapes are inhomogeneously broadened and dominated by their orientation-dependent g tensors.

Gd^{3+} complexes are an alternative to $S = 1/2$ electron spins for use as spin-probes in a variety of systems. Gd^{3+} is a spin-7/2 ion with seven unpaired electrons in its half-filled 4f-orbital, leading to magnetic moment 7 times larger than that of a $S = 1/2$ radical. While Gd^{3+} by itself is quite reaction-prone and is acutely toxic, Gd^{3+} coordinated by a

chelating complex is stable and relatively biological compatible [100].

The ground state of a $S = 7/2$ Gd^{3+} complex is highly symmetric, with a nearly isotropic g value generally around $g = 1.992$. The Gd^{3+} lineshape is dominated by the zero-field splitting (ZFS) interaction, which, though small for most Gd chelates ($D \sim 0.2 - 2$ GHz) when compared to other Lanthanides and high-spin transition metal complexes, nevertheless is second only to the Zeeman interaction in terms of importance in the effective spin Hamiltonian [156]. At high field, the ZFS can be treated perturbatively, leading to a first-order correction to the transition energy between states labeled by S_z quantum numbers $m, m+1$

$$E^{(1)} = g\mu_B B_0 + \frac{1}{2}(2m+1)\hbar D(3\cos^2\theta - 1) \tag{4.13}$$

where θ is the angle between the principal axis of the ZFS tensor and the external magnetic field. $E^{(1)}$ differs from the Zeeman transition energy $E_Z = g\mu_B B_0$ for all transitions except for the $m = -1/2 \rightarrow m = +1/2$ "central" transition, which is only broadened at second order in perturbation theory, where the correction for the ZFS is given by

$$E^{(2)} = \frac{1}{16}\frac{\hbar^2 D^2}{g\mu_B B_0}(4S(S+1) - 3)(\sin^4\theta - 2\sin^2 2\theta) \tag{4.14}$$

Therefore to leading order, the ZFS modifies the Zeeman energy difference between the $m = -1/2$ and $m = +1/2$ states by an amount which scales with D^2/ω_L, where $\omega_L = g_m u_B B_0/\hbar$ is the Larmor frequency. As the B_0 field increases, the linewidth of the $m = -1/2 \rightarrow m = +1/2$ central transition decreases as $(B_0)^{-1}$. At 8.6 T, the $m = -1/2 \rightarrow m = +1/2$ transition narrows to $\sim 0.5mT$, leading to an enormous

sensitivity gain [100].

Gd^{3+} complexes generally have much shorter spin-lattice relaxation times than $S = 1/2$ organic radicals due to relaxation driven by coupling between molecular vibrations and motion and the spin degrees of freedom through the ZFS [100, 102]. However, the electron spin transverse relaxation time generally remains quite long for dilute Gd3+ spins at cryogenic temperatures.

Another property of $S = 7/2$ Gd^{3+} is that the matrix elements of the magnetic dipole transitions coupling different S_z eigenstates are larger than for $S = 1/2$, leading to stronger couplings between spins and microwaves. The matrix elements $\langle S, m \pm 1|S^{\pm}|S, m\rangle$ of the raising and lowering operators $S^{\pm}$ are given by [58]

$$\langle S, m \pm 1|S^{\pm}|S, m\rangle = \hbar\sqrt{(S \mp m)(S \pm m + 1)} \tag{4.15}$$

so that for the $m = -1/2 \rightarrow m = +1/2$ transition of a $S = 7/2$ spin, the transition matrix element is 4 times larger than the transition matrix element connecting $m = -1/2 \rightarrow m = +1/2$ transition of a $S = 1/2$ spin,

$$\begin{gathered}\langle 7/2, 1/2|S^{+}|7/2, -1/2\rangle = \\ 4 \times \langle 1/2, 1/2|S^{+}|1/2, -1/2\rangle\end{gathered} \tag{4.16}$$

Therefore, microwaves drive the $m = -1/2 \rightarrow m = +1/2$ central transition of a $S = 7/2$ spin with a Rabi frequency four times higher than for a $S = 1/2$ spin.

4.5 Phase Memory Time and Spin-Lattice Relaxation Time Measurements of Gd^{3+}

Measurements of the electron phase memory time T_M and the spin-lattice relaxation time T_1 were performed at 8.6 T, corresponding to $\omega_L/2\pi = 240$ GHz, as a function of temperature and Gd^{3+} complex concentration for two Gd^{3+} complexes: Gd-DOTA and iodo-(Gd-PyMTA) Figure 4.2. Gd-DOTA is a commercially available MRI contrast agent, with a small axial zero-field splitting with $D = 700$ MHz [156] and a narrow high-field $m = \mp 1/2 \rightarrow m = \pm 1/2$ central transition. PyMTA is a pyridine-based tetracarboxylate ligand synthesized for use as a lanthanide- or transition metal-based spin-label. Iodo-(Gd-PyMTA), the variant studied here, has a somewhat larger zero-field splitting than Gd-DOTA, with $D = 1900$ MHz [156].

Pulsed EPR experiments were performed using a home-build 240 GHz EPR spectrometer operating in "low-power" mode, with microwaves generated by a 55 mW solid-state microwave source (Virginia Diodes, Inc). The 240 GHz spectrometer can also operate with the UCSB mm-wave free electron laser as source of microwave radiation for high-power pulsed experiments, however the FEL was not used for these experiments. Details about the spectrometer operating in low-power pulsed mode can be found in Appendix A.1.

Two-pulse Hahn echo decay experiments (Figure 4.1) were performed on the $m = \mp 1/2 \rightarrow m = \pm 1/2$ central transition for several concentrations of Gd-complex (Figure

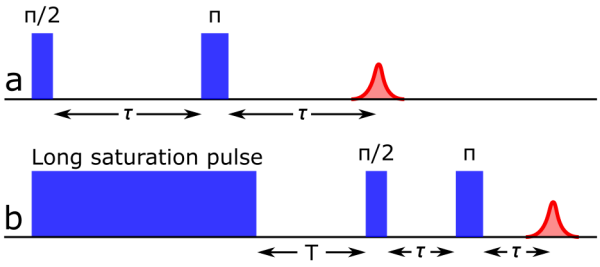

Figure 4.1: (a) Hahn echo decay pulse sequence used to measure T_M. The echo amplitude is recorded as a function of τ. (b) Saturation-recovery pulse sequence used to measure T_1. The echo amplitude is recorded as a function of the delay between the saturation pulse and the echo sequence T, while keeping τ fixed.)

4.2) in frozen 60/40 detuerated glycerol/D_2O matrices. Protonated solvents were chosen in order reduce the decohering effects of proton spins. For a random and uniform distribution of spins with density N/V, the average nearest-neighbor inter-spin distance $\bar{r}$ is given by [157]

$$\bar{r} = 0.554 \left(\frac{N}{V}\right)^{-1/3} \tag{4.17}$$

Average nearest-neighbor distances $\bar{r}$ are tabulated with their corresponding concentrations in Table 4.1. Echo decays were exponential, with a single time constant T_M. T_M was found to depend sensitively both on the Gd^{3+} spin concentration and on temperature over a range of temperatures between 5 K and 90 K.

Saturation-recovery experiments (Figure 4.1) were performed on the $m = \mp 1/2 \rightarrow m = \pm 1/2$ central transition to measure the spin-lattice relaxation time T_1. T_1 was found to increase with decreasing temperature across the temperature range 4.2. T_1 was found to be shorter by roughly a factor of two for iodo-(Gd-PyMTA) as compared to Gd-DOTA for temperatures below ~ 40 K. This difference in T_1 is consistent with spin-

lattice coupling being mediated primarily by the zero field splitting interaction, which is roughly twice as large in iodo-(Gd-PyMTA) than in Gd-DOTA [54, 156]. T_1 was found within error to be concentration-independent in this concentration range.

Spin-lattice relaxation is found to follow a relationship of the form $T_1 \propto T^{-}x$, where $x = 1.4 \pm 0.2$ for Gd-DOTA and $x = 0.92 \pm 0.05$ for iodo-(Gd-PyMTA), as shown in Figure 4.3. This temperature dependence is roughly consistent with spin-lattice relaxation being driven by a direct phonon process, which has a characteristic temperature dependence $1/T_1 \propto T$ [54]. In a direct phonon process, collisions with single 240 GHz phonons lead to spin-lattice energy transfer, which in this case is likely mediated by the zero-field splitting interaction. Spin-phonon coupling is independent of spin concentration, explaining the lack of an observed T_1 concentration dependence.

Concentration	$\bar{r}$ (nm)
1 mM	6.6
500 μM	8.3
100 μM	14.1
50 μM	17.8

Table 4.1: Average nearest-neighbor distances $\bar{r}$ assuming randomly and uniformly distributed spins in a glassy matrix for several spin concentrations, given by Equation 4.17.

At the upper end of the temperature range shown in Figure 4.2, $1/T_M$ and $1/T_1$ adopt similar a similar dependence on temperature, with $1/T_M$ approaching $2/T_1$, indicating that the spin-lattice relaxation processes driving T_1 relaxation are also coming to dominate electron spin dephasing.

At the lower end of the temperature range in Figure 4.2, $1/T_M$ appears to converge to

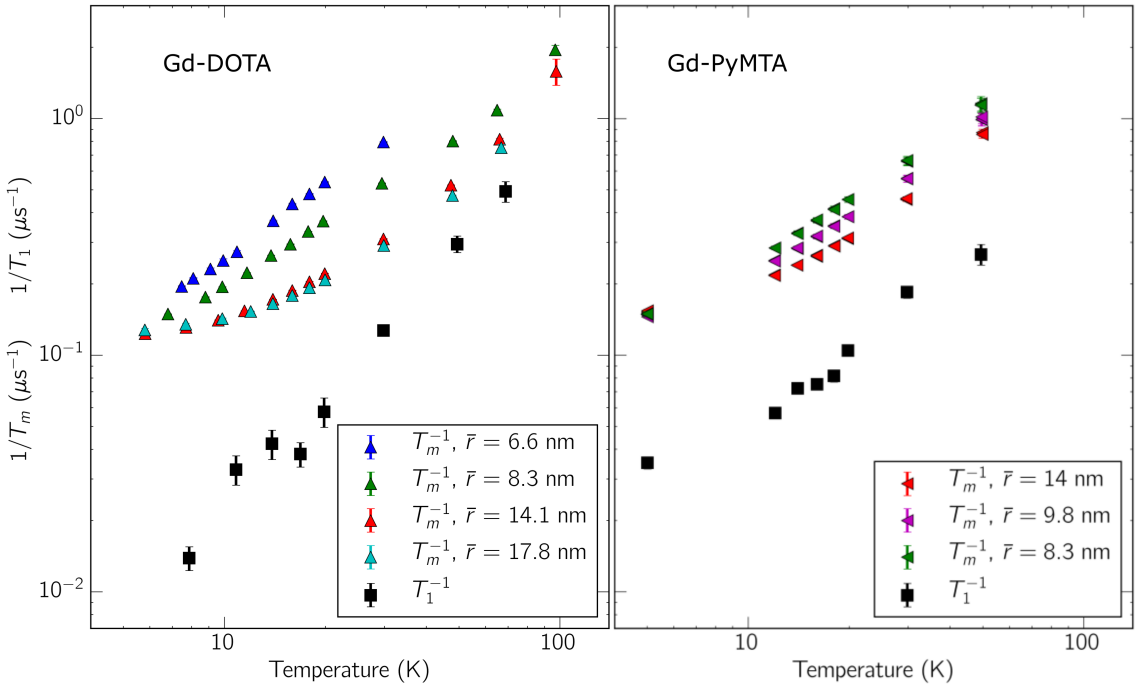

Figure 4.2: Left: inverse phase memory time $1/T_M$ (triangles) and $1/T_1$ (black squares) for Gd-DPTA in 60/40 deuterated glycerol/D_2O as a function of temperature and concentration measured on the central $m = \mp 1/2 \rightarrow m = \pm 1/2$ transition. Right: inverse phase memory time $1/T_M$ (triangles) and $1/T_1$ (black squares) for iodo-(Gd-PyMTA) in 60/40 deuterated glycerol/D_2O as a function of temperature and concentration measured also on the central $m = \mp 1/2 \rightarrow m = \pm 1/2$ transition. Measurements were performed at 8.6 T / $\omega_L/2\pi$ = 240 GHz. For both complexes, the phase memory time shows a strong concentration dependence even for average nearest-neighbor distances $\bar{r} > 10$ nm. At $1/T_M$ begins to converge which begin to converge. T_1 was found to be concentration-independent for both complexes in this temperature range.

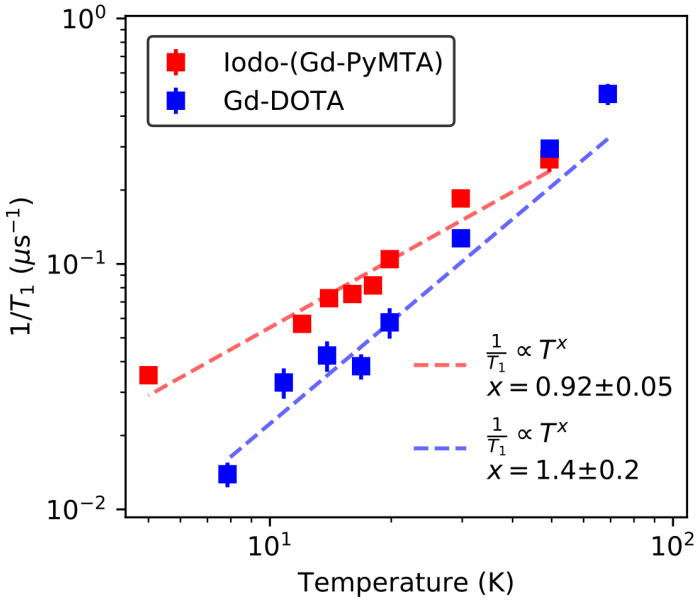

Figure 4.3: Inverse spin-lattice relaxation time $1/T_1$ at 8.6 T / $\omega_L = 240$ GHz as a function of temperature measured in frozen 60/40 deuterated glycerol/D_2O, for Gd-DOTA and iodi-(Gd-PyMTA). Dashed lines indicate power-law fits, consistent with T_1 being driven by a direct phonon relaxation process.

concentration-independent values. This convergence is consistent with dephasing at low temperatures being driven by inter-electron dipolar modulated flip-flops, which freeze out as the spin bath polarizes. Spin-bath polarization proceeds differently in high-spin Gd^{3+} complexes than for the $S = 1/2$ case described in Section 4.3, because there are eight Zeeman states involved instead of only two. The thermal populations n_m in each Zeeman state labeled with S_z quantum number m are given by

$$n_m = \frac{1}{Z} e^{-mg\mu_B B_0/k_B T} \tag{4.18}$$

where

$$Z = \sum_{m=-S}^{S} e^{-mg\mu_B B_0/k_B T} \tag{4.19}$$

where zero-field splitting and dipolar coupling contribute small corrections which have been neglected. Figure 4.4 shows the occupation numbers n_m for $B_0 = 8.6$ T corresponding to $\omega_L/2\pi = 240$ GHz. As the temperature is lowered, n_m for states m with higher Zeeman energy are depopulated first, leading to a more complicated temperature dependence to the dipolar flip-flop contribution to decoherence than Equation 4.10. Furthermore, the matrix elements of the dipolar flip-flop term (Equation 4.6) are different for different transitions $m \to m + 1$.

A model which describes the contribution of high-spin dipolar-modulated flip-flops to T_m was put forward by Takahashi *et al.* in the context of molecular magnets [158],

$$\frac{1}{T_M} = A \sum_{m=-S}^{S-1} W(m) n_m n_{m+1} + \Gamma \tag{4.20}$$

where A and Γ are temperature-independent rates, and $W(m)$ gives the flip-flop transi-

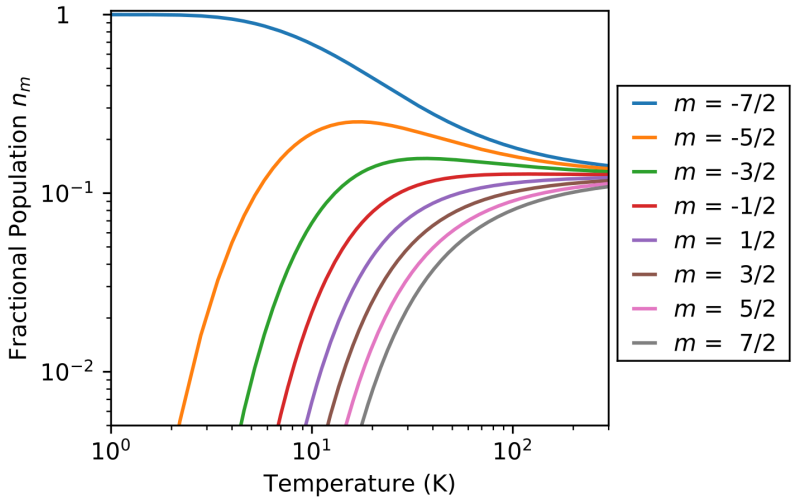

Figure 4.4: Boltzmann population in each Zeeman state, labeled by the S_z quantum number m for a $S = 7/2$ system at 8.6 T, $\omega_L/2\pi = 240$ GHz, and a Zeeman temperature $T_Z = 11.6$ K.

tion probability between two spins from Equation 4.6

$$W(m) = \left| \left\langle m+1, m \left| \frac{S_1^+}{\hbar} \frac{S_2^-}{\hbar} \right| m, m+1 \right\rangle \right|^2 + \left| \left\langle m, m+1 \left| \frac{S_1^-}{\hbar} \frac{S_2^+}{\hbar} \right| m+1, m \right\rangle \right|^2 \tag{4.21}$$

where $|m, m+1\rangle$ is a state where the first spin has S_z quantum number m and the second spin has S_z quantum number $m+1$. However, this model only takes into account transitions where the two spins swap S_z quantum numbers. For a single crystal molecular magnet like the one considered in [158], a large zero field splitting means that the only energy-conserving transitions were those in which S_z quantum numbers were swapped, so this assumption made sense.

Gd complexes have much smaller zero field splittings. More importantly, unlike system considered in [158], the frozen solutions considered here are not single crystals.

Therefore, each Gd complex is oriented randomly with respect to the external field, leading to broad, overlapping Zeeman transitions due to the orientation dependence of the zero-field splitting interaction (Equations 4.13 and 4.14). In addition, a recent comprehensive treatment by Clayton *et al.* of the zero-field splitting interaction for Gd complexes in frozen glycerol-water solutions showed that the EPR lineshape is consistent with a distribution of zero-field splitting parameters, corresponding to a distribution of molecular conformations [156]. These complications mean that for a wide range of orientation angles, we can expect flip-flops between many different pairs of Zeeman states to be energy-conserving.

A more general model of Equation 4.20, taking into account the fact that energy conserving flip-flops can occur for some orientations between any pair of Zeeman states, can be written as follows,

$$\frac{1}{T_m} = A \sum_{m=-S}^{S-1} \sum_{m'=-S+1}^{S} T(m,m') n_m n_{m'} + \Gamma \tag{4.22}$$

where $A \propto 1/\bar{r}^3$ is a temperature-independent rate proportional to the inverse nearest-neighbor inter-spin distance $\bar{r}$ cubed, Γ is a residual relaxation rate, and $T(m,m')$ is proportional to the flip-flop transition probability

$$\begin{aligned} T(m,m') = &\left| \left\langle m+1, m' \left| \frac{S_1^+}{\hbar} \frac{S_2^-}{\hbar} \right| m, m'+1 \right\rangle \right|^2 \\ &+ \left| \left\langle m, m'+1 \left| \frac{S_1^-}{\hbar} \frac{S_2^+}{\hbar} \right| m+1, m' \right\rangle \right|^2 \end{aligned} \tag{4.23}$$

Equation 4.22 is closer to a complete model for the processes driving electron spin

decoherence at high field and low temperatures. However, it neglects three important temperature-dependent sources of decoherence: 1) spin-lattice relaxation, 2) dipolar field fluctuations caused by spin-lattice relaxation-driven spin flips, and 3) transient zero-field splitting fluctuations. Recall that the spin system is composed of α spins, which are excited by the microwave pulses, and β spins, which form a background spin bath. Spin-lattice relaxation will cause spins to relax to thermal equilibrium with time constant T_1, contributing directly to a loss of phase coherence for every α spin which relaxes. Additionally, as spin-lattice relaxation flips β spins, local magnetic field felt by α spins which are dipolar coupled to the flipped β spins will be changed on a timescale T_1, which adds another source of decoherence.

Transient zero-field splitting fluctuations are small, short-lived changes in the zero field splitting proposed to be caused by short-timescale (100 - 1000 MHz) small angle librations or "wobbling" on the atomic scale [102]. Transient zero-field splitting leads to temperature and transition-dependent relaxation rates, affecting outlying transitions far more than the $m = -1/2 \rightarrow m = +1/2$ central transition.

Focusing on the central $m = -1/2 \rightarrow m = +1/2$ central transition so that transient zero-field splitting fluctuations can be neglected, a model for the phase memory time temperature dependence which include spin-lattice relaxation effects is given by

$$\frac{1}{T_m} = A_1 \omega_{dd}(\bar{r}) \sum_{m=-S}^{S-1} \sum_{m'=-S+1}^{S} T(m,m') n_m n_{m'} + \frac{A_2 \omega_{dd}(\bar{r})}{T_1} + \frac{B}{T_1} + \Gamma_{res} \tag{4.24}$$

where A_1, A_2, B are temperature-independent factors, and Γ_{res} is a temperature-independent

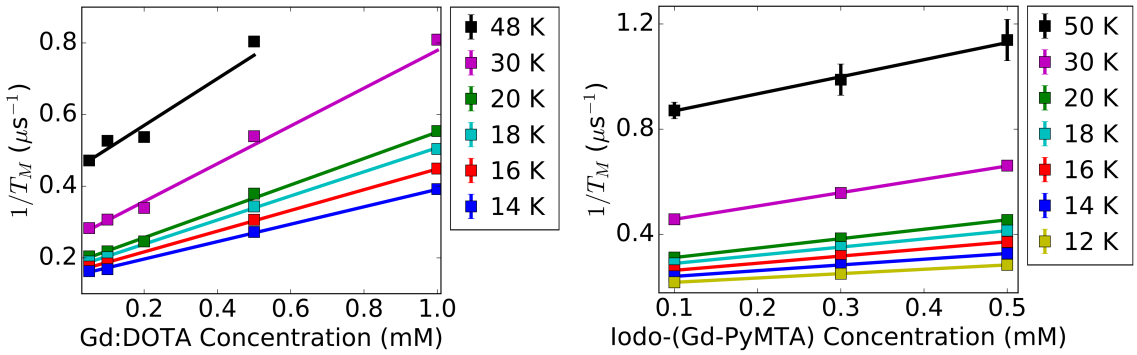

Figure 4.5: Inverse phase memory time $1/T_M$ for Gd-DOTA (left) and iodo-(Gd-PyMTA) (right) plotted as a function of concentration, at the indicated temperatures. Solid lines indicate fits of $1/T_M$ to Equation 4.25.

residual relaxation rate. The first term is due to dipolar coupling-driven flip-flops, and the second term is due to dipolar field modulation caused by lattice relaxation-driven spin flips, and should both therefore scale in proportion to the electron spin concentration since $\omega_{dd} \propto N/V$. The third term is the decoherence of caused directly by spin-lattice relaxation, which is electron spin concentration-independent for this system, and the fourth term is a temperature independent residual relaxation rate, consisting primarily of electron-nuclear coupling.

Equation 4.24 predicts that the rate of decoherence at a fixed temperature T will scale with Gd^{3+} spin concentration N/V according to

$$\frac{1}{T_M(T)} = R_0(T) + R_1(T) \times \frac{N}{V} \tag{4.25}$$

where $R_0(T)$ is the sum of terms three and four in Equation 4.24 evaluated at T, and

$R_1(T)$ consists of terms one and two in Equation 4.24 evaluated at T.

$$R_0(T) = \frac{B}{T_1(T)} + \Gamma_{res} \tag{4.26a}$$

$$R_1(T) = a_1 \sum_{m=-S}^{S-1} \sum_{m'=-S+1}^{S} T(m,m') n_m n_{m'} + \frac{a_2}{T_1(T)} \tag{4.26b}$$

Figure 4.5 shows $1/T_M$ plotted as a function of concentration at fixed temperature, measured on the $m = -1/2 \rightarrow m = +1/2$ central transition, for temperatures $T > 10K$ where the the $m = \pm 1/2$ Zeeman states are still populated (Figure 4.4). The concentration dependence of $1/T_M$ is found to be in excellent agreement with Equation 4.25.

Figure 4.6 shows the electron spin concentration-independent decoherence rate R_0 and the concentration-dependent decoherence term R_1. The concentration-independent contribution to decoherence, given by terms three and four in Equation 4.24, is well described by Equation 4.26b. From a simultaneous fit of the concentration-independent rate for Gd-DOTA and iodo-(Gd-PyMTA), $R_0 = B/T_1 + \Gamma_{res}$, where $B = 2.3 \pm 2$ and $\Gamma_{res} = 0.05 \pm 0.03\ \mu\text{s}^{-1}$. From this, we can conclude that spin-lattice relaxation dominates the concentration-independent mechanism.

The concentration-dependent contribution to decoherence R_1 was described using two variants of the model introduced in Equation 4.24. Model 1 considered both dipolar-modulated flip-flops and spin-lattice (T_1) spin-flips, while Model 2 considered only dipolar-modulated flip-flops. The two models were fit using Equation 4.26a, with $a_2 = 0$ enforced

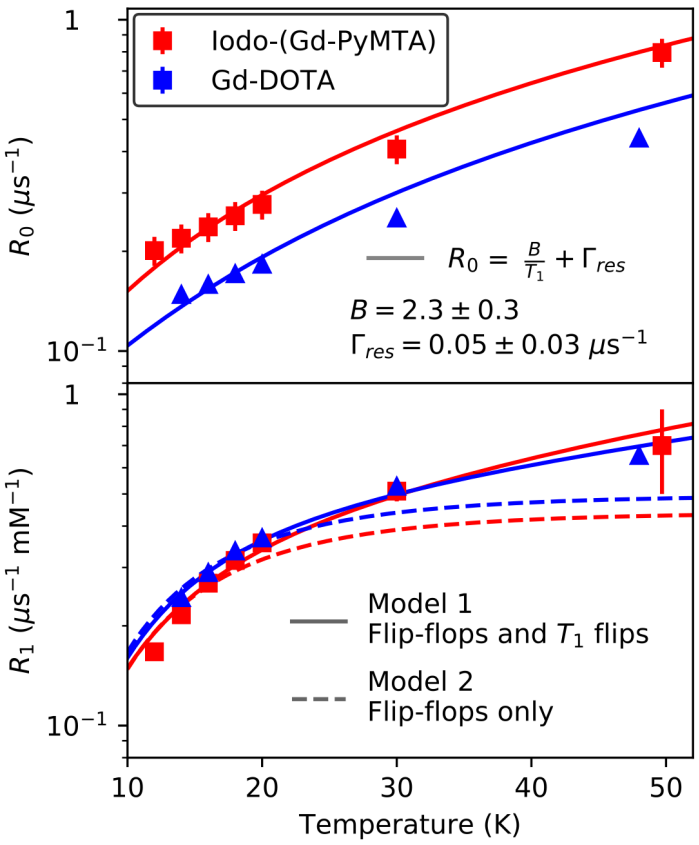

Figure 4.6: Top: concentration-independent rate R_0 (Equation 4.25) as a function of temperature. Solid lines indicate a fit to Equation 4.26a, where B and Γ_{res} were fit simultaneously. Bottom: concentration-dependent rate R_1 (Equation 4.25) as a function of temperature. Solid lines indicate fits to Model 1, given by Equation 4.26b. Dashed lines indicate a fit to Model 2, which considers only dipolar-modulated flip-flops.

Sample	Concentration-dependent				Concentration independent	
	Model 1: flip-flops and T_1 flips		Model 2: flip-flops only			
	a_1 (μs^{-1} mM^{-1})	a_2 (mM^{-1})	a_1 (μs^{-1} mM^{-1})	a_2 (mM^{-1})	B	Γ_{res} (μs^{-1})
Gd-DOTA	0.0017 ± 0.0001	1.6 ± 0.2	0.00231 ± 0.00002	-	2.3 ± 0.3	0.05 ± 0.03
Iodo-(Gd-PyMTA)	0.0011 ± 0.0003	1.6 ± 0.5	0.00205 ± 0.00004	-		
	A_1	A_2 (μs)	A_1	A_2 (μs)		
Gd-DOTA	$(1.48 \pm 0.06) \times 10^{-3}$	1.43 ± 0.16	$(2.02 \pm 0.01) \times 10^{-3}$	-		
Iodo-(Gd-PyMTA)	$(9 \pm 3) \times 10^{-4}$	1.4 ± 0.4	$(1.80 \pm 0.03) \times 10^{-3}$	-		
		r_c (nm)		r_c (nm)		
Gd-DOTA		7.7 ± 0.3		-		
Iodo-(Gd-PyMTA)		7.8 ± 0.7		-		

Table 4.2: Parameters extracted the model described in Equation 4.24 for Gd-DOTA and iodo-(Gd-PyMTA). Parameters related to concentration-dependent effects are presented in three forms: the form described in Equation 4.26b (a_1, a_2, top), the form described in Equation 4.24 (A_1, A_2, middle), and in the form described in Equation 4.28 (A_1, r_c, bottom). Best fit parameters are shown for both Model 1, which considers dipolar-driven flip-flips and T_1-driven flips, and Model 2, which considers only dipolar-driven flip-flops. Parameters related to concentration-independent terms B and Γ_{res} are presented to the right, and were found by simultaneously fitting Equation 4.26a for both complexes.

for the second model. Table 4.2 records the model parameters for the two complexes. Model 1 was found to be in better agreement with the data than the Model 2, indicating that T_1-driven spin flips which modulate the dipolar field are an important mechanism of electron spin decoherence at low temperatures.

4.5.1 Interpreting the Model

Equation 4.24 has four free parameters: A_1, A_2, B, and Γ_{res}. These four parameters weigh the importance of the four main processes driving decoherence in Gd^{3+} complexes at low temperature, which are dipolar coupling-driven spin flip-flops, local magnetic field fluctuations due to spin-lattice relaxation-driven spin flips, direct spin-lattice relaxation, and residual coupling to nuclear spins. Of these four processes, the first two scale with the electron concentration N/V, since the average dipolar coupling strength ω_{dd} between nearest-neighbor spins scales with $1/\bar{r}^3$.

Flip-flops

Parameter A_1 is a dimensionless number which scales the contribution to $1/T_M$ of the dipolar coupling-modulated flip-flops. A_1 is analogous to F from Equation 4.10, in that it is expected to characterize the amount of spectral overlap between electron spin packets which must overlap in frequency in order for flip-flops to be energy conserving. In the simplest approximation, we can expect A_1 to scale inversely with the EPR linewidth, since the broader the EPR line, the smaller the chance any two spin-packets will overlap in energy. Accordingly, A_1 was found for Gd-DOTA to be $A_1^{\mathrm{DOTA}} = (1.48 \pm 0.06) \times 10^{-3}$,

and for iodo-(Gd-PyMTA) to be $A_1^{\mathrm{PyMTA}} = (9 \pm 3) \times 10^{-4}$. Zero-field splitting is the dominant contribution to the EPR linewidth of both compounds, with $D = 700$ MHz for Gd-DOTA, and $D = 1900$ MHz for iodo-(Gd-PyMTA). Taking D as a proxy for linewidth, we find $A_1 \propto 1/D$ to be consistent with our expectations.

We can compare A_1 to F from Equation 4.10, where for the nitroxide radical 4-amino-TEMPO, Edwards *et al.* found $F^{\mathrm{4ATEMPO}} = 1/10.2 = 0.0980$ [85]. Adopting Equation 4.22 for $S = 1/2$, we see $A_1^{\mathrm{4ATEMPO}} = F^{\mathrm{4ATEMPO}}/2 = 0.049$ is about a factor of 40-50 larger than A_1^{DOTA} or A_1^{PyMTA}, where the factor of $1/2$ comes from the definition of $T(m, m')$. Gd^{3+} complexes have broader EPR spectra as compared to 4-amino-TEMPO by a factor of 10-30 at 8.6 T, with typical widths of ~ 0.5 to ~ 1.5 T [156] where 4-amino-TEMPO is about ~ 40 mT broad, consistent with our expectation that A_1 is inversely proportional to linewidth.

There are at least two complications to this model of dipolar-driven spin flip-flops in Gd3+ complexes which deserve addressing. The first complication is the assumption made in proposing Equation 4.24, and more specifically the definition of $T(m, m')$ in Equation 4.23, that all flip-flops $m \rightarrow m \pm 1, m' \rightarrow m' \mp 1$ can be energy conserving with equal probability. The large distribution of D parameters in Gd^{3+} complexes [156], together with the orientation dependence of the ZFS interaction, means that flip-flops between any two states will certainly be energy conserving for some orientations and D values. However, because ZFS broadens different transitions differently, energy conserving flip-flops will be most likely to occur between nearest neighbors for

certain transitions, and for certain orientations, than for others. For example since the $m = -1/2 \rightarrow m = 1/2$ central transition is only broadened to second order by ZFS, flip-flops of the form $|\mp 1/2, \pm 1/2\rangle \rightarrow |\pm 1/2, \mp 1/2\rangle$ are likely to be energy conserving. Conversely, flip-flops of the form $|-7/2, 7/2\rangle \rightarrow |-5/2, 5/2\rangle$ are much less likely to be energy conserving, and will only occur only with a strong orientation dependence (Equation 4.13). A more accurate model for dipolar-driven flip-flops for Gd^{3+} complexes, taking into account the spectral overlap of each pair of transitions and the orientation dependence of the ZFS, would predict a contribution to electron spin decoherence of the form

$$\frac{1}{T_{M,flip-flop}} = \omega_{dd}(\bar{r}) \sum_{m=-S}^{S-1} \sum_{m'=-S+1}^{S} A(m, m') T(m, m') n_m n_{m'} \tag{4.27}$$

where the $A(m, m')$ coefficients include details about the ZFS interaction, and the overall Gd^{3+} lineshape. Since lineshape details were neglected in Equation 4.24 except for an overall parameter A_1, our model likely over-estimates contributions from most transitions and under-estimates contributions from the central $m = \pm 1/2 \rightarrow m = \mp 1/2$ transition.

The second complication is that the model proposed in Equation 4.24 only takes into account flip-flops between nearest-neighbor spins, when the dipolar interaction is long-ranged and can mediate interactions between remote spins [54, 144, 146]. Including contributions from flip-flops between spins which are further apart than nearest-neighbors means that the chance a spin can undergo flip-flops which are only energy-conserving for certain orientations increases, since more orientations are available. This will tend to counteract the point made in the last paragraph that Equation 4.24 over-estimates

contributions from outlying transitions.

T_1 Spin Flips

Parameter A_2 has units of time, and scales the contribution to electron spin decoherence from dipolar field fluctuations caused by off-resonance β spins undergoing spin-flips due to spin-lattice relaxation. These spin-flips occur in the bath with a rate $1/T_1$. A possible physical interpretation of A_2 is $A_2 = 1/\omega_{dd}(r_c)$ where $\omega_{dd}(r_c)$ is the dipolar frequency of two spin separated by a characteristic distance r_c. Spins in the bath which undergo T_1-induced spin-flips will modify the local magnetic field seen by an α spin through the dipolar interaction, which follows a r^{-3} dependence. Equation 4.24 predicts a characteristic length scale r_c over which these spin-flip induced dipolar fluctuations are important, with T_1-induced spin-flips contributing to decoherence falling off as $(r_c/r)^3$.

For Gd-DOTA, the model proposed in Equation 4.24 gives $A_2^{\mathrm{DOTA}} = 1.43 \pm 0.16$ μs, corresponding to the inverse dipolar coupling frequency for two spins separated by $r_c = 7.7 \pm 0.3$ nm. For Gd-PyMTA, we find $A_2^{\mathrm{DOTA}} = 1.43 \pm 0.16$ μs, corresponding to $r_c = 7.8 \pm 0.7$ nm. The fact that the characteristic length scale r_c is the same for the two complexes is evidence that r_c does not depend sensitively on the particulars of the EPR lineshape, but rather is perhaps characteristic of the magnetic and dielectric and magnetic properties of the material.

In this light, the model presented in Equation 4.24 can be rewritten as

$$\frac{1}{T_m} = A_1\omega_{dd}(\bar{r}) \sum_{m=-S}^{S-1} \sum_{m'=-S+1}^{S} T(m,m')n_m n_{m'} + \left(\left(\frac{r_c}{\bar{r}}\right)^3 + B\right)\frac{1}{T_1} + \Gamma_{res} \tag{4.28}$$

It is tempting to also rewrite the first term in Equation 4.28 in terms of a characteristic length, however it seems caution must be used here, for at least two reasons. First, as discussed earlier, dipolar-modulated flip-flops lead to decoherence in two different ways- they lead both directly to flips (or flops) of α spins, and to dipolar field fluctuations which change the local magnetic field seen by α spins, where the latter is of a similar effect to T_1-induced flips in the bath. It is reasonable to expect that these two processes will have different characteristic lengths. Second, since these spin flip-flops are themselves driven by dipolar coupling, there may be a higher-order dependence to be considered.

Spin-Lattice and Residual Relaxation

Identical parameters $B = 2.3 \pm 0.3$ and $\Gamma_{res} = 0.05 \pm 0.03$ μs^{-1}, or $\Gamma_{res}/2\pi = 10 \pm 5$ kHz, were found to describe the concentration-independent direct spin-lattice contribution, and the residual relaxation due to nuclear spin flip-flops, respectively.

4.5.2 Discussion and Conclusion

Electron spin decoherence of Gd^{3+} complexes is considerably more complicated in the low temperature, high-field regime than that of $S = 1/2$ organic radicals, for two main reasons. First, decoherence in $S = 1/2$ organic radicals at low temperature is simplified by long spin-lattice relaxation times T_1, which are typically 2-3 orders of magnitude longer than for Gd^{3+} complexes under the same conditions. The much shorter T_1 means that spin-lattice relaxation contributes significantly to shortening of T_M in Gd^{3+} complexes. Second, the fact that Gd^{3+} has seven unpaired electrons for a total spin $S = 7/2$ leads

to much richer spin physics.

These results have important implications for future applications of high-field EPR with Gd^{3+} labels. At high field, the phase memory time of the central transition seems ultimately to be limited by the T_1 of the Gd^{3+} spins, when the environment is deuterated. This is very much in contrast to nitroxide-type radicals, where T_1 is typically orders of magnitude longer than T_M. On the one hand, T_1 puts a "hard limit" on Gd^{3+} coherence times, especially at higher temperatures where T_1 shortens. Longer coherence times are desirable for DEER experiments, where Gd^{3+} spin labels have been shown to be especially useful for measuring long-range distance constraints in biological systems. If the coherence time is ultimately set by T_1, it is reasonable to expect that T_M will decrease with increasing applied field. Gd-Gd DEER at high field will therefore likely benefit from Gd^{3+} spin labels with longer high-field T_1. On the other hand, for pulsed dipolar spectroscopy experiments such as RIDME, having T_M approach T_1 may be beneficial since the RIDME oscillation arises due to T_1-driven spin flips. For Gd-X RIDME, where X is a different radical, short Gd^{3+} T_1 and long X T_M is of course desired. For high-field Gd-Gd RIDME, having T_1 be short while having T_M be ultimately limited by T_1 means the phase memory time is "as long as it can get."

Phase memory time measurements of $S = 1/2$ spins at low temperatures and high magnetic fields have been shown to be a sensitive way to measure local average inter-spin distances [85, 155] in environments where there are not too many ^1H spins. The data presented here, and the model proposed to describe decoherence for high-spin systems,

indicate measurements of T_M and T_1 can be used together to extract average local inter-spin distances between Gd^{3+} spin probes as well, with an increased sensitivity to longer inter-spin distances.

Moreover, inter-spin distance information enters into T_M for Gd^{3+} complexes through two different mechanisms: dipolar-driven spin flip-flops and dipolar field changes due to spin-lattice relaxation-driven spin flips. The second mechanism is not important for nitroxide spin probes [85] or for diamond P1 and NV centers [155], since at low temperatures T_1 is extremely long and spin-lattice relaxation-driven spin flips are negligible on the timescale of T_M. Therefore, all of the inter-spin distance information for these previously studied systems came from measurements at high field and at low temperatures, where dipolar-driven flip-flops are frozen out by high spin polarization.

Gd^{3+} complexes, with much shorter spin-lattice relaxation times T_1, provide an extra mechanism which can be effectively exploited to measure local average inter-spin distances. Crucially, decoherence due to field fluctuations caused by spin-lattice relaxation-driven spin-flips depends only on T_1, on the local electron spin density, and on knowledge of the characteristic length scale r_c. Therefore, this decoherence mechanism can be used to measure average inter-spin distances through T_M and T_1 measurements without the need to highly polarize the electron spin bath, removing the requirement that measurements be performed at low temperatures and at high magnetic field. This opens the door for measurements of the local concentration of, for example, biomolecules tagged with Gd^{3+} spin-labels by EPR relaxation measurements at lower magnetic fields, and at

higher temperatures.

Chapter 5

High-field EPR as an optics problem - sample holder design and optimization

Abstract

This chapter discusses high-field CW EPR lineshape measurements, with the aim of showing how principles from optics can be used to optimize high-field EPR experiments. A simple approach based on transfer matrix calculations to efficiently design and optimize non-resonant sample holder geometries is presented. Dramatic sensitivity enhancements are realized using a flat, layer-by-layer geometry optimized for aqueous samples at room temperature, enabling room temperature measurements of paramagnetic molecules at biologically relevant concentrations and temperatures.

Acknowledgements

CBW developed performed calculations, and performed EPR experiments under the supervision of Mark Sherwin and Songi Han. Mian Qi designed and synthesized the iodo-(Gd-PyMTA) complexes mentioned at the end of this chapter under the supervision of Adelheid Godt.

5.1 The EPR Lineshape: What Are We Measuring?

EPR spectroscopy uses electron spins as quantum mechanical probes of their environment. The effective spin Hamiltonian, which was introduced in Chapter 1, describes how electron spin probes interact with their environment. EPR can report on the electron's spatial wavefunction, on the strengths and orientations of chemical bonds, on nuclear spin states, on local magnetic field fluctuations, on magnetic ordering, on long-range (1-10 nm) distances through electron magnetic dipole-dipole coupling, and on atomic and molecular motion through the partial or complete averaging of anisotropic interactions.

The EPR lineshape contains all of this information, and more. The EPR lineshape characterizes a spin system's response to an external perturbation in the form of a time-varying magnetic field, or equivalently, the EPR lineshape is the Fourier transform of the magnetic dipole time-correlation function [54]. However, we as spectroscopists never directly measure the EPR lineshape. Instead, we measure some property of the sample response to microwave magnetic fields, usually microwave absorption, dispersion, or transmission. Part of the job of the spectroscopist is to connect the microwave response

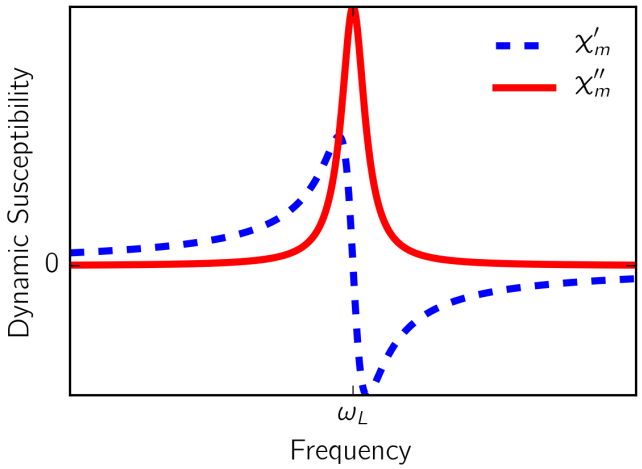

Figure 5.1: The real (χ'_m) and imaginary (χ''_m) parts of the dynamic susceptibility calculated for an isolated spin-1/2 with Larmor frequency ω_L.

to the underlying quantum mechanical spin Hamiltonian.

5.2 High-Field CW EPR Spectroscopy with Induction Mode Detection

The connection between the effective spin Hamiltonian H_S and the EPR absorption lineshape $f(\omega)$ is the dynamic magnetic susceptibility $\chi(\omega) = \chi'(\omega) + i\chi''(\omega)$, also called the AC susceptibility (Figure 5.1) [53, 55]. The dynamic magnetic susceptibility describes how a material responds to an applied AC magnetic field in the linear response regime. EPR lineshape simulation, whether by solving the Bloch equations in the steady state, diagonalizing the effective spin Hamiltonian H_S, solving the Stochastic Liouville equation, etc., is fundamentally a calculation of the dynamic susceptibility [53, 54, 65].

The power per unit volume P absorbed in a material due to interactions with a monochromatic AC magnetic field is proportional to χ_m'', the imaginary part of the dynamic susceptibility [53, 138]. Therefore, a measurement of microwave absorption as a function of magnetic field or as a function of frequency by an EPR spectroscopist can be directly related to underlying spin physics.

High-field EPR spectrometers such as our 240 GHz instrument [51] do not directly measure microwave absorption. Rather, our spectrometer measures the complex reflectance of a sample at 240 GHz as a function of magnetic field. In order to extract from the complex reflectance of a material the EPR lineshape, some optical and geometric properties of the material must be known. In general, we must know 1) the sample geometry, and 2) the sample's dielectric properties, 3) the spin density, and 4) the width of the resonance.[1]

5.2.1 Reflectance calculations

This section outlines how the EPR absorption lineshape, or equivalently the dynamic susceptibility, can be extracted from the measured complex 240 GHz reflectance. The main results are the following: when the magnitude of the dynamic susceptibility is everywhere small $|\chi_m| \ll 1$, the measured signal will be proportional to χ_m, with an overall phase shift and an amplitude which depends on the sample's thickness and dielectric susceptibility ε.

[1]It is only strictly necessary to know points 3 and 4 when the "weak" resonance condition $|\chi_M| \ll 1$ breaks down. For more on this, see Appendix C.

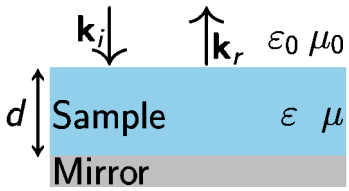

Figure 5.2: Sample geometry as used to calculate the reflectance calculation. A sample of thickness d, with electric permittivity ε and magnetic permeability μ, is backed by a mirror. The incident and reflected wavevectors $\mathbf{k}_i$ and $\mathbf{k_r}$ are shown.

Consider a sample with geometry as shown in Figure 5.2. The sample is a flat disk of thickness d, placed at the end of a waveguide, and backed by a mirror. The complex reflectance r as a function of frequency ω for circularly polarized light is given by the ratio of the reflected electric field to the incident electric field E_r/E_i. For the geometry in Figure 5.2[2],

$$r(\omega) = \frac{E_r}{E_i} = -\frac{e^{2i\phi}\left(\sqrt{\varepsilon_R}+\sqrt{\mu_R}\right)+\sqrt{\varepsilon_R}-\sqrt{\mu_R}}{e^{2i\phi}\left(\sqrt{\varepsilon_R}-\sqrt{\mu_R}\right)+\sqrt{\varepsilon_R}+\sqrt{\mu_R}} \tag{5.1}$$

where $\varepsilon_R = \varepsilon/\varepsilon_0$ is the relative permittivity (dielectric constant), $\mu_R = \mu/\mu_0$ is the relative permeability, and

$$\phi = \frac{\omega d}{c}\sqrt{\varepsilon_R \mu_R} \tag{5.2}$$

is the phase shift induced in the light as it passes through a sample of thickness d [24].

The relative magnetic permeability μ_R is given in terms of the dynamic susceptibility χ_m by

$$\mu_R = 1 + \chi_m = 1 + \chi_m' + i\chi_m'' \tag{5.3}$$

[2]For derivation, see Appendix D.3.

Our 240 GHz EPR spectrometer sends to our sample one polarization of linearly polarized light, and measures the reflected signal in the orthogonal linear polarization. Linearly polarized light is a superposition of left and right circularly polarized (co- and counter-rotating) light. The dynamic magnetic susceptibility breaks time reversal symmetry, so that the co- and counter-rotating waves are reflected differently. As a consequence, the reflected light is elliptically polarized with a component polarized perpendicular to the incident light. In our spectrometer we measure the signal at the perpendicular polarization in order to isolate our detector from our microwave source, a detection scheme called induction-mode detection [31].

We can define a "co-polar" reflectance $r_{\text{co-polar}}$, which is the reflectance of the linearly polarized incident light as measured along the same polarization axis,

$$r_{\text{co-polar}} = \frac{1}{2}\Big(r(\omega)_{\text{co}} + r(\omega)_{\text{counter}}\Big) \tag{5.4}$$

where r_{co} and r_{counter} are the reflectance of the co- and counter-rotating polarizations. We can further define an "induction mode reflectance" r_{ind}, given by

$$r_{\text{ind}} = \frac{i}{2}\Big(r(\omega) - r(\omega)_{\text{counter}}\Big) \tag{5.5}$$

which gives the reflectance along the polarization direction orthogonal to the incident polarization.

5.3 "Weak" Resonance: Linear EPR Regime

When $|\chi_m| \ll 1$, we can expand r_{ind} to first order in χ_m,

$$r_{\text{ind}}(\chi_m) = r_{\text{ind}}(0) + \frac{\partial r_{\text{ind}}}{\partial \chi_m}\chi_m = K\chi_m \tag{5.6}$$

where

$$K = \left.\frac{\partial r_{\text{ind}}}{\partial \chi_m}\right|_{\chi_m=0} \tag{5.7}$$

and where $r_{\text{ind}}(0) = 0$ due to time-reversal symmetry unbroken by the magnetic field.

The measured induction-mode reflectance is proportional to the dynamic magnetic susceptibility. The term K is a function of the sample's properties not related to the spins, including the dielectric constant, the sample thickness, and the sample composition. K also depends on the microwave frequency. For the geometry shown in Figure 5.2,

$$K = \frac{\sqrt{\varepsilon_R}}{2}\frac{(\phi_0 + \cos\phi_0 \sin\phi_0)}{\left(\sqrt{\varepsilon_R}\cos\phi_0 - i\sin\phi_0\right)^2} \tag{5.8}$$

$$\phi_0 = \frac{\omega d}{c}\sqrt{\varepsilon_R} \tag{5.9}$$

When $|\chi_m| \ll 1$, the co-polarized reflection coefficient $r_{\text{co-polar}}$ is given by

$$r_{\text{co-polar}} = 1 - \frac{2\sqrt{\varepsilon_R}\cos\phi_0}{\sqrt{\varepsilon_R}\cos\phi_0 - i\sin\phi_0} - iK\chi_m \tag{5.10}$$

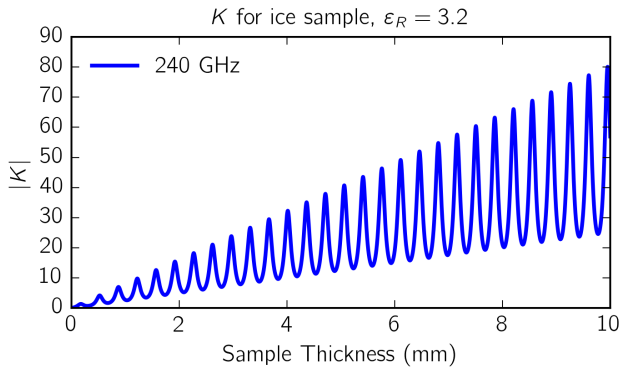

Figure 5.3: Plot of the magnitude of K vs sample thickness assuming the sample is made of ice, with dielectric constant $\varepsilon_R = 3.2$. $|K|$ scales the strength of the induction mode signal. Oscillations come from standing waves inside the sample. For frozen samples, the general trend is that thicker is better.

5.3.1 Field-Swept EPR

In a field-swept EPR experiment, the frequency ω is fixed, so K is a constant which both scales the intensity of the EPR signal and introduces an overall phase shift. For lossless or low-loss samples, such as frozen water-glycerol mixtures, K can be a sensitive function of sample thickness. Figure 5.3 shows the magnitude of K, which scales the strength of the induction mode signal, for a sample made predominantly of water ice with the geometry shown in Figure 5.2. For a frozen sample, thicker samples lead to a larger EPR signal as there is a longer sample region with which the incident beam can interact.

For lossy samples, such as samples made predominantly of water, the dependence on sample thickness is quite different. Thick lossy samples absorb most of the incident light, so that the induction-mode signal is dominated by reflections from the air-sample interface. For thin lossy samples, less of the incident light is absorbed, and the induction mode signal again depends sensitively on sample thickness, with much of the signal

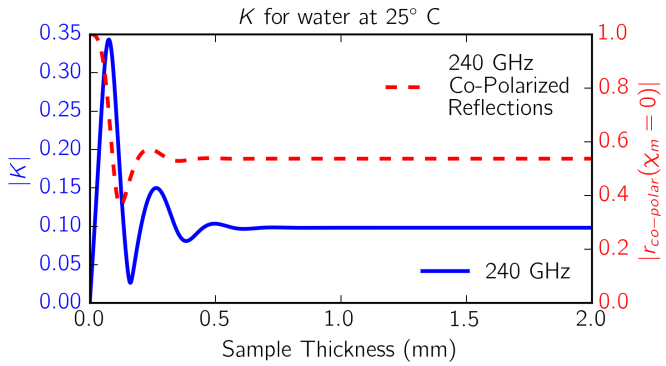

Figure 5.4: Plot of the magnitude of K at 240 GHz vs sample thickness assuming the sample is made of water, with a dielectric constant ε_R calculated following [159]. The co-polarized reflections $r_{\text{co-polar}}$ are included. Samples less than ~ 500 μm thick show a sensitive dependence on sample thickness, where the measured EPR signal comes both from absorption, and from a phase shift introduced as the microwaves pass through the sample. Samples thicker than ~ 500 μm absorb all light which makes it past the surface, so that both the induction-mode reflectance and the co-polar reflectance depend only on reflections from the air-water interface.

coming from the difference between the phase shift induced in the co-rotating beam, which is on resonance, and the counter rotating beam, which is off resonance (Equation 5.5). Figure 5.4 shows $|K|$ for a sample made of water, which has an index of refraction $n = 2.676 + 1.248i$ [159] at 240 GHz.

By controlling sample thickness, it is possible to tune the response of the sample to increase the strength of the induction-mode reflectance, and therefore improve EPR sensitivity. Crucially, for lossy samples such those composed of water, thin samples seem to offer the best performance- see for example Figure 5.4. This means that in many cases a smaller amount of sample at a given concentration can lead to a larger measured EPR signal.

K also introduces a frequency-dependent phase shift, so that absorption and dis-

persion signals are mixed in the induction-mode signal. In a field-swept experiment at constant frequency, this phase shift is constant. Correcting for this phase shift is not particularly troubling, since the absolute phase is in any case ill-defined in our spectrometer and must be determined from the complex signal in post-processing.[3]

5.3.2 Frequency-Swept EPR

It is worth briefly addressing here frequency-swept EPR. K depends on the frequency of incident light through ϕ_0 and ε_R. This means that in a frequency-swept (or frequency-stepped) experiment, K is not a constant, but changes across the EPR line. This manifests itself as a distortion in the EPR line in two ways: 1) a change in signal strength across the EPR line, and 2) a phase shift across the EPR line.

In addition to the phase shift introduced by the sample, the phase shift introduced by the rest of the quasioptics in the spectrometer must be accounted for. In a field-swept experiment conducted at a single frequency, this phase shift is a constant which can be corrected for in post-processing by applying a global phase correction. By contrast, in a frequency-swept experiment this phase shift is a function of frequency and will therefore cause additional distortions of the EPR line that will depend on the optical path length, and on any standing waves.

[3]For more on phase determination in 240 GHz EPR spectroscopy with induction-mode detection, see Appendix C.

5.3.3 Breakdown of "Weak" Resonance

When the magnitude of the dynamic susceptibility is not small, the measured signal is no longer proportional to χ_m and must be caculated from Equation 5.5. The reflectance in general becomes a sensitive function of sample thickness and ε.

In the extreme case that $|\chi_m| > 1$, measured signal becomes dominated by a paramagnetic polariton. Some work towards understanding this regime is discussed in Appendix E.

5.4 Sample Holders for Aqueous EPR

One of EPR's most important strengths is its ability to perform useful measurements in "messy," disordered, highly heterogeneous environments. As discussed in Chapter 1, EPR can be powerfully employed to study biological systems, such as proteins and other biological macromolecules, under native conditions. For the overwhelming majority of biological systems, "native conditions" are warm, wet, and crowded.

Wet conditions, especially aqueous conditions, are a challenge for high-field EPR because water is very efficient at absorbing microwave radiation. High microwave dielectric losses in water lead to severely attenuated signals, and, if high microwave power is used, to sample heating. Furthermore, conventional EPR cavities and resonant structures are of limited usefulness for aqueous samples, since losses destroy the quality factor. Recent work has shown that these challenges can be overcome with novel cavity designs based on photonic bandgap resonators [160], or, as we will see, by careful sample holder design.

A common sample loading procedure for high-field EPR experiments with frozen or liquid solution samples is to load the sample into a bucket made of a microwave-transparent material, and to place the sample bucket atop a mirror. 240 GHz EPR performed at UCSB on these kinds of samples had, until a few years ago, been performed almost exclusively using 5 mm-diameter outer-diameter ($\sim$3 mm inner diameter) Teflon sample buckets with Teflon lids. A cross-sectional view of a Teflon bucket containing a liquid sample and backed by a mirror is shown in Figure 5.5. Teflon sample buckets are convenient sample holders for EPR samples because they can accommodate a variety of samples including liquids, frozen solutions, powders, and gels, are non-reactive, are easy to clean, and have no intrinsic EPR signal.

The typical historical sample volume used in the 240 GHz EPR experiment was 8 μl, for a sample thickness between 1 and 1.5 mm. In practice, EPR measurements of liquid samples performed with bucket-style sample geometries were extremely inconsistent, sometimes providing a passable signal-to-noise ratio for one sample and an unworkably low SNR for another, nominally identical sample.

Bucket-style sample holders are not well suited for lossy, aqueous samples, however, for several reasons. Figure 5.4 shows that the thickness of the water layer is an extremely important parameter to optimize in an EPR experiment, however it is difficult to control the thickness of a liquid sample in a bucket holder. Worse still, the surface of the liquid sample in the bucket is not generally flat, with the liquid typically beading or forming a meniscus. The curved surface of a meniscus is particularly problematic for high-frequency

EPR, since reflections from the air-water interface will not be at normal incidence, leading to a significant amount of light being scattered out of the beam path.

5.4.1 Optimizing EPR Sample Geometry for Liquid Samples

Equations 5.6 and 5.7 relate the optical and geometric properties of an EPR sample to the size of the measured EPR signal in a CW EPR experiment through the K parameter. K is independent of the magnetic resonance properties of a sample, and provides a single, dimensionless parameter which scales the size of the induction-mode reflectance for a given dynamic magnetic susceptibility χ_m. K is analogous to the parameter ηQ encountered in EPR experiments based on resonators, where Q is the resonator quality factor and η is the filling factor [52]. K is given for a simple experimental geometry consisting of a thin layer of sample backed by a mirror, shown in Figure 5.2, by Equation 5.8.

For a more complicated experimental geometry consisting of many flat dielectric layers, K can be calculated using transfer matrix equations, which are outlined in Appendix D. In practice, this is done by calculating r_{ind} for an infinitesimal χ_m, and then taking $K = r_{\mathrm{ind}}/\chi_m$.

Figure 5.6 shows $|K|$ calculated for a Teflon bucket-style sample holder of the kind historically used for 240 GHz EPR at UCSB for liquid or frozen solution samples. For sample depths greater than $\sim$0.5 mm, $|K|$ is found to oscillate about a value of 0.1 as a function of depth, with the oscillations coming from reflections between the surface of

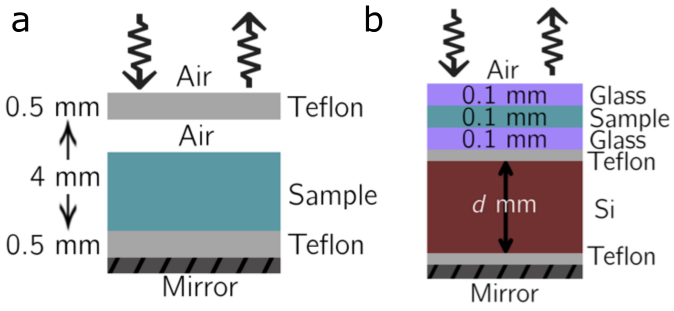

Figure 5.5: Left: cross-section view of a Teflon bucket-style sample holder backed by a mirror, filled with liquid to a depth d with air between the surface of the liquid and the Teflon bucket lid. The inner-diameter of the bucket was around $\sim$3 mm, and sample depths typically ranged from $\sim$1 mm to $\sim$3 mm. Right: cross-section view of a rectangular capillary sample holder, with a 0.1 mm thick sample region and 0.1 mm thick glass walls. Between the capillary and the mirror is a dielectric layer consisting of a piece of high-resistivity silicon sandwiched between two layers of Teflon tape.

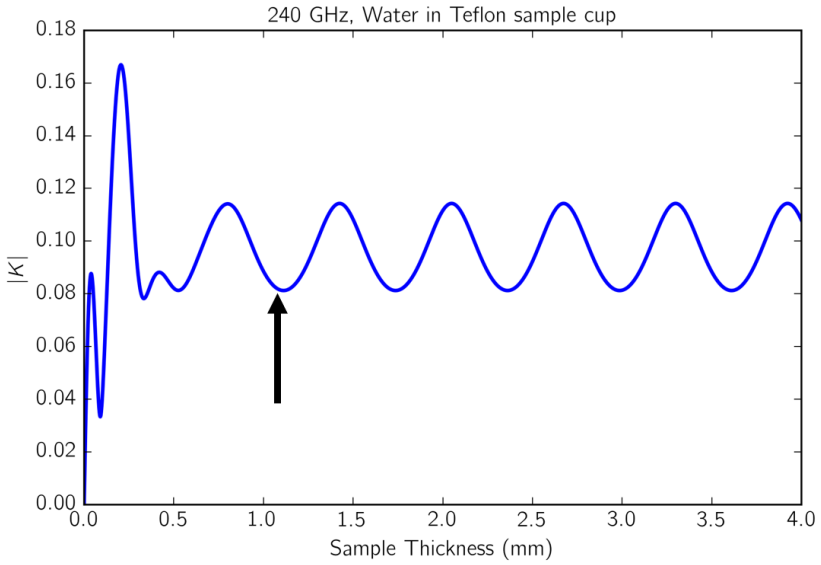

Figure 5.6: $|K|$ simulated for the Teflon bucket-style sample holder shown in Figure 5.5 as a function of the depth d of the water, while keeping the lid at a fixed height 4 mm above the base. For a water layer thicker than $\sim$ 0.5 mm, $|K|$ shows a periodic modulation due to reflections between the water surface and the Teflon lid. Arrow indicates the depth water depth for an 8 μl sample, assuming the water is perfectly flat, with no meniscus.

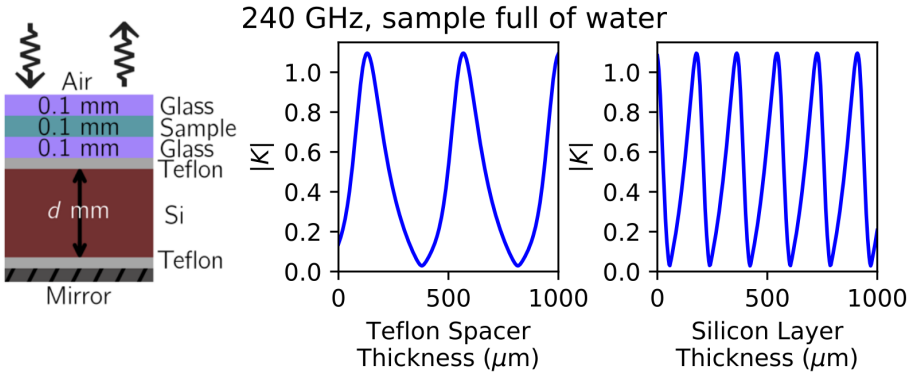

Figure 5.7: Left: cross-section view of a rectangular capillary sample holder, with a 0.1 mm thick sample region and 0.1 mm thick glass walls, separated from a mirror with a dielectric spacer. Center: simulated $|K|$ for the geometry shown to the left, with no silicon, as a function of Teflon thickness. Maxima are separated by 437 μm, the half-wavelength of 240 GHz microwaves in Teflon. Right: simulated $|K|$ for the geometry shown to the left as a function of silicon thickness, with the total Teflon thickness fixed to 140 μm (70 μm thick strips of Teflon tape sandwiching the silicon) calculated as a function of silicon thickness. Maxima are separated by 180 μm, the half-wavelength of 240 GHz in silicon. For optimized dielectric thickness (Teflon, or Teflon-silicon sandwich), $|K|$ is enhanced by a factor of 10-20 as compared to the Teflon bucket-style sample holder (Figure 5.6).

the water and the underside of Teflon lid. $|K|$ appears to be maximized for a thin sample around 100 μm deep, but this is somewhat misleading. Figure 5.6 sweeps many important details under the rug, including the important fact that the liquid water inside the sample cup will not form a perfectly flat layer, but will instead form a meniscus. Furthermore, for sample volumes below around 5-6 μl, the sample will not form a layer at all, but will instead tend to form beads. For these reasons, Figure 5.6 over-estimates the size $|K|$, likely drastically so.

Figure 5.4 suggests that a thickness of 70 - 100 μm will give the optimal performance for an aqueous sample at 240 GHz. In this range, the sample is around one quarter of

the wavelength of 240 GHz microwaves in water. Thin, flat water samples with well-defined thicknesses can acheived using thin capillaries with rectangular cross-sections, as shown in Figure 5.5. Figure 5.5 shows a cross-sectional view of a rectangular capillary holding a 100 μm thick layer of water, and placed on top of a dielectric with a mirror backing. The dielectric layer moves the 100 μm sample region into the maximum of the microwave magnetic field standing wave which forms above the mirror, maximizing the microwave B_1 field at the sample position. Simultaneously, the maximum of the magnetic field standing wave coincides with a minimum of the electric field standing wave, which minimizes dielectric losses in the sample.

$|K|$ was simulated for a number of capillary geometries, in order to optimize both the sample thickness and the dielectric spacer. Figure 5.7 shows the results of one such simulation, where $|K|$ is calculated for the rectangular capillary geometry shown in Figure 5.5. With no dielectric between the mirror and the capillary, (corresponding to a Teflon layer thickness of 0 μm in Figure 5.7), the simulation predicts $|K| \sim 0.14$, or roughly a factor of ~ 1.5 times larger than for the Teflon bucket-style sample holder shown in Figure 5.6. With a Teflon layer of 130 μm, $|K|$ reaches a maximum value of 1.1, leading to a predicted ~ 10 enhancement of the EPR signal compared to the capillary alone, or a factor of ~ 15 enhancement relative to the Teflon bucket-style sample holder. With increased Teflon thickness, $|K|$ is shown to vary periodically with maxima separated by 437 μm, corresponding to the half-wavelength of 240 GHz in Teflon.

The right-most plot in Figure 5.7 shows a simulation of $|K|$ for the rectangular cap-

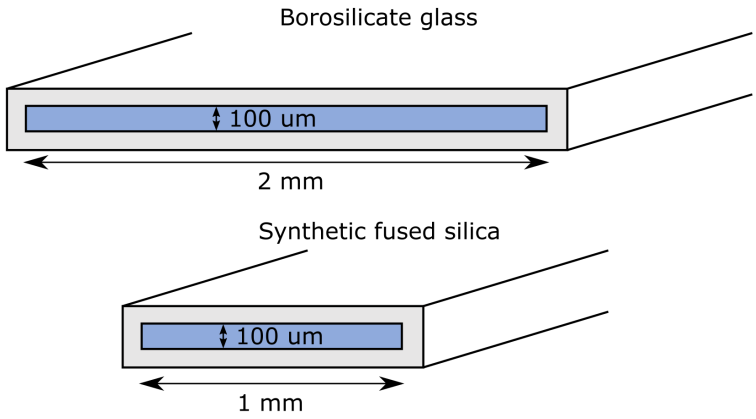

Figure 5.8: Rectangular cross-section capillaries (VitroCom) used for room-temperature solution-state EPR. Top: a borosilicate glass capillary, with 100 μm thick walls, a 100 μm thick sample region, and a sample width of 2 mm. Bottom: synthetic fused silica (Suprasil®) capillary, also with 100 μm thick walls and a 100 μm thick sample region, but with a sample width of 1 mm. Synthetic fused silica capillaries are EPR silent around $g = 2$, while borosilicate glass has a background EPR signal at $g = 2$ from impurities.

illary geometry shown in Figure 5.5, with Teflon layers 70 μm thick for a total Teflon thickness of 140 μm, sandwiching a piece of high-resistivity silicon. $|K|$ is shown to vary periodically with the thickness of the silicon layer, with maxima spaced by 180 μm, which is the half-wavelength of 240 GHz in silicon.

Importantly, for a range of silicon thicknesses, $|K|$ as calculated for this geometry is a factor of 10 to 20 times larger than $|K|$ calculated for the Teflon bucket-style geometry (Figure 5.6), indicating that this capillary geometry will perform better for room-temperature, aqueous samples. To test this hypothesis, rectangular cross-section capillaries (VitroTubes$^{\text{TM}}$) with a 100 μm thick sample region, shown in Figure 5.8, were purchased from VitroCom. Capillaries were purchased in two sizes, shown in Figure 5.8: 2 mm wide borosilicate capillaries, and 1 mm wide synthetic fused silica (Suprasil®)

capillaries. 2 mm × 0.1 mm glass capillaries offered the best trade-off between surface area and sample thickness, but came with an unfortunate drawback, which is that they have a background EPR signal due to impurities in the glass, including a ∼ 40 mT broad feature centered at around $g = 2$. As the impurity line does not overlap with the central $|-1/2\rangle \rightarrow |1/2\rangle$ transition of Gd^{3+} ($g = 1.992$), these glass capillaries are still suitable for performing EPR with gadolinium spin labels. These capillaries are also suitable for pulsed EPR experiments, since the impurity signal is to broad and fast-relaxing to produce a FID or a spin-echo signal.[4]

1 mm × 0.1 mm synthetic fused quartz capillaries have a lower surface area, and so are less well optimized for reflection-mode measurements. However, they are EPR silent around $g = 2$, and are therefore a better choice for performing EPR on a variety of organic radicals, including nitroxide-type radicals.

5.4.2 CW EPR Experiments

Figure 5.9 shows the results of EPR lineshape measurements performed on 300 μM $GdCl_3$ in liquid D_2O at room temperature, in a variety of sample configurations. $GdCl_3$ disassociates in aqueous solutions, and the Gd^{3+} ion provides a strong, narrow EPR signal. 3oo μM is close to the minimum Gd^{3+} concentration which can be observed in a single scan for liquid samples in Teflon bucket-style sample holders at 240 GHz. 8 μl of

[4]No FID or echo signal from the capillary background has been detected between room temperature and 100 K using the FEL, or between room temperature and 5 K using the low-power, 55 mW solid-state microwave source. No FEL-EPR experiments have been performed using capillaries below 100 K. Possibly, the background impurities produce an echo signal in FEL-EPR below 10 K but this has not been verified.

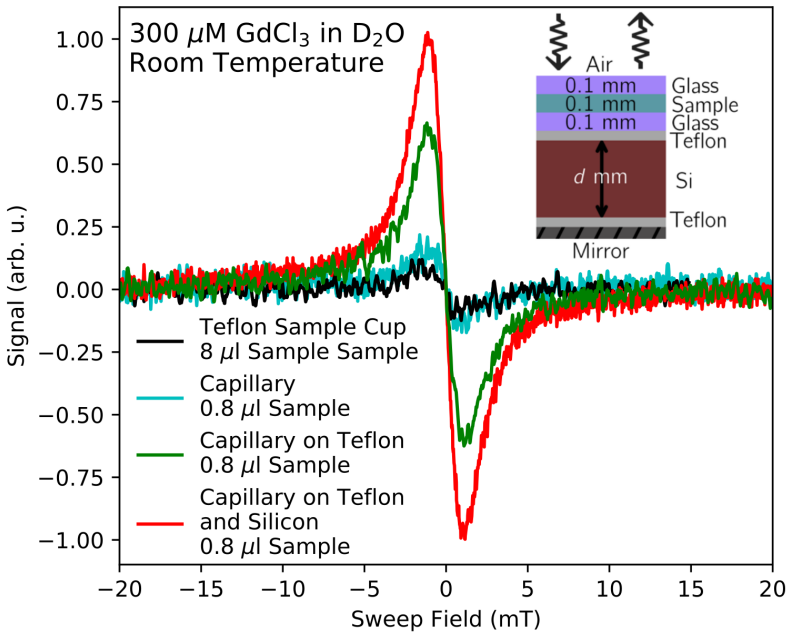

Figure 5.9: EPR signal from 300 μm $GdCl_3$ dissolved in D_2O, measured at room temperature in a Teflon bucket, or in a borosilicate glass capillary with 100 μm thick walls, a 100 μm thick sample region, a sample width of 2 mm, and a length of 4 mm. Signal from 0.8 μl of liquid in a capillary placed directly on the surface of a mirror (teal) is enhanced by a factor of 2 compared to signal from 8 μl of liquid in a Teflon sample bucket (black). Signal from the capillary sample is enhanced by $\sim 4\times$ when the capillary is backed by two layers of Teflon tape, and enhanced by $\sim 6\times$ when the capillary is backed by a 190 μm layer of high-resistivity silicon sandwiched between single layers of Teflon tape.

liquid in a Teflon bucket gave a roughly half the signal of just 0.8 μl of liquid in a 2 mm wide, 0.1 mm deep borosilicate glass capillary cut 4 mm long and placed directly on top of the mirror.

With the capillary placed directly on the mirror, the distance between the liquid sample and the mirror is set by the wall thickness of the capillary. Figure 5.7 suggests that introducing a dielectric spacer of appropriate thickness between the capillary and the mirror can lead to an increase in $|K|$, and therefore an enhanced induction-mode EPR signal. Figure 5.9 shows the EPR lineshape measured for 0.8 μl of sample backed with a dielectric consisting of either two layers of 70 μm thick Teflon tape for a total Teflon thickenss of 140 μm, or with a 190 μm thick high-resistivity silicon layer sandwiched between 70 μm layers of Teflon tape. Relative to the capillary alone, with the Teflon spacer the EPR signal is enhanced by a factor of $\sim$4, while with the Teflon and silicon structure the EPR signal is enhanced by a factor of ~ 6. This enhancement is consistent with simulations shown in Figure 5.7.

The silicon and Teflon structure outperforms Teflon alone due practical concerns relating to sample holder construction. Teflon tape holds the sample setup together, keeping the silicon secured to the mirror and the capillary secured to the silicon. From Figure 5.7, it is apparent that one of the $|K|$ maxima coincides with a silicon layer 0 mm thick, corresponding to the dielectric between the capillary and the mirror consisting of only two layers of Teflon tape. Silicon plays an essential role in helping to keep the Teflon tape flat, however, reducing losses due to microwave scattering.

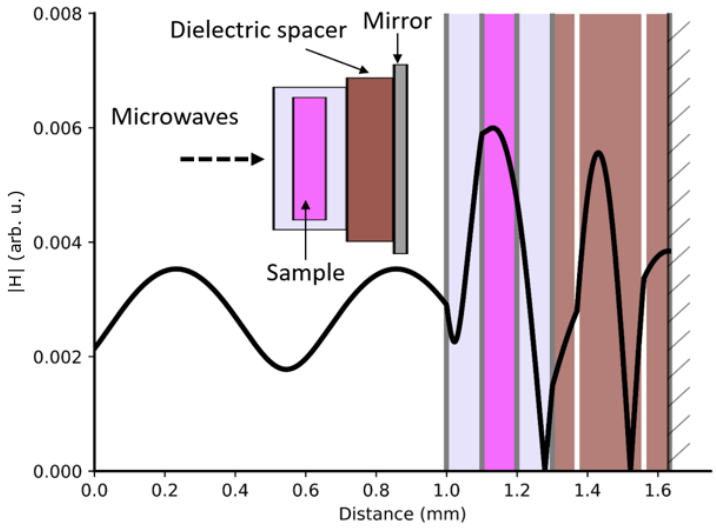

Figure 5.10: Magnitude of the microwave magnetic field $|H_1|$ simulated along the direction of propagation for a capillary backed by a 190 μm thick high-resistivity silicon layer sandwiched between 70 μm layers of Teflon tape, with a mirror behind, assuming a liquid water sample. The sample is located at nearly the maximum of the $|H_1|$ field standing wave, with $|H_1|$ enhanced in the sample relative to at the surface of the mirror.

Figure 5.10 shows a transfer matrix simulation of the magnitude $|H_1|$ of the magnetic component of the 240 GHz microwave field incident from air onto a borosilicate glass capillary with 100 μm thick walls and a 100 μm thick sample region filled with water, backed by a 190 μm thick high-resistivity silicon layer sandwiched between 70 μm layers of Teflon tape and terminated with a mirror. $|H_1|$ forms a standing wave, with maxima occurring inside the silicon and inside the sample layer. $|H_1|$ is enhanced over the maximum value it takes in air by a factor of 1.5-2. The sample is thin enough to fit within the standing wave maximum, taking maximum advantage of the enhanced microwave magnetic field while minimizing dielectric losses by keeping the sample thin. Another important detail is that the maximum of the H_1 field coincides with a node in the electric component E_1 of the microwave field, further reducing dielectric losses.

5.4.3 FEL-EPR Experiments

Capillary sample holders were originally adopted in the 240 GHz EPR experiment at UCSB for CW EPR measurements of liquid samples. However, capillary geometries have proved to be transformative for pulsed EPR experiments carried out with the FEL-EPR spectrometer [51, 86]. Figure 5.11 compares the result of one-pulse FID-detected FEL-EPR experiments performed at room temperature on solutions of OX063 trityl, an organic $S = 1/2$ radical with $g = 2.003$, dissolved in D_2O. Using a Teflon sample bucket containing 8 μl of solution, the trityl FID generated by a 10 ns FEL pulse is barely detectable above the background scattered and leaked FEL radiation which makes it to

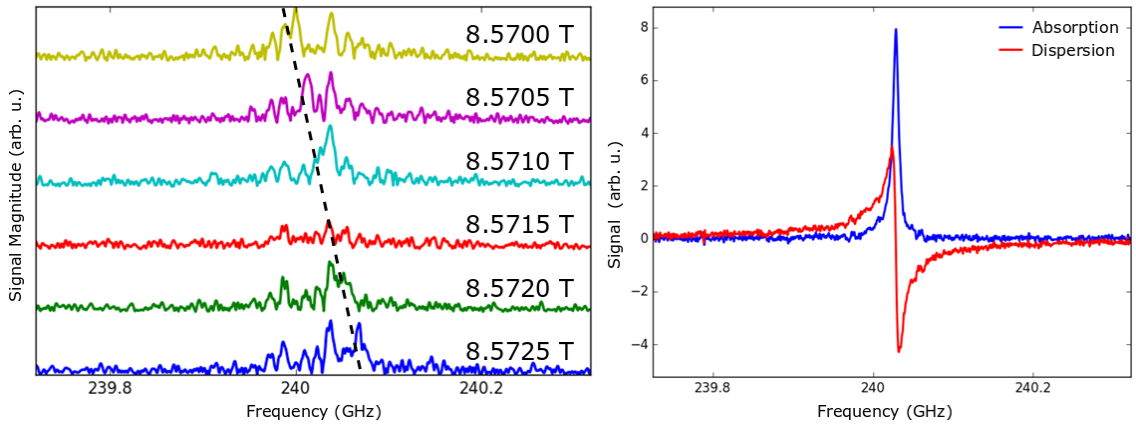

Figure 5.11: FT-EPR of 3.7 mM Ox063 trityl in D_2O at room temperature performed with the UCSB FEL-EPR spectrometer, using a 10 ns 240 GHz pulse and FID detection. Left: FID Fourier transform recorded at different magnetic fields (shown on traces) for 8 μl of sample loaded in a Teflon bucket. Each trace consists of 50 scans averaged coherently [92], and the Fourier transform magnitude is plotted for clarity. Dashed lines track the trityl signal as the field moves. The signal is dominated by leaked light from the FEL. Right: FID Fourier transform recorded in 15 scans on resonance for 0.8 μl of sample in a borosilicate glass capillary with 100 μm thick walls and a 100 μm thick sample region, backed by a 190 μm thick high-resistivity silicon layer sandwiched between 70 μm layers of Teflon tape and terminated with a mirror. Leaked light from the FEL, if present, is completely obscured by the strong FID.

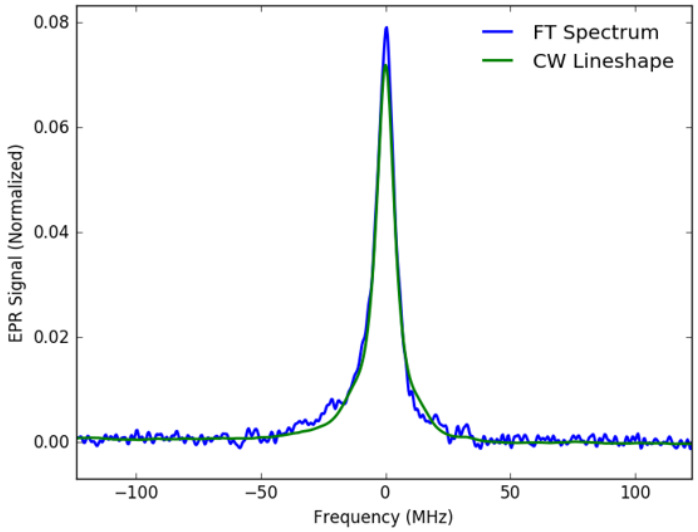

Figure 5.12: In blue: FT-EPR absorption lineshape of OX063 trityl (3.7 mM) in D_2O at room temperature, generated by a 10 ns FEL pulse and recorded in 15 scans, for 0.8 μl of sample in a borosilicate glass capillary with 100 μm thick walls and a 100 μm thick sample region, backed by a 190 μm thick high-resistivity silicon layer sandwiched between 70 μm layers of Teflon tape and terminated with a mirror. In green: integrated CW-EPR lineshape acquired in a single scan with field modulation, for 0.4 μl of the same sample solution in an EPR background-free synthetic fused silica capillary with 100 μm thick walls and a 100 μm thick sample region, with the same mirror and dielectric backing. Both lineshapes are normalized to the area under the curve.

our detector. The trityl resonance is only observable when the experiment is performed as a function of magnetic field and the trityl resonance is tracked, as indicated by the dotted line in Figure 5.11. By contrast, the same experiment performed on 0.8 μl of the same trityl solution loaded into a 2 mm wide borosilicate glass capillary with a Teflon-silicon-Teflon dielectric spacer backed by a mirror generates a large FID easily detectable in a single scan.

Figure 5.12 compares the real part of the Fourier transform of the FID generated by a 10 ns FEL pulse applied to a 3.7 mM solution of OX063 trityl to the integrated CW-EPR

lineshape acquired with field modulation. There is excellent agreement between the two signals, showing that FID-detected FT-EPR of solution samples is viable at 240 GHz with FEL-EPR. This sample holder technology enabled the trityl FEL-EPR T_1 measurements reported in Wilson *et al.* [86].

Microwave magnetic field inhomogeneity is a challenge in high-field EPR, where the wavelength of the incident microwaves is often of around the same size as the sample. Another benefit of keeping samples thin by confining them in capillaries is that the microwave field homogeneity along the direction of propagation is improved, so that more spins see the same strength driving field.

This field homogeneity improvement can also be exploited for frozen solution samples loaded into capillaries, leading to improved experimental fidelity. Figure 5.13 shows a echo-detected Fourier-transform EPR lineshape measurements performed at 115 K on two Gd^{3+} complexes: iodo-(Gd-PyMTA), a complex containing a single Gd^{3+} ion, and a bis-Gd ruler molecule consisting of two PyMTA ligands, each binding a single Gd^{3+} ion, separated by a rigid ruler [161, 25]. The intra-molecular distance between the two Gd^{3+} spins was 2.1 nm. At 240 GHz, the central $|-1/2\rangle \rightarrow |1/2\rangle$ transition of the 2.1 nm bis-Gd ruler is significantly broadened relative to the iodo-(Gd-PyMTA) "monomer" due to dipolar coupling between the two spins. This broadening can be measured and quantified using the CW EPR lineshape, as reported by Clayton *et al.* [25]. Here, we see similar broadening in the FT-EPR lineshape as acquired by FEL-EPR.

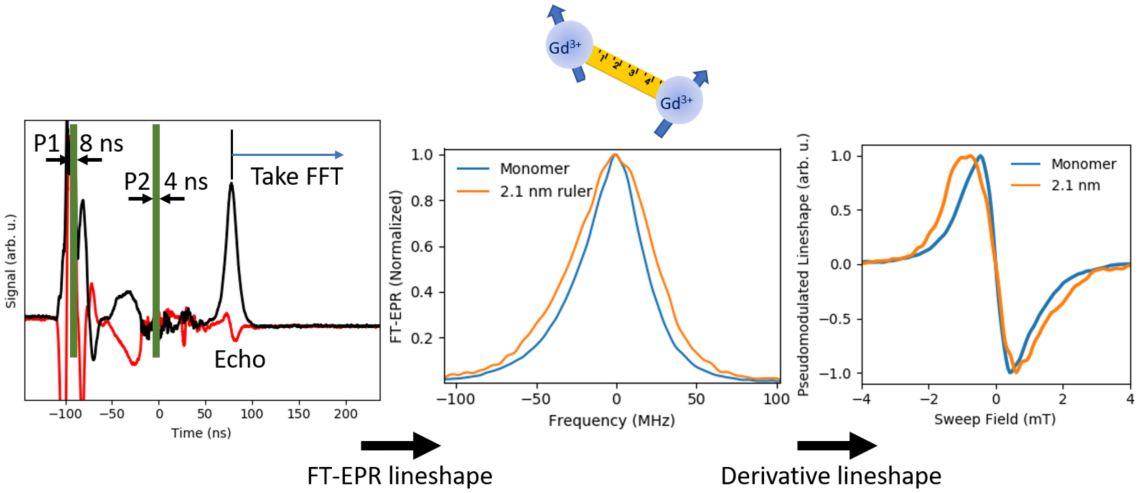

Figure 5.13: Left: Demodulated two-pulse electron spin-echo measurement performed at 115 K on the central $|-1/2\rangle \rightarrow |1/2\rangle$ transition of iodo-(Gd-PyMTA), using an 80 ns inter-pulse delay. Black and red traces are the real and imaginary quadrature signals. The first pulse P1 was 8 ns long, and was applied during the long portion of the quasi-CW FEL pulse with a Rabi frequency $\omega_1/2\pi = 32$ MHz ($\pi/2$ pulse: 8 ns). The inversion pulse P2 was applied during the cavity dump portion of the FEL pulse, where power was boosted by a factor of ~ 11 relative to the long portion of the quasi-CW FEL pulse, for a Rabi frequency $\omega_1/2\pi = 106$ MHz (π pulse: 4.7 ns). FT-EPR lineshape was acquired by beginning the Fourier transform at the peak of the spin-echo signal [87]. Two-step phase cycling with optomechanical phase shifters (POPS) was performed [86]. Center: FT-EPR lineshape of iodo-(Gd-PyMTA) (a Gd^{3+} "monomer") at a 1 mM concentration, and of a PyMTA-spacer-PyMTA ruler molecule [25] with an inter-spin distance of 2.1 nm at a 500 μM concentration. Total spin concentration was the same for both samples, as the "rulers" have two spins per molecule. Right: derivative of the EPR lineshapes shown to the left.

5.4.4 Chapter summary

In practice, all 240 GHz CW EPR experiments at UCSB performed on liquid samples are now conducted using capillary sample holders, due to their significant EPR signal enhancement for lossy samples over bucket-style sample holders. Capillary sample holders have the added benefit of reducing the required sample volume by a factor of 10-20, conserving precious samples.

The adoption of glass and synthetic fused silica capillaries has been transformative in terms of the kinds of experiments which can now be performed at room temperature. Room-temperature EPR of proteins spin-labeled with Gd^{3+} spin labels are now routinely measured with concentrations below 40 μM with good signal to noise, which has enabled quantitative Gd^{3+} spin counting at room temperature as discussed in Reference [57].

Frozen solution samples are also now routinely measured in background-free synthetic fused silica capillaries, in order to take advantage of the flat, well-defined sample geometry they afford, and to leverage the reduction in required sample volume.

Capillary sample holders have enabled FEL-EPR measurements of room-temperature solution samples, including the first reported FEL-EPR T_1 measurements performed on solutions of OX063 trityl [86]. Additionally, capillary sample holders have enabled high-fidelity FT-EPR lineshape measurements by FT-EPR at cryogenic temperatures (Figure 5.13), which are an important step towards bringing the incredible power of Fourier transform pulsed NMR experiments to high-field EPR.

Chapter 6

Correlating motion with photointermediates in Proteorhodopsin with time-resolved high-field EPR

Abstract

Proteorhodopsin (PR) is a retinal-binding, seven alpha helical trans-membrane protein found in a range of bacterioplankton, and which functions as a light-activated proton pump. Green PR function is triggered by the absorption of a 520 nm photon at the bound retinal chromophore. After photoexcitation, PR undergoes a characteristic photocycle consisting of several photointermediates, which results in the transport of a proton

across the cellular membrane [162]. Proton transport in PR is accompanied by large-scale conformational changes [163] which have been studied using time-resolved EPR together with site-directed spin-labeling at 10 GHz / 0.35 T. Time-resolved EPR at higher frequencies offers greatly enhanced spectral resolution, allowing for more straightforward lineshape interpretation and for a higher sensitivity to fast timescale motion. In this chapter I present 240 GHz time-resolved EPR of MTSL-labeled PR, which reports on protein conformational changes. Time-resolved EPR measurements are compared to time-resolved optical absorption spectroscopy, and correlations between photointermediates and protein structural changes are explored.

Acknowledgements

PR samples studied in this chapter were prepared and spin labeled by several graduate and undergraduate students working in the lab of Professor Songi Han at UCSB, including Chung-ta Han, Sirish Narayan, Matthew Idso, and Jichao Song.

EPR, optical absorption spectroscopy, and flash photolysis experiments presented in this chapter were performed by CBW. Kunal Lakhanpal assisted with some of the flash photolysis experiments. Carmen Roelcke assisted in designing the optical absorption instrument.

6.1 Introduction

Understanding connections between protein structure and function lies at the heart of much of modern molecular biology. Work in the Sherwin and Han labs over the last several years has aimed towards developing tools to study structure, and time-resolved structural changes, in proteins and other biological systems at physiological temperatures using high-field EPR measurement together with site-directed spin-labeling, with the ultimate goal of "filming proteins in action." This sixth and final chapter presents a series of EPR and time resolved transient optical absorption (flash photolysis) measurements applied to study light-activated conformation changes in a membrane protein called proteorhodopsin (PR). This study is an ongoing work, involving instrumentation, methods development, applied magnetic resonance spectroscopy, and protein science.

This chapter will begin by introducing PR, and then move on to discussing how we can use high-field EPR to study the timescales on which conformational changes take place in parts of the protein. A home-built optical absorption spectrometer for time-resolved measurements of photoinduced absorption changes is described, and optical measurements to characterize the PR photocycle are correlated with EPR measurements of time-resolved conformational changes.

6.2 Proteorhodopsin: a light-activated Proton Pump

Proteorhodopsin (PR) is a retinal-binding trans-membrane protein that functions as a light-activated proton pump. PR is a rhodopsin, a member of a large class of retinal-binding proteins which transduce light to carry out diverse functions. Rhodopsin proteins are found in nearly all phyla of life, and may be the phototropic mechanism most widely used by life on Earth [164, 165]. PR is a structural homologue to a range of other more well-known proteins, such as bacteriorhodopsin (BR), and human G-protein coupled receptors (GPCRs), which share a 7-alpha-helical transmembrane (7TM) structure.

PR was first isolated in 2000 from marine bacterioplankton from Monterey Bay in California [166]. PR was the first bacterial rhodopsin to be discovered[1]. Like its cousin BR, PR is a ^{1}H pump. PR absorbs photons from the visible spectrum in a retinal chromophore bound to a lysine residue (K231) via a protonated Schiff-base, and pumps ^{1}H ions across bacterial cell membranes. Upon absorbing a photon of visible light, the retinal chromophore isomerizes from an all-*trans* to a 13-*cis* conformation, which triggers a sequence of large-scale protein conformational changes [165]. These conformational changes result in a proton being released towards the extracellular side of the membrane and the uptake of a proton from the cytoplasmic side of the membrane.

Variants of PR have been found in a number of environments throughout the ocean, with spectra tuned to optimize light absorption based on the amount of light available at different ocean depths [167, 165]. Green-absorbing PR (GPR), which absorbs most

[1]Bacteriorhodopsin, despite the name, is actually an archaeal rhodopsin [166]

strongly between 520 nm and 540 nm, is typically found in bacterioplankton near the ocean surface, while blue-tuned PR (BPR) is found at greater depths [168, 169]. The PR variant studied in this chapter (BAC31A8) is green-absorbing PR which exhibits a broad absorption peak centered at around 520 nm in its "dark" state.

The PR photocycle

PR carries out its proton pumping function in a series of intermediate steps which have been characterized by time-resolved optical absorption spectroscopy. A model for the PR photocycle, which was derived by analogy to the previously-characterized BR photocycle, was proposed in 2003 [162], and is shown in Figure 6.1. Under alkaline conditions, where PR natively functions, the model contains three spectrally distinct intermediate states, with two extra states included in order to explain the multi-exponential growth and decay of some of the distinct photointermediates [162].

In its native "dark" state, PR absorbs most strongly between 520 nm and 525 nm. After photoexcitation, the retinal undergoes a series of ultrafast configuration changes on the ∼ps timescale, which result in the retinal isomerizing from an *trans* to a 13-*cis* configuration [171]. The isomerized retinal has a red-shifted absorption spectrum, with an absorption peak around 555 nm [162]. After several μs, the retinal Schiff base deprotonates, giving up a proton to the primary proton acceptor, an aspartic acid at residue 97 on the extra-cellular side of PR. The deprotonated Schiff base causes the absorption spectrum to blue-shift, with an absorption peak shifted to 405-410 nm. The red-shifted all-*trans* retinal photointermediate is labeled K and the blue-shifted deprotonated Schiff

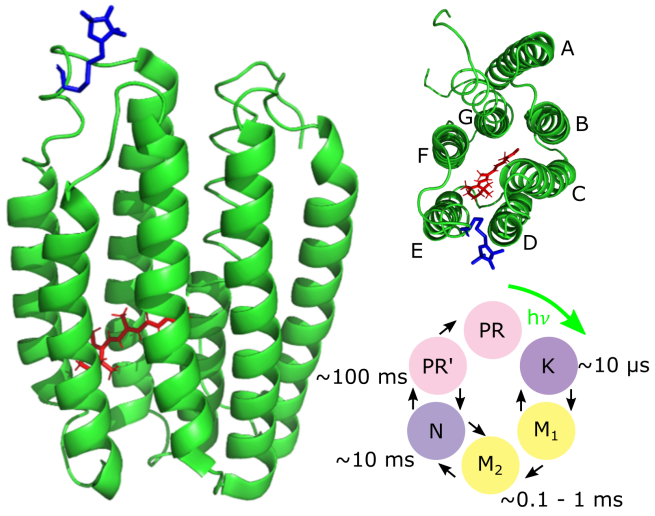

Figure 6.1: Left: the structure of PR, as obtained from solution NMR spectroscopy [170]. The retinal chromophore is shown in red. An MTSL spin label is attached at site 174 on the loop connecting the E and F helices. Top right: PR viewed from the cytoplasmic side of the membrane, looking out of the cell. Trans-membrane alpha helices A-G are labeled. Bottom right: a model for the PR photocycle [162], labeled with characteristic lifetimes of the various photointermediates.

base intermediate is labeled M, by analogy with the BR photocycle [162]. In the PR photocycle proposed by Varo *et al.*, two spectrally identical M intermediates are identified, labeled M_1 and M_2 (see Figure 6.1), in order to explain the multi-exponential rise and fall of the blue-shifted state.

The retinal Schiff base is then reprotonated by a proton donated from a glutamic acid at residue 108 on the endocellular side of PR, shifting the absorption peak back to around 555 - 560 nm to a new photointermediate labeled N (see Figure 6.1). N and K have nearly identical absorption spectra, but occur at different times in the PR photocycle. Reprotonation occurs on the 0.1 ms to 5 ms timescale. Finally, the retinal isomerizes back to the all-*trans* configuration on the 10 - 100 ms timescale with an absorption peak

at around 520-525 nm. Varo *et al.* identified one additional intermediate state, labeled PR' or O in some models, which is spectrally identical to dark-state PR but which serves to describe the observed multi-exponential N intermediate decay [162].

This series of steps, roughly summarized as 1) all-*trans* to 13-*cis* isomerization, 2) Schiff base deprotonation, 3) Schiff base reprotonation, and 4) 13-*cis* to all-*trans* isomerization, result in a proton being transported from the endocellular side of the cell membrane to the extracellular side of the cell membrane. Upon returning to the dark state, PR is ready to absorb another photon and begin the photocycle over again.

The spectral properties and the kinetics of PR's photocycle are modified by a range of point mutations in the PR sequence. One mutation which has been played an important role in furthering the understanding of proton transport in PR is a mutation which substitutes the primary proton donor for the retinal Schiff base, a glutamic acid at residue 108, for a glutamate (hereafter referred to as the E108Q mutation) [172, 173, 162, 174, 175, 176]. Removing the primary proton donor dramatically slows down reprotonation of the retinal Schiff base, lengthening the lifetime of the M intermediates by 2-3 orders of magnitude.

Structure and oligomerization

Membrane proteins are difficult to study under native conditions with many of the tools commonly used for structure determination, such as X-ray crystallography and electron microscopy (EM). GPR has not yet been successfully crystallized, and no high-resolution X-ray crystallography or EM structure of it exists. Insights into GPR's native structure

in lipid membranes have come from atomic force microscopy (AFM) [177] and solid-state NMR [178, 179, 180], and by homology to other rhodopsins, such as blue PR [181] and bacteriorhodopsin.

Much of the work on PR structure determination has been carried out on PR solubilized in surfactant micelles rather than in lipid bilayers. A solution NMR structure of GPR in β-D-dodecyl-maltoside (DDM) surfactant micelles was reported in 2011, which has informed much of the subsequent work on GPR structure [170].

Like many membrane proteins, PR tends to form oligomers in host membranes [177]. PR tends to form characteristic radial hexamers or pentamers, both in lipid bilayers and in surfactant micelles. Oligomerization is accompanied by functional changes in PR, principally observed in the lengthening of the photocycle, with the M state decaying more slowly in oligomeric PR [176]. PR's propensity to oligomerize can be controlled when solubilized in surfactant micelles by changing the detergent composition and concentration [182]. Additionally, PR oligomerization can be suppressed by a point mutation substituting the glutamic acid at site 50 for a glutamate (hereafter referred to as the E50Q mutation) [183].

EPR spectroscopy together with site-directed spin-labeling has been a useful tool for structural determination in PR, particularly when it comes to understanding oligomeric structure and assembly. Stone *et al.* used CW lineshape analysis of PR labeled with MTSL (S-(2,2,5,5-tetramethyl-2,5-dihydro-1H-pyrrol-3-yl)methyl methanesulfonothioate), a nitroxide-type radical, to probe oligomer assembly [175], and Edwards *et al.* used pulsed

dipolar spectroscopy techniques to measure long distances between Gd^{3+} spin labels attached to different proteins which were part of the same oligomer [20]. Intra-oligomer distance constraints have also been obtained using lineshape analysis of PR labeled with Gd^{3+} spin labels [57].

A picture of PR has developed from information derived from a range of sources [165]. PR consists of seven hydrophobic trans-membrane alpha helices labeled A-G which span the lipid membrane, and six loops connecting the hydrophobic helices which protrude out of the membrane into the cytoplasm or into the extracellular region. The core of PR which is surrounded by the trans-membrane helices facilitates proton transport.

EPR has been used to refine regions of the PR structure which are poorly constrained by NMR spectroscopy. Hussain *et al.* used CW EPR together with side-directed spin-labeling to study the loop connecting the E and F helicies, which is poorly constrained by both solution and solid-state NMR, and which appears disordered in solution NMR structures [170]. EPR lineshape measurements of spin-labels attached at sites along the E-F loop showed that the loop region was partially ordered, with a short alpha-helical section bridging flexible ends [184].

Conformational changes which accompany proton transport

Proton transport in PR is accompanied, as in bacteriorhodopsin, by large-scale conformational changes. These conformation changes have been detected and modeled using time-resolved wide-angle X-ray scattering [163]. Andersson *et al.* concluded proton transport induced by photoexcitation is accompanied in both BR and PR by motion of the

F helix and to a lesser extent to the E helix in the direction of the cytoplasm, away from the retinal, and by motion of the C helix inwards from the extracellular side of the membrane and towards retinal [163]. However, while in BR motion can be correlated fairly well with the appearance of BR spectral intermediates L and M, these experiments could not conclusively correlate motion in PR with particular photointermediates.

EPR measurements performed at 10 GHz / 0.34 T of PR spin-labeled with MTSL along the E-F loop were found to be sensitive reporters of the motion of the E and F helices [184] in PR with the E108Q mutation (hereafter referred to as "slow" PR), which removes the primary proton donor for the retinal Schiff base and therefore lengthens the lifetime of the M spectral intermediate. Spin-labels tethered along the E-F loop of PR were found to exhibit lineshape changes when PR was photoactivated, which occurred on a similar timescale to changes in visible light absorption [184, 176]. This evidence supports the picture that motion of the E and F helices are correlated with the lifetime of the M photointermediates, with the observed lineshape changes being consistent with a conformation-change induced modification of the local spin-label mobility. However, time-resolved EPR of spin-labeled PR without the E108 Q mutation (hereafter referred to as "fast" PR) was not reported at the time, leaving open the question of how conformation changes correlate with photointermediates in native PR without the E108Q mutation.

Motivation for high-field EPR studies of PR

High-field EPR offers increased spectral resolution over low-field EPR. Increased spectral resolution ensures that the EPR lineshape is more sensitive to small changes in the envi-

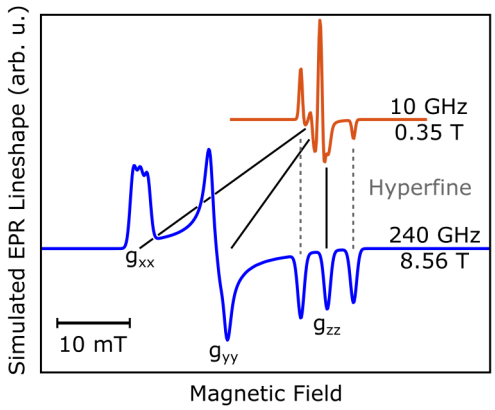

Figure 6.2: EPR lineshape of a nitroxide radical simulated at 10 GHz and at 240 GHz. Solid black lines indicate the field dependence of line-broadening broadening the anisotropic Zeeman interaction, which grows linearly with applied field and which dominates the lineshape at 240 GHz. Dashed gray lines indicate the field-independent line-broadening due to the z component of the anisotropic hyperfine interaction, which dominates the lineshape at 10 GHz.

ronment around the spin label, or to changes in the dynamics of the spin label, making the nitroxide spin label a more effective probe of change at high magnetic field. At high magnetic fields, the nitroxide radical lineshape is dominated by inhomogeneous orientational broadening due to an anisortropic Zeeman interaction expressed by an anisotropic g-tensor. This is an entirely different regime when compared to 10 GHz EPR of nitroxide radicals, where the linewidth is dominated by the field-independent hyperfine interaction. Figure 6.2 illustrates the field-dependence of the EPR lineshape at high and low field. The hyperfine interaction is also partially anisotropic for nitroxide radicals, leading to a complicated, overlapping contributions to the EPR lineshape and making it difficult to disentangle contributions to the lineshape from hyperfine coupling and from g-anisotropy. At high magnetic field, however, the much larger Zeeman anisotropy dominates the line-

shape so that different molecular orientations are well-separated in the lineshape, making it straightforward to independently quantify contributions each interaction.

Another important advantage offered by high-field EPR is access to new spin probes, with favorable high-field spectral properties. One such class of spin probes are spin-labels base on high-spin ($S = 7/2$) Gd^{3+} ions contained within molecular cages. As discussed in Chapter 4, $m = -1/2 \rightarrow m = 1/2$ central transition in Gd^{3+} narrows inversely with magnetic field. At 240 GHz, the Gd^{3+} central transition becomes sufficiently narrow that dipolar broadening due to spin-spin interactions becomes resolvable, allowing for measurements of inter-spin distances with lineshape measurements [24, 25]. Crucially, Clayton *et al.* showed that broadening of the Gd^{3+} central transition can be used to extract Gd-Gd distances at physiological temperatures, using simple lineshape measurements which take ∼minutes, as opposed to pulsed dipolar spectroscopy techniques which require cryogenic temperatures, and hours to days of signal averaging.

Measurements of electron dipolar coupling between spin labels have already been successful employed to study PR structure, however these measurements have either lacked sensitivity to distances beyond $\sim$ 1.8 nm [175], or rely on pulsed dipolar spectroscopy techniques which require cryogenic temperatures [20]. Time-resolved EPR with Gd^{3+} spin labels therefore represents a promising technique for detecting room temperature, time-resolved distance changes in spin-labeled, active proteins, which could be powerfully employed to study light-induced conformation changes in PR at physiological temperatures [57].

Work in the Sherwin and Han labs over the last few years has been aimed towards measuring distances, and time-resolved distance changes, in proteins at physiological temperatures using high-field EPR measurements with Gd^{3+} spin labels, with the ultimate goal of "filming proteins in action." The rest of this chapter is dedicated to describing instrumentation and methods development carried out towards this goal.

First, 240 GHz time-resolved EPR is demonstrated on photoexcited PR spin-labeled with MTSL. Second, a home-built time-resolved optical absorption spectrometer is described, and applied to study the PR photocycle to track photointermediates.

Third, the power of high-field EPR is demonstrated with nitroxide spin labels, which, while not suitable for performing time-resolved distance measurements, are nevertheless capable of reporting on conformation changes, and can be used to characterize motional timescales [184, 176] with improved spectral and temporal resolution, allowing for time-resolved EPR measurements of photoexcited conformational changes in native "fast" PR. Finally, time-resolved optical absorption spectroscopy and time-resolved EPR are used together to correlate protein motion with photointermediates in the PR photocycle.

6.3 Experimental techniques

Two primary techniques were used to study PR: time-resolved 240 GHz CW EPR together with site-directed spin-labeling, and flash photolysis.

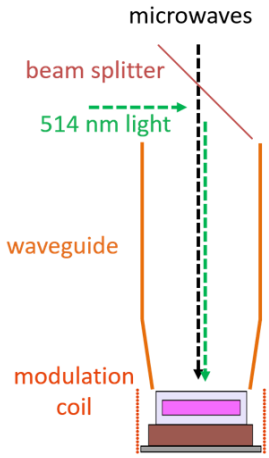

Figure 6.3: Schematic showing how light activation was incorporated into the 240 GHz EPR spectrometer. A pellicle beam splitter which is transparent to 240 GHz was used to direct light from a 514 nm laser down the bore of the waveguide to the sample position. Laser power at the sample position was 6.5 mW. Samples were contained in rectangular glass capillaries made of synthetic fused silica (Suprasil®) with a 100 μm thick sample region, 100 μm thick walls, and sample width of 1 mm. Capillaries were cut into 4 mm long sections, filled with sample, and the ends were sealed with wax. Capillaries were backed by a dielectric made of a piece of high-resistivity silicon 190 μm thick, sandwiched between two pieces of Teflon tape. For more on sample holder design and development, see Chapter 5.

6.3.1 Time-Resolved High-Field EPR to Track Conformational Changes

In order to perform EPR measurements of PR to study light-induced conformational changes, a method for light activation was incorporated into the 240 GHz EPR spectrometer. Figure 6.3 illustrates the scheme used for light activation. Light from a 514 nm diode laser (FlexPoint) was reflected off of a pellicle beam splitter placed above the top of the corrugated waveguide which couples microwaves to the sample position. The pellicle reflected ~35% of the incident light, delivering roughly 6.5 mW of green light to the sample position. The 514 nm diode laser can operate in CW mode, or it can generate

pulses via a TTL modulation input port, with a maximum modulation frequency of 10 kHz.

Following Hussain *et al.* [176], initial EPR experiments were performed on "slow" PR samples with the E108Q mutation, where the primary proton donor for the retinal Schiff base (glutamic acid 108) was substituted for glutamate, a poor proton donor [172, 173, 162, 174, 175, 176]. This mutation slows down the PR photocycle by extending the lifetime of the M_2-intermediate by 2-3 orders of magnitude, so that the M to N transition takes place over seconds rather than ms. "Slow" PR with the E108Q mutation was spin-labeled with the nitroxide radical MTSL at site 174, located on the loop connecting the E and F helices (Figure 6.1). PR was solubilized in β-D-dodecyl-maltoside (DDM) surfactant micelles. Spin labeling was carried out in the lab of Songi Han in the UCSB chemistry department, using established procedures [175, 176] (see Appendix A).

PR samples were hyper-concentrated using a procedure developed in collaboration with Mattew Idso, whereby a solution of PR solubilized in DDM was dried on a glass slide overnight, and rehydrated with a minimal volume of pH 8.5 buffer. This procedure boosted the concentration of PR for EPR measurements, and was found to dramatically increase the measured EPR signal.

Samples were loaded into rectangular cross-section synthetic fused silica capillaries cut to 4 mm long, with a 100 μm thick sample region, 100 μm thick walls, and sample width of 1 mm. Immediately before measurements, PR solution was pipetted into the capillary, and the capillary ends were sealed with wax. Capillaries were backed by a

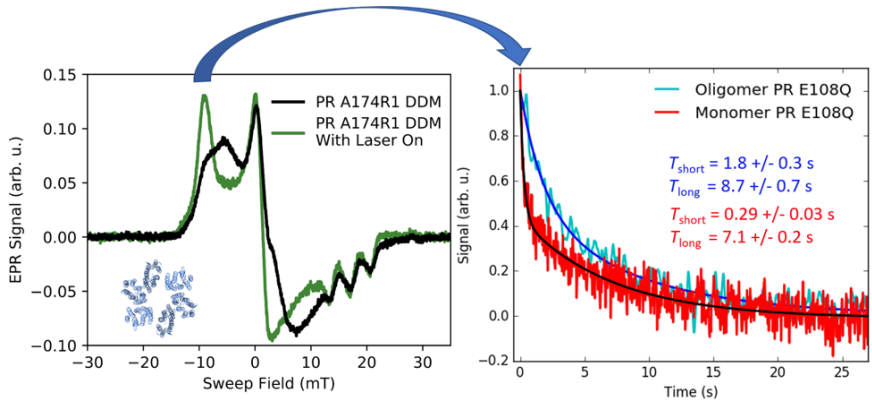

Figure 6.4: Left: 240 GHz EPR lineshape of hexameric "slow" (with the E108Q mutation) PR in DDM detergent micelles labeled at site 174 with MTSL, in the dark (black) and under CW illumination from a 514 nm diode laser (green). Right: a 0.5 s 514 nm pulse induces conformational changes in PR. Time-resolved EPR acquired at the field position indicated with the arrow tracks the protein conformation decay back to the dark state. Signal decay is bi-exponential, as reported in 10 GHz time-resolved EPR experiments by Hussain *et al.*. (Experimental conditions were: pH 8.5, temperature 289 K) [176].

dielectric made of a piece of high-resistivity silicon 190 μm thick, sandwiched between two pieces of Teflon tape (for details, see Chapter 5).

Figure 6.4 shows the CW EPR lineshape of "slow," hexameric PR labeled at site 174 with MTSL, in the dark and under CW illumination from a 514 nm laser. EPR lineshape measurements were performed under constant 240 GHz irradiation while slowly sweeping the main magnetic field about a central magnetic field of 8.56 T. Sinusoidal field modulation at 70 kHz with an amplitude of 5 gauss was applied during EPR detection by a coil which surrounded the sample. Lock-in detection was used, and the measured signal was proportional to the derivative of the EPR lineshape [52].

The MTSL lineshape is dominated at 240 GHz by broadening due to an anisotropic g-tensor, as shown in Figure 6.2, so that the resonance of each spin label is a function of the

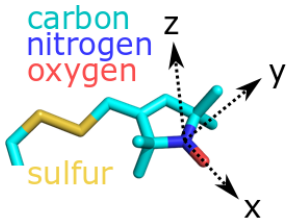

Figure 6.5: MTSL spin label, with the conventional molecular coordinate system defined. Atoms are color-coded according to the legend. The x-axis points along the direction of the nitrogen-oxygen bond, and the z axis points orthogonal to the plane of the molecule.

molecule's orientation with respect to the external magnetic field $\mathbf{B}_0$. When the molecule is free to rotate and tumble, the orientation-dependence of the Zeeman interaction can be partially or entirely averaged out, if rotations are faster than $1/\Delta\omega$, where $\Delta\omega$ is the contribution to the inhomogeneous linewidth from g-anisotropy [53]. Figure 6.4 shows the EPR lineshape spans ~ 35 mT, corresponding to $\Delta\omega = \gamma\Delta B \sim 1$ GHz. Therefore, we can expect that motion of the spin label which occurs on the $\sim ns$ timescale will begin to cause orientational averaging in the lineshape. Figure 1.2 illustrates this effect for isotropic tumbling with a single rotational corrrelation time τ_c.

The differences observed between the PR lineshape in the dark and under green illumination can be explained by changes in the MTSL label's ability to rotate about its tether. In the light-activated state, the MTSL lineshape shows a sharp feature in the low-field derivative lineshape, corresponding to a well-defined shoulder in the absorption spectrum. This feature is indicative of incomplete orientational averaging, since the signal at this shoulder corresponds to spin-labels oriented so that the external magnetic field aligns with the x-axis of the nitroxide molecular frame, as shown in Figure 6.5. In

order for this feature to be prominent in the EPR spectrum, molecules must rotate slowly enough that they maintain this orientation for ∼ns. By contrast, in the dark state this low-field feature is largely smoothed out, indicating that the spin labels are tumbling faster in the dark state.

As similar feature can be seen at feature centered at the zero of the sweep field. This central feature corresponds to those spin-labels oriented with the external field along the y axis of the nitroxide molecular frame, and the fact that it is narrower in the light-activated state than in the dark state is consistent with the spin labels tumbling faster in the dark state than in the light state.

The EPR lineshape reports on the molecular rotation of the spin-label, which is tethered to the E-F loop of PR. Barring any steric restrictions, the spin label is mostly free to rotate about the bonds that make up the tether, and generally undergoes much faster motion than the underlying protein [65]. The change in the EPR lineshape seen in the light-on vs light-off experiments reports on changes in the spin-label dynamics, rather than on changes in the underlying protein dynamics. However, we can understand this change in the label dynamics as resulting from a change in the protein conformation, which leads to steric clashes between the spin label and the protein in the light-activated. Steric clashes then restrict the label's ability to rotate in the light-activated state until the conformational change relaxes back to the dark state, where the spin label's rotation is not hindered.

Time-resolved EPR can be used to track this transition from light-active conformation

to the dark-state conformation. Figure 6.4 shows the EPR signal measured as a function of time at a constant external magnetic field position indicated by the arrow connecting the left and right figures. The same 5 gauss field modulation, together with lock-in detection, was used during time-resolved EPR measurements. After a 0.5 s pulse of 514 nm light, the lineshape relaxes over the course of several seconds from the light-activated state back to the dark state.

These measurements represent the first time-resolved measurements of protein dynamics performed with 240 GHz EPR at UCSB. Interpreting the observed change in the EPR lineshape upon light activation at high magnetic field is far more straightforward than for similar measurements performed at 10 GHz / 0.34 T [176], because line broadening due to an anisotropic g-tensor scales linearly with the applied magnetic field. At 10 GHz, the contribution to the linewidth from g-anisotropy is 24$\times$ weaker, so that at low field g-anisotropy contributes less to the overall linewidth than hyperfine coupling, which is field-independent. Hyperfine coupling is also anisotropic in MTSL, leading to a convoluted low-field lineshape where disentangling the g-anisotropy from the anisotropic hyperfine interaction is not easy. At 240 GHz, the anisotropic hyperfine interaction is comparatively less important and it is far more straightforward to interpret the observed lineshape changes as we have done here (see Figure 6.2).

Time-resolved EPR measurements were performed both on "slow" hexameric PR and on "slow" monomeric PR. For both, the decay was bi-exponential in character, but for monomeric PR the decay was considerably faster than for hexameric PR, consistent with

the findings of Hussain *et al.* [176].

6.3.2 Optical Spectroscopy to Track Photointermediates

Optical absorption spectroscopy is an established technique for studying PR photointermediates and PR photocycle kintetics [162, 185, 182]. The different PR photocycle intermediates have absorption peaks at different wavelengths. Time-resolved measurements of absorption changes induced by photoexcitation can be used to track the state of the retinal chromophore as it transduces proton transport.

The optical properties of PR, and kinetics of the PR photocycle, depend on several variables both internal and external to the protein. Internal variables include various point mutations [165], and external variables include temperature, pH [185], lipid or surfactant environment [182], or oligomeric state [176].

In order to 1) characterize the impact of any mutations made to PR, for example to attach spin-labels, and 2) perform measurements to correlate photointermediates with time-resolved conformational changes, an optical spectrometer capable of tracking time-resolved absorption changes induced by photoexcitation was constructed in the Sherwin lab.

Figure 6.6 shows the layout of the home-built instrument. "White" light from a 60 W halogen bulb is sent through a pinhole, collimated with a lens, and then focused to a $\sim$ 2 mm diameter spot on the sample. Solution samples are loaded into a cuvette made of special optical glass (SOG, from Starna Cells, Inc.) with outer dimensions of

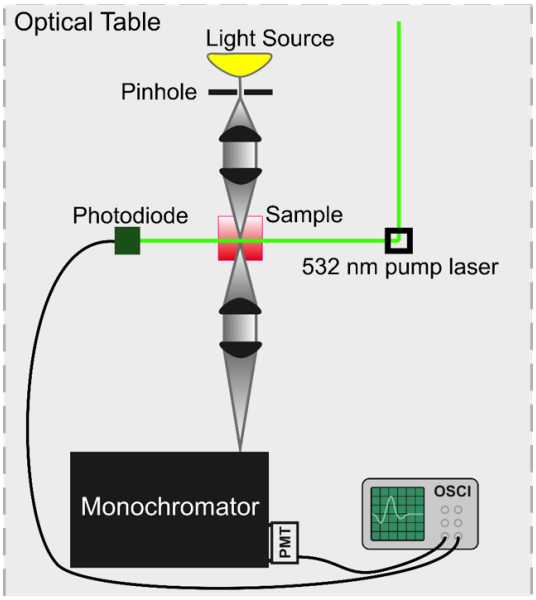

Figure 6.6: Schematic showing the layout of the home-built optical absorption / flash photolysis spectrometer. For flash photolysis measurements, a high-power, $\sim$ 6 ns 532 nm pulse from a frequency-doubled, Q-switched Nd:YAG laser (Quanta Ray) is directed at the sample as shown. Additionally, a 514 nm, 18 mW diode laser can be used to apply longer pulses, or CW laser excitation. Detection is synchronized to the laser excitation with a photodiode detector.

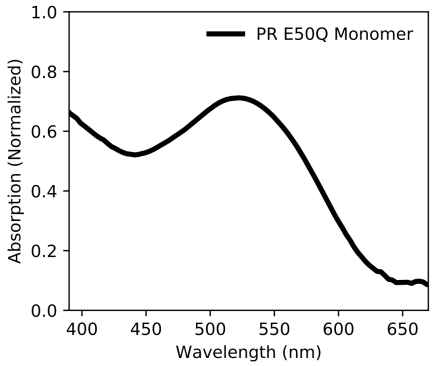

Figure 6.7: "Dark" state absorption spectrum of monomeric "fast" PR with the E50Q mutation which promotes monomer formation, in DDM detergent. Peak absorption occurs at 522 nm. (pH 8.5, 295 K).

$12.5 \times 12.5 \times 45$ mm. Typical sample volumes are ~ 0.6 ml, though smaller volumes can be accommodated, and typical protein concentrations are $\sim$10 μM. Light transmitted through the sample is recollimated, and sent into a f/1.6 triple-grating monochromator (Acton SpectraPro 500) by another pair of lenses for wavelength-selective measurements. Detection is achieved with a photomultiplier tube (PMT) (Hamamatsu R11568) with a passive high-voltage divider (VORG electronics). The PMT voltage is read out using an oscilloscope (Keysight DSOX1102A).

Figure 6.7 shows the absorption spectrum of monomeric PR with the E50Q mutation, which promotes monomeric PR, measured in DDM detergent micelles. PR absorption spectrum are recorded in three steps. First, the monochromator is stepped through a range of wavelengths λ, and the intensity of light $I_{PR}(\lambda)$ at each wavelength is recorded by the PMT. The experiment is then repeated with the PR sample replaced by a mixture of buffer and DDM, and the intensity of light $I_0(\lambda)$ with no PR is recorded as a function of

wavelength. Finally, the signal due to the "dark" signal of the PMT I_{dark} is measured by blocking port leading into the monochromator. The normalized PR absorption spectrum $A_{PR}(\lambda)$ is then given by

$$A_{PR}(\lambda) = 1 - \frac{I_{PR}(\lambda) - I_{dark}}{I_0(\lambda) - I_{dark}} \tag{6.1}$$

Measurements of time-resolved absorption changes induced by photoexcitation, hereafter referred to as "flash photolysis," can be carried out for any wavelength by recording the time-domain signal from the PMT on an oscilloscope. Photoexcitation is initiated by a$\sim$6 ns pulse of 532 nm light from a frequency-doubled Q-switched Nd:YAG laser (Quanta Ray) which is coupled to the sample and which arrives orthogonally to the white light source. The laser spot is $\sim$10 mm in diameter, many times larger than the white light spot size.

Flash photolysis experiments performed at multiple wavelengths can be used to generate time-resolved absorption spectra, as shown in the absorption difference spectra plotted in Figure 6.8. Flash photolysis was carried at regular wavelengths spaced by 7 nm in the region between 390 nm and 630 nm, and compiled into a large dataset. Slices taken at constant time are plotted, and show a general trend of red-shifted absorption, with a small blue-shifted absorption peak appearing in the 100 μs time-slice.

Following Varo *et al.*, the difference spectra were subjected to principal component analysis (PCA) [162]. PCA revealed two dominant principal components, plotted in Figure 6.8: a primary, red-shifted component, and a secondary, blue-shifted component.

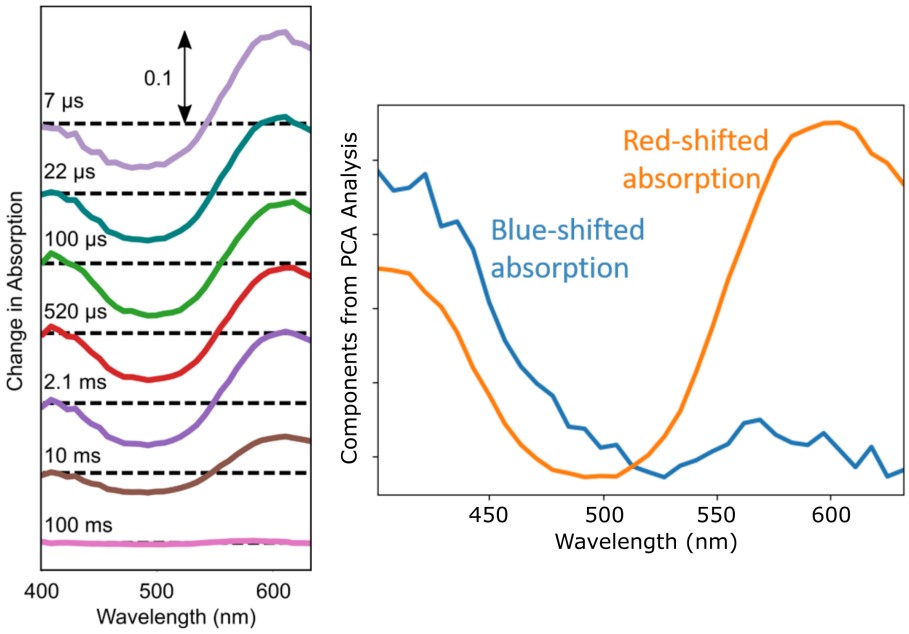

Figure 6.8: Left: difference spectra acquired by flash photolysis for monomeric PR with the E50Q mutation, measured at the indicated time delays after a 6 mJ, 532 nm excitation pulse. Right: principal component difference spectra derived from a singular value decomposition of the full difference spectra dataset. Principal component analysis (PCA) shows a red-shifted spectral component identified with the K and N intermediate states, and a blue-shifted component identified with the M intermediates [162].

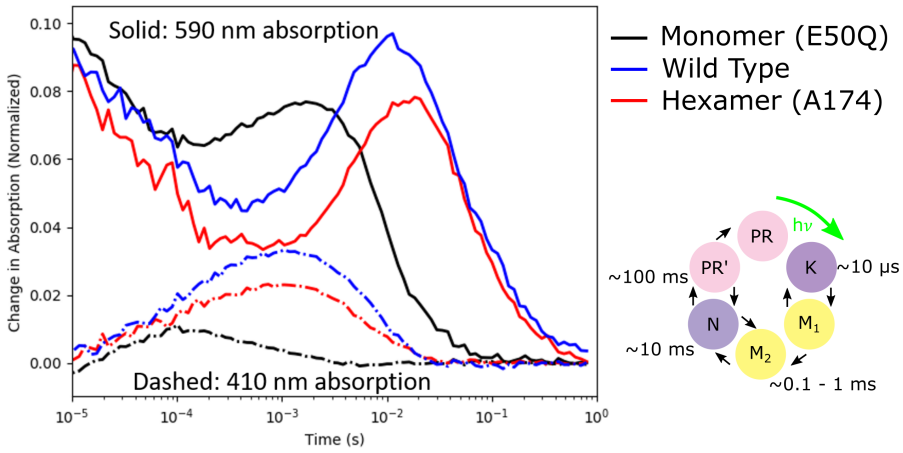

Figure 6.9: Absorption change at two wavelengths for monomer PR (with the E50Q mutation), oligomeric PR, and wild-type PR, which is a mix of monomer, dimer, and oligomer PR, in DDM detergent micelles at pH 8.5, at 295 K. Absorption change at 590 nm tracks the decay of the K state into the M states, the growth of the N state from the *M* states, and the decay of the N state to the dark states. Absorption change at 410 nm tracks the growth and decay of the M intermediates. Oligomeric PR is found to exhibit a 10× slower decay from the M states to the N state, and from the N state to the dark states, as compared to monomeric PR.

We can interpret the red-shifted component as being due to the K and N intermediates, both of which have red-shifted absorption spectra relative to "dark" state PR. Similarly, we can treat the blue-shifted component, which peaks around 400-410 nm, as being primarily associated with the M intermediates, which peaks at 405 nm.

Figure 6.9 shows the change in "fast" PR's absorption at two wavelengths, 590 nm and 410 nm, as a function of time after the arrival of a pulse with 6 mJ of energy. Three variants of "fast" PR are shown, all solubilized in DDM detergent and at pH 8.5: monomeric PR, which also had the E50Q mutation which inhibits oligomer formation, hexameric PR, which had a cysteine substituted at site 174 and an MTSL spin label attached, and "wild type" PR, which consists predominantly of hexamers with some dimers

and monomers mixed in. For the monomer and hexamer PR samples, fast protein liquid chromatography (FPLC) was used to isolate only the desired oligomeric populations.

A pulse of green light initiates the PR photocycle, the first step of which is the K intermediate, corresponding to an all-*trans* to 13-*cis* isomerization of the retinal chromophore [162]. Isomerization occurs within ∼10 ps [171], much faster than the length of the green excitation pulse, and is accompanied by a red-shift in PR's absorption spectrum. The absorption at 590 nm is initially increased above absorption in the dark state, consistent with the presence of the K intermediate.

The K intermediate decays to the M intermediates in the time it takes for the retinal Schiff base to give up a proton to the primary proton acceptor, an aspartic acid at residue 97. The M intermediates have a blue-shifted absorption peak around 405 nm. In the time-resolved absorption data shown in Figure 6.9, the 590 nm absorption is decaying in the beginning of the detection window, while the absorption at 410 nm, which is initially unchanged from the absorption in the dark state, begins to increase over the first 100 μs. In monomeric PR, the absorption change at 410 nm peaks at around 100 μs after photoexcitation and then begins to decay, accompanied by an increase in absorption at 590 nm as the M intermediates decay to the N intermediate, which corresponds to a reprotonated retinal Schiff base. In hexameric PR, absorption at 410 nm continues to rise, peaking after around 1 ms after the excitation pulse. The subsequent increase in the 590 nm absorption is similarly delayed. The peak and then the decay of the 590 nm absorption corresponds to the N intermediate transitioning to the PR' intermediate,

which occurrs as the retinal undergoing isomerization from 13-*cis* to all-*trans*. PR' is spectrally indistinct from the PR dark state, so no further changes in absorption are recorded.

Generally, hexameric "fast" PR exhibited slower photocycle kinetics than monomeric PR. Wild type PR, which exists in a mix of oligomer states, exhibits kinetics similar to hexameric PR, but with slightly shortened lifetimes in each photointermediate.

6.4 Correlating Photointermediates with Protein Conformational Changes

Two experimental techniques, time-resolved 240 GHz EPR with light activation and time-resolved optical spectroscopy, have been developed to study PR in the Sherwin lab. In this section, these techniques are applied together to investigate how conformational changes, as reported by time-resolved EPR, correlate with absorption changes as reported by optical spectroscopy. The improved spectral resolution of high-field EPR is used to perform time-resolved EPR spectroscopy on native, "fast" PR for the first time.

6.4.1 "Slow" PR: Tracking Absorption Change

Figure 6.10 shows the EPR lineshape, and the optical absorption spectrum, of hexameric "slow" PR labeled at site 174 with MTSL, in the dark and under CW illumination by light from a 514 nm diode laser. In Section 6.3.1, the light-activated lineshape was

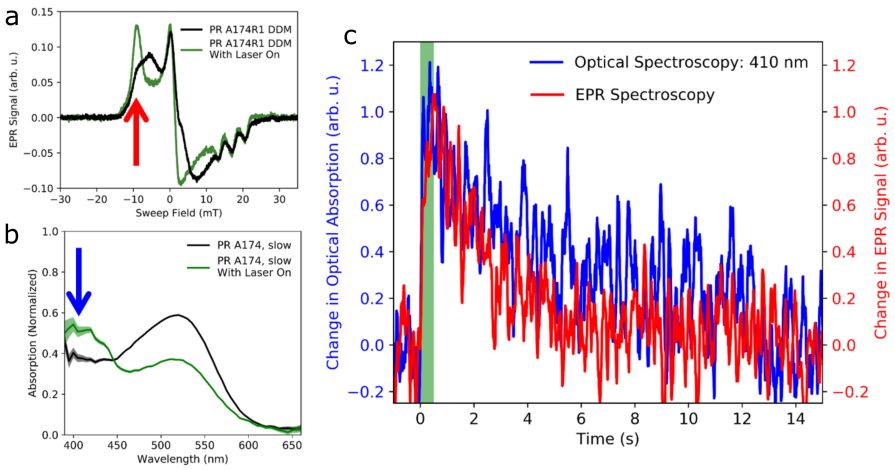

Figure 6.10: **a** 240 GHz EPR lineshape for hexameric "slow" (E108Q) PR in DDM detergent micelles labeled at site 174 with MTSL (reproduced from Figure 6.4). **b** Optical absorption spectroscopy of hexameric "slow" (E108Q) PR in DDM detergent micelles labeled at site 174 with MTSL, under CW illumination from an 18 mW 514 nm diode laser (green trace) and without green laser light (black). Under CW light-activation, PR shows decreased absorption at the peak of the "dark" absorption spectrum, and increased absorption at wavelengths where M intermediates absorb most strongly. (Conditions: pH 8.5, 295 K) **c** Time-resolved EPR spectroscopy (in red) together with time-resolved measurements of the change in 410 nm absorption (in blue) for oligomeric PR in DDM detergent micelles. Excitation was initiated by a 0.5 s pulse of 514 nm light (shown in green). EPR tracks conformational changes, while absorption spectroscopy reports on PR photointermediates. (Conditions: pH 8.5, 295 K for optical measurements, 297 K for EPR measurements).

discussed, and the change in the EPR lineshape was interpreted as arising from a conformation change which restricts the motion of the spin label in the light-active state. The light-activated absorption spectrum exhibits a decreased absorption across much of the spectrum, except for the portion of the spectrum below 450 nm, where absorption is dramatically increased. This blue-shifted absorption is consistent with the M photointermediates, which correspond to the deprotonated retinal Schiff base. No evidence of red-shifted K or N photointermediates are observed.

From the absorption spectrum acquired under constant illumination, we can conclude that photoexcitation driven by the 514 nm laser shifts the "slow" E108Q PR mutant population equilibrium from being dominated by the "dark" state to being dominated by the M intermediates. The M intermediates decay to the N intermediates over the course of seconds, whereupon the photocycle proceeds as normal to the PR' and "dark" PR states. With a constant flux of 514 nm photons, PR in the "dark" state can then be re-excited, decay to the M intermediates, and once again remain in the M intermediate for an extended period of time. The M to N transition is apparently the rate-limiting step in the "slow" E108Q PR photocycle.

With this result from optical absorption spectroscopy, we can briefly return to consider the implications this has for our interpretation of the light-induced CW lineshape change. The EPR lineshape under CW illumination reveals a shift in the equilibrium PR conformation detected by a change in the spin-label mobility. This conformational change is apparently associated with the deprotonated retinal Schiff base, since both the

conformationally modified state and the M intermediate are over-populated under CW illumination.

Next, the decay of the light-activated state back to the dark state was studied for "slow" E108Q PR with time-resolved optical spectroscopy. Figure 6.10 shows both the optical response measured at 410 nm and the EPR signal change caused by a 0.5 s pulse of 514 nm light. The time-resolved EPR lineshape change and the time-resolved absorption change are plotted simultaneously, and show the protein decaying from the respective excited states to the respective dark states over a similar timescale of many seconds.

6.4.2 "Fast" PR: Flash Photolysis

Figure 6.11 shows CW EPR lineshape measurements of hexameric "fast" PR spin-labeled at site 174 with MTSL in the dark and under light activation. It has been challenging to perform time-resolved EPR on "fast," non-E108Q PR, due to the much shorter timescales associated with the native PR photocycle, which is a factor of 10-100 faster, with a M intermediate lifetime 100-1000 times shorter. Despite the relatively poor signal to noise as compared to Figure 6.4, a clear light-induced lineshape change of similar character to the change seen wiht E108Q PR is observed. Specifically, the light-activated "fast" PR spectrum exhibits a shoulder-like feature on the low-field side of the lineshape, which is similar to, but less proncounced than, the shoulder observed in light-activated "slow" PR spectra.

Figure 6.11 also shows the result of optical absorption spectroscopy performed on

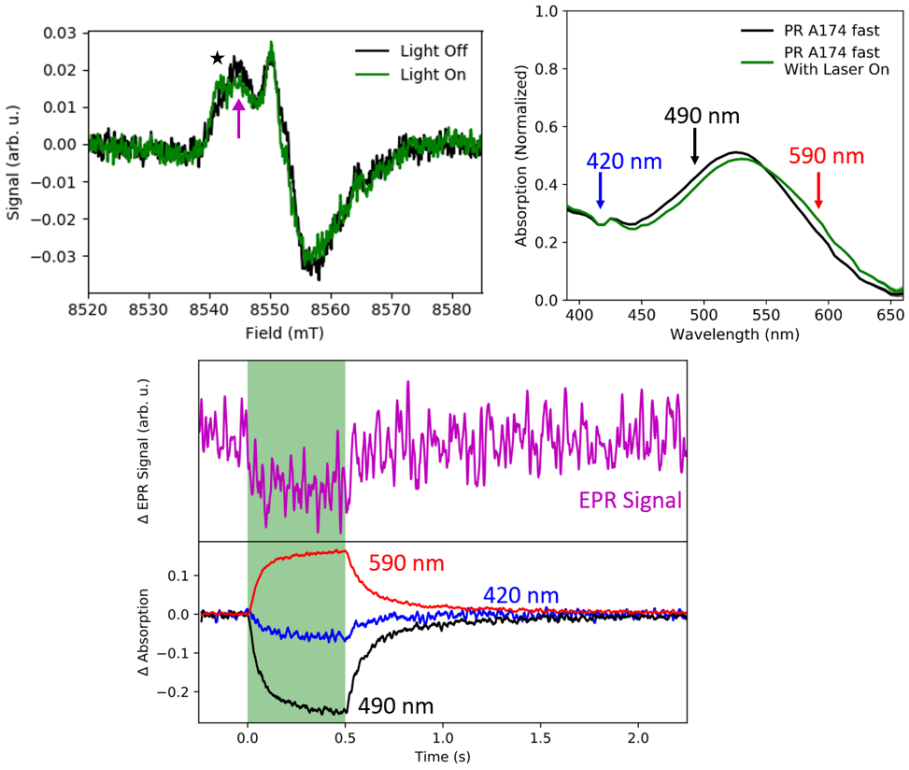

Figure 6.11: Top left: 240 GHz EPR lineshape of hexameric "fast" (without the E108Q mutation) PR in DDM detergent micelles labeled at site 174 with MTSL, in the dark (black) and under CW illumination from a 514 nm diode laser (green). Black star highlights the low-field shoulder which appears under light-activation. Arrow indicates the field position where time-resolved EPR measurements were performed. (Conditions: pH 8.5, 289 K) Top right: optical absorption spectroscopy of oligomeric "fast" PR in DDM detergent micelles under CW illumination from an 18 mW 514 nm diode laser (green trace) and without green laser light (black). Under CW light-activation, fast PR shows increased red-shifted absorption and decreased absorption at the peak of the "dark" absorption spectrum, with little change observed in the blue (around 410 nm) where M intermediates absorb most strongly, evidence that under CW illumination, for fast PR there is a sizable population in the N state. Arrows indicate wavelengths where time-resolved absorption spectroscopy was performed. (Conditions: pH 8.5, 295 K) Bottom: comparison of time-resolved EPR signal to time-resolved optical absorption change. Timescale of EPR signal change matches timescale of absorption change at all wavelengths.

"fast" PR. In contrast to "slow" PR, the absorption of "fast" PR is dominated by an overall red-shift. This red-shift can be understood by considering the PR photocycle as characterized by flash photolysis (Figure 6.9, and [162]. The slowest step in the "fast," native PR photocycle which is associated with an absorption change is the N to PR' transition. The transition from PR' to PR is even slower, with these two states having identical absorption spectra. Therefore, the N to PR' and the PR' to PR transitions become rate-limiting under CW illumination, and the population equilibrium shifts towards a combination of red-shifted N intermediates and PR'. This situation is in marked contrast to "slow" PR, where the rate-limiting step was the transition from the M to the N intermediates.

Time-resolved EPR lineshape measurements and time-resolved absorption spectroscopy were performed on "fast" PR samples, with results shown in Figure 6.11. The change in the EPR lineshape caused by a 0.5 ns pulse of 514 nm light, measured at a constant field position indicated by the magenta arrow, is plotted together with the change in absorption as measured at three different wavelengths: 590 nm, 490 nm, and 420 nm. At 590 nm, absorption increases as photoexcitation begins, while at 490 nm and 420 nm, absorption decreases, consistent with the overall red-shift of the absorption due to a sizable N state population. The EPR signal measured at the indicated field position undergoes a change upon light activation as well, which occurs on a timescale which matches that of the optical signals.

When the laser pulse turns off, absorption is seen to decay back to the "dark" spec-

trum over the course of ∼1 s. The EPR signal also decays back to the dark state, and though the signal to noise is too poor to conclusively determine the timescale of the decay, it appears that the EPR signal returns to the dark state faster than the absorption signal. This discrepancy is consistent with a picture where the bulk of the conformational changes reported by EPR taking place during the M intermediates, which are constantly decaying to the N intermediate which subsequently dominates the observed absorption change.

6.5 Going Forward

Instrumentation and methods development has enabled time-resolved high-field EPR lineshape measurements, as well as time-resolved optical absorption spectroscopy. In this chapter, these two techniques were used, together with site-directed spin-labeling with MTSL spin labels, to investigate correlations between light-induced conformational changes and PR photointermediates. Additionally, time-resolved EPR of "fast" native PR was reported.

The evidence presented here supports the hypothesis that conformational changes are predominantly associated with the M intermediates in both "slow" E108Q and "fast" native PR. However, there are many questions left unanswered. In particular, poor signal to noise made conclusively determining whether or not EPR lineshape changes occur with specific photointermediates difficult, especially for "fast" PR.

One approach moving forward will be to improve the signal to noise, and the time

resolution, available to time-resolved EPR. This could be accomplished by constructing sample holders with a larger surface area to take advantage of larger sample volumes while keeping the sample thickness thin, or by designing a modest-Q resonator structure to boost the EPR sensitivity. In particular, it has been recently shown that photonic bandgap resonators can be used to dramatically improve EPR sensitivity at high field, even when working with lossy, aqueous samples [160].

Another approach will be to move away from nitroxide spin labels, and to turn instead to Gd^{3+} spin labels with the aim of measuring time-resolved distance changes. Having information about distanes would be transformative in terms of the science which could be accomplished. In this study, lineshape changes due to restricted label mobility were used as a proxy for tracking protein conformational changes. Having access to real distance changes between different parts of a protein would remove any ambiguity about the origin of the light-activated lineshape change, and could be used to map out in three dimensions the conformational changes which take place.

Finally, measurement techniques which better leverage the spectral and temporal resolution of high-field EPR can be developed, with the hope of performing measurements using current hardware and with the currently available PR mutants. The last section of this chapter will be dedicated to one such technique, which relies on modulating absorption and/or conformational changes and using lock-in detection to study quickly-decaying photointermediates even when time-resolved changes are poorly resolved.

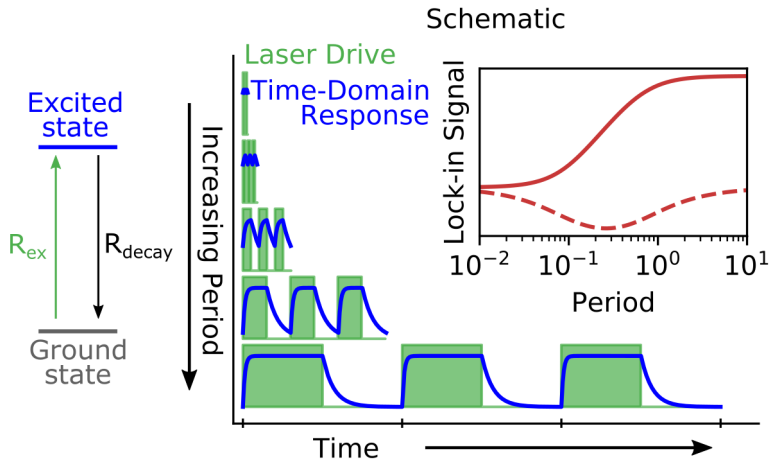

Figure 6.12: Schematic of laser modulation experiment, presented in the context of a two-level system shown to the left, where the laser drives population from the ground to the excited state with rate R_{ex} and the excited state decays to the ground state with rate R_{decay}. The laser is pulsed in a square wave (shown in green), and the excited state population change (shown in blue) is recorded by a lock-in amplifier as a function of period (shown in maroon, where the solid and dashed lines are the in-phase and quadrature signals, respectively). When the period is short compared to the rates of excitation and decay, the lock-in response is small. As the period decreases, the response increases.

6.6 New technique: Laser Modulation Experiments

Figure 6.12 shows a schematic illustrating an experiment which can be implemented in our 240 GHz EPR spectrometer with the currently existing hardware. A low-power laser directed at the sample position and pulsed in a square wave drives conformational changes in PR which depend on the rate of excitation, and on the period of the square wave drive. The response of the PR system to the periodic drive can be recorded with a lock-in amplifier, which captures both the amplitude and the phase of the response. If the period of the drive is much shorter than the relaxation time of the conformational changes, then the PR ensemble will be driven to an equilibrium where the difference in

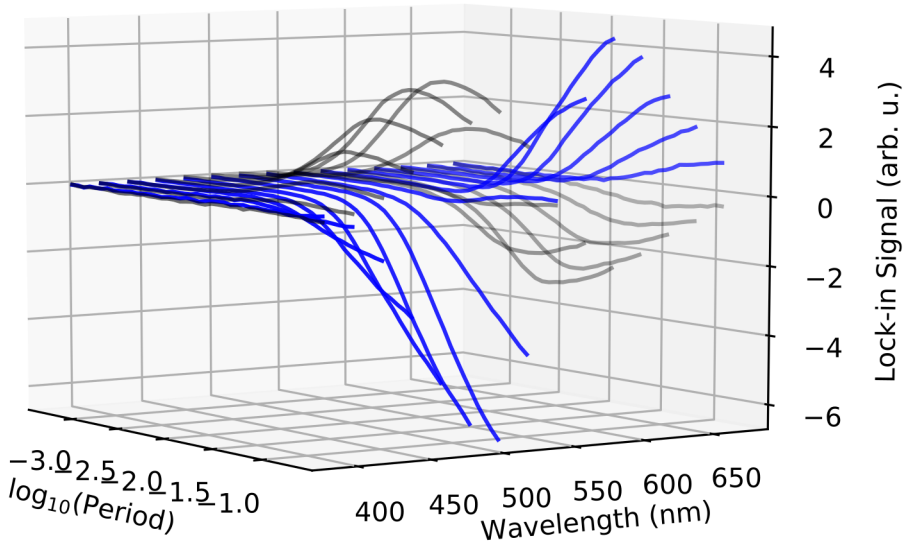

Figure 6.13: In-phase (blue) and quadrature (black) lock-in signals measured with a lock-in amplifier as a function of laser modulation period, measured every 20 nm between 390 nm and 650 nm, measured for monomeric (E50Q) "fast" PR in DDM detergent micelles, at pH 8.5, 295 K.

the response over one drive period is small. This is illustrated in Figure 6.12, in the context of a simple two-level system with an analytical solution for the excited state population as a function of time (as shown in Appendix A.2.5).

If the drive period is long compared to the relaxation time of the conformation changes, then the PR ensemble will respond in phase with the drive. In the intermediate regime, the response will be partially out of phase, with an amplitude that is sensitive to the excitation and decay rates and to the drive period.

Optical absorption measurements were carried out with laser modulation using the optical absorption instrument (Figure 6.6). The excitation light came from a 514 nm, 18 mW diode laser periodically modulated by a TTL pulse generated by a lock-in amplifier (SRS 830). The absorption change under a periodic laser drive was recorded by coupling

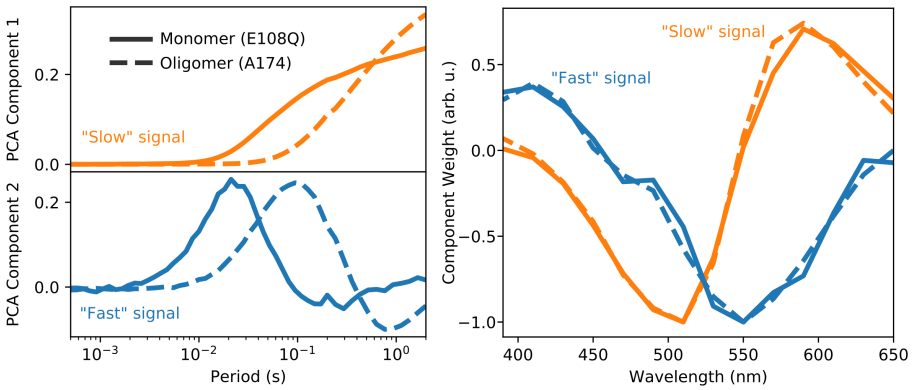

Figure 6.14: Left: first (top) and second (bottom) principal components from a principal component analysis (PCA) of the lock-in detected laser modulation experiment performed as a function of laser modulation period, and measured every 20 nm between 390 nm and 650 nm, for monomeric (E50Q) fast PR (solid lines) and for oligomeric (A174) fast PR, in DDM detergent micelles (pH 8.5, 295 K). For simplicity, only the in-phase signal is plotted. PCA analysis applied to the laser modulation technique identifies a "slow" signal maximized for longer modulation periods and a "fast" signal, which peaks for sorter modulation periods. Right: wavelength dependence of the "slow" and "fast" components for fast monomeric (solid lines) and fast hexameric (dashed lines) PR. The "slow" and "fast" components agree well with the wavelength dependence of the red-shifted and blue-shifted difference absorption signals identified by flash photolysis (Figure 6.8).

the output of the PMT to a preamplifier (SR 560) and then to a lock-in amplifier (SRS 830).

Figure 6.13 shows the in-phase and quadrature response recorded as a function of laser modulation period for wavelengths between 390 and 650 nm, recorded in steps of 20 nm, for monomeric E50Q "fast" PR in DDM detergent. The pulsed drive period was varied from 500 μs to 2 s. When the drive period is short compared to the timescale of the photocycle, the response was minimal. As the drive period was lengthened, the response increased in amplitude, with both an in-phase component and an out-of-phase component.

Principal component analysis of the lock-in response as a function of drive period was carried out for the data shown in Figure 6.13. Results of the PCA are presented in Figure 6.14. PCA revealed a dominant "slow" response, and a secondary "fast" response. The two principle responses can be interpreted by considering the weights of the "slow" and "fast" components at different wavelengths, as shown in Figure 6.14. The "slow" and "fast" component weights qualitatively agree with the red-shifted and blue-shifted principal components, respectively, derived from PCA of the difference spectra generated by flash photolysis as shown in Figure 6.8. This agreement suggests an interpretation where the "slow" component is identified with the red-shifted N photointermediate, which appears late in the PR photocycle, and the "fast" component is identified with the blue-shifted M intermediates which appear earlier in the PR photocycle.

Figure 6.14 further shows the results of optical absorption experiments with laser modulation carried out under the same conditions for hexameric "fast" PR. PCA again revealed "slow" and "fast" components, with the same weights as a function of wavelength, but each component appeared for longer drive periods than the corresponding component in monomeric "fast" PR. This is consistent with the time-domain flash photolysis data shown in Figure 6.9, and with established results [176], which show that hexameric PR exhibits slower photocycle kinetics.

No third component corresponding to a K intermediate was observed. Likely this is due the rapid decay of the K intermediate, which results in no significant K state population under low-power laser drive.

Laser modulation experiments can be straightforwardly implemented with EPR detection, as they do not rely on fast time resolution and they exploit the power of lock-in detection to improve signal to noise. Comparing the EPR response under a periodic laser drive with the optical absorption change as reported here will enable correlations between protein conformational changes and the PR photocycle to be more carefully explored.

6.7 Outlook

Time-resolved EPR at 240 GHz together with site-directed spin-labeling can be a powerful tool for studying protein conformational changes. With nitroxide spin-labels, conformation changes can be detected if they result in changes to the local environment seen by a spin-label. High-field EPR provides increased spectral resolution over low-field EPR, resulting in an EPR lineshape that is can be more sensitive to small changes in label mobility.

Moving forward, time-resolved EPR with Gd^{3+} spin-labels offers the promise of time-resolved distance measurements, something that is impossible with nitroxide spin labels for inter-spin distances longer than $\sim$1.8 nm. PR labeled with pairs of Gd^{3+} spin labels could be used to measure pair-wise distance changes across different parts of the protein, so that a full "film" of PR's motion can be recorded.

Distance changes could either be recorded using a laser modulation technique, as discussed in Section 6.6, or, more ambitiously, by time-resolved Fourier transform EPR of the Gd^{3+} central transition as demonstrated in Chapter 5 with FEL-EPR. Performing

echo-detected Fourier transform EPR of Gd^{3+}-labeled PR will be experimentally challenging, and will require a further reduction in experimental deadtime, which is currently limited in FEL-EPR experiments to 50 ns for echo experiments with phase cycling [86]. However, the advantages of this technique are enormous. The entire central-transition lineshape can be recorded in a single experiment using FT-EPR, allowing for broadening due to dipolar coupling to be resolved across the entire line. Furthermore, spin-echo experiments take just a few 100s of ns to perform, and so provide superior time resolution to time-resolved CW EPR.

Appendix A

Experiments and Methods

A.1 240 GHz EPR Spectrometer

EPR experiments discussed in this dissertation were performed on a home-built 240 GHz EPR spectrometer at UCSB. The EPR spectrometer can operate in high-power pulsed mode using the UCSB mm-wave free electron laser (FEL), or in low-power CW or pulsed mode with a 240 GHz solid-state microwave source. FEL-powered EPR results are presented in Chapters 2, 3, and 5. Results from low-power EPR using the solid-state microwave source are presented in Chapters 2, 4, 5, and 6. FEL-powered EPR is discussed in detail in Chapter 2, and is further addressed on a practical level in Appendix B. Further details can be found elsewhere [51, 92, 56, 86]. This section discusses details particular to low-power operation.

The low-power 240 GHz EPR spectrometer was developed to complement the FEL-powered EPR spectrometer, and shares many components. The low-power spectrometer

has been described in detail elsewhere [85, 24, 25, 156], and is similar in operation to other high-field EPR spectrometers [186].

In low-power operation, 240 GHz microwaves are produced using a solid-state frequency-multiplied source (Virginia Diodes, Inc). A 15 GHz source is multiplied 16× to produce 55 mW at 240 GHz, which is coupled into free space using a corrugated microwave horn which converts a waveguide mode (WR 4.3) to a Gaussian free-space mode [187]. Microwaves are transported quasioptically via the "EPR bridge" and coupled into a 1.25 m long overmoded waveguide (Thomas Keating Inc). The waveguide is housed inside a home-build EPR probe, which is mounted inside a continuous-flow cryostat (Janis Research Company, LLC) contained in the room-temperature bore of a sweepable -12.5 to 12.5 T superconducting magnet (Oxford Instruments plc). The waveguide ends in a corrugated taper, with a final inner diameter of 5 mm. Samples are placed directly at the end of the waveguide, or slightly below the end of the waveguide, in the center of the magnetic field. Induction-mode detection is employed [31]. The spectrometer uses superheterodyne detection with a Schotky subharmonic mixer (Virginia Diodes Inc) and a home-built 10 GHz intermediate frequency (IF) stage, which is mixed down to base-band by a pair of mixers operating in quadrature. For CW-EPR measurements, lock-in detection utilizing a pair of lock-in amplifiers (SRS 830) is used. For pulsed EPR measurements, the signal is digitized by a fast digitizer (National instruments PXIe-5186).

240 GHz power delivered to the sample can be controlled through a voltage-controlled attenuator build into the solid-state source ("user controlled attenuation"), or by a pair

of crossed wire grid polarizers.

Temperature at the sample position can be controlled continuously between 2.3 K and 300 K, and between 1.5 K and 2.3 K in "batch" mode. For temperatures between 4.2 K and room temperature, the cryostat can either be operated under atmospheric pressure or under vacuum. For operation between 2.3 K and 4.2 K, a rotary vain pump can be used to reduce the pressure on the sample space. Operation between 1.5 K and 2.3 K is achieved in "batch" mode, a three-step process where 1) the transfer line's needle valve is opened fully while the cryostat is pumped, 2) the cryostat is allowed to fill with liquid helium for $\sim$ 30 minutes, and 3) the needle valve is closed, while the pump is still on. Temperatures as low as 1.5 K can be maintained for $\sim$ 1 hour, until all liquid helium in the cryostat has evaporated. Sample temperature is recorded with a Cernox temperature sensor (Lakeshore Cryogenics Inc) mounted to the waveguide taper just above the sample position. Cryostat temperature is recorded by a second sensor mounted near the heater position. This second sensor and the heater are used to control the temperature with a PID feedback optimized temperature controller (Lakeshore Cryogenics, Inc. Model 332).

CW EPR experiments are typically acquired with lock-in detection, which requires applying a small sinusoidal modulation to the magnetic field. The modulation field is produced by an AC current run through a coil, which is wrapped around the sample position. The modulation coil used to conduct all CW lineshape measurements presented in this dissertation produces a modulation sinusoidal field with a peak-to-peak amplitude of 0.92 Gauss/mA.

Further details of spectrometer and magnet operation and maintenance can be found in the spectrometer user's manual. A guide to processing raw data from the CW EPR spectrometer to extract absorption spectra is given in Appendix C.

Digital Attenuator Correction

Before being mixed down to baseband, the 10 GHz signal in the IF stage passes through a digitally controlled attenuator. In practice, the attenuation value is changed from experiment to experiment. When the amplitude of the EPR signal is important, the digital attenuator must be accounted for. The digital attenuator scales the signal amplitude by an $\exp(-0.135 * DA)$ where DA is the digital attenuator setting.

A.2 Experimental Details

A.2.1 Chapter 2

Samples

$GdCl_3$ samples were prepared by dissolving $GdCl_{36}H_{20}$ (gadolinium chloride hexahydrate) in a solution of glycerol-d_8/D_2O (60:40 v:v) to a concentration of 1 mM. $GdCl_{36}H_2O$ and D_2O were purchased from Sigma Aldrich, and deuterated glycerol was purchased from Cambridge Isotope Labs.

Measurements of P1 centers were performed on a piece of type-1b diamond with a nitrogen concentration < 100 ppm, with dimensions 4.9 mm $\times$ 4.9 mm $\times$ 0.5 mm.

Trityl OX063 samples were prepared by dissolving OX063 (GE Healthcare) in D_2O to a concentration of 3.7 mM. $\sim$ 0.8 μl of solution was pipetted into a 4 mm long, rectangular cross section capillary made of borosilicate glass (VitroCom) 2 mm wide, with a 0.1 mm thick sample region and 0.1 mm thick glass walls, separated from a mirror with a dielectric spacer consisting of a layer of high resistivity silicon 190 μm thick, sandwiched between single layers of Teflon tape.

Two-pulse Hahn echo experiments with phase cycling

Two-pulse Hahn echo experiments were carried out at $\sim$8.56 T. In a two-pulse Hahn echo experiment, the each pulse is controlled by a single Nd:YAG laser synchronized to the firing of the FEL. Each laser produces a high-energy pulse which is split by beam splitters, to activate both a silicon "on" switch and two silicon "off" switches. The length of each pulse is set by variable-length laser delay lines, while the delay between the pulses is set electronically by controlling the timing of the lasers, using a trio of digital delay generators (one SRS DG645, two SRS DG535's). The second pulse is timed to coincide with the cavity dump pulse, and therefore has its power boosted relative to the first pulse by $\sim 10\times$ at the beginning of the pulse slicing optics.

The phase difference between the two pulses is determined by small differences in the optical path length through which each pulse travels. This phase difference is modified by inserting precision machined dielectric plates in pairs at Brewster's angle into the path of the first pulse.

Experiments on $GdCl_3$ were performed at cryogenic temperatures utilizing a flow

cryostat (Janis Research Co.). 14 μL of sample was placed in a cylindrical Teflon sample cup with a $\sim$3.5 mm inner diameter and a height of $\sim$5 mm, backed by a mirror, and placed at the end of the waveguide taper. Cooling was achieved with cold nitrogen gas boiled off of a liquid nitrogen reservoir. Pulse lengths were 11 ns for pulse one, and 7 ns for pulse two.

Experiments on P1 centers in diamond were performed at room temperature. The diamond sample was backed with a mirror and placed at the end of the waveguide taper. Pulse lengths were 11 ns for pulse one, and 18 ns for pulse two. Attenuation of the second pulse for quantification of instantaneous spectral diffusion was achieved by placing calibrated neutral density filters in the arm of the pulse slicer generating the second pulse.

Saturation recovery experiments with phase cycling to measure T_1

Saturation pulses were generated by replacing the "on" switch for the first pulse with a mirror allowing for a saturation pulse of 1.5-2 μs long and was turned off with silicon switches. After an electronically controlled delay, the sample magnetization was read out with a free induction decay (FID) using a 10 ns pulse, making use of the cavity dump.

Diamond P1 center lineshape and relaxation time measurements

EPR lineshape and low-power relaxation measurements were carried out on the type 1b diamond sample under the same experimental conditions, and in the same spectrometer, using a 55 mW solid-state 240 GHz source (Virginia Diodes Inc.), which is the same source as used for injection locking for FEL-EPR. Detection is the same, except that

the signal is mixed down to DC rather than to 500 MHz for digitization. The P1 center CW EPR lineshape was measured with the superconducting sweep coil, with the 240 GHz source attenuated to ~ 3 mW. Measurements of T_m with the low-power source were conducted using 55 mW of source power, with pulse lengths of 500 ns. Decay curves were fit to a single exponential.

Retrospective phase correction and phase cycling calculations

Retrospective phase correction [92] was implemented in LabView, offering real-time coherent signal averaging. Calculations of the correct set of receiver phases were carried out in python, once a set of phase cycled data had been acquired.

The least-squares method of assigning receiver phases was carried out using a Levenberg-Marquardt algorithm, implemented in python using the `curve_fit` function from the scipy library. The algorithm was provided with a suitable guess for the receiver phases in the form of the phases satisfying the following equations

$$\Delta\varphi_0 = \Delta\varphi_2 + \pi \mod 2\pi \tag{A.1a}$$

$$\Delta\varphi_1 = \Delta\varphi_3 + \pi \mod 2\pi \tag{A.1b}$$

$$\theta_0 + \Delta p\Delta\varphi_0 = \theta_1 + \Delta p(\Delta\varphi_1 + \pi) \mod 2\pi \tag{A.1c}$$

$$\theta_2 + \Delta p\Delta\varphi_2 = \theta_3 + \Delta p(\Delta\varphi_3 + \pi) \mod 2\pi \tag{A.1d}$$

in a least squares sense,

$$\vec{\theta} = (A^T A)^{-1} A^T \vec{X}_{\Delta p} \tag{A.2}$$

where

$$A = \begin{pmatrix} 1 & 0 & -1 & 0 \\ 0 & 1 & 0 & -1 \\ 1 & -1 & 0 & 0 \\ 0 & 0 & 1 & -1 \end{pmatrix} \tag{A.3a}$$

$$\vec{X}_{\Delta p} = \begin{pmatrix} \Delta p\pi \\ \Delta p\pi \\ \Delta p(\Delta\varphi_0 - \Delta\varphi_1 - \pi) \\ \Delta p(\Delta\varphi_2 - \Delta\varphi_3 - \pi) \end{pmatrix} \tag{A.3b}$$

where $\vec{\theta} = (\theta_0, \theta_1, \theta_2, \theta_3)$.

A.2.2 Chapter 3

Samples

BDPA (1,3-bisdiphenylene-2-phenylallyl) crystallized 1:1 with benzene was purchased from Sigma Aldrich and used without modification. Individual grains were selected for their small size and for their flat aspect ratio.

Nutation Experiments

Single BDPA grains were used for nutation experiments. The detuning between the resonance condition and the FEL pulse was controlled by moving the magnetic field at

constant FEL frequency. The resonance condition was determined by at four-step process, where 1) the FEL frequency and the FID frequency were observed for a short tip-angle pulse, 2) the field was moved so the FID frequency is ~ 6 MHz below the FEL frequency, 3) a nutation experiment was performed to observe the tip-angle dependent frequency shift, to determine the maximum and minimum FID frequencies, and 4) the field was moved once again so the FEL was positioned at the center point of the maximum and minimum FID frequencies. In practice, steps 3 and 4 were often iterated two to three times until step 4 yielded the result with each repetition.

Nutation experiments were performed using a single pulse "sliced" from the long FEL pulse. In a one-pulse experiment, slicing was accomplish using two Nd:YAG lasers, with the first laser (the Quanta Ray) activating a silicon "on" switch and the second laser (the Ekspla) activating two silicon "off" switches. Using two lasers to control the length of one pulse allows the pulse length to be adjusted over a wide range, limited only by the length of the FEL pulse (up to several μs).

After an experimental deadtime limited by scattered light from the FEL (typically around 70 ns for FID-detected experiments and 50 ns echo-detected experiments with phase cycling), the protection switch is activate by pulse from a Nd:YAG laser (the Litron).

Two-pulse Hahn echo and FID-detected saturation recovery experiments were performed as described in the previous section.

A.2.3 Chapter 4

Samples

Gd-DOTA was purchased from Sigma Aldrich. A stock solution was made by dissolving Gd-DOTA in D_2O (Sigma Aldrich), from which samples of varying concentration were prepared by dilution with a 60:40 (v:v) solution of glycerol-d_8 (Cambridge Isotope Labs) and D_2O.

Iodo-(Gd-PyMTA) was provided by Mian Qi, in a 3 mM stock solution which also contained the following: 5 mM F_2CCO_2H/F_3CCO_2Na, 15 mM NaCl, 120 mM H_2O. Samples of varying concentration were prepared by dilution with a 60:40 (v:v) solution of glycerol-d_8:D_2O.

Hahn Echo Decay and Saturation Recovery Experiments

Phase memory time measurements were carried out with a Hahn echo decay pulse sequence of the form $\mathrm{P1}-\tau-\mathrm{P2}-\tau-\mathrm{echo}$. Echo decay time was not found to be sensitive to the lengths of pulses P1 and P2. Gd-DOTA measurements were performed with P1 = 175 ns, P2 = 275 ns. Iodo-(Gd-PyMTA) measurements were performed with P1 = 350 ns, P2 = 350 ns, corresponding to roughly $3\pi/2$ pulses, which were empirically found to maximize the echo. T_m was found by fitting the echo decay curve $y(2\tau)$ to a single exponential function of the form

$$y(2\tau) = A \times e^{-2\tau/T_m} + C \tag{A.4}$$

Spin-lattice relaxation time measurements were carried out with a saturation-recovery sequence of the for $\mathrm{P1} - T - \mathrm{P2} - \tau - \mathrm{P3} - \tau - \mathrm{echo}$, where τ was kept fixed and T was incremented. For Gd-DOTA, saturation pulses of 200-300 μs were used, with P2 = 175 ns, $\tau = 2$ μs, and P3 = 275 ns. For iodo-(Gd-PyMTA), P1 ranged from 200-500 μs, with P2 = P3 = 350 ns, and with τ varing between 1 and 2 μs. T_1 was found by fitting the echo recovery curve to $x(T)$ to a bi-exponential function of the form

$$x(T) = A \times e^{T/T_1} + B \times e^{T/T_{SD}} + C \tag{A.5}$$

where T_{SD} is a shorter time-constant interpreted as arising from spectral diffusion.

A.2.4 Chapter 5

Samples

$GdCl_3$ samples were prepared by dissolving $GdCl_{36}H_{20}$ (gadolinium chloride hexahydrate, Sigma Aldrich) in D_2O (Sigma Aldrich) to a concentration of 300 μM.

Trityl OX063 samples were prepared as described in Appendix A.2.1.

The iodo-(Gd-PyMTA) sample was prepared as described in Appendix A.2.3. The 2.1 nm ruler molecules were synthesized by Mian Qi as described elsewhere [161] and provided as a 5 mM stock solution (also containing 37 mM NaCl, 100 mM H_2O). A 500 μM concentration ruler molecule sample was prepared by dilution of the stock with a 60:40 (v:v) solution of glycerol-d_8:D_2O.

A.2.5 Chapter 6

PR production and spin labeling

Site-directed spin labeling (SDSL) was carried out using site-directed mutagenesis to introduce or remove cystine residues at specific sites on PR. Cystine mutations form covalent bonds with the MTS linker, and are used to tether MTSL to the desired location(s) on a protein. PR has three native cystine residues, at sites 107, 156, and 175. The template gene used for protein expression, which is referred to as "wild type" in Chapter 6, had the three native cystines removed and substituted with serines, so that MTSL does not bind to PR unless further mutations are made, and had six histidine tags attached to the C-terminus. These mutations have been shown to not affect the overall function of PR [175]. A cystine residue was substituted for a native alanine at site 174 for those PR samples which were to be spin-labeled, which are referred to as "A174" in Chapter 6. Additional mutations added to some PR samples were (1) the E50Q mutation, where the glutamic acid at site 50 is substituted for a glutamate, which destabilizes PR oligomer formation [183], and (2) the E108Q mutation (referred to as "slow" PR), where the glutamic acid at site 108 which serves as the primary proton donor for the Schiff base in the PR photocycle [172, 173, 162, 174, 175] was substituted for a glutamate, which extends the lifetime of the M-intermediate state by 2-3 orders of magnitude.

Mutations were generated using standard site-directed mutagenesis techniques. The gene template for wild-type PR was modified by applying two-stage polymerase chain reaction (PCR) and then recloned into a pET26b(+) vector (Novagen). PR expression was

carried out in *E. Coli* strain BL21(DE3) cells transformed with the desired vector. Protein overexpression was induced by adding IPTG (isopropyl-β-D-thiogalactopyranoside) and retinal (Vitamin A aldehyde) to flasks of *E. Coli*. The cells were harvested by centrifugation, and PR was then separated and purified by first lysing the cells, followed by ultracenterfugation, and then solubilizing in β-D-dodecyl-maltoside (DDM) surfactants. Further purification was carried out in a metal affinity resin which selectively binds to the six histidine tags attached to the C-terminus. Unbound proteins and other debris were then washed away, and for those batches of PR which were to be spin-labaled, MTSL was added. Finally, for those measurements which required monomeric or hexameric PR, purified PR was separated into monomers and hexamers using a BioRad Duoflow FPLC.

EPR experiments were carried out on PR which was hyperconcentrated using an evaporation and rehydration technique. Solutions of PR solubilized in DDM was pipetted onto a glass slide in 2 μl drops and left to dry overnight. The resulting dried, gel-like mixture of PR and DDM was scrapped off of the slide, and rehydrated with a minimal amount ($\sim$ 2 μl) of pH 8.5 buffer.

EPR measurements of the hyperconcentrated sample pre-hydration showed rigid-limit EPR spectrum, with no changes observed under light-activation. The dark spectrum is shown in Figure A.1.

Time-Resolved Absorption Measurements

Time-resolved measurements of absorption change were performed by recording the PMT signal on an oscilloscope. Flash photolysis measurements were performed with pulses of

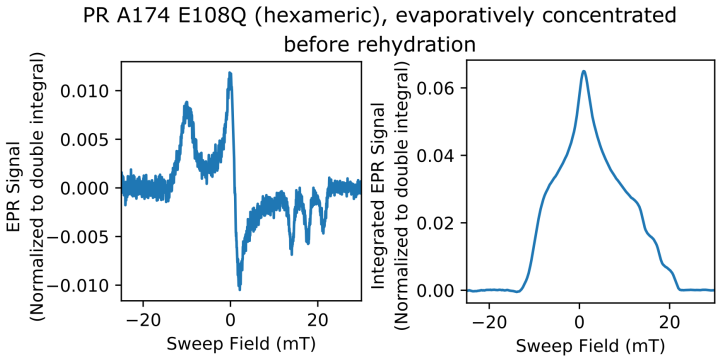

Figure A.1: Left: 240 GHz lineshape measured on evaporatively hyperconcentrated, gel-like PR sample. Sample was scraped off of a glass slide and packed into a Teflon sample bucket. Right: integrated EPR lineshape.

532 nm light from a Q-switched Nd:YAG laser (Quanta Ray), with ∼6 mJ per pulse. Detection was synchronized to the excitation pulse with a photodiode set up to detect the 532 nm pulse after it passes through the sample.

Time-resolved difference spectra as shown in Figure 6.8 were assembled as follows. Time-domain absorption data measurements acquired at a single wavelength were repeated in steps of 7 nm over the range desired range of wavelengths. At each wavelength, the absorption change $\Delta A(\lambda)$ was calculated from the change in signal intensity $\Delta I(\lambda)$ as measured by the PMT according to

$$\Delta A(\lambda) = -\frac{\Delta I(\lambda)}{I_0(\lambda) - I_{dark}} \tag{A.6}$$

where $I_0(\lambda)$ was the PMT signal measured for a sample containing buffer and DDM, but no PR, and I_{dark} was the PMT signal measured with the port into the monochromator blocked, so that nominally no light reaches the PMT.

The time-domain absorption change data was logarithmically sampled in post-processing,

and a dataset was assembled in the form of a matrix M where the rows were the logarithmically sampled time-domain datasets measured at different wavelengths. Absorption difference spectra were then given at particular times by the columns of M.

Principal component analysis (PCA) was carried out using singular value decomposition (SVD). The matrix M, whose columns were the difference absorption spectra, was subject to SVD giving

$$M = U\Sigma V^T \tag{A.7}$$

where Σ is a diagonal matrix of singular values, U is an orthogonal matrix whose columns are the principal components of the spectra assembled in M, and V^T is an orthogonal matrix whose rows are the "kinetic vectors" weighting the different principal components and singular values at different times.

Time-domain absorption data shown in Figure 6.9 were generated from a reconstruction of M, using only the first two principal components as shown in Figure 6.8.

Laser Modulation Experiments: Analytic Solution for Two-Level System

Consider a two-level system like the one shown in 6.12, with a ground state G and an excited state E, and with an intrinsic rate of population decay from the excited state to the ground state R_{decay}. When a laser shines on this two-level system in a square wave with period τ, photoexcitation drives population from the ground to the excited state

with a rate R_{ex}. This system is governed by a pair of coupled rate equations

$$\frac{d}{dt}E(t) = -R_{decay}E(t) + R_{ex}(t)G(t) \tag{A.8a}$$

$$\frac{d}{dt}G(t) = R_{decay}E(t) - R_{ex}(t)G(t) \tag{A.8b}$$

where $R_{ex}(t)$ is a time-dependent rate of excitation given by

$$R_{ex}(t) = \begin{cases} R_{ex} & n\tau \leq t < (n+1/2)\tau \\ 0 & (n+1/2)\tau \leq t < (n+1)\tau \end{cases} \qquad n = 1, 2, 3, \ldots \tag{A.9}$$

where $R_{ex}(t)$ is periodic with period τ, $R_{ex}(t) = R_{ex}(t+\tau)$.

Equation A.8 conserves the total population, so that $G(t) + E(t) = 1$. Using this conservation law, Equation A.8 can be written as a first-order linear differential equation in terms of the excited state only

$$\frac{d}{dt}E(t) + (R_{decay} + R_{ex}(t))E(t) = R_{ex}(t) \tag{A.10}$$

This equation admits an analytical solution based on an integrating factor $U(t)$,

$$U(t) = \exp\left(\int (R_{decay} + R_{ex}(t))dt\right) \tag{A.11}$$

so that $E(t)$ is given in terms of $E(t_0)$ evaluated at any other time t_0 by

$$E(t) = \frac{1}{U(t)}\int_{t_0}^{t} U(x)R_{ex}(x)dx + \frac{U(t_0)E(t_0)}{U(t)} \tag{A.12}$$

Enforcing periodicity on $E(t)$, so that $E(t) = E(t+\tau)$, the excited state $E(t)$ is given over the course of one period by

$$E(t) = \begin{cases} \frac{R_{ex}}{R_{ex}+R_{decay}} + C_0 e^{-(R_{decay}+R_{ex})t} & 0 \leq t < \tau/2 \\ C_1 e^{-R_{decay}(t-\tau/2)} & \tau/2 \leq t < \tau \end{cases} \tag{A.13}$$

where

$$C_0 = -\frac{R_{ex}}{R_{ex} + R_{decay}} \frac{1 - e^{R_{decay}\tau/2}}{1 - e^{-R_{decay}\tau - R_{ex}\tau/2}} \tag{A.14a}$$

$$C_1 = \frac{R_{ex}}{R_{ex} + R_{decay}} + C_0 e^{-(R_{decay}+R_{ex})\tau/2} \tag{A.14b}$$

Lock-in detection measures harmonics of the time-domain signal which can be calculated from Equation A.13 by taking Fourier expansion. The in-phase and quadrature harmonics a_n and b_n are given by

$$a_n = \frac{2}{\tau} \int_0^\tau E(t) \sin\left(\frac{2\pi n}{\tau} t\right) dt \tag{A.15a}$$

$$b_n = \frac{2}{\tau} \int_0^\tau E(t) \cos\left(\frac{2\pi n}{\tau} t\right) dt \tag{A.15b}$$

$$\tag{A.15c}$$

Typically the first harmonic is measured with lock-in detection, which corresponds to taking $n = 1$.

Appendix B

Practical FEL-EPR

In this Appendix I attempt to give a practical overview to performing FEL-EPR experiments.

B.1 UCSB mm-wave FEL

FEL-EPR is performed with the UCSB mm-wave free electron laser. FEL-EPR is carried out at 240 GHz, at the low end of the mm-wave FEL's frequency range. The mm-wave FEL is one of two FELs currently operating at the UCSB free electron laser facility in the Institute for Terahertz Science and Technology. The mm-wave FEL covers the frequency range between $\sim$ 200 GHz and $\sim$ 700 GHz. The second FEL, the far infrared (FIR) FEL, produces radiation at frequencies between 1 THz and 4.5 THz. A third FEL is under development which is optimized for the lower frequencies, for operation between 150 GHz and $\sim$ 500 GHz.

A FEL produces electromagnetic radiation through interactions between a relativistic electron beam and a periodically modulated magnetic field. As the relativistic electron beam is steered through the region of periodically modulated magnetic field, the electrons oscillate and produce synchrotron radiation at a frequency that depends on the beam energy, the magnetic field strength, and the magnetic field periodicity. The interaction region is called an "undulator." In practice, we control the radiation frequency by changing the electron beam energy while leaving the magnetic field strength and periodicity constant. The electron beam energy is set by varying the electrostatic potential, also called the terminal voltage, across which it is excited.

The UCSB FELs operate off of a relativistic electron beam supplied by a 6 MV linear electrostatic accelerator. Electrons are produced by thermionic emission off of a hot cathode, are accelerated across the high electrostatic potential, and are steered through an ultra-high vacuum (UHV) beamline to one of two currently operating undulators. The electrostatic accelerator produces a "quasi-DC" electron beam which lasts for several microseconds, which can in turn produce coherent pulses of sub-THz and THz radiation many microsecond long. After passing through the undulator, the electron beam is decelerated against the same electrostatic potential which was used to produce it, the electrons are recollected in a "collector." In this way, the electron beam is continuously circulated and the high electrostatic potential difference across the linear accelerator is maintained even for high electron beam currents. Maintaining efficient electron beam recirculation is of paramount importance for stable FEL operation.

Every FEL experiment begins with optimizing the alignment of the electron beam for the terminal voltage required to produce the desired frequency of radiation. This process is called "tuning the FEL." The electron beam position and shape are controlled by a series of electromagnets which provide steering (dipole magnets and steering coils) and focusing (quadrupole magnets). Changing the terminal voltage necessitates changing the currents in all of the electromagnets which make up the electron beam optics. Fortunately, we have a system which saves and loads experimental settings which makes most of the tuning process automatic. At the start of an experiment, the user loads a saved configuration for their desired terminal voltage, which sets the electromagnet currents and other experimental parameters to the saved values. A general discussion of FEL tuning is well beyond the scope of this Appendix. Suffice to say, there are a great many parameters which are important for FEL operation, which need to be considered by all users. Going forward, I will try to focus only on the particular details which are unique for FEL-EPR.

B.1.1 Tuning for FEL Operation at 240 GHz

240 GHz radiation is produced from the mm-wave FEL when the terminal voltage is set to 2.93 MV. The electron beam is much more "forgiving" at this terminal voltage than at higher voltages, and because the mm-wave FEL has very high gain at 240 GHz, it is quite easy to get the FEL to lase. Nevertheless, it is still important to be cautious when running the FEL. It is always best to work in teams of two or more, so that one person

can keep an eye on the FEL at all times.

When tuning the FEL, here are some general guidelines to follow (or break, at your peril):

- One small adjustment far upstream is better than many adjustments downstream
- Given the choice between increasing the current in component A and decreasing the current in component B, choose to decrease the current in component B.
- Avoid changing the polarity of a steering coils when possible.
- Avoid changing the polarity of a quadrupole at all, without a very very good reason.
- Never change the currents of any of the magnets in the achromatic bends.

Here is a rough guide to tuning the FEL for 240 GHz operation

1. Make sure the beam block is in, and that the pulse length is set to $\sim$1.5 μs.
2. Look at the beam coming out of the accelerator. Make sure it is in the correct place, and is the correct size and shape.
3. Look at the beam just after the first bend. Look at the current monitor in the first bend. Are you getting the correct current out?[1] If not, adjust the beam position with first steering coil inside the accelerator (and the second if necessary) until you are getting the correct current out.

[1] As of Spring 2019, we typically operated at a beam current of 1.2 A.

4. Repeat Step 3 for each for each bend, making sure that you aren't loosing current in the beamline. By the time you get to the switchyard before the undulator, you may need to play with the focus a bit as well. Your goal here is just to get all of the current through the undulator. At this stage, don't worry about the last current monitor. You are now tuning to optimize beam current and position.

5. Adjust the beam position so it passes through the center of all quadrupoles. This is best done sequentially, starting from the first pair of quadrupoles after the bend. Look at a screen downstream from the quadrupole in question. Move the beam around until it passes through the quadrupole in such a way that changing the current in the quadrupole changes the beam shape but not the beam position. Once the beam is passing through the center of each quadrupole, try not to make any further up-stream changes to steering magnets. Stop when you get to the undulator, don't try to adjust the quadrupoles after the undulator just yet.

6. Once the beam is aligned through all quadrupoles before the undulator, look at the last screen and current monitor. Adjust the beam until the you get all of the current to the last current monitor, and the beam spot looks ok on the screen.

7. Shorten the electron beam to $\sim$ 800 ns, remove the beam block, and pull up the CP signal. Now, you are tuning for recirculation. Make adjustments, starting at the decelerator and moving in the upstream direction, to improve recirculation. As recirculation improves, lengthen the electron beam pulse.

8. Once recirculation is $\sim 95\%$ or higher, start looking for signs of lasing.

9. Once you see lasing, tune the electron beam to try to get lasing to start as early as possible, while maintaining good recirculation. Now, you are tuning for lasing.

10. Once you are happy with lasing, measure the power coming out of the FEL. Are you happy with the power? If not, position yourself so you can see both the real-time power reading at your detector and the FEL control system. Tune the beam to maximize power. You are now tuning for power.

B.2 FEL Outcoupler Options

Radiation can be coupled out of the FEL in two ways: through the silicon coupler, or through the hole coupler. The silicon coupler also provides the option of cavity dumping the FEL. Figure B.1 summarizes the modes of operation.

For FEL-EPR, the silicon coupler is usually the right choice. Typically in a two-pulse EPR experiment, we want to place the second pulse inside the cavity dump pulse to maximize the power. Additionally, firing the cavity dump stops any further lasing in the FEL cavity, which leads to a cleaner "off" at the end of the pulse sequence.

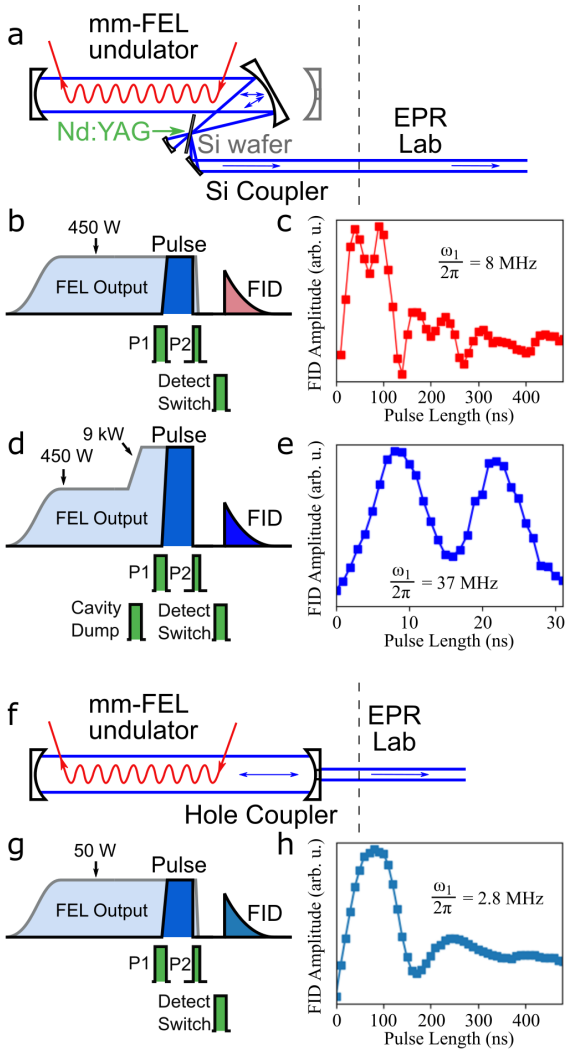

Figure B.1: **a** A 240 GHz, quasi-CW pulse generated by the mm-wave UCSB FEL is coupled out of the FEL cavity by the silicon coupler. **b** A short pulse is "sliced" from the quasi-CW pulse using light-activated silicon switches activated by 532 nm laser pulses P1 and P2, generating an FID. **c** The FID amplitude, acquired by integrating the FT-EPR lineshape, plotted as a function of pulse length is used to determine the nutation (Rabi) frequency $\omega_1/2\pi$. The silicon coupler nutates spin-1/2 electrons with $\omega_1/2\pi$ up to 8 MHz, corresponding to $B_1 = 3$ gauss in the rotating frame. When the cavity dump is activated by a Nd:YAG laser **d** the output power is boosted for the last 40 ns of the quasi-cw pulse, which results in a higher spin-1/2 nutation frequency. Rabi frequencies up to 37 MHz **e**, corresponding to $B_1 = 13$ gauss in the rotating frame, can be generated with the cavity dump. **f** The hole coupler can also be used to generate quasi-CW microwave pulses, though at 240 GHz the power is lower than the silicon coupler **g**. **h** $\omega_1/2\pi$ is typically around 2.8 MHz, corresponding to $B_1 \simeq 1$ gauss in the rotating frame.

Appendix C

How to process CW EPR Data

This is an overview of the procedure I use to process high-field CW EPR data. An example script can be found with comments in the file `phasing_step_by_step.py`, saved in my directory on the shared drive in the sub-folder `cw_data_processing_routines/Demo_Routines_with_data`. Included are example data files.

C.1 Outline

Our CW EPR experiment produces four signals: the real and imaginary (X and Y) signals from two lock-in amplifiers. These signals are labeled X1, Y1 for X and Y from lock-in 1, and X2, Y2 for X and Y from lock-in 2.

The final signal we want is the EPR absorption lineshape A (and/or the dispersion lineshape D, they are related by Kramers-Kronig relations so if you have one you have the other). A is extracted from X1, Y1, X2, Y2 in three basic steps. This document walks

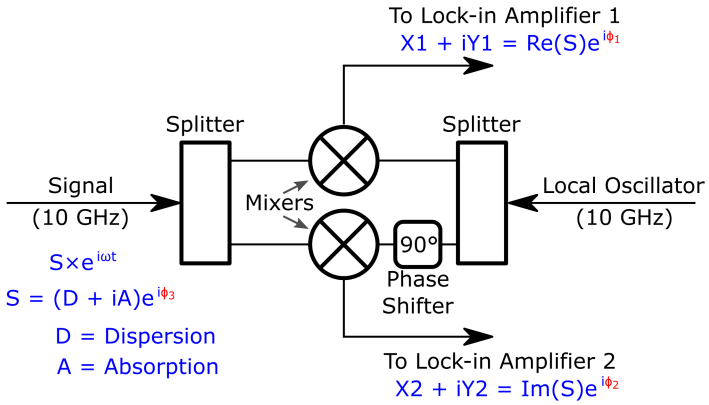

Figure C.1: Simplified signal diagram. Signal S, which has been mixed down from 240 GHz to a 10 GHz intermediate frequency, is mixed with a 10 GHz local oscillator, resulting in DC signal oscillating at the modulation frequency (not shown). Lock-in amplifiers 1 and 2 locked to the modulation frequency each record in-phase X and quadrature Y signals, for a total of 4 signals (X1, Y1, X2, Y2). The final four signals are related to signal S by two phases, ϕ_1 and ϕ_2. S is related to the absorption and dispersion signals by a third phase, ϕ_3.

through each step, with example data. Example data was taken on 11/19/2015, on a sample of type 1B diamond with many P1 centers and few NV centers.

Figure C.1 shows a simplified signal pathway. The pair of signals from each lock-in amplifier are related to the signal real and imaginary parts of ths signal S by

$$\mathrm{X1} + i\mathrm{Y1} = \mathrm{Re(S)}e^{i\phi_1} \tag{C.1a}$$

$$\mathrm{X2} + i\mathrm{Y2} = \mathrm{Im(S)}e^{i\phi_2} \tag{C.1b}$$

where ϕ_1 and ϕ_2 are phases relating to the modulation phase and the phase of the local oscillator signal.

The S is the signal which makes it to the mixers, and is itself a mixture of the

absorption and dispersion signals A and D with phase shift ϕ_3,

$$\mathrm{S} = (\mathrm{D} + \mathrm{A})e^{i\phi_3} \tag{C.2}$$

where ϕ_3 is due to a great many effects, including the phase shift due to the optical path traveled by the microwaves, any relative phase difference between transmitter and receiver, and to some degree to the behavior of electronics in the intermediate frequency stage.

The procedure to recover the absorption signal A from the output signals $\mathrm{X1}, \mathrm{Y1}, \mathrm{X2}, \mathrm{Y2}$ shown in Figure C.2 consists of the following steps:

1. Apply phase shifts θ_1, θ_2 to each pair of lock-in signals to generate new signals $\mathrm{X1}', \mathrm{Y1}', \mathrm{X2}', \mathrm{Y2}'$,

$$\mathrm{X1}' + i\mathrm{Y1}' = (\mathrm{X1} + i\mathrm{Y1})e^{-i\theta_1} = \mathrm{Re(S)}e^{i(\phi_1 - \theta_1)} \tag{C.3a}$$

$$\mathrm{X2}' + i\mathrm{Y2}' = (\mathrm{X2} + i\mathrm{Y2})e^{-i\theta_2} = \mathrm{Im(S)}e^{i(\phi_2 - \theta_2)} \tag{C.3b}$$

   where $\theta_1 = \phi_1$ and $\theta_2 = \phi_2$, so that $\mathrm{X1}' = \mathrm{Re}(S)$ and $\mathrm{X2}' = \mathrm{Im}(S)$, and $\mathrm{Y1}' = \mathrm{Y2}' = 0$. In practice this is done by applying a phase shifts to each pair of lock-in signals until the Y signals disappear. This is illustrated in Figure C.3.

   This step can either be done manually by manipulating the first two phases in `rephase.vi`, or it can be done automatically, using a procedure outlined in [188] and implemented in the Python script `lockin_phase_null.py` I wrote.

   If this step is accomplished successfully, all of the useful information contained in

the EPR signal will now be shifted into the signals, X1′ and X2′, and the Y1′ and Y2′ channels will be "nulled."

2. Perform a background subtraction on each of the two signals $\mathrm{X1}', \mathrm{X2}'$. This is typically done by fitting a polynomial to the baseline of each signal, as shown in Figure C.4.

   If you are quickly processing the data by hand using `rephase.vi`, it is safe to skip this step.

3. Apply a phase shift θ_3 to the two X′ signals, to transfer the absorption signal into one channel and the dispersion signal into the other,

$$\mathrm{D} + i\mathrm{A} = \mathrm{S}e^{-i\theta_3} = (\mathrm{X1}' + i\mathrm{X2}')e^{-i\theta_3} \tag{C.4}$$

   This is accomplished for $\theta_3 = \phi_3$. For quick processing, this step can be accomplished by manipulating the third phase in `rephase.vi`.

   Correctly choosing the phase shift θ_3 is the most difficult step in processing the data. Correctly determining the phase θ_3 is crucial to extracting the absorption and dispersion signals from the measured data. If θ_3 is chosen incorrectly, data will be miss-interpreted.

There are three approaches I have used with success to determine this last phase shift.

Method 1: fit the lineshape

The most consistent way to correctly determine the phase θ_3 is to fit the measured signal $S = X1' + iX2'$ to a model which describes the underlying spin physics, with the phase ϕ_3 included as a fit parameter. Using this method requires that you know something about the lineshape you are measuring.

I have had success implementing the fitting method when measuring Lorentzian lines, or when measuring nitroxide lineshapes in either the rigid limit or the rapid tumbling regime. A process for fitting a complex Lorentzian derivative to a measured lineshape in order to extract the phase is included in `/sherwin/BlakeWilson/cw_data_processing_routines/complex_lorentzian`.

Method 2: maximize the double integral

When you do not have a good model to describe the EPR lineshape and Method 1 does not work, the best approach is to choose the value of θ_3 which maximizes the double integral of the imaginary part of $(X1' + iX2')e^{-i\theta_3}$, since when correctly phased, the imaginary signal should be purely absorptive.

Maximizing the double integral is demonstrated in Figures C.5 and C.6.

Maximizing the double integral can be tricky in practice if the baseline is not flat, or if the signal-to-noise is not good, because the double integral is very sensitive to the baseline. Additionally, this method will in general fail if you don't capture the entire EPR signal within your experiment (for example, if the EPR signal has a broad component

which extends beyond your measurement window). For Gd^{3+}, this last requirement is problematic, since we are typically interested in measuring the central $m = -1/2 \rightarrow m = +1/2$ transition which sits on top of a number of broader transitions which form a baseline much wider than the EPR sweep coil. Luckily, for Gd^{3+} the baseline signals are slow-changing enough that they can usually be subtracted in the polynomial baseline subtraction step.

Scripts which attempt to maximize the double integral can be found in `sherwin/BlakeWilson/cw_data_processing_routines/maximize_double_integral`. This can also be accomplished by hand, by varying the phase shift θ_3 while looking at the integrated data, until the imaginary part of the integrated lineshape is absorptive.

Method 3: symmetrize

This method only works if the lineshape you are measuring is symmetric (for example, it is a Lorentzian, Gaussian, etc.). If the lineshape is symmetric, a quick and easy way to compare lineshapes is to apply a phase shift θ_3 so that the derivative lineshape is symmetric about zero, so that the maximum positive value the derivative takes is equal to the minimum negative value the derivative takes.

My Python function `Balance.py` accomplishes this, which can be found in `sherwin/BlakeWilson/cw_data_processing_routines`. This last method is fairly robust to baseline noise or drift, and to any background signals which might or might not contaminate your signal of interest, but is sensitive to any noise in the few datapoints right around the positive and negative peaks in the derivatite lineshape. This method should be used

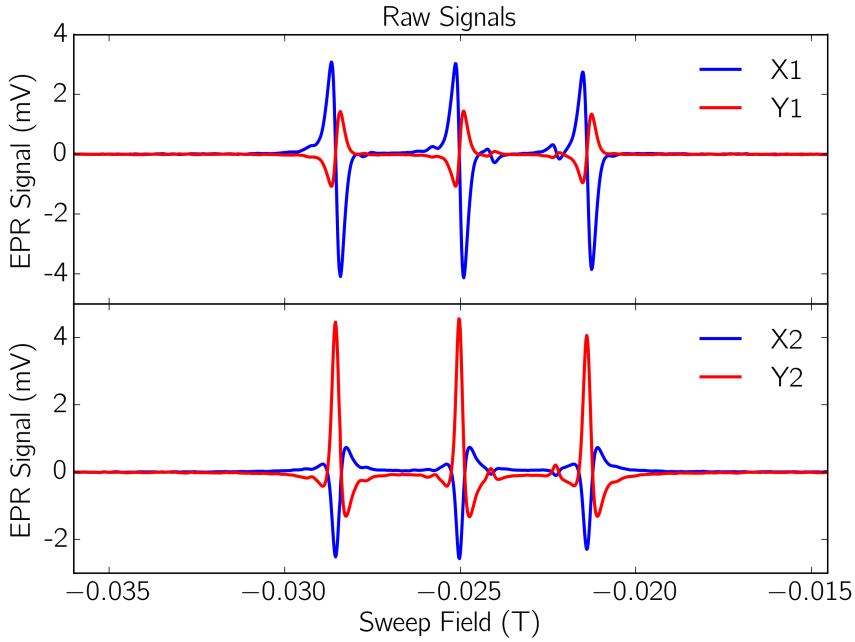

Figure C.2: Top: Raw signals from lock-in amplifier 1. Bottom: Raw Signals from lock-in amplifier 2. In-phase signals are shown in blue, quadrature signals in red.

with caution if the lineshape is not symmetric.

C.2 Data Processing

The raw data files as saved by Sweep.vi are eight column csv files, with a user-provided header that contains information about the experiment. The eight columns are the recorded Time, Field, the I and Q signals from each lock-in amplifier (labeled X1, Y1, X2, Y2), the temperature as read at the top of the probe, and the temperature as read just above the sample.

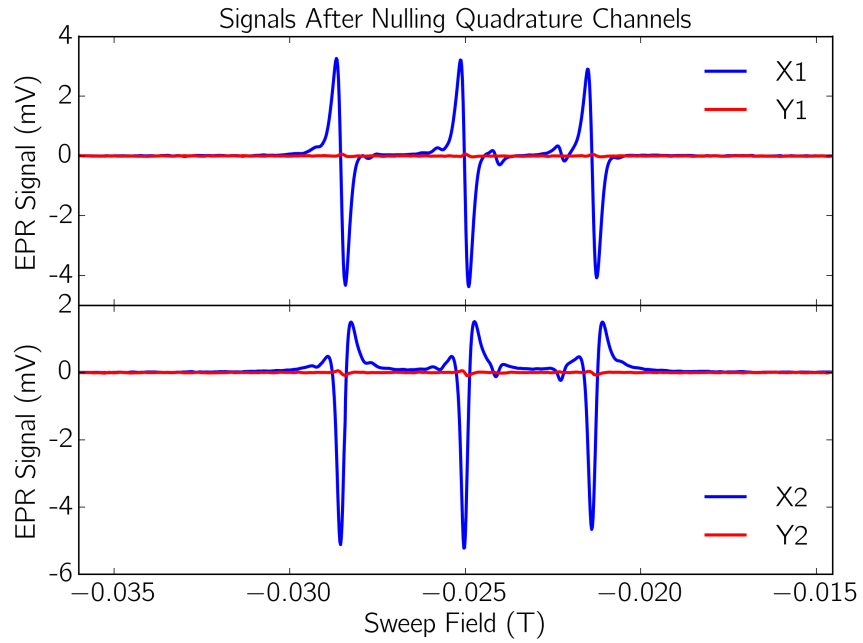

Figure C.3: A phase shift is applied independently to the complex signal from each lock-in amplifier. This is done to transfer the EPR signal into the in-phase (real) channel, and null the quadrature (imaginary) channel. A procedure to carry out this phase correction is outlined in [188]. Top: Signals from lock-in 1, with quadrature channel Y1 nulled. Bottom: Signals from lock-in 2, with quadrature channel Y2 nulled.

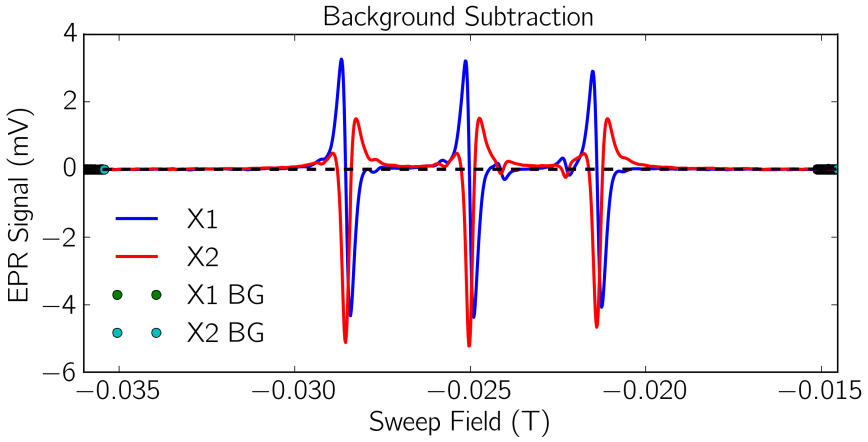

Figure C.4: Signals X1 and X2 from lock-ins 1 and 2 respectively, with the points used to define a background and the linear background itself.

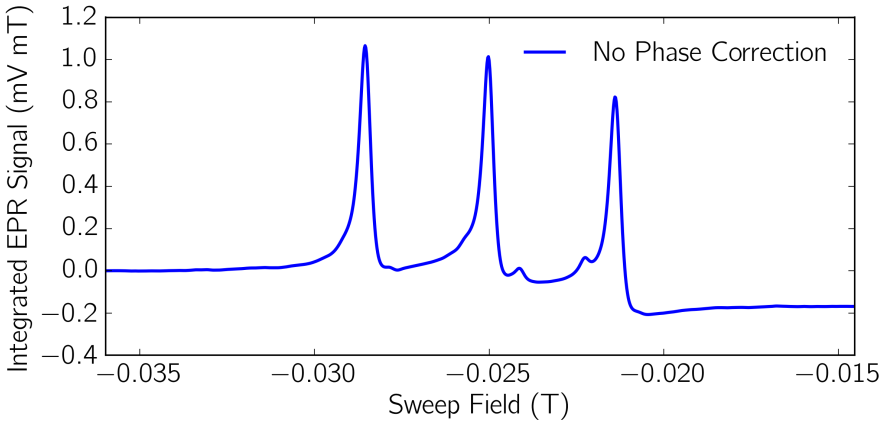

Figure C.5: The integrated X1 signal from Figure C.4. A linear background correction has been applied, but no phase shift between X1 and X2 has been applied.

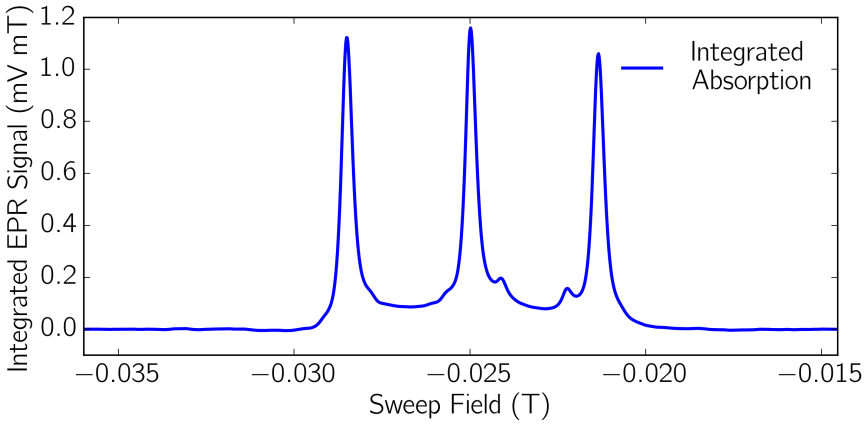

Figure C.6: Integrated absorption signal, after a phase shift of 28.89 degrees was applied between X1 and X2 (from Figure C.4). Phase shift was set by maximizing the double integral of the absorption signal.

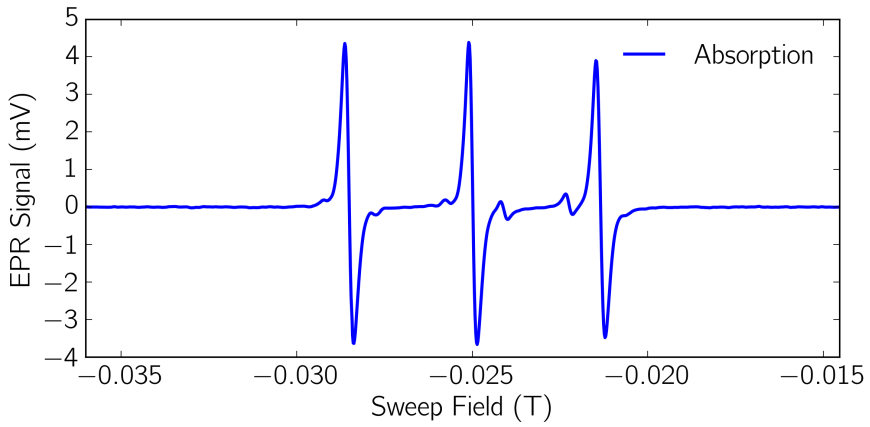

Figure C.7: First derivative absorption signal, after a phase shift of 28.89 degrees was applied between X1 and X2 (from Figure C.4). Phase shift was set by maximizing the double integral of the absorption signal.

Appendix D

Transfer Matrix Calculations of Reflection and Transmission

D.1 Transfer matrix calculations for reflection and transmission calculations

Calculations follow Chapter 17 of *Modern Electrodynamics* by Zangwill [138].

Write the total electric field $\mathbf{E}(z) = E(z)\hat{x}$ as the sum of a right-going wave $E^+(z)$ and a left-going wave $E^-(z)$.

As each wave passes across a layer with thickness d_j, permittivity ε_j, and permeability μ_j, it picks up a phase ϕ_j

$$\phi_j = \omega d_j \sqrt{\varepsilon_j \mu_j} = \omega n_j d_j / c \tag{D.1}$$

where $n_j = \sqrt{\varepsilon_{R,j}\mu_{R,j}}$, and $\varepsilon_{R,j} = \varepsilon_j/\varepsilon_0$ is the relative permittivity and $\mu_{R,j} = \mu_j/\mu_0$ is

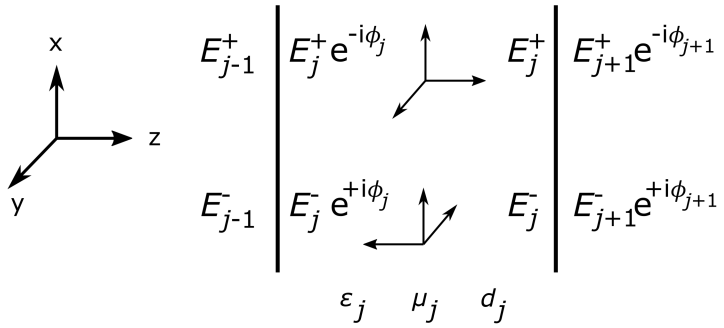

Figure D.1: Wave picks up phase shift ϕ_j as it passes through each layer.

the relative permeability.

We can write the electric and magnetic fields E and H in the $j-1$ layer in terms of E and H in the j layer as follows,

$$\begin{pmatrix} E_{j-1} \\ H_{j-1} \end{pmatrix} = \begin{pmatrix} \cos\phi_j & -iZ_j \sin\phi_j \\ -iZ_j^{-1}\sin\phi_j & \cos\phi_j \end{pmatrix} \begin{pmatrix} E_j \\ H_j \end{pmatrix} \tag{D.2}$$

where the impedance Z_j of the jth layer is given by $Z_j = \sqrt{\mu_j/\varepsilon_j}$.

D.1.1 Calculating reflection and transmission coefficients

Consider the case where the incident wave travels to the right and passes N layers. The boundary condition on the left side is that $E_N^-(z) = 0$, there are no reflections from infinity on the left side. Therefore, on the extreme left side of the stack, the electric and magnetic fields are given by $E_N = E_N^+ = t$ and $H_N = H_N^+ = t/Z_N$, where t is the transmission coefficient and Z_N is the wave impedance of the region to the left of the stack. On the right side of the stack of layers, E and H are given by $E = 1 + r$ and $H = (1 - r)/Z$ where r is the reflection coefficient and Z is the wave impedance of the region from where the wave originates.

We have a system of equations with two unknowns, r and t,

$$\begin{pmatrix} 1+r \\ (1-r)Z^{-1} \end{pmatrix} = \prod_{j=0}^{N-1} \begin{pmatrix} \cos\phi_j & -iZ_j \sin\phi_j \\ -iZ_j^{-1}\sin\phi_j & \cos\phi_j \end{pmatrix} \begin{pmatrix} t \\ tZ_N^{-1} \end{pmatrix} \tag{D.3}$$

The procedure is to solve for r and t. Writing the product of each matrix j as

$$\prod_{j=0}^{N-1} \begin{pmatrix} \cos\phi_j & -iZ_j \sin\phi_j \\ -iZ_j^{-1}\sin\phi_j & \cos\phi_j \end{pmatrix} = \begin{pmatrix} \alpha & \beta \\ \gamma & \delta \end{pmatrix}$$

we have

$$t = \frac{2}{\alpha + \frac{\beta}{Z_N} + Z\gamma + \frac{Z}{Z_N}\delta}$$
$$r = \frac{\alpha + \frac{\beta}{Z_N} - Z\gamma - \frac{Z}{Z_N}\delta}{\alpha + \frac{\beta}{Z_N} + Z\gamma + \frac{Z}{Z_N}\delta}$$

D.2 Sample backed by a perfect mirror

For a sample backed by a perfect flat mirror, the boundary condition is that $t = 0$, and that H_N is locally maximized at the mirror's surface. The two unknowns to solve for in this case are r and H_N, the magnetic field at the surface of the mirror. We write

$$\begin{pmatrix} 1+r \\ (1-r)Z^{-1} \end{pmatrix} = \prod_{j=0}^{N-1} \begin{pmatrix} \cos\phi_j & -iZ_j \sin\phi_j \\ -iZ_j^{-1}\sin\phi_j & \cos\phi_j \end{pmatrix} \begin{pmatrix} 0 \\ H_N \end{pmatrix} \tag{D.4}$$

We can solve for r and H_N in this case in a straightforward fashion. Calculating the total transfer matrix as before

$$\prod_{j=0}^{N-1} \begin{pmatrix} \cos\phi_j & -iZ_j \sin\phi_j \\ -iZ_j^{-1}\sin\phi_j & \cos\phi_j \end{pmatrix} = \begin{pmatrix} \alpha & \beta \\ \gamma & \delta \end{pmatrix}$$

we have

$$r = \frac{\beta - Z\delta}{\beta + Z\delta} \tag{D.5}$$

D.3 Reflection from a simple sample geometry

In the sample geometry shown in Figure 5.2, an electromagnetic wave with frequency ω is incident from air, into a material of thickness d with electric permittivity ε and magnetic permeability μ, which is backed by a mirror, which is taken to be a perfect conductor.

Calculating first the general case, where the electromagnetic wave is incident from a material with electric permittivity ε' and magnetic permeability μ' onto a material of thickness d with electric permittivity ε and magnetic permeability μ, the reflection coefficient $r = E_r/E_i$, where E_r is the reflected electric field and E_i is the incident electric field, is given by Equation D.5,

$$r = \frac{\beta - Z'\delta}{\beta + Z'\delta}$$

where $Z' = \sqrt{\mu'/\varepsilon'}$ is the impedance of free space and

$$\beta = -iZ\sin\phi, \qquad \delta = \cos\phi$$

where

$$Z = \sqrt{\frac{\mu}{\varepsilon}} \tag{D.6a}$$

$$\phi = \omega d\sqrt{\varepsilon\mu} = \frac{\omega d}{c}\sqrt{\varepsilon_R\mu_R} \tag{D.6b}$$

and $\varepsilon_R = \varepsilon/\varepsilon_0$ is the relative permittivity (dielectric constant) and $\mu_R = \mu/\mu_0$ is the relative permeability.

Therefore, we have

$$r = \frac{-iZ\sin\phi - Z'\cos\phi}{-iZ\sin\phi + Z'\cos\phi} \tag{D.7}$$

which can be rewritten

$$r = -\frac{Z'(e^{i\phi} + e^{-i\phi}) + Z(e^{i\phi} - e^{-i\phi})}{Z'(e^{i\phi} + e^{-i\phi}) - Z(e^{i\phi} - e^{-i\phi})}$$

Rearranging terms, we have,

$$r = -\frac{e^{2i\phi}(Z' + Z) + Z' - Z}{e^{2i\phi}(Z' - Z) + Z' + Z} \tag{D.8}$$

or, written in terms of the relative permittivities and permeabilities,

$$r = -\frac{e^{2i\phi}(\sqrt{\mu'_R\varepsilon_R} + \sqrt{\mu_R\varepsilon'_R}) + \sqrt{\mu'_R\varepsilon_R} - \sqrt{\mu_R\varepsilon'_R}}{e^{2i\phi}(\sqrt{\mu'_R\varepsilon_R} - \sqrt{\mu_R\varepsilon'_R}) + \sqrt{\mu'_R\varepsilon_R} + \sqrt{\mu_R\varepsilon'_R}} \tag{D.9}$$

Equation D.9 gives the reflection coefficient for a wave incident from a medium with impedance $Z = \sqrt{\mu/\varepsilon}$ onto a material of thickness d with impedance $Z' = \sqrt{\mu'/\varepsilon'}$, backed by a perfect conductor. Taking the first medium to be air, so that $Z' \simeq Z_0 = \sqrt{\mu_0/\varepsilon_0}$, the reflection simplifies to

$$r = -\frac{e^{2i\phi}(\sqrt{\varepsilon_R} + \sqrt{\mu_R}) + \sqrt{\varepsilon_R} - \sqrt{\mu_R}}{e^{2i\phi}(\sqrt{\varepsilon_R} - \sqrt{\mu_R}) + \sqrt{\varepsilon_R} + \sqrt{\mu_R}} \tag{D.10}$$

Appendix E

Paramagnetic Polaritons

This Appendix picks up where Chapter 5 leaves off, by asking the question- what happens when the assumption of "weak" resonance $|\chi_m| \ll 1$ is no longer valid? For a system with a large number of spins and a narrow EPR transition, it is possible to enter a regime where line broadening is observed due to optical effects. For a good overview of refractive broadening, see references [24] and [56]. For similar calculations performed in a transmission-mode experiment, see [189].

We typically think of CW EPR lineshapes as being directly proportional to the complex dynamic magnetic susceptibility. The magnetic susceptibility tells us how a material responds to applied magnetic fields in the linear response regime. For example, the power absorbed per unit volume in a magnetic material is proportional to χ_m'', the imaginary part of the dynamic susceptibility. More specifically, when we calculate an EPR lineshape, whether by solving the Bloch equations in the steady state, diagonalizing the spin

Hamiltonian, etc., we are calculating the dynamic susceptibility (Figure 5.1). Specifically, when we calculate the absorption lineshape, we are calculating χ''_m.

Our spectrometer measures the complex reflectance of a sample using induction-mode detection. These notes outline how we extract the EPR absorption lineshape, or equivalently the dynamic susceptibility, from the measured induction mode signal. In order to do this, we will need to know several things about our sample: 1) geometry, 2) magnetization, 3) width of resonance, and 4) the dielectric constant.

Broadly speaking: when the magnitude of the dynamic susceptibility is everywhere small $|\chi_m| \ll 1$, our measured signal will be proportional to χ_m, with an overall phase shift. When the magnitude of the dynamic susceptibility is not small, the signal we measure is no longer proportional to χ_m, and becomes a sensitive function of sample thickness and dielectric constant.

In the extreme case that $|\chi_m| > 1$, measured signal becomes dominated by a paramagnetic polariton.

The following calculations assume the sample geometry shown in Figure 5.2.

E.1 Breakdown of weak resonance

When χ_m is no longer small, the observed induction-mode signal is no longer proportional to χ_m. Instead, measured signal $S'(B)$ or $S'(\omega)$ can be calculated from the dynamic susceptibility χ_m, following Equations 5.1 and 5.5.

The difficulty here becomes calculating χ_m. Simulated EPR spectra (generated by, for

example, Easyspin) are proportional to χ_m, but are normalized according to conventions established by the software. Equation 5.1, however, is quite sensitive to the magnitude of χ_m.

For a single $S = 1/2$ homogeneously broadened line with width $1/T_2$, the dynamic magnetic susceptibility $\chi_m = \chi'_m + i\chi''_m$ is given for circularly polarized light (ignoring saturation effects) by

$$\chi'_m = \mu_0 \frac{N}{V} \frac{g\mu_B}{2} \tanh\left(\frac{T_Z}{2T}\right) \frac{g\mu_B}{\hbar} \frac{\omega - \omega_L}{(\omega - \omega_L)^2 + 1/T_2^2} \tag{E.1}$$

$$\chi''_m = \mu_0 \frac{N}{V} \frac{g\mu_B}{2} \tanh\left(\frac{T_Z}{2T}\right) \frac{g\mu_B}{\hbar} \frac{1/T_2}{(\omega - \omega_L)^2 + 1/T_2^2} \tag{E.2}$$

where N/V is the number density of spins, $\omega_L = g\mu_B B_0/\hbar$ is the Larmor frequency, and $T_Z = \omega_L \hbar/k_B$ is the Zeeman temperature [55]. In the high temperature approximation, this becomes

$$\chi'_m = \chi_0 \omega_L \frac{\omega_L - \omega}{(\omega_L - \omega)^2 + 1/T_2^2} \tag{E.3}$$

$$\chi''_m = \chi_0 \omega_L \frac{1/T_2}{(\omega_L - \omega)^2 + 1/T_2^2} \tag{E.4}$$

where χ_0 is the static magnetic susceptibility,

$$\chi_0 = \mu_0 \frac{N}{V} \frac{(g\mu_B)^2}{4k_B T} \tag{E.5}$$

Putting in some numbers: χ''_m is maximal on resonance, where $\omega = \omega_L$. At 240 GHz,

$T_Z = 11.5$ K. For a 1 mM solution of $g = 2$ spins at 240 GHz, 300K, with a T_2 of 100 ns, we have $\chi''_m = 0.0023$ on resonance. Since the measured lineshape is no longer proportional to χ_m, it becomes difficult to extract the undistorted EPR lineshape from Equation 5.5. Rather than working backwards from $S'(B)$ or $S'(\omega)$, it is likely easier to simulate $S'(B)$ or $S'(\omega)$ for a given sample, starting from an undistorted lineshape appropriately scaled (χ_m) and applying Equations 5.1 and 5.5.

E.2 Strong resonance: Paramagnetic polaritons

When the dynamic susceptibility $|\chi_m|$ is small, the measured lineshape $S(B)$ is proportional χ_m (Equation 5.6). When $|\chi_m|$ is not small, simulating the measured lineshape becomes possible only given knowledge of the sample geometry, electric, and magnetic properties (Equations 5.1 and 5.5).

When $|\chi_m|$ approaches 1, however, it becomes difficult to think about the reflected signal in terms of the EPR lineshape. This is best illustrated by considering the dispersion relation obeyed by the electric and magnetic fields as they propagate in a paramagnetic sample.

E.2.1 Dispersion Relation

Inside a material, the electric field obeys the equation

$$\nabla^2 \mathbf{E} = \mu\varepsilon \frac{\partial^2}{\partial t^2} \mathbf{E} \tag{E.6}$$

which has the solution $\mathbf{E} = \mathbf{E}_0 e^{i(\mathbf{k}\cdot\mathbf{x}-\omega t)}$. Taking $\varepsilon = \varepsilon_0\varepsilon_R$ and $\mu = \mu_0(1 + \chi'_m + i\chi''_m)$, where χ'_m, χ''_m are given by Equations E.3 and E.4, $\mathbf{K}$ and ω are related by

$$k^2 = \frac{\omega^2\varepsilon_R}{c^2}\left[1 + \chi_0\omega_L\frac{\omega_L - \omega + i/T_2}{(\omega_L - \omega)^2 + 1/T_2^2}\right] \tag{E.7}$$

This expression is best rewritten in terms of the dimensionless variables $k' = ck/\sqrt{\varepsilon_R}\omega_L$, $\omega' = \omega/\omega_L$, and $\Gamma = (T_2\omega_L)^{-1}$.

Plotted below is the dispersion relation $\omega' = f(k')$, for several values of χ_0, and Γ. χ_0 is the static magnetic susceptibility, given in the high temperature approximation for a spin-1/2 by

$$\chi_0 = \mu_0\frac{N}{V}\frac{(g\mu_B)^2}{4k_BT}$$

For "strong" resonance, that is large χ_0 and a narrow linewidth, the dispersion relation changes dramatically as a function of frequency. For a sufficiently strong resonance, in a window around $\omega - \omega_L$, light does not propagate (see Figure E.2). The measured induction mode signal will not look anything like an EPR lineshape.

Some numbers: BDPA at room temperature has $\chi_0 \simeq 4 \times 10^{-4}$, and $\Gamma \simeq 10^{-4}$

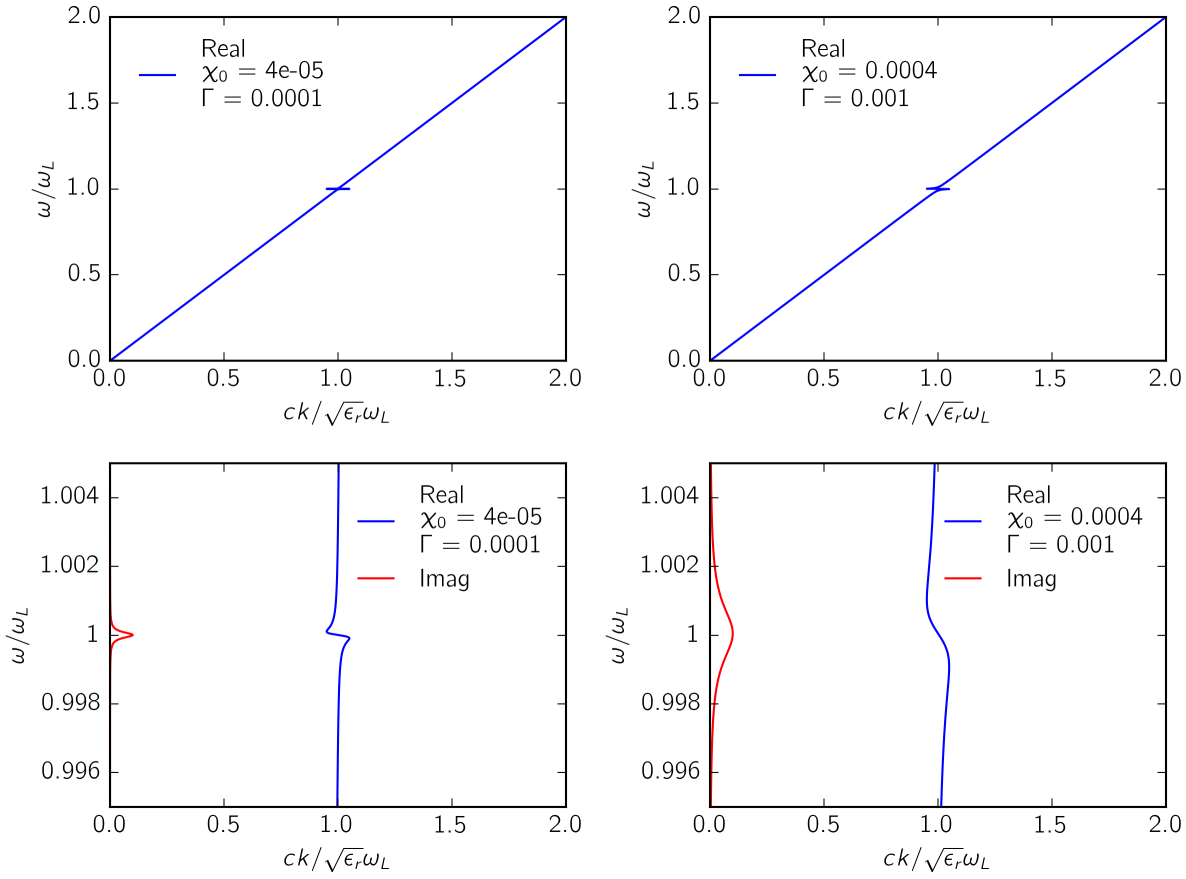

Figure E.1: Lower two: Dispersion relation for $\chi_0 = 4\times10^{-5}, \Gamma = 10^{-4}$. At 240 GHz, this is a narrow line (on the order of 1 Gauss). Top: dispersion relation differs from that of free space near resonance. Bottom: real and imaginary parts of the dispersion relation, plotted around $\omega = \omega_L$. Upper two: Dispersion relation for $\chi_0 = 4 \times 10^{-4}, \Gamma = 10^{-3}$. At 240 GHz, this is a linewidth of order 1 mT. Top: dispersion relation differs from that of free space near resonance. Bottom: real and imaginary parts of the dispersion relation, plotted around $\omega = \omega_L$.

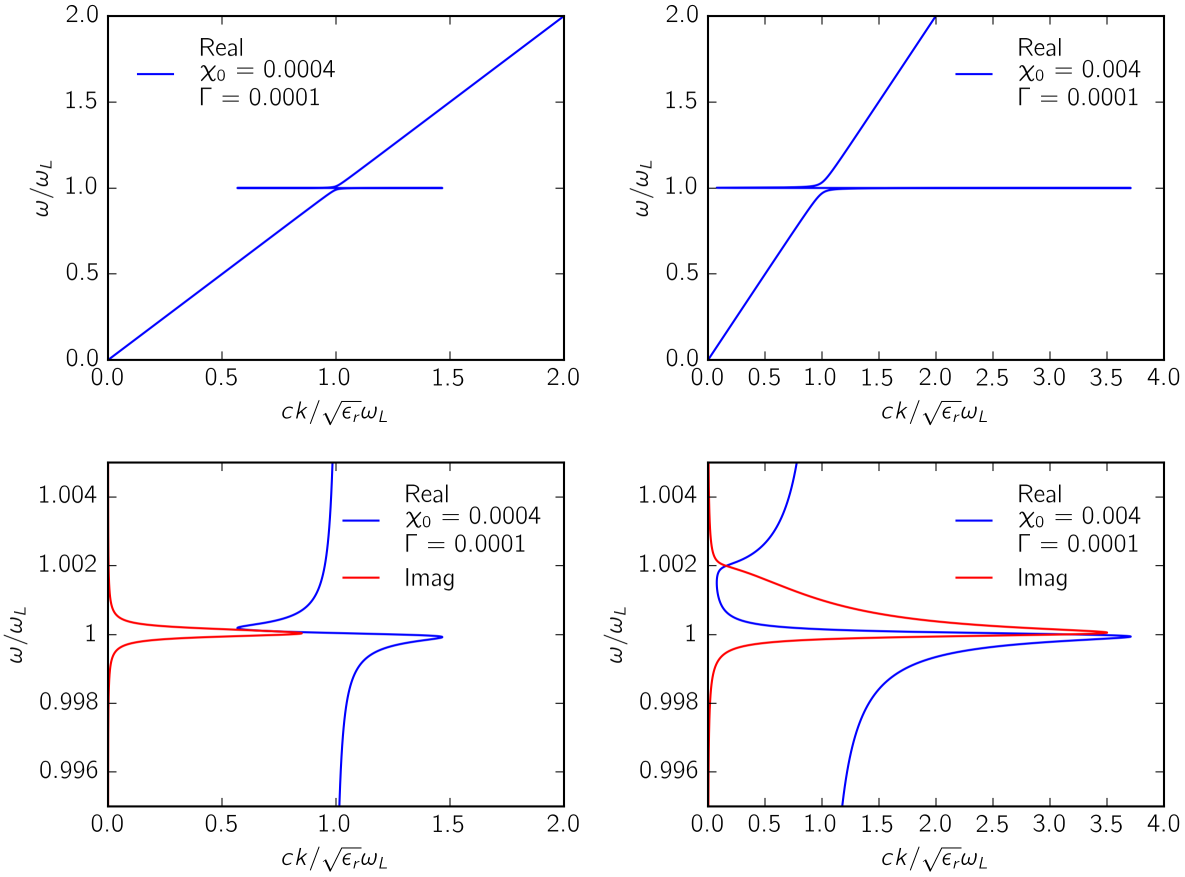

Figure E.2: Lower two: Dispersion relation for $\chi_0 = 4 \times 10^{-4}, \Gamma = 10^{-4}$. At 240 GHz, this is a narrow line (on the order of 1 Gauss). Top: dispersion relation differs from that of free space near resonance. (Think, BDPA at room temperature.) Bottom: real and imaginary parts of the dispersion relation, plotted around $\omega = \omega_L$. Upper two: Dispersion relation for $\chi_0 = 4 \times 10^{-3}, \Gamma = 10^{-4}$. At 240 GHz, this is a linewidth of order 1 Gauss. (Think, BDPA at 30 K.) Top: dispersion relation differs from that of free space near resonance. Bottom: real and imaginary parts of the dispersion relation, plotted around $\omega = \omega_L$.Note that for a range of frequencies, light almost does not propagate in the sample.

Bibliography

[1] Evgeni Zavoisky. The paramagnetic absorption of a solution in parallel fields. *Journal of Physics, USSR*, 8:377–380, 1944.

[2] TJ Stone, T Buckman, PL Nordio, and HM McConnell. Spin-Labeled Biomolecules. *Proceedings of the National Academy of Sciences of the United States of America*, 54(4):1010+, 1965.

[3] Anton Savitsky and Klaus Möbius. High-field epr. *Photosynthesis Research*, 102(2):311–333, Dec 2009.

[4] Thomas Lohmiller, Vera Krewald, Montserrat Pérez Navarro, Marius Retegan, Leonid Rapatskiy, Marc M. Nowaczyk, Alain Boussac, Frank Neese, Wolfgang Lubitz, Dimitrios A. Pantazis, and Nicholas Cox. Structure, ligands and substrate coordination of the oxygen-evolving complex of photosystem ii in the s2 state: a combined epr and dft study. *Phys. Chem. Chem. Phys.*, 16:11877–11892, 2014.

[5] HJ Steinhoff, N Radzwill, W Thevis, V Lenz, D Brandenburg, A Antson, G Dodson, and A Wollmer. Determination of interspin distances between spin labels attached to insulin: Comparison of electron paramagnetic resonance data with the x-ray structure. *BIOPHYSICAL JOURNAL*, 73(6):3287–3298, DEC 1997.

[6] Andrea Martorana, Giuliano Bellapadrona, Akiva Feintuch, Enza Di Gregorio, Silvio Aime, and Daniella Goldfarb. Probing protein conformation in cells by epr distance measurements using gd3+ spin labeling. *Journal of the American Chemical Society*, 136(38):13458–13465, 2014. PMID: 25163412.

[7] Dieter Kurad, Gunnar Jeschke, and Derek Marsh. Lipid membrane polarity profiles by high-field epr. *Biophysical Journal*, 85(2):1025 – 1033, 2003.

[8] Ziwei Zhang, Mark R. Fleissner, Dmitriy S. Tipikin, Zhichun Liang, Jozef K. Moscicki, Keith A. Earle, Wayne L. Hubbell, and Jack H. Freed. Multifrequency electron spin resonance study of the dynamics of spin labeled t4 lysozyme. *The Journal of Physical Chemistry B*, 114(16):5503–5521, 2010. PMID: 20361789.

[9] Laxman Mainali, James S. Hyde, and Witold K. Subczynski. Using spin-label w-band epr to study membrane fluidity profiles in samples of small volume. *Journal of Magnetic Resonance*, 226:35 – 44, 2013.

[10] Vasyl P. Denysenkov, Daniele Biglino, Wolfgang Lubitz, Thomas F. Prisner, and Marina Bennati. Structure of the tyrosyl biradical in mouse r2 ribonucleotide reductase from high-field peldor. *Angewandte Chemie International Edition*, 47(7):1224–1227, 2008.

[11] Stefan Stoll, Alexander Gunn, Marcin Brynda, Wesley Sughrue, Amanda C. Kohler, Andrew Ozarowski, Andrew J. Fisher, J. Clark Lagarias, and R. David Britt. Structure of the biliverdin radical intermediate in phycocyanobilin:ferredoxin oxidoreductase identified by high-field epr and dft. *Journal of the American Chemical Society*, 131(5):1986–1995, 2009. PMID: 19159240.

[12] M Pannier, S Veit, A Godt, G Jeschke, and H.W Spiess. Dead-time free measurement of dipole–dipole interactions between electron spins. *Journal of Magnetic Resonance*, 142(2):331 – 340, 2000.

[13] L.V. Kulik, S.A. Dzuba, I.A. Grigoryev, and Yu.D. Tsvetkov. Electron dipole–dipole interaction in eseem of nitroxide biradicals. *Chemical Physics Letters*, 343(3):315 – 324, 2001.

[14] Bela E. Bode, Jörn Plackmeyer, Michael Bolte, Thomas F. Prisner, and Olav Schiemann. Peldor on an exchange coupled nitroxide copper(ii) spin pair. *Journal of Organometallic Chemistry*, 694(7):1172 – 1179, 2009. Organo-Transition Metal Complexes.

[15] Bela E. Bode, Jörn Plackmeyer, Thomas F. Prisner, and Olav Schiemann. Peldor measurements on a nitroxide-labeled cu(ii) porphyrin: Orientation selection, spin-density distribution, and conformational flexibility. *The Journal of Physical Chemistry A*, 112(23):5064–5073, 2008. PMID: 18491846.

[16] Angeliki Giannoulis, Claire L. Motion, Maria Oranges, Michael Buhl, Graham M. Smith, and Bela E. Bode. Orientation selection in high-field ridme and peldor experiments involving low-spin coii ions. *Phys. Chem. Chem. Phys.*, pages –, 2018.

[17] Zhehong Gan, Ivan Hung, Xiaoling Wang, Joana Paulino, Gang Wu, Ilya M. Litvak, Peter L. Gor'kov, William W. Brey, Pietro Lendi, Jeffrey L. Schiano, Mark D. Bird, Iain R. Dixon, Jack Toth, Gregory S. Boebinger, and Timothy A. Cross. Nmr spectroscopy up to 35.2t using a series-connected hybrid magnet. *Journal of Magnetic Resonance*, 284:125 – 136, 2017.

[18] Shinji Kawasaki, Chengtian Lin, Philip L. Kuhns, Arneil P. Reyes, and Guo-qing Zheng. Carrier-concentration dependence of the pseudogap ground state of su-

perconducting $bi_2sr_{2-x}la_xcuo_{6+\delta}$ revealed by ^{63,65}Cu-nuclear magnetic resonance in very high magnetic fields. *Phys. Rev. Lett.*, 105:137002, Sep 2010.

[19] Alexey Potapov, Hiromasa Yagi, Thomas Huber, Slobodan Jergic, Nicholas E. Dixon, Gottfried Otting, and Daniella Goldfarb. Nanometer-scale distance measurements in proteins using gd3+ spin labeling. *Journal of the American Chemical Society*, 132(26):9040–9048, 2010. PMID: 20536233.

[20] DevinT. Edwards, Thomas Huber, Sunyia Hussain, KatherineM. Stone, Maia Kinnebrew, Ilia Kaminker, Erez Matalon, MarkS. Sherwin, Daniella Goldfarb, and Songi Han. Determining the oligomeric structure of proteorhodopsin by gd3+-based pulsed dipolar spectroscopy of multiple distances. *Structure*, 22(11):1677 – 1686, 2014.

[21] Mian Qi, Andreas Groß, Gunnar Jeschke, Adelheid Godt, and Malte Drescher. Gd(iii)-pymta label is suitable for in-cell epr. *Journal of the American Chemical Society*, 136(43):15366–15378, 2014. PMID: 25325832.

[22] Debamalya Banerjee, Hiromasa Yagi, Thomas Huber, Gottfried Otting, and Daniella Goldfarb. Nanometer-range distance measurement in a protein using mn2+ tags. *The Journal of Physical Chemistry Letters*, 3(2):157–160, 2012.

[23] H. Y. Vincent Ching, Florencia C. Mascali, Hélène C. Bertrand, Eduardo M. Bruch, Paul Demay-Drouhard, Rodolfo M. Rasia, Clotilde Policar, Leandro C. Tabares, and Sun Un. The use of mn(ii) bound to his-tags as genetically encodable spin-label for nanometric distance determination in proteins. *The Journal of Physical Chemistry Letters*, 7(6):1072–1076, 2016. PMID: 26938795.

[24] Devin T. Edwards, Zhidong Ma, Thomas J. Meade, Daniella Goldfarb, Songi Han, and Mark S. Sherwin. Extending the distance range accessed with continuous wave epr with gd3+ spin probes at high magnetic fields. *Phys. Chem. Chem. Phys.*, 15:11313–11326, 2013.

[25] Jessica A. Clayton, Mian Qi, Adelheid Godt, Daniella Goldfarb, Songi Han, and Mark S. Sherwin. Gd3+-gd3+ distances exceeding 3 nm determined by very high frequency continuous wave electron paramagnetic resonance. *Phys. Chem. Chem. Phys.*, 19:5127–5136, 2017.

[26] G. Feher. Observation of nuclear magnetic resonances via the electron spin resonance line. *Phys. Rev.*, 103:834–835, Aug 1956.

[27] W. B. Mims. Pulsed endor experiments. *Proceedings of the Royal Society of London. Series A. Mathematical and Physical Sciences*, 283(1395):452–457, 1965.

[28] E.R. Davies. A new pulse endor technique. *Physics Letters A*, 47(1):1 – 2, 1974.

[29] Albert W. Overhauser. Polarization of nuclei in metals. *Phys. Rev.*, 92:411–415, Oct 1953.

[30] A Abragam and M Goldman. Principles of dynamic nuclear polarisation. *Reports on Progress in Physics*, 41(3):395–467, mar 1978.

[31] G. M. Smith, J. C. G. Lesurf, R. H. Mitchell, and P. C. Riedi. Quasi-optical cw mm-wave electron spin resonance spectrometer. *Rev. Sci. Instrum.*, 69(11):3924, 1998.

[32] M. M. Hertel, V. P. Denysenkov, M. Bennati, and T. F. Prisner. Pulsed 180-GHz EPR/ENDOR/PELDOR spectroscopy. *Magnetic Resonance in Chemistry*, 43(S1):S248–S255, dec 2005.

[33] V. P. Denysenkov, T. F. Prisner, J. Stubbe, and M. Bennati. High-frequency 180 GHz PELDOR. *Applied Magnetic Resonance*, 29(2):375–384, jun 2005.

[34] Gavin W. Morley, Louis-Claude Brunel, and Johan van Tol. A multifrequency high-field pulsed electron paramagnetic resonance/electron-nuclear double resonance spectrometer. *Review of Scientific Instruments*, 79(6):064703, 2008.

[35] Albert A. Smith, Björn Corzilius, Jeffrey A. Bryant, Ronald DeRocher, Paul P. Woskov, Richard J. Temkin, and Robert G. Griffin. A 140ghz pulsed epr/212mhz nmr spectrometer for dnp studies. *Journal of Magnetic Resonance*, 223(Supplement C):170 – 179, 2012.

[36] Igor Tkach, Karin Halbmair, Claudia Höbartner, and Marina Bennati. High-frequency 263 GHz PELDOR. *Appl. Magn. Reson.*, 45(10):969–979, oct 2014.

[37] Franklin H. Cho, Viktor Stepanov, Chathuranga Abeywardana, and Susumu Takahashi. Chapter Five – 230/115GHz Electron Paramagnetic Resonance/Double Electron–Electron Resonance Spectroscopy. In *Methods in Enzymology*, volume 563, pages 95–118. 2015.

[38] Viktor Stepanov and Susumu Takahashi. Determination of nitrogen spin concentration in diamond using double electron-electron resonance. *Phys. Rev. B*, 94:024421, Jul 2016.

[39] W. Hofbauer, K. A. Earle, C. R. Dunnam, J. K. Moscicki, and J. H. Freed. High-power 95 ghz pulsed electron spin resonance spectrometer. *Review of Scientific Instruments*, 75(5):1194–1208, 2004.

[40] Daniella Goldfarb, Yaakov Lipkin, Alexey Potapov, Yehoshua Gorodetsky, Boris Epel, Arnold M Raitsimring, Marina Radoul, and Ilia Kaminker. HYSCORE and DEER with an upgraded 95 GHz pulse EPR spectrometer. *J. Magn. Reson.*, 194:8–15, 2008.

[41] Paul A. S. Cruickshank, David R. Bolton, Duncan A. Robertson, Robert I. Hunter, Richard J. Wylde, and Graham M. Smith. A kilowatt pulsed 94 ghz electron paramagnetic resonance spectrometer with high concentration sensitivity, high instantaneous bandwidth, and low dead time. *Review of Scientific Instruments*, 80(10):103102, 2009.

[42] E. A. Nanni, S. M. Lewis, M. A. Shapiro, R. G. Griffin, and R. J. Temkin. Photonic-band-gap traveling-wave gyrotron amplifier. *Phys. Rev. Lett.*, 111:235101, Dec 2013.

[43] Emilio A. Nanni, Sudheer Jawla, Samantha M. Lewis, Michael A. Shapiro, and Richard J. Temkin. Photonic-band-gap gyrotron amplifier with picosecond pulses. *Applied Physics Letters*, 111(23):233504, 2017.

[44] Gerald Ramian. The new ucsb free-electron lasers. *Nuclear Instruments and Methods in Physics Research Section A: Accelerators, Spectrometers, Detectors and Associated Equipment*, 318(1):225 – 229, 1992.

[45] Susumu Takahashi, Gerald Ramian, and Mark S. Sherwin. Cavity dumping of an injection-locked free-electron laser. *Applied Physics Letters*, 95(23):234102, 2009.

[46] Keishi Sakamoto, Atsushi Kasugai, Koji Takahashi, Ryutaro Minami, Noriyuki Kobayashi, and Ken Kajiwara. Achievement of robust high-efficiency 1 mw oscillation in the hard-self-excitation region by a 170 ghz continuous-wave gyrotron. *Nature Physics*, 3:411 – 414, 2007.

[47] S. Alberti, F. Braunmueller, T. M. Tran, J. Genoud, J-Ph. Hogge, M. Q. Tran, and J-Ph. Ansermet. Nanosecond pulses in a thz gyrotron oscillator operating in a mode-locked self-consistent q-switch regime. *Phys. Rev. Lett.*, 111:205101, Nov 2013.

[48] Lino R. Becerra, Gary J. Gerfen, Richard J. Temkin, David J. Singel, and Robert G. Griffin. Dynamic nuclear polarization with a cyclotron resonance maser at 5 T. *Physical Review Letters*, 71(21):3561–3564, 1993.

[49] Changsik Song, Kan-Nian Hu, Chan-Gyu Joo, Timothy M. Swager, and Robert G. Griffin. TOTAPOL: A Biradical Polarizing Agent for Dynamic Nuclear Polarization Experiments in Aqueous Media. *Journal of the American Chemical Society*, 128(35):11385–11390, 2006.

[50] Edward P. Saliba, Erika L. Sesti, Faith J. Scott, Brice J. Albert, Eric J. Choi, Nicholas Alaniva, Chukun Gao, and Alexander B. Barnes. Electron Decoupling with Dynamic Nuclear Polarization in Rotating Solids. *Journal of the American Chemical Society*, 139(18):6310–6313, 2017.

[51] S. Takahashi, L-C Brunel, D. T. Edwards, J. van Tol, G. Ramian, S. Han, and M. S. Sherwin. Pulsed electron paramagnetic resonance spectroscopy powered by a

free-electron laser. *Nature*, 489(7416):409–13, Sep 20 2012. Copyright - Copyright Nature Publishing Group Sep 20, 2012; Document feature - ; Graphs; Diagrams; Last updated - 2014-03-08; CODEN - NATUAS.

[52] Charles P Poole. *Electron Spin Resonance - A Comprehensive Treatise on Experimental Techniques*. Dover Publications, Inc., second edition, 1983.

[53] John A. Weil and James R. Bolton. *Electron Paramagnetic Resonance: Elementary Theory and Practical Applications*. Wiley, second edition, 2007.

[54] A. Schweiger and G. Jeschke. *Principles of pulse electron paramagnetic resonance*. Oxford University Press, Oxford, UK ; New York, 2001.

[55] Jeno Solyom. *Fundamentals of the Physics of Solids*. 1st edition, 2007.

[56] Devin T. Edwards. *High-Field EPR for Studies of Structure in Biological Systems*. PhD thesis, University of California, Santa Barbara, 2013.

[57] Jessica A. Clayton. *High-field CW EPR with Gd(III) spin labels for structure studies of membrane proteins*. PhD thesis, University of California, Santa Barbara, 2017.

[58] David J. Griffiths. *Introduction to Quantum Mechanics*. Benjamin Cummings, 2nd edition, April 2004.

[59] Arthur Rich and John C. Wesley. The current status of the lepton g factors. *Rev. Mod. Phys.*, 44:250–283, Apr 1972.

[60] Robert S. Van Dyck, Paul B. Schwinberg, and Hans G. Dehmelt. New high-precision comparison of electron and positron g factors. *Phys. Rev. Lett.*, 59:26–29, Jul 1987.

[61] B. Odom, D. Hanneke, B. D'Urso, and G. Gabrielse. New measurement of the electron magnetic moment using a one-electron quantum cyclotron. *Phys. Rev. Lett.*, 97:030801, Jul 2006.

[62] F. Bloch. Nuclear induction. *Physical Review*, 70(7-8):460–474, 1946.

[63] N. Bloembergen, E. M. Purcell, and R. V. Pound. Relaxation effects in nuclear magnetic resonance absorption. *Phys. Rev.*, 73:679–712, Apr 1948.

[64] A. Abragam. *The Principles of Nuclear Magnetism*. Oxford University Press, 1961.

[65] David E. Budil. Chapter seven - cw-epr spectral simulations: Slow-motion regime. In Peter Z. Qin and Kurt Warncke, editors, *Electron Paramagnetic Resonance Investigations of Biological Systems by Using Spin Labels, Spin Probes, and Intrinsic Metal Ions, Part A*, volume 563 of *Methods in Enzymology*, pages 143 – 170. Academic Press, 2015.

[66] J H Freed. Electron spin resonance. *Annual Review of Physical Chemistry*, 23(1):265–310, 1972.

[67] Jack H. Freed. 3 - theory of slow tumbling esr spectra for nitroxides. In LAWRENCE J. BERLINER, editor, *Spin Labeling*, Molecular Biology: An International Series of Monographs and Textbooks, pages 53 – 132. Academic Press, Amsterdam, 1976.

[68] Eva Meirovitch, Dan Igner, Eva Igner, Giorgio Moro, and Jack H. Freed. Electron-spin relaxation and ordering in smectic and supercooled nematic liquid crystals. *The Journal of Chemical Physics*, 77(8):3915–3938, 1982.

[69] Giorgio Moro and Jack H. Freed. Efficient computation of magnetic resonance spectra and related correlation functions from stochastic liouville equations. *The Journal of Physical Chemistry*, 84(22):2837–2840, 1980.

[70] B. H. Robinson, L. J. Slutsky, and F. P. Auteri. Direct simulation of continuous wave electron paramagnetic resonance spectra from brownian dynamics trajectories. *The Journal of Chemical Physics*, 96(4):2609–2616, 1992.

[71] Kevin J. Waldron, Julian C. Rutherford, Dianne Ford, and Nigel J. Robinson. Metalloproteins and metal sensing. *NATURE*, 460(7257):823–830, AUG 13 2009.

[72] Christian Altenbach, Sabine L. Flitsch, H. Gobind Khorana, and Wayne L. Hubbell. Structural studies on transmembrane proteins. 2. spin labeling of bacteriorhodopsin mutants at unique cysteines. *Biochemistry*, 28(19):7806–7812, 1989. PMID: 2558712.

[73] C Altenbach, T Marti, HG Khorana, and WL Hubbell. Transmembrane protein structure: spin labeling of bacteriorhodopsin mutants. *Science*, 248(4959):1088–1092, 1990.

[74] Wayne L. Hubbell and Christian Altenbach. Investigation of structure and dynamics in membrane proteins using site-directed spin labeling. *Current Opinion in Structural Biology*, 4(4):566 – 573, 1994.

[75] V W Cornish, D R Benson, C A Altenbach, K Hideg, W L Hubbell, and P G Schultz. Site-specific incorporation of biophysical probes into proteins. *Proceedings of the National Academy of Sciences*, 91(8):2910–2914, 1994.

[76] J.E. Banham, C.M. Baker, S. Ceola, I.J. Day, G.H. Grant, E.J.J. Groenen, C.T. Rodgers, G. Jeschke, and C.R. Timmel. Distance measurements in the borderline region of applicability of cw epr and deer: A model study on a homologous series of spin-labelled peptides. *Journal of Magnetic Resonance*, 191(2):202 – 218, 2008.

[77] A.D. Milov, K.M. Salikhov, and M.D. Shirov. Application of endor in electron-spin echo for paramagnetic center space distributions in solids. *Fiz. Tverd. Tela.*, 23:975–982, 01 1981.

[78] Peter P. Borbat, Elka R. Georgieva, and Jack H. Freed. Improved sensitivity for long-distance measurements in biomolecules: Five-pulse double electron–electron resonance. *The Journal of Physical Chemistry Letters*, 4(1):170–175, 2013. PMID: 23301118.

[79] G. Jeschke, M. Pannier, A. Godt, and H.W. Spiess. Dipolar spectroscopy and spin alignment in electron paramagnetic resonance. *Chemical Physics Letters*, 331(2):243 – 252, 2000.

[80] Sergey Milikisyants, Francesco Scarpelli, Michelina G. Finiguerra, Marcellus Ubbink, and Martina Huber. A pulsed epr method to determine distances between paramagnetic centers with strong spectral anisotropy and radicals: The dead-time free ridme sequence. *Journal of Magnetic Resonance*, 201(1):48 – 56, 2009.

[81] Sunil Saxena and Jack H. Freed. Double quantum two-dimensional fourier transform electron spin resonance: Distance measurements. *Chemical Physics Letters*, 251(1):102 – 110, 1996.

[82] Sunil Saxena and Jack H. Freed. Theory of double quantum two-dimensional electron spin resonance with application to distance measurements. *The Journal of Chemical Physics*, 107(5):1317–1340, 1997.

[83] Petr P. Borbat and Jack H. Freed. Multiple-quantum esr and distance measurements. *Chemical Physics Letters*, 313(1):145 – 154, 1999.

[84] Margaret H. Rakowsky, Kundalika M. More, Alexander V. Kulikov, Gareth R. Eaton, and Sandra S. Eaton. Time-domain electron paramagnetic resonance as a probe of electron-electron spin-spin interaction in spin-labeled low-spin iron porphyrins. *Journal of the American Chemical Society*, 117(7):2049–2057, 1995.

[85] Devin T. Edwards, Susumu Takahashi, Mark S. Sherwin, and Songi Han. Distance measurements across randomly distributed nitroxide probes from the temperature dependence of the electron spin phase memory time at 240ghz. *Journal of Magnetic Resonance*, 223:198 – 206, 2012.

[86] C. Blake Wilson, Samuel Aronson, Jessica A. Clayton, Steffen J. Glaser, Songi Han, and Mark S. Sherwin. Multi-step phase-cycling in a free-electron laser-powered pulsed electron paramagnetic resonance spectrometer. *Phys. Chem. Chem. Phys.*, 20:18097–18109, 2018.

[87] Malcolm H Levitt. *Spin dynamics : basics of nuclear magnetic resonance*. John Wiley & Sons, Chichester, England ; Hoboken, NJ, 2nd ed.. edition, 2008.

[88] Geoffrey Bodenhausen, Herbert Kogler, and R.R. Ernst. Selection of coherence-transfer pathways in nmr pulse experiments. *Journal of Magnetic Resonance (1969)*, 58(3):370 – 388, 1984.

[89] C Gemperle, G Aebli, A Schweiger, and R.R Ernst. Phase cycling in pulse epr. *Journal of Magnetic Resonance (1969)*, 88(2):241 – 256, 1990.

[90] Thomas Kaufmann, Timothy J. Keller, John M. Franck, Ryan P. Barnes, Steffen J. Glaser, John M. Martinis, and Songi Han. Dac-board based x-band epr spectrometer with arbitrary waveform control. *Journal of Magnetic Resonance*, 235:95 – 108, 2013.

[91] Ilia Kaminker, Ryan Barnes, and Songi Han. Arbitrary waveform modulated pulse epr at 200ghz. *Journal of Magnetic Resonance*, 279:81 – 90, 2017.

[92] Devin T. Edwards, Yun Zhang, Steffen J. Glaser, Songi Han, and Mark S. Sherwin. Phase cycling with a 240 ghz, free electron laser-powered electron paramagnetic resonance spectrometer. *Phys. Chem. Chem. Phys.*, 15:5707–5719, 2013.

[93] Susumu Takahashi, Gerald Ramian, Mark S. Sherwin, Louis-Claude Brunel, and Johan van Tol. Submegahertz linewidth at 240ghz from an injection-locked free-electron laser. *Applied Physics Letters*, 91(17):174102, 2007.

[94] M. F. Doty, B. E. Cole, B. T. King, and M. S. Sherwin. Wavelength-specific laser-activated switches for improved contrast ratio in generation of short thz pulses. *Review of Scientific Instruments*, 75(9):2921–2925, 2004.

[95] J.R. Birch, J.D. Dromey, and J. Lesurf. The optical constants of some common low-loss polymers between 4 and 40 cm-1. *Infrared Physics*, 21(4):225 – 228, 1981.

[96] R. Piesiewicz, C. Jansen, S. Wietzke, D. Mittleman, M. Koch, and T. Kürner. Properties of building and plastic materials in the thz range. *International Journal of Infrared and Millimeter Waves*, 28(5):363–371, May 2007.

[97] Detlef Reichert and Günter Hempel. Receiver imperfections and cyclops: An alternative description. *Concepts in Magnetic Resonance*, 14(2):130–139, 2002.

[98] Natala Ivchenko, Colan E Hughes, and Malcolm H Levitt. Multiplex phase cycling. *Journal of Magnetic Resonance*, 160(1):52 – 58, 2003.

[99] Daniella Goldfarb. Gd3+ spin labeling for distance measurements by pulse epr spectroscopy. *Phys. Chem. Chem. Phys.*, 16:9685–9699, 2014.

[100] Arnold M. Raitsimring, Chidambaram Gunanathan, Alexey Potapov, Irena Efremenko, Jan M. L. Martin, David Milstein, and Daniella Goldfarb. Gd3+ complexes as potential spin labels for high field pulsed epr distance measurements. *Journal of the American Chemical Society*, 129(46):14138–14139, 2007. PMID: 17963387.

[101] Sahand Razzaghi, Mian Qi, Anna I. Nalepa, Adelheid Godt, Gunnar Jeschke, Anton Savitsky, and Maxim Yulikov. Ridme spectroscopy with gd(iii) centers. *The Journal of Physical Chemistry Letters*, 5(22):3970–3975, 2014. PMID: 26276479.

[102] A. Raitsimring, A. Dalaloyan, A. Collauto, A. Feintuch, T. Meade, and D. Goldfarb. Zero field splitting fluctuations induced phase relaxation of Gd3+ in frozen solutions at cryogenic temperatures. *Journal of Magnetic Resonance*, 248(Supplement C):71–80, 2014.

[103] J A van Wyk, E C Reynhardt, G L High, and I Kiflawi. The dependences of esr line widths and spin - spin relaxation times of single nitrogen defects on the concentration of nitrogen defects in diamond. *Journal of Physics D: Applied Physics*, 30(12):1790, 1997.

[104] Zhi-Hui Wang and Susumu Takahashi. Spin decoherence and electron spin bath noise of a nitrogen-vacancy center in diamond. *Phys. Rev. B*, 87:115122, Mar 2013.

[105] A. Jarmola, V. M. Acosta, K. Jensen, S. Chemerisov, and D. Budker. Temperature- and magnetic-field-dependent longitudinal spin relaxation in nitrogen-vacancy ensembles in diamond. *Phys. Rev. Lett.*, 108:197601, May 2012.

[106] Thomas Wolf, Philipp Neumann, Kazuo Nakamura, Hitoshi Sumiya, Takeshi Ohshima, Junichi Isoya, and Jörg Wrachtrup. Subpicotesla diamond magnetometry. *Phys. Rev. X*, 5:041001, Oct 2015.

[107] C. Grezes, B. Julsgaard, Y. Kubo, W. L. Ma, M. Stern, A. Bienfait, K. Nakamura, J. Isoya, S. Onoda, T. Ohshima, V. Jacques, D. Vion, D. Esteve, R. B. Liu, K. Mølmer, and P. Bertet. Storage and retrieval of microwave fields at the single-photon level in a spin ensemble. *Phys. Rev. A*, 92:020301, Aug 2015.

[108] J. R. Klauder and P. W. Anderson. Spectral diffusion decay in spin resonance experiments. *Phys. Rev.*, 125:912–932, Feb 1962.

[109] K.M Salikhov, S.A Dzuba, and A.M Raitsimring. The theory of electron spin-echo signal decay resulting from dipole-dipole interactions between paramagnetic centers in solids. *Journal of Magnetic Resonance (1969)*, 42(2):255 – 276, 1981.

[110] Alexei M. Tyryshkin, Shinichi Tojo, John J. L. Morton, Helge Riemann, Nikolai V. Abrosimov, Peter Becker, Hans-Joachim Pohl, Thomas Schenkel, Michael L. W. Thewalt, Kohei M. Itoh, and S. A. Lyon. Electron spin coherence exceeding seconds in high-purity silicon. *NATURE MATERIALS*, 11(2):143–147, FEB 2012.

[111] Carol A. Popp and James S. Hyde. Effects of oxygen on EPR spectra of nitroxide spin-label probes of model membranes. *Journal of Magnetic Resonance (1969)*, 43(2):249 – 258, 1981.

[112] Rikard Owenius, Gareth R. Eaton, and Sandra S. Eaton. Frequency (250mhz to 9.2ghz) and viscosity dependence of electron spin relaxation of triarylmethyl radicals at room temperature. *Journal of Magnetic Resonance*, 172(1):168–175, January 2005.

[113] W. K. Subczynski and James S. Hyde. The diffusion-concentration product of oxygen in lipid bilayers using the spin-label T1 method. *Biochimica et Biophysica Acta (BBA) - Biomembranes*, 643(2):283–291, May 1981.

[114] Boris Epel, Michael K. Bowman, Colin Mailer, and Howard J. Halpern. Absolute oxygen R1e imaging in vivo with pulse electron paramagnetic resonance. *Magnetic Resonance in Medicine*, 72(2):362–368, August 2014.

[115] W. K. Subczynski, L. Mainali, T. G. Camenisch, W. Froncisz, and J. S. Hyde. Spin-label oximetry at Q- and W-band. *Journal of Magnetic Resonance*, 209(2):142–148, April 2011.

[116] Andrey A. Kuzhelev, Dmitry V. Trukhin, Olesya A. Krumkacheva, Rodion K. Strizhakov, Olga Yu. Rogozhnikova, Tatiana I. Troitskaya, Matvey V. Fedin, Victor M. Tormyshev, and Elena G. Bagryanskaya. Room-Temperature Electron Spin Relaxation of Triarylmethyl Radicals at the X- and Q-Bands. *The Journal of Physical Chemistry B*, 119(43):13630–13640, October 2015.

[117] P.W. Anderson. Resonating valence bonds: A new kind of insulator? *Materials Research Bulletin*, 8(2):153 – 160, 1973.

[118] R. Coldea, D. A. Tennant, A. M. Tsvelik, and Z. Tylczynski. Experimental realization of a 2d fractional quantum spin liquid. *Phys. Rev. Lett.*, 86:1335–1338, Feb 2001.

[119] Leon Balents. Spin liquids in frustrated magnets. *Nature*, 464(7286):199, 2010.

[120] Lucile Savary and Leon Balents. Quantum spin liquids: a review. *Reports on Progress in Physics*, 80(1):016502, nov 2016.

[121] Matthias Vojta. Frustration and quantum criticality. *Reports on Progress in Physics*, 81(6):064501, may 2018.

[122] Dominic V. Else, Bela Bauer, and Chetan Nayak. Floquet time crystals. *Phys. Rev. Lett.*, 117:090402, Aug 2016.

[123] Soonwon Choi, Joonhee Choi, Renate Landig, Georg Kucsko, Hengyun Zhou, Junichi Isoya, Fedor Jelezko, Shinobu Onoda, Hitoshi Sumiya, Vedika Khemani, et al. Observation of discrete time-crystalline order in a disordered dipolar many-body system. *Nature*, 543(7644):221, 2017.

[124] Charles Slichter. *Principles of Magnetic Resonance*. Springer-Verlag Berlin Heidelberg, 3 edition, 1990.

[125] C. F. Koelsch. Syntheses with triarylvinylmagnesium bromides. 1,3-bisdiphenylene-2-phenylallyl, a stable free radical. *Journal of the American Chemical Society*, 79(16):4439–4441, 1957.

[126] M. Bennati, C.T. Farrar, J.A. Bryant, S.J. Inati, V. Weis, G.J. Gerfen, P. Riggs-Gelasco, J. Stubbe, and R.G. Griffin. Pulsed electron-nuclear double resonance (endor) at 140 ghz. *Journal of Magnetic Resonance*, 138(2):232 – 243, 1999.

[127] C. Durkan and M. E. Welland. Electronic spin detection in molecules using scanning-tunneling- microscopy-assisted electron-spin resonance. *Applied Physics Letters*, 80(3):458–460, 2002.

[128] Eric L. Dane and Timothy M. Swager. Synthesis of a water-soluble 1,3-bis(diphenylene)-2-phenylallyl radical. *The Journal of Organic Chemistry*, 75(10):3533–3536, 2010.

[129] Patrick Giraudeau, Yoav Shrot, and Lucio Frydman. Multiple ultrafast, broadband 2d nmr spectra of hyperpolarized natural products. *Journal of the American Chemical Society*, 131(39):13902–13903, 2009. PMID: 19743849.

[130] William Duffy, John F. Dubach, Piero A. Pianetta, Joseph F. Deck, Donald L. Strandburg, and Andries R. Miedema. Antiferromagnetic linear chains in the crystalline free radical bdpa. *The Journal of Chemical Physics*, 56(6):2555–2561, 1972.

[131] N. Azuma, T. Ozawa, and J. Yamauchi. Molecular and crystal-structures of complexes of stable free-radical bdpa with benzene and acetone. *Bulletin of the Chemical Society of Japan*, 67(1):31–38, 1994.

[132] Deborah G. Mitchell, Richard W. Quine, Mark Tseitlin, Ralph T. Weber, Virginia Meyer, Azure Avery, Sandra S. Eaton, and Gareth R. Eaton. Electron spin relaxation and heterogeneity of the 1:1 1,3-bisdiphenylene-2-phenylallyl (bdpa)/benzene complex. *The Journal of Physical Chemistry B*, 115(24):7986–7990, 2011. PMID: 21574594.

[133] J. Yamauchi and Y. Deguchi. Low dimensionality in organo-magnetic material - 9-(alpha-fluorenylidene-para-chlorobenzyl)-9-fluorenyl. *Bulletin of the Chemical Society of Japan*, 50(10):2803–2804, 1977.

[134] W. O. Hamilton and G. E. Pake. Linear antiferromagnetism in the organic free radical 1,3-bisdiphenylene-2-phenyl allyl. *The Journal of Chemical Physics*, 39(10):2694–2697, 1963.

[135] P. W. Anderson and P. R. Weiss. Exchange narrowing in paramagnetic resonance. *Rev. Mod. Phys.*, 25:269–276, Jan 1953.

[136] I. I. Rabi. Space quantization in a gyrating magnetic field. *Phys. Rev.*, 51:652–654, Apr 1937.

[137] Charles Kittel. On the theory of ferromagnetic resonance absorption. *Phys. Rev.*, 73:155–161, Jan 1948.

[138] Zangwill Andrew. *Modern Electrodynamics*. Cambridge University Press, 1st edition, 2013.

[139] Malcolm H. Levitt. Demagnetization field effects in two-dimensional solution nmr. *Concepts in Magnetic Resonance*, 8(2):77–103, 1996.

[140] Hommo T Edzes. The nuclear magnetization as the origin of transient changes in the magnetic field in pulsed nmr experiments. *Journal of Magnetic Resonance (1969)*, 86(2):293 – 303, 1990.

[141] R. Bowtell, R.M. Bowley, and P. Glover. Multiple spin echoes in liquids in a high magnetic field. *Journal of Magnetic Resonance (1969)*, 88(3):643 – 651, 1990.

[142] G. Deville, M. Bernier, and J. M. Delrieux. Nmr multiple echoes observed in solid 3he. *Phys. Rev. B*, 19:5666–5688, Jun 1979.

[143] A.S Bedford, R Bowtell, and R.M Bowley. Multiple spin echoes in multicomponent liquids. *Journal of Magnetic Resonance (1969)*, 93(3):516 – 532, 1991.

[144] WS Warren, W Richter, AH Andreotti, and BT Farmer. Generation of impossible cross-peaks between bulk water and biomolecules in solution nmr. *Science*, 262(5142):2005–2009, 1993.

[145] W Richter, S Lee, WS Warren, and Q He. Imaging with intermolecular multiple-quantum coherences in solution nuclear magnetic resonance. *Science*, 267(5198):654–657, 1995.

[146] Warren S. Warren, Sangdoo Ahn, Marlene Mescher, Michael Garwood, Kamil Ugurbil, Wolfgang Richter, Rahim R. Rizi, Jeff Hopkins, and John S. Leigh. Mr imaging contrast enhancement based on intermolecular zero quantum coherences. *Science*, 281(5374):247–251, 1998.

[147] J. Jeener. Equivalence between the "classical" and the "warren" approaches for the effects of long range dipolar couplings in liquid nuclear magnetic resonance. *The Journal of Chemical Physics*, 112(11):5091–5094, 2000.

[148] Masahiro Kitagawa and Masahito Ueda. Squeezed spin states. *Phys. Rev. A*, 47:5138–5143, Jun 1993.

[149] S. D. Bennett, N. Y. Yao, J. Otterbach, P. Zoller, P. Rabl, and M. D. Lukin. Phonon-induced spin-spin interactions in diamond nanostructures: Application to spin squeezing. *Phys. Rev. Lett.*, 110:156402, Apr 2013.

[150] Yong-Hong Ma, Xue-Feng Zhang, Jie Song, and E Wu. Bistability and steady-state spin squeezing in diamond nanostructures controlled by a nanomechanical resonator. *Annals of Physics*, 369:36 – 44, 2016.

[151] Marie Ramirez Cohen, Veronica Frydman, Petr Milko, Mark A. Iron, Elwy H. Abdelkader, Michael D. Lee, James D. Swarbrick, Arnold Raitsimring, Gottfried Otting, Bim Graham, Akiva Feintuch, and Daniella Goldfarb. Overcoming artificial broadening in gd3+–gd3+ distance distributions arising from dipolar pseudo-secular terms in deer experiments. *Phys. Chem. Chem. Phys.*, 18:12847–12859, 2016.

[152] Nurit Manukovsky, Akiva Feintuch, Ilya Kuprov, and Daniella Goldfarb. Time domain simulation of gd3+–gd3+ distance measurements by epr. *The Journal of Chemical Physics*, 147(4):044201, 2017.

[153] Katharina Keller, Valerie Mertens, Mian Qi, Anna I. Nalepa, Adelheid Godt, Anton Savitsky, Gunnar Jeschke, and Maxim Yulikov. Computing distance distributions from dipolar evolution data with overtones: Ridme spectroscopy with gd(iii)-based spin labels. *Phys. Chem. Chem. Phys.*, 19:17856–17876, 2017.

[154] C. Kutter, H. P. Moll, J. van Tol, H. Zuckermann, J. C. Maan, and P. Wyder. Electron-spin echoes at 604 ghz using far infrared lasers. *Phys. Rev. Lett.*, 74:2925–2928, Apr 1995.

[155] Susumu Takahashi, Ronald Hanson, Johan van Tol, Mark S. Sherwin, and David D. Awschalom. Quenching spin decoherence in diamond through spin bath polarization. *Phys. Rev. Lett.*, 101:047601, Jul 2008.

[156] Jessica A. Clayton, Katharina Keller, Mian Qi, Julia Wegner, Vanessa Koch, Henrik Hintz, Adelheid Godt, Songi Han, Gunnar Jeschke, Mark S. Sherwin, and Maxim Yulikov. Quantitative analysis of zero-field splitting parameter distributions in gd(iii) complexes. *Phys. Chem. Chem. Phys.*, 20:10470–10492, 2018.

[157] S. Chandrasekhar. Stochastic problems in physics and astronomy. *Rev. Mod. Phys.*, 15:1–89, Jan 1943.

[158] Susumu Takahashi, Johan van Tol, Christopher C. Beedle, David N. Hendrickson, Louis-Claude Brunel, and Mark S. Sherwin. Coherent manipulation and decoherence of $s = 10$ single-molecule magnets. *Phys. Rev. Lett.*, 102:087603, Feb 2009.

[159] N. Q. Vinh, Mark S. Sherwin, S. James Allen, D. K. George, A. J. Rahmani, and Kevin W. Plaxco. High-precision gigahertz-to-terahertz spectroscopy of aqueous

salt solutions as a probe of the femtosecond-to-picosecond dynamics of liquid water. *The Journal of Chemical Physics*, 142(16), 2015.

[160] Sergey Milikisiyants, Alexander A. Nevzorov, and Alex I. Smirnov. Photonic band-gap resonators for high-field/high-frequency epr of microliter-volume liquid aqueous samples. *Journal of Magnetic Resonance*, 296:152 – 164, 2018.

[161] Mian Qi, Miriam Hülsmann, and Adelheid Godt. Spacers for geometrically well-defined water-soluble molecular rulers and their application. *The Journal of Organic Chemistry*, 81(6):2549–2571, 2016. PMID: 26900782.

[162] G Varo, LS Brown, M Lakatos, and JK Lanyi. Characterization of the photochemical reaction cycle of proteorhodopsin. *BIOPHYSICAL JOURNAL*, 84(2, 1):1202–1207, FEB 2003.

[163] Magnus Andersson, Erik Malmerberg, Sebastian Westenhoff, Gergely Katona, Marco Cammarata, Annemarie B. Wohri, Linda C. Johansson, Friederike Ewald, Mattias Eklund, Michael Wulff, Jan Davidsson, and Richard Neutze. Structural Dynamics of Light-Driven Proton Pumps. *STRUCTURE*, 17(9):1265–1275, SEP 9 2009.

[164] Omri M. Finkel, Oded Beja, and Shimshon Belkin. Global abundance of microbial rhodopsins. *ISME JOURNAL*, 7(2):448–451, FEB 2013.

[165] Christian Bamann, Ernst Bamberg, Josef Wachtveitl, and Clemens Glaubitz. Proteorhodopsin. *Biochimica et Biophysica Acta (BBA) - Bioenergetics*, 1837(5):614 – 625, 2014. Retinal Proteins.

[166] O Beja, L Aravind, EV Koonin, MT Suzuki, A Hadd, LP Nguyen, S Jovanovich, CM Gates, RA Feldman, JL Spudich, EN Spudich, and EF DeLong. Bacterial rhodopsin: Evidence for a new type of phototrophy in the sea. *SCIENCE*, 289(5486):1902–1906, SEP 15 2000.

[167] Dikla Man, Weiwu Wang, Gazalah Sabehi, L. Aravind, Anton F. Post, Ramon Massana, Elena N. Spudich, John L. Spudich, and Oded Béjà. Diversification and spectral tuning in marine proteorhodopsins. *The EMBO Journal*, 22(8):1725–1731, 2003.

[168] WW Wang, OA Sineshchekov, EN Spudich, and JL Spudich. Spectroscopic and photochemical characterization of a deep ocean proteorhodopsin. *JOURNAL OF BIOLOGICAL CHEMISTRY*, 278(36):33985–33991, SEP 5 2003.

[169] D Man-Aharonovich, G Sabehi, OA Sineshchekov, EN Spudich, JL Spudich, and O Beja. Characterization of RS29, a blue-green proteorhodopsin variant from the Red Sea. *PHOTOCHEMICAL & PHOTOBIOLOGICAL SCIENCES*, 3(5):459–462, MAY 2004.

[170] Sina Reckel, Daniel Gottstein, Jochen Stehle, Frank Löhr, Mirka Kristin Verhoefen, Mitsuhiro Takeda, Robert Silvers, Masatsune Kainosho, Clemens Glaubitz, Josef Wachtveitl, Frank Bernhard, Harald Schwalbe, Peter Güntert, and Volker Dötsch. Solution NMR structure of proteorhodopsin. *Angew. Chem. Int. Ed.*, 50(50):11942–11946, 2011.

[171] Martin O. Lenz, Robert Huber, Bernhard Schmidt, Peter Gilch, Rolf Kalmbach, Martin Engelhard, and Josef Wachtveitl. First steps of retinal photoisomerization in proteorhodopsin. *Biophysical Journal*, 91(1):255 – 262, 2006.

[172] Andrei K. Dioumaev, Leonid S. Brown, Jennifer Shih, Elena N. Spudich, John L. Spudich, and Janos K. Lanyi. Proton transfers in the photochemical reaction cycle of proteorhodopsin. *Biochemistry*, 41(17):5348–5358, 2002. PMID: 11969395.

[173] Andrei K. Dioumaev, Jennifer M. Wang, Zoltán Bálint, György Váró, and Janos K. Lanyi. Proton transport by proteorhodopsin requires that the retinal schiff base counterion asp-97 be anionic. *Biochemistry*, 42(21):6582–6587, 2003. PMID: 12767242.

[174] Jochen Stehle, Frank Scholz, Frank Löhr, Sina Reckel, Christian Roos, Michaela Blum, Markus Braun, Clemens Glaubitz, Volker Dötsch, Josef Wachtveitl, and Harald Schwalbe. Characterization of the ground state dynamics of proteorhodopsin by nmr and optical spectroscopies. *Journal of Biomolecular NMR*, 54(4):401–413, Dec 2012.

[175] K. M. Stone, J. Voska, M. Kinnebrew, A. Pavlova, M. J. N. Junk, and S. Han. Structural insight into proteorhodopsin oligomers. *Biophys. J.*, 104:472, 2013.

[176] Sunyia Hussain, Maia Kinnebrew, Nicole S. Schonenbach, Emily Aye, and Songi Han. Functional consequences of the oligomeric assembly of proteorhodopsin. *Journal of Molecular Biology*, 427:1278–1290, 2015.

[177] A. L. Klyszejko, S. Shastri, S. A. Mari, H. Grubmüller, D. J. Muller, and C. Glaubitz. Folding and assembly of proteorhodopsin. *J. Mol. Biol.*, 376:35, 2008.

[178] Lichi Shi, Mumdooh A M Ahmed, Wurong Zhang, Gregg Whited, Leonid S Brown, and Vladimir Ladizhansky. Three-Dimensional Solid-State NMR Study of a Seven-Helical Integral Membrane Proton Pump-Structural Insights. *Journal of Molecular Biology*, 386(4):1078–1093, 2009.

[179] Meaghan E Ward, Lichi Shi, Evelyn Lake, Sridevi Krishnamurthy, Howard Hutchins, Leonid S Brown, and Vladimir Ladizhansky. Proton-detected solid-state NMR reveals intramembrane polar networks in a seven-helical transmembrane protein proteorhodopsin. *Journal of the American Chemical Society*, 133(43):17434–17443, 2011.

[180] Daniela Lalli, Matthew N. Idso, Loren B. Andreas, Sunyia Hussain, Naomi Baxter, Songi Han, Bradley F. Chmelka, and Guido Pintacuda. Proton-based structural analysis of a heptahelical transmembrane protein in lipid bilayers. *Journal of the American Chemical Society*, 139(37):13006–13012, 2017. PMID: 28724288.

[181] Tingting Ran, Gabriel Ozorowski, Yanyan Gao, Oleg A. Sineshchekov, Weiwu Wang, John L. Spudich, and Hartmut Luecke. Cross-protomer interaction with the photoactive site in oligomeric proteorhodopsin complexes. *Acta Crystallographica Section D: Biological Crystallography*, 69(10):1965–1980, 2013.

[182] Matthew N. Idso, Naomi R. Baxter, Sirish Narayanan, Evelyn Chang, Julia Fisher, Bradley F. Chmelka, and Songi Han. Proteorhodopsin function is primarily mediated by oligomerization in different micellar surfactant solutions. *The Journal of Physical Chemistry B*, 123(19):4180–4192, 2019. PMID: 30924654.

[183] Jakob Maciejko, Michaela Mehler, Jagdeep Kaur, Tobias Lieblein, Nina Morgner, Olivier Ouari, Paul Tordo, Johanna Becker-Baldus, and Clemens Glaubitz. Visualizing specific cross-protomer interactions in the homo-oligomeric membrane protein proteorhodopsin by dynamic-nuclear-polarization-enhanced solid-state nmr. *Journal of the American Chemical Society*, 137(28):9032–9043, 2015. PMID: 26102160.

[184] Sunyia Hussain, John M. Franck, and Songi Han. Transmembrane protein activation refined by site-specific hydration dynamics. *Angewandte Chemie - International Edition*, 52(7):1953–1958, 2013.

[185] Thomas Köhler, Ingrid Weber, Clemens Glaubitz, and Josef Wachtveitl. Proteorhodopsin photocycle kinetics between ph 5 and ph 9. *Photochemistry and Photobiology*, 93(3):762–771, 2017.

[186] J. van Tol, L.-C. Brunel, and R. J. Wylde. A quasioptical transient electron spin resonance spectrometer operating at 120 and 240 ghz. *Review of Scientific Instruments*, 76(7):074101, 2005.

[187] P.A.S. Cruickshank, D. R. Bolton, D. A. Robertson, R. J. Wylde, and G. M. Smith. Reducing standing waves in quasi-optical systems by optimal feedhorn design. *2007 Joint 32nd International Conference on Infrared and Millimeter Waves and the 15th International Conference on Terahertz Electronics*, pages 941–942, 2007.

[188] F.P Auteri, A.H Beth, and B.H Robinson. An automated method to find the proper modulation phase in continuous wave epr spectroscopy. *Journal of Magnetic Resonance (1969)*, 80(3):493 – 501, 1988.

[189] Denise Friselli, Carlo-Andrea Massa, Massimo Martinelli, Luca Pardi, and Irene Ricci. Simulation of the propagation effects in the hf-epr spectra of non-diluted magnetic materials. *Inorganica Chimica Acta*, 361(14–15):4164 – 4166, 2008. Protagonists in Chemistry: Dante Gatteschi (Part {II}).